THE UNIVERSITY OF
WARWICK

University of Warwick institutional repository: http://go.warwick.ac.uk/wrap

A Thesis Submitted for the Degree of PhD at the University of Warwick

http://go.warwick.ac.uk/wrap/34630

This thesis is made available online and is protected by original copyright.

Please scroll down to view the document itself.

Please refer to the repository record for this item for information to help you to cite it. Our policy information is available from the repository home page.

GLASS-CERAMIC COATINGS FOR METALS

by

ANDREW JOHN STURGEON

Submitted for the Degree of Doctor of Philosophy

UNIVERSITY OF WARWICK

Department of Physics

JANUARY 1987

MEMORANDUM

This dissertation is submitted to the University of Warwick in support of my application for admission to the degree of Doctor of Philosophy. It contains an account of my work carried out at the Department of Physics of the University of Warwick in the period October 1983 to October 1986 under the general supervision of Dr. D. Holland and the late Professor P.W. McMillan. No part of it has been used previously in a degree thesis submitted to this or any other University. The work described is the result of my own independent research except where specifically acknowledged in the text.

A.J. Sturgeon

Andrew John Sturgeon

January 1987

ACKNOWLEDGEMENTS

I would like to take this opportunity to thank the Science and Engineering Research Council for providing the financial support for this study, and also to thank the Department of Physics for making the facilities available for the research work. I am grateful to Dr. D. Holland for her supervision and guidance throughout the duration of this project. I am also grateful to the late Professor P.W. McMillan for his supervision during the early part of the project. In addition I should like to thank my colleagues in the Glass-Ceramic Group for their assistance and helpful discussions, and in particular the technical assistance of Mr. H. Mathers and Mr. R. Lamb. I also wish to thank Mr. D. Lee and Mr. P. Beecraft for their help. And to thank Mr. G. Smith and Mr. S. York for their assistance with the electron microscopy. I would like to thank Mrs S. Beaufoy for the time and effort spent in typing this thesis.

I would also like to acknowledge the assistance provided by the Stafford Laboratories, GEC Research, both financially and in use of their facilities. I am grateful to Mr. G. Partridge and Mr. C. Elyard for being my industrial supervisors.

ABSTRACT

An investigation was conducted into the coating of metal substrates with a glass-ceramic enamel. Two metal types were coated, a 17% chrome-iron and a low carbon mild steel. The glass-ceramic was based on a complex lithium aluminosilicate glass.

The enamel was applied using a vitreous enamelling coating technique, followed by conversion to a glass-ceramic. The coating process strongly influenced the microstructural form developed.

For both metal substrate types it was possible to produce coatings which wet well and exhibit good adhesion. Crystalline substrate oxide is observed at the interfaces of these coatings. Abrasion prior to preoxidation is an essential requirement for good coating adhesion on a chrome-iron substrate.

The interface region for a coating on chrome-iron exhibits little interaction or microstructural change. However the coating on mild steel exhibits extensive interaction, with a reaction zone extending into the coating. The marked difference between the two coated substrate types can be explained by the different substrate oxide formed, solubility of the substrate oxide in the coating and nucleating ability of the substrate oxide surface.

Addition of adherence oxides (NiO, CoO) to the coating on mild steel was examined. The adherence oxides participate in complex reactions which result in the formation of metallic alloys adjacent the interface. Both adherence oxides promote wetting under conditions where wetting is not possible if they are absent. Nickel oxide is detremental to coating adhesion. This may be related to its ability to cause a rapid dissolution of iron oxide present at the interface.

		page
Chapter 1. Introduction		
1.1	Background.	1
1.2	Traditional enamels.	2
1.3	Glass-ceramic enamels.	3
1.3.2	Advantages of glass-ceramic enamels.	5
1.3.3	Vitreous enamel coating method.	9
1.3.4	Applications of glass-ceramic enamels.	11
1.4	Aims and Outline of the project.	11
1.5	Thesis plan.	12
Chapter 2. Principles of enamel to metal bonding.		
2.1	Introduction.	14
2.2	Thermal expansion matching.	14
2.3	Wetting of a metal by a glass or enamel.	16
2.4	Enamel adherence.	
2.4.1	Introduction	21
2.4.2	Mechanical bonding.	21
2.4.3	Chemical bonding.	22
2.4.4	Interfacial reactions.	28
Chapter 3 Experimental Investigative Techniques.		
3.1	Measurement of coating adhesion.	
3.1.1	Introduction.	34
3.1.2	Tensile pull adhesion method.	36
3.2	Scanning electron microscopy and microanalysis.	
3.2.1	Introduction	42
3.2.2	Instrumentation.	47
3.2.3	Specimen preparation.	48
3.2.4	Qualitative Microanalysis.	49
3.2.5	Elemental distribution: X-ray area scanning.	50
3.2.6	Element distribution: Line scans.	51
3.2.7	Quantitative X-ray microanalysis.	51
3.2.8	Windowless analysis.	53
3.2.9	Problems with glasses and interfaces.	57
3.3	X-ray diffraction.	59
3.4	Measurement of thermal expansion Coefficient.	60
3.5	Differential thermal analysis.	62
3.6	Thermogravimetric analysis.	63

Chapter 4. Experimental preparative techniques.

4.1 Materials.
4.1.1 Composition. 64
4.1.2 Glass preparation. 67
4.1.3 Glass and glass-ceramic characteristics. 68

4.2 Coating techniques.
4.2.1 Glass powder formation. 74
4.2.2 Metal pretreatment and oxidation. 76
4.2.3 Screen printing technique. 85
4.2.4 Firing conditions. 86
4.2.5 Heat-treatment. 91

4.3 Firing of bulk glass on oxide discs. 92

4.4 Bulk glass containing substrate oxides. 93

Chapter 5. Results

5.1 Coating on chrome-iron.
5.1.1 Introduction. 97
5.1.2 Enamel coating on chrome-iron quenched after firing, 97
5.1.3 Enamel coating on chrome-iron heat-treated after firing, C5H. 107
5.1.4 Microstructural development during firing. 111
5.1.5 Reaction between the substrate and coating. 119
5.1.6 Influence of firing time on interdiffusion. 124
5.1.7 Variation in metal pre-treatment. 126
5.1.8 Tensile adhesion of the enamel coatings. 133

5.2 Coating on mild steel.
5.2.1 Wetting ability of glass B on mild steel. 138
5.2.2 Enamel coating on mild steel quenched after firing. 140
5.2.3 Enamel coating on mild steel heat-treated after firing. 153
5.2.4 Oxide formation under screen printed powder. 161
5.2.5 Variation in firing parameters. 163
5.2.6 Iron oxide dissolution. 163
5.2.7 Microstructure development. 171
5.2.8 Diffusion of ferrous oxide in the coating. 175
5.2.9 Coating adhesion. 180
5.2.10 Influence of adherence oxides. 184
5.2.11 Bulk glass B fired on iron oxide discs. 200

Chapter 6 Discussion

6.1 Devitrification of the bulk enamel coating. 204

6.2 Enamel coatings on chrome-iron.
6.2.1 Interfacial structure. 210
6.2.2 Interfacial interaction. 213
6.2.3 Dissolution of substrate oxides into the coating. 216
6.2.4 The influence of substrate oxides on coating crystallisation. 220
6.2.5 Variation in preoxidation of the substrate. 220
6.2.6 Wetting and adhesion for coatings on chrome-iron. 223

6.3 The coating of mild steel.

6.3.1 Introduction. 228
6.3.2 Iron oxide dissolution. 228
6.3.3 Diffusion of ferrous oxide into the coating during firing. 231
6.3.4 Interfacial enrichment of litrium in the coating. 233
6.3.5 Coating cyrstallistion - dendritic growth. 238
6.3.6 Coating crystallisation - Microstructural development of the fired only coating. 242
6.3.7 Coating crystallistion - Microstructural development of the heat-treated coating. 243
6.3.8 Potassium distribution. 245
6.3.9 Wetting. 248
6.3.10 Coating adhesion 250

Chapter 7 Conclusions and future work. 259

Appendix A.1. Glass-ceramics.
A.2. Diffusion.
A.3. Spectrometer method for the determination of the ferrous-ferric ratio in glass.
A.4. LIMA analysis.
A.5. Properties of Various cations.

LIST OF FIGURES page

Figure 2.1 Periphery forces for a liquid drop on a solid surface. 18

Figure 2.2 Interface bonding between a glass and metal. (a) discrete metal oxide layer, (b) mono-oxide layer, (c) Van-der-Waals bonding. 25

Figure 2.3 Activity of metal oxide across a glass-metal interface. 27

Figure 3.1 Tensile pull adhesion test apparatus. 40

Figure 3.2 Signal emissions resulting from electron beam-sample interaction. 43

Figure 3.3 Sample position in scanning electron microscope. 43

Figure 3.4 Fused silica dilatometer. 61

Figure 4.1 DTA curves for glass A and glass B. 69

Figure 4.2 Thermal expansion of glass A, glass-ceramic A and 17% chrome-iron. 73

Figure 4.3 Thermal expansion of glass B, glass-ceramic B and mild steel. 73

Figure 4.4 Glass powder size distribution after milling. 75

Figure 4.5 XRD patterns of a unoxidised and preoxidised 17% chrome-iron surface. 77

(a) unoxidised metal surface.

(b) oxidised in wet hydrogen.

(c) oxidised in air at 970°C for 5 minutes.

Figure 4.6 Electron micrographs of chrome-iron surface. 78

(a) abraded but not oxidised.

(b) preoxidised in wet hydrogen.

Figure 4.7 XRD patterns of a unoxidised and preoxidised mild steel surface. 81
(a) unoxidised metal surface.
(b) 15 minutes at 650°C.
(c) 15 minutes at 750°C.
Figure 4.8 Iron oxide weight gain with time at 500, 600, 650, 700, 800 and 900°C. 83
Figure 4.9 Thermogravimetric measurement on powder plus binder. 87
Figure 4.10 Tube furnace used to fire and heat-treat the coatings. 87
Figure 5.1.1 Backscattered electron micrographs of a coating on chrome-iron subjected to a firing C5. 98
Figure 5.1.2 XRD pattern collected from exposed chromium oxide layer. 102
Figure 5.1.3 Backscattered and secondary electron micrographs of fired only coating etched in HF acid. 103
Figure 5.1.4 XRD pattern collected from removed coating ground to a powder. 104
(a) fired only C5
(b) heat-treated C5H
Figure 5.1.5 Element distribution collected from linescans conducted across the interface. 105
(a) fired only C5
(b) heat-treated C5H
Figure 5.1.6 Quantitative element distribution across the interface of a fired only coating, C5. 106
Figure 5.1.7 Backscattered electron micrographs of a coating on chrome-iron fired and heat-treated, C5H. 109
Figure 5.1.8 Different microstructure forms of heat-treated coating. 110

Figure 5.1.9 Backscattered electron micrographs of coatings subjected to increasing firing times. 115
(a) 0.5 minutes (C1), (b) 1 minute (C2),
(c) 2 minutes (C3), (d) 4 minutes (C4),
(e) 40 minutes (C7), (f) 180 minutes (C10)

Figure 5.1.10 XRD patterns collected from coatings subjected to increasing firing time. 116
(a) 0.5 minutes (C1), (b) 1 minute (C2),
(c) 2 minutes (C3), (d) 4 minutes (C4),
(e) 40 minutes (C7), (f) 180 minutes (C10).

Figure 5.1.11 XRD patters collected from bulk glass A subjected to various thermal treatments 117
(a) fired only, 5 minutes 967°C
(b) fired and heat-treated
(c) heat-treated only.

Figure 5.1.12 Backscattered electron micrographs of bulk glass A subjected to various thermal treatments. 118
(a) fired only
(b) fired and heat-treated
(c) heat-treated only.

Figure 5.1.13 Coating on Chrome-iron preoxidised in wet hydrogen and fired for 6 hours at 970°C, (C11). 122

Figure 5.1.14 Width of lithium chromium silicate layer for increasing firing times. 123

Figure 5.1.15 Glass A heated at 970°C for 10 days on a chromium oxide disc. 122

Figure 5.1.16 Quantitative element distribution across the interface of coatings fired for increasing times. 125
(a) 40 minutes, C7
(b) 2 hours, C9
(c) 24 hours, C13

Figure 5.1.17 Backscattered electron micrographs for coats on chrome-iron substrates given different pretreatments and preoxidations. 129

Figure 5.1.18 X-ray maps of $Fe_{k\alpha}$ and $Cr_{k\alpha}$. 131

(a) for a coating on chrome-iron initially preoxidised in air, C18H.

(b) for a coating on chrome-iron not initially preoxidised, C20H.

Figure 5.1.19 Quantitative element distributions across the interfaces of coatings on various pretreated chrome-iron substrates. 132

(a) Preoxidised in wet hydrogen, C17H.

(b) Preoxidised in air, C18H.

(c) not preoxidised, C20H.

Figure 5.1.20 Backscattered electron micrographs of exposed coating surfaces, 137

(a) preoxidised in wet hydrogen, C17H.

(b) preoxidised in air, C18H.

(c) not preoxidised, C20H.

Figure 5.2.1 Appearance of coating on mild steel. 141

(a) fired only coating

(b) heat-treated coating.

Figure 5.2.2 Backscattered electron micrographs of a coating on mild steel subjected to a firing only, M9. 142

Figure 5.2.3 XRD patterns collected from removed coating. 145

(a) fired only, M9

(b) heat-treated, M9H.

Figure 5.2.4 XRD patterns collected from the exposed coating surface, 146

(a) fired only coating, M9.

(b) heat-treated coating, M9H.

Figure 5.2.5 Element distribution collected from line scans conducted across the interface. 149
(a) fired only, M9
(b) heat-treated, M9H.
Figure 5.2.6 Quantitative element distribution across the interface of a fired only coating, M9. 150
Figure 5.2.7 Quantitative element distribution across the interface of a fired only coating, M9. 150
(a) "windowless" EDX
(b) L.I.M.A.
Figure 5.2.8 Backscattered electron micrographs of a coating on mild steel fired and heat-treated, M9H. 154
Figure 5.2.9 XRD patterns collected from a removed coating, M9H. 159
(a) ground to a powder
(b) exposed coating surface
(c) exposed glass B ferrous oxide interface.
Figure 5.2.10 Backscattered electron micrograph of iron oxide present at interface, M3. 162
Figure 5.2.11 Backscattered electron micrographs of coatings subjected to various firing conditions.
(a) M5, (b) M7, (c) M10, (d) M12, (e) M15, (f) M17, (g) M18. 164
Figure 5.2.12 Backscattered electron micrographs of coatings subjected to various firing conditions then given a "standard" heat-treatment. 165
(a) M5, (b) M7, (c) M10, (d) M12, (e) M15, (f) M17, (g) M18.

Figure 5.2.13 Quantitative element distribution across the interface of coatings subjected to various firing conditions. 166
(a) M5, (b) M7, (c) M10, (d) M12, (e) M15, (f) M17, (g) M18.

Figure 5.2.14 Schematic representation of microstructural development. 173
(a) fired only coatings
(b) heat-treated coatings.

Figure 5.2.15 (a) Plot of M_{FeO} with increasing firing time ($t^{\frac{1}{2}}$). 178
(b) Plot of D_{FeO} with reciprocal of temperature.

Figure 5.2.16 (a) Plot of X_b with increasing firing time ($t^{\frac{1}{2}}$). 179
(b) Plot of D_{FeO} with reciprocal of temperature.

Figure 5.2.17 Backscattered electron micrograph of exposed surface of coating removed during tensile adhesion testing (M9H). 183

Figure 5.2.18 Backscattered electron micrographs of coatings containing 0.25 wt% CoO on mild steel. 187

Figure 5.2.19 XRD patterns collected from the exposed coating surface. 189
(a) fired only coating, M19.
(b) heat-treated coating, M19H.

Figure 5.2.20 Element distribution collected from linescans conducted across the interface. 190
(a) fired only coating, M19.
(b) heat-treated coating, M19H.

Figure 5.2.21 Quantitative element distribution across the interface of a fired only coating, M19. 191

Figure 5.2.22 Backscattered electron micrographs of coatings containing 0.25 wt% NiO on mild steel. 194

Figure 5.2.23 XRD patterns collected from the exposed coating surface. 195
(a) fired only coating, M22.
(b) heat-treated coating, M22H.
Figure 5.2.24 Element distribution collected from linescans conducted across the interface. 196
(a) fired only coating, M22.
(b) heat-treated coating, M22H.
Figure 5.2.25 Quantitative element distribution across the interface of a fired only coating, M22. 197
Figure 5.2.26 Backscattered electron micrographs of the interface between, 203
(a) ferrous oxide and glass B,
(b) ferrous oxide and glass B plus 0.25 wt% CoO,
(c) ferrous oxide and glass B plus 0.25 wt% NiO,
(d) ferric oxide and glass B,
(e) ferric oxide and glass B plus 0.25 wt% CoO,
(f) ferric oxide and glass B plus 0.25 wt% NiO.

Figure 6.1 Potassium movement. 209
Figure 6.2 Schematic representation of interface boundary layers for a coating on chrome-iron preoxidised in "wet" hydrogen. 212
(a) short firing time.
(b) long firing time.
Figure 6.3 Schematic representation of interface features for a coating on chrome-iron. 214
(a)preoxidised in air
(b) not preoxidised.

Figure 6.4 Ternary molar composition diagram $FeO-Li_2O-SiO_2$+ minor oxides. 234

Figure 6.5 Possible representation of the psuedo-binary system FeO - glass B. 239

LIST OF TABLES

		page
1.1	Composition of traditional enamels.	4
1.2	Typical ranges of properties for glasses, glass-ceramics and common ceramics.	6
1.3	Properties of some specific glasses, glass-ceramics and common ceramics.	7
2.1	Free energies of formation of metal oxides at 1000°C.	32
3.1	Typical strength of adhesives under tensile loading conditions.	37
3.2	Chromic acid pretreatment solution.	37
3.3	Adhesion as measured by the tensile loading method.	41
3.4	Primary modes of contrast.	44
3.5	Characteristics of the EDX Spectrometer.	47
3.6	Characteristic X-ray lines for elements of interest.	50
3.7	Composition of iron containing glasses.	54
3.8	Compoosition of iron containing glasses (windlowless EDX analysis).	56
4.1	Glass composition.	65
4.2	Role of oxides in glass.	65
4.3	Metal composition.	66
4.4	Composition of prepared glasses.	67
4.5	Heat-treatment schedules.	70
4.6	Thermal expansion coefficients for glass A, glass-ceramic A and chrome-iron.	71

4.7	Thermal expansion coefficients for glass B, glass-ceramic B and mild-steel.	72
4.8	Composition of oxide scale on chrome-iron oxidised in wet hydrogen.	79
4.9	Oxidation of mild steel.	84
4.10	Weight of oxide determined by equation 4.1.	84
4.11	Firing conditions for enamels on chrome-iron.	89
4.12	Firing conditions for enamels on mild steel.	90
4.13	Glass-oxide couples.	93
4.14	Composition of bulk glass A containing Chromium oxide.	95
4.15	Composition of bulk glass B containing iron oxides.	96
5.1.1	Thermal treatment of bulk glass A.	119
5.1.2	Thickness of lithium chromium silicate layer.	120
5.1.3	Composition of lithium chromium silicate layer.	121
5.1.4	X-ray pattern collected from a chromium oxide glass A interface.	121
5.1.5	Influence of pretreatment and preoxidation.	128
5.2.1	Influence of preoxidation.	139
5.2.2	Influence of preoxidation.	139
5.2.3	Composition of dendrite phase	143
5.2.4	XRD patterns for iron oxide formed under different conditions.	147
5.2.5	Measured concentration after removal of iron.	153
5.2.6	Composition of interfacial Crystal phases.	157
5.2.7	Composition of interfacial matrix phases.	157
5.2.8	Position of peaks on x-ray patterns collected from exposed glass-ferrous oxide interfaces.	158
5.2.9	Measured concentration after removal of iron.	161

5.2.10	Coating properties.	170
5.2.11	Mass of iron oxide taken into solution by the coating.	171
5.2.12	Influence of ferrous oxide on crystallisation.	175
5.2.13	Coating adhesion.	181
5.2.14	Composition of exposed coating surfaces.	181
5.2.15	Influence of adherence oxides on wetting ability of coating on mild steel.	185
5.2.16	Composition of metallic alloy phase.	188
5.2.17	Coating adhesion.	199
5.2.18	Interfacial compositions of glass B fired on various substrate materials.	199
6.1.	Crystallisation process	207
6.2	Mass of iron oxide taken into solution by a coating on chrome-iron preoxidised in wet hydrogen.	219
6.3	The interfacial composition of the coating determined by various methods for a coating on mild steel.	231
6.4	Self diffusion coefficients for various ions in several glass types at 1000°C.	237
6.5	Reducing power of various ions in a molten sodium disilicate glass.	258
A.1	Typical glass-ceramic systems.	

CHAPTER ONE

INTRODUCTION

1.1 Background

The requirement for ceramic coatings on metals is of significant technological importance. Ceramics, when compared to metals, exhibit many superior properties particular at elevated temperatures. Important improvements are a greater hardness, chemical and thermal stability. By coating a metal substrate or article the beneficial properties of ceramics can be utilised while avoiding problems such as brittle fracture which have traditionally limited their use in engineering applications. Coatings find many uses based on the ability to provide resistance to oxidation, chemical corrosion, and abrasion. Such a coating may also act as a thermal or electrical barrier.

Ceramic coatings may be divided into two groups: Vitreous or Porcelain enamels and refractory ceramic coatings.

Enamels are glassy coatings applied to metals, usually sheet steel, cast iron or aluminium, to provide protection and improve appearance. They can be distinguished from the second group of ceramic coatings by their predominantly vitreous nature and types of applications for which they are used. The traditional applications of enamels for domestic ware has expanded to include an extensive range of industrial applications from protection of chemical processing vessels, agricultural storage tanks, piping and pump components to architectural panels and microcircuitry components.

The second group are high temperature coatings based on oxides, nitrides and carbides which are applied to the substrate by several

deposition techniques. Such coatings have found varied applications dependent on the ceramic properties and method of coating. A list of present uses would include furnace components, chemical processing equipment, heat exchangers, jet engine parts and nuclear plant components.

The coating of metal articles with vitreous enamels has been limited to essentially chemical protection. Glasses show only limited resistance to abrasion, thermal and mechanical shock and have a relatively low thermal stability. The properties of vitreous enamels may be considerably improved by conversion to a polycrystalline material or glass-ceramic. Significant improvements in mechanical properties, hardness and thermal stability are obtained. This will also allow use of enamel coatings to be extended into more technical applications where the refracting oxide coatings are generally used.

1.2 Traditional Enamels

Enamels have a wide variety of compositions based on alkali-borosilicates with several minor additions. They can be applied to most metals but usually only sheet steel, cast iron and aluminium are enamelled in significant quantities. Good reviews exist, see White (1), Andrews (2), Vargen (3) and Hlavac (4), so only a brief outline will be given, concentrating on low carbon (< 0.1% C) sheet steel, which is by far the most commonly coated metal.

Enamels for Steels may be classified as either ground coat or cover coat enamels. Ground coats are applied directly to the metal surface and contain oxides that promote adherence (NiO, CoO, CuO).

Two important functions of the ground coat are to provide satisfactory coating adherence and act as a protective layer which minimises surface defects caused by the substrate or preparation method. A typical composition is given in Table 1.1.

Cover coats are applied over the ground coat to improve appearance, provide the required colour and degree of opacity, and give the desired protective properties of the coating. Zirconia and antimony oxide have been used in the past for opacification. The most significant advance in modern enamels has been the development of titania cover coats. The incorporation of up to 30 wt% TiO_2 smelted into a clear glass frit, recrystallises as anatase and rutile during firing - See Epper (5), Epper and Mcleran (6), Patrick (7). A high degree of opacity is obtained and a proportion of TiO_2 remaining dissolved in the glass imparts improved chemical resistance. These partially crystallised titania enamels represent a marked improvement and most commercial enamel compositions are based upon them. A typical composition is given in Table 1.1.

1.3 Glass-Ceramic Enamels

1.3.1 Glass-ceramics

Glass-ceramics are a group of materials which are essentially polycrystalline solids, prepared by the controlled crystallisation of suitable glasses producing one or more crystalline phases and a residual glass phase. See McMillan (9) and Appendix A.1.

The tendency for crystallisation to occur depends on two factors: Nucleation and Growth. Crystallisation requires firstly the formation of nucleation centres upon which growth may subsequently

Constituent	Ground Coat Regular Blue-Black Enamel	Cover Coat Titania White Enamel
	Wt%	
SiO_2	33.74	41.55
B_2O_3	20.16	12.85
Na_2O	16.74	7.18
K_2O	0.90	7.96
Li_2O	-	0.59
CaO	8.48	-
BaO	9.24	-
ZnO	-	1.13
Al_2O_3	4.11	-
TiO_2	-	21.30
CuO	-	3.03
MnO_2	1.43	-
NiO	1.25	-
Co_3O_4	0.59	-
P_2O_5	1.04	3.03
F_2	2.32	4.41

From Metals Handbook [8]

Table 1.1: Composition of traditional enamels

proceed. To produce a fine microstructure the nucleation and crystallisation temperature intervals should only have a small overlap. This allows the glass to be held at a temperature which will produce a high density of nucleation sites. Followed by an increase to a temperature where these nuclei undergo crystal growth. In producing a glass-ceramic, nucleating agents are added to the parent glass. These may be noble metals (Au, Ag, Cu) or oxides (TiO_2, P_2O_5). They cause an increase in the density of nucleation sites producing a finer microstructure after crystal growth.

Glass-ceramics have outstanding mechanical, thermal and electrical properties, which are related to composition, crystallographic constitution and microstructure. The microstructure is of a very fine polycrystalline nature, typically submicron crystal size, with a small residual glass fraction. Glass-ceramics are isotropic and are generally free of porosity. Many of the properties are controllable, by variations in compositions and thermal treatments, allowing a required property to be tailored to a particular application.

1.3.2 Advantages of Glass-ceramic enamels

Comparison of some relevant properties of oxide glasses, glass-ceramics and conventional ceramics are given in Tables 1.2 and 1.3.

Glass-ceramics show improvements over glasses in moduli of rupture, hardness and refractory properties. An increase in hardness is important for improving abrasion and erosion characteristics, work by Waternale (10), Stookey (11), and Atkinson (12) show

Property	Units	Glasses	Glass-Ceramics	Ceramics*
Modulus of rupture	MNm^{-2}	55-70	70-350	0-1000
Modulus of elasticity	$10^4\ MNm^{-2}$	6-8	8-14	7-40
Thermal expansion coefficient	$10^{-7}{}^oC^{-1}$	5-120	-40-+200	20-120
Max. Usable temperature	^oC	400-600	800->1000	> 1000
Hardness (Knoop)	$kg\,mm^{-2}$	400-500	600-700	1000-4000
Thermal conductivity	$Wm^{-1}K^{-1}$	1.5-1.7	2-5	4-200
Electrical resistivity	Ωcm	10^7-10^{11}	10^8-10^{11}	10^7-10^{10}
Dielectric strength	$kV\ mm^{-1}$	50-150	30-50	20-50

*Ceramics refers to common, single oxide, materials.

Table 1.2: Typical ranges of properties for glasses, glass-ceramics and ceramics (25°C)

Property	Unit	Soda-lime glass	Lithium-alumino Zinc silicate Glass-ceramic	Porcelain	Sintered Al_2O_3	Sintered ZrO_2
Moduli of rupture	MNm^{-2}	50	270	40-90	150-400	150
Moduli of elasticity	$10^4\ MNm^{-2}$	6.9	8.7	6.9	36.6	15
Thermal expansion	$10^7 {}^oC^{-1}$	90	80-130	35-45	76	90
Maximum usable temp.	^oC	550	850	1100	1800	2300
Thermal conductivity	$W(mK)^{-1}$	1.5-1.6	2.8	1.4-1.6	10	2
Hardness (Knoop)	$Kg\ mm^2$	450-500	600	800	1600	1000-1500
Electrical resistivity 100°C	Ωcm	10^7	10^{11}	10^8-10^{12}	10^{12}	10^5
Dielectric strength	$kVmm^{-1}$	40	47	25-60	20-50	-

Table 1.3 Properties of some specific glasses, glass-ceramics and ceramics

glass-ceramics have significant improvements in hardness over glasses although not as good as the best ceramic materials.

Another advantageous property is the wide range of values of thermal expansion coefficient possible for a glass-ceramic, exceeding that of both glasses and common ceramics. The value of expansion is controllable by variations in the initial parent glass and subsequent heat treatment. This allows close matching to a particular metal or alloy.

Impact strength and thermal shock resistance are two important properties for coatings. Both are complex quantities determined by a number of characteristics of the bulk material (elasticity, thermal expansion), Kingery (13), and by stresses set up at the coating metal interface. McMillan and Tesh (14) have shown the impact strength of bulk glass-ceramics to be superior to glasses. Partridge (15) has looked at the development of a glass-ceramic enamel exhibiting improved impact strength, thermal shock resistance and abrasion resistance compared to a conventional cover coat enamel. The chemical durability was found to be comparable to conventional enamels with the addition of small amounts of oxides such as Al_2O_3 or ZnO. This is confirmed by Makarova (16).

The isotropic nature and absence of porosity of a bulk glass-ceramic may be achievable in a coating. This offers distinct advantages compared to some of the traditional ceramic coatings. For example plasma sprayed coatings, as described by Scott (17), exhibit a lamellar structure and often have a high residual porosity.

Glass-ceramics can be seen to offer significant potential for improving enamel properties and extending their usage, particularly where high strength and temperature capability are required.

1.3.3 Vitreous enamel coating method

To achieve a glass-ceramic or enamel coating the vitreous enamelling coating technique is most widely used. A glass powder is fused to produce a thin, continuous amorphous layer on the metal surface. This is subsequently converted to a polycrystalline solid or glass-ceramic by a suitable thermal treatment. The principles are extensively discussed by the Pfandler Permutit Company (18). The process may be divided into four steps, each influencing the final properties and adhesion of the coating:-

- Preparation of the parent glass and conversion to a glass powder.
- Application of the glass powder to the metal surface.
- Fusion to produce an amorphous coating.
- Subsequent heat-treatment producing a conversion to a glass-ceramic.

A glass batch of the required composition, including one or more nucleating agents is melted to produce an amorphous mass. This is cast into water (or another suitable fluid) forming a glass frit. The frit is converted to a fine powder by conventional dry or wet milling techniques. A common method is milling with alumina balls. Wet milling in organic solvants is usually found to give the most suitable powder characteristics. The resulting slurry may be kept or dried and passed through a series of sieves to select the required powder size fraction.

Numerous possibilities for applying the glass powder to the metal are feasible. They may initially require the mixing of the powder with suitable aqueous or organic solvents dependent upon the coating method and required rheological properties. Typical application methods include the simple pouring of a slurry, wet spraying, dry electrostatic spraying, electrophoretic deposition and screen printing.

The coated metal is placed into a preheated furnace in which the glass is heated to a sufficient temperature to allow the glass particles to coalesce and fuse on the metal surface forming a continuous adherent, glassy coating. The lower limit of the firing temperature is set by the viscosity characteristics of the glass and the upper temperature set by that at which excessive deformation of the metal base occurs. When uncoated metal surfaces are susceptible to extensive oxidation it is necessary to restrict the oxygen content of the furnace by passing a reducing or inert gas through the furnace.

The coating may be formed directly on the metal surface, or if required, on a ground coat conventionally used in vitreous enamelling. The maximum temperature attained in applying the subsequent glass-ceramic coat must be lower than the maximum temperature to which the ground coat has previously been fired.

The amorphous coating is subjected to a two stage, nucleation and growth, heat-treatment causing the glass to convert to a glass-ceramic. During these longer heat-treatment times it may be necessary to again provide a non oxidising atmosphere. Often it is possible to fuse and crystallise the coating in a single firing without a second heat-treatment stage, as discussed by Davis et al (19). This would be expected to occur when the firing temperature is below, but near to, the liquidus temperature of the major crystal

phase present. Crystallisation can be enhanced by the large surface area of the initial glass powder, and surface crystallisation could even be the predominant crystallisation mechanism. The result is a much reduced thermal treatment time required for complete crystallisation as it is achieved during the short firing period.

1.3.4 Applications of glass-ceramic enamels

Glass-ceramic enamels have been developed for mild steel based on a Li_2O-Al_2O_3-SiO_2 composition. Davis et al (19) and a Li_2O-B_2O_3-SiO_2 composition, Partridge (15). These are used essentially to provide protection from oxidation and corrosion. A glass-ceramic coating based on a BaO-MgO-B_2O_3-SiO_2 composition has been developed by Andrus (20) and the RCA company (21) to provide an electrically insulating layer for use as electrical substrates.

A coating for copper based on a Li_2O-ZnO-SiO_2 system for use in multilayer electrical circuits is described by McMillan (22).

The other metals for which coatings have been developed are Tungsten and Molybdenum. Compositions based on ZnO-Al_2O_3-B_2O_3-SiO_2 have been used (23) and also by McMillan and Partridge (24). Such coatings provide these refractory metal$ with resistance against oxidation up to temperatures in excess of 1100^{o}C.

1.4 Aims and Outline of the project

Glass-ceramic coatings have found a growing number of applications since the original patent by Pfandler Permutit Company (18). However, little fundamental information is available on the interactions between the glass-ceramic and metal, on adhesion

mechanisms and on possible effects, at the glass-metal interface, on crystal nucleation and growth processes in the original glass coating. The project aims to provide some answers to these questions based on investigations into the coating of a 17% chrome-iron alloy and low carbon mild steel, with glass-ceramics derived from lithium alumino silicate glasses.

The addition of small amounts of transition metal oxides [CoO and NiO] to the coating composition has long been known to promote adherence of vitreous enamels to metal substrates. The project also aims to investigate the role of these oxides in glass-ceramic enamels.

1.5 Thesis Plan

The thesis is divided into seven chapters.

Chapter 1 reviews enamel coatings and the potential offered by glass-ceramic enamels. It includes a discussion of the vitreous enamelling technique as applied to glass-ceramic coatings.

Chapter 2 discusses the theories on enamel adhesion and the function of adherence oxides.

Chapter 3 discusses the experimental techniques, in particular, scanning electron microscopy with microanalysis and the development of a method to measure coating adhesion.

Chapter 4 describes the materials used, method of coating and heat treatments used to produce a glass-ceramic coating.

Chapter 5 contains the results for coatings on chrome-iron and mild steel substrates.

Chapter 6 discusses the overall experimental results.

Chapter 7 summarises the main conclusions of the work and generally concludes the discussion. Suggestions for future work are made.

CHAPTER TWO

Principles of enamel to metal bonding

2.1 Introduction

Although little information exists on glass-ceramic to metal bonding, substantial research has been conducted into the bonding mechanisms and interfacial reactions between glasses or traditional enamels and metals. Most of the investigations have concentrated on the porcelain enamelling of low carbon mild steel. It is essential to understand these as they may play a part in glass-ceramic enamel to metal bonding.

Three principle requirements need to be met to produce a good quality, well adhering coating:-

1. Close matching of thermal expansion coefficients of the metal and the glass-ceramic.
2. Wetting of the metal by the glass.[1]
3. Attainment of a strong bond between the glass-ceramic and metal.

2.2 Thermal expansion matching

When coating a metal substrate it is important to avoid the creation of destructive stresses at the coating-metal interface. As the coated metal begins to cool, after the initial fusion of the glass during coating, the metal starts to contract. So long as the glass is

---

1. The term glass will be used for a coating in a highly vitreous state, not having been subjected to a controlled heat-treatment.

in a plastic form it can deform and relieve any stresses present. On further cooling the glass viscosity increases to a value when it behaves as a rigid body. The glass can no longer accommodate changes in the metal base once a viscosity of about 10^{12} poises is reached. On continued cooling below the set temperature, both the metal and glass contract each at their own rate dependant upon their thermal expansion coefficient. If the glass has a thermal expansion coefficient smaller than that of the metal, it contracts less rapidly and will be in compression once cooled to room temperature. In the reverse case the glass will be in tension. The magnitude of the stresses set up will depend on the relative thermal expansion coefficients, the temperature at which the glass sets and on the modulus of elasticity etc. of the materials.

As a glass is mechanically weak in tension, and strong in compression, the expansion curves should be matched to cause the glass to be slightly in compression. It is generally regarded that a compressive stress of 5-21 MNm^{-2}, preferably about 10 MNm^{-2}, is desirable for optimum coating properties such as impact strength. Matching is not such an essential requirement for very thin coatings and when using ductile metals (e.g. copper) provided compressive stresses still exist.

The same will be true for crystallisable glasses. The stresses set up at the interface will now also depend on the heat-treatment which determines the crystal composition, volume fraction and residual glass composition, which in turn determine the thermal expansion.

The parent glass may have a coefficient of expansion much less than the metal being coated with excessive stresses produced on cooling. This problem can be avoided provided the temperature does

not fall below the set point, of the glass, on transfer to the heat-treatment stage.

It is also important to consider changes in dimensions which may occur during crystallisation. However McMillan [25] has shown this is not a problem for a lithium-aluminosilicate glass-ceramic. The viscosity at which significant volume change occurs is below 10^{10} poises, allowing stress release by deformation.

Crystal phases which exhibit phase inversions, below the set point, accompanied by marked volume changes should be avoided. Crystobalite is an unsuitable crystal phase due to the α-β transformation at 250°C accompanied by a 5% volume decrease on cooling, McMillan [9].

2.3 Wetting of a metal by a glass or enamel

The degree of wetting of a metal surface by a molten glass is an important factor in producing a glass layer on the metal during the firing process before conversion to a glass-ceramic. It is determined by the ability to form a glass-metal interface and on reactions which may occur at this interface.

The basic principles for the wetting of a solid by a liquid in a solid-liquid-vapour system are described by Johnson [26] and Aksay [27].

Consider a liquid drop placed on a flat, rigid metal surface. A solid-liquid interface will form provided a decrease in the free energy of the system is achieved. Under conditions of constant temperature, pressure, and ignoring the effects of gravity the system will achieve a state of thermodynamic equilibrium when it is in chemical and mechanical equilibrium. Assuming chemical equilibrium is

achieved, with no mass transport across the interface, deformation of the liquid drop will occur due to mechanical forces. If mechanical equilibrium has not yet been attained, the decrease of free energy of formation of an interface can be represented by:

$$\delta G = \delta\int\gamma_{sl}dA_{sl} + \delta\int\gamma_{sv}dA_{sv} + \delta\int\gamma_{Lv}dA_{Lv} < 0 \qquad 2.1$$

δG = change in Gibbs free energy

γ_{sl} = interfacial surface tension between solid and liquid

γ_{sv} = surface tension between solid and vapour

γ_{Lv} = surface tension between liquid and vapour

dA = differential change in area.

This results in a driving force acting on the liquid drop to wet the solid that, because of the rigid nature of the solid, is resisted by an increase in the liquid-vapour surface area caused by deformation of the liquid.

The attainment of mechanical equilibrium requires a balance at the liquid periphery of the forces present, Figure 2.1. The decrease in surface energy manifests itself as a tensile force acting on the periphery of the drop. The horizontal component of the surface tension of the liquid opposes the spreading yielding Youngs equation [28].

$$\gamma_{sv} - \gamma_{sl} = \gamma_{Lv}\cos\theta \qquad 2.2$$

The contact angle has been determined for various magnitudes of $\gamma_{sv}, \gamma_{sl}, \gamma_{lv}$ Aksay (27). The contact angle is always obtuse when:-

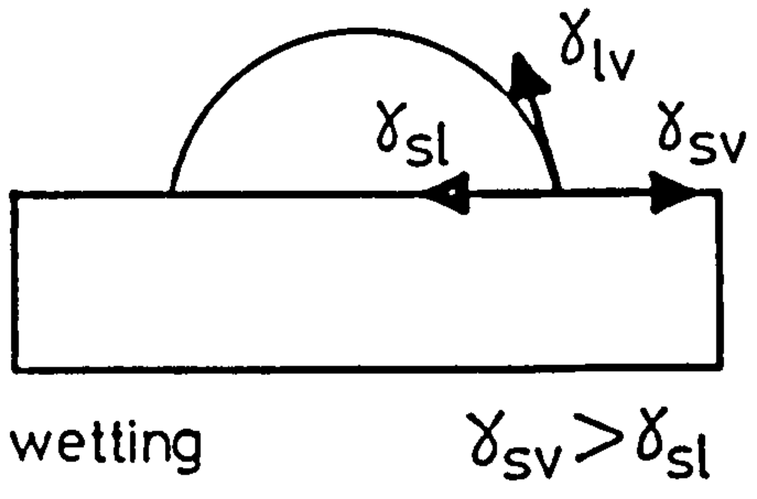

Figure 2.1 Periphery forces for a liquid drop on a solid surface.

$$\gamma_{sv} < \gamma_{sl} < \gamma_{Lv}$$

$$\gamma_{sv} < \gamma_{sl} > \gamma_{Lv} \quad \text{regardless if } \gamma_{sv} > \text{or} < \gamma_{Lv}$$

$$\gamma_{sl} < \gamma_{sv} + \gamma_{Lv}$$

and is always acute when:-

$$\gamma_{sv} > \gamma_{sl} > \gamma_{Lv}$$

$$\gamma_{sv} > \gamma_{sl} < \gamma_{Lv} \quad \text{regardless if } \gamma_{sv} > \text{or} < \gamma_{Lv}$$

When $\gamma_{sv} > \gamma_{sl}$ a reduction in the surface energy of the solid by the liquid has occurred and is defined as wetting. The condition $\gamma_{sv} < \gamma_{sl}$ is defined as non-wetting.

For a glass-metal-air (or other atmosphere) system some observations can be made regarding the surface energies. Metals due to their high co-ordination number and absence of screening by oppositely charged ions have high surface energies. The actual values are difficult to measure as such high energies provide a strong driving force to reduce surface energy by adsorbtion or reaction with gases. Typical values are between 1-1.8 x 10^{-4} J cm^{-2}, Pask [29]. Molten glasses have a more mobile and variable structure, with the presence of screening by oppositely charge ions, consequently a much lower value of surface energy, typically 0.2-0.3 x 10^{-4} J cm^{-2}, Shartsis [30].

From experimental evidence of wetting measurements, Pask and Fulrath [31], Pask and Tomsia [32], Pask [29], the contact angle observed is between 0^{o} and 50^{o}. The metal-glass system corresponds to $\gamma_{sv} > \gamma_{sl} > \gamma_{Lv}$. Often it may be more suitable to consider the solid as an oxide. The formation of an interface will result in an interface

structure with an interfacial surface energy γ_{sl}. The actual magnitude of γ_{sl} depends on the degree of chemical bonding or minimisation of structural discontinuity across the interface.

It is generally observe that good bonding requires small contact angles, Pask [29]. Should $\gamma_{sv} - \gamma_{sl} > \gamma_{Lv}$ then decrease in free energy on forming an interface exceeds the increase due to extension at the liquid (glass) surface. Mechanical equilibrium is no longer achievable, equation 2.2 becomes inoperable, and a dynamic situation exists with the liquid (glass) spreading over the solid surface.

When chemical equilibrium is not established on the initial formation of a solid-liquid-vapour system, reactions or mass transport will occur through the interfaces to achieve chemical equilibrium. During this period the contact angles and interface surface energies will continually change. The transfer of mass across the interface must result in a net decrease of interfacial free energy for the process to proceed.

There now exists a contribution to the reduction of the surface energy of the solid by the free energy of the reaction per unit area, at a given time, as a function of time. The dynamic driving force for wetting can now be expressed as

$$\gamma_{sv} - (\gamma_{sl} + dG_R) \qquad 2.3$$

dG_R free energy of reaction per unit area

γ_{sl} interfacial surface energy as a function of time.

The contact angle will decrease as a result and if the driving force exceeds γ_{lv} (as discussed above) spreading will occur. When the reaction is completed, a steady state is reached and the surface

energies have static values, with chemical and mechanical equilibrium established. The reaction will contribute to the driving force of wetting only if the solid is an active participant in the chemical reaction at the interface. Reactions which introduce an additional rigid phase at the interface, while the liquid is able to adjust its self, will introduce additional complications. The mobility of the liquid may be reduced as a result of viscosity changes, also the surface energy of the rigid phases will differ from that of the liquid. A continuous solid phase at the interface formed by a reaction creates a complex situation with two interfaces present. The liquid phase must be considered as wetting the solid reaction product surface.

2.4 Enamel adherence

2.4.1 Introduction

The theories on enamel adherence to metals may be divided into two categories; Mechanical or Chemical bonding.

The mechanical theories are based on the development of a mechanical bond or interlocking between an enamel and a roughened metal surface. Chemical theories propose the development of a chemical bond or the presence of an oxide layer between the enamel and metal.

2.4.2 Mechanical Bonding

Mechanical theories are based on observations that good adherence is often associated with a highly irregular or roughened interface with the enamel envisaged as being keyed to the irregular

metal surface. The various theories differ in how the irregular interface is produced. The dendritic theory, discussed by Healy [33] and King [34] proposes that the interlocking is a result of precipitation of metallic dendrites running from the metal surface into the glass. The electrolytic theory, Dietzel [35] and Stanley [36], suggests that an electrolytic attack roughens the metal surface.

There are many objections to the mechanical theories as listed by King et al [37].

- Excellent adherence can be obtained on smooth metal surfaces.
- The presence of a roughened interface does not insure good adherence under conditions deviating only slightly from those when adherence was excellent.
- Measured values of bond strength would require extremely high values for the strength of the metal as a result of only a small fraction of the total metal surface providing anchor points.

An irregular or roughened metal surface may be considered to contribute to adhesion but is not the principal mechanism by which it is achieved.

2.4.3 Chemical Bonding

The chemical theory was initially suggested by Kantz [38] who proposed that discrete ferrous oxide phases existed between mild steel and an enamel. There were however many objections to this because of the poor adhesion ferrous oxides exhibits on mild steel.

The essential requirements for a chemical bond came from extensive investigations conducted by King et al [37] on the adherence

of enamels to several metal substrate types. He concluded:-

- Good adherence requires the enamel to be saturated with the oxide of the metal substrate, and that this oxide should not be reducible by the substrate metal.
- Good adherence is the result of metal to metal bonding between atoms in the base metal and enamel when certain thermodynamic and chemical requirements are met.

This concept was the basis for a series of investigations by Fulrath and Pask [31] and Pask [29], [39] to determine the requirements at the interface which must be satisfied for good adherence. The discussion below is based on this theory.

Good adherence requires the development and maintenance of a chemical bond between the enamel and metal. This occurs with continuity of both atomic and electronic structure across the interface, which necessitates a transition zone or layer in equilibrium and compatible with both the metal and enamel at the interface.

When a molten glass is placed on an oxidised metal surface, dissolution of this metal oxide into the glass will start to occur. The driving force is the decrease in internal energy of the glass body as a result of the increased screening of the silicon ions or higher O/Si ratio. This will be countered by the screening, or co-ordination demands, of the metal ion associated with the oxide and eventually the glass will become saturated with the metal oxide at the interface. Provided the solution reaction exceeds the rate at which the metal oxide diffuses into the bulk glass, the glass at the interface will remain saturated with the metal oxide. As a result of the similar

[1]The activity may be regarded as the effective concentration. In a real solution the effective concentration may differ greatly from the true concentration as a result of interactions between molecules. Equal chemical potential between two phases implies equal activities. For a more detailed explination see Smith (124).

ionic-covalent nature of bonds in the metal oxide and glass a chemical bond would be expected to exist between an oxide and glass saturated with this oxide. The presence of such a discrete metal oxide layer enables continuity of the chemical bond across the interface. Figure 2.2(a) illustrates this situation schematically.

On continued solution of the metal oxide, a chemical bond will persist provided at least a monolayer of oxygen exists, shared between the metal and glass, which is in equilibrium with both the metal and glass. This requires that both the metal and glass still remain saturated with the metal oxide so no driving force for its removal is present. Continuity of the chemical bond occurs across the interface with a surface layer of metal atoms having both metallic and ionic-covalent characteristics and a shared layer of oxygen ions between the oxide and glass. Figure 2.2(b).

With continued diffusion of the metal oxide into the bulk, the glass at the interface will no longer be saturated with this oxide. The glass will then dissolve the surface oxygens and associated metal ions and come in direct contact with the metal without an intermediate oxide layer, or attainment of saturation of the adjacent glass. Electronic continuity is lost as no transfer or sharing of electrons occurs across this interface. Only a weak Van der Waals type of bond exists, Figure 2.2(c).

Chemical equilibrium between phases is expressed by equal chemical potentials or activities[1] for each species. The activity of the metal oxide is essentially one across the interface when an oxide layer is present and the adjacent metal and glass are saturated with the oxide. In figure 2.3, time t_o represents the situation when no metal oxide has been dissolved. By a time t_1 glass at the interface has dissolved the equilibrium or saturation amount of metal oxide, as

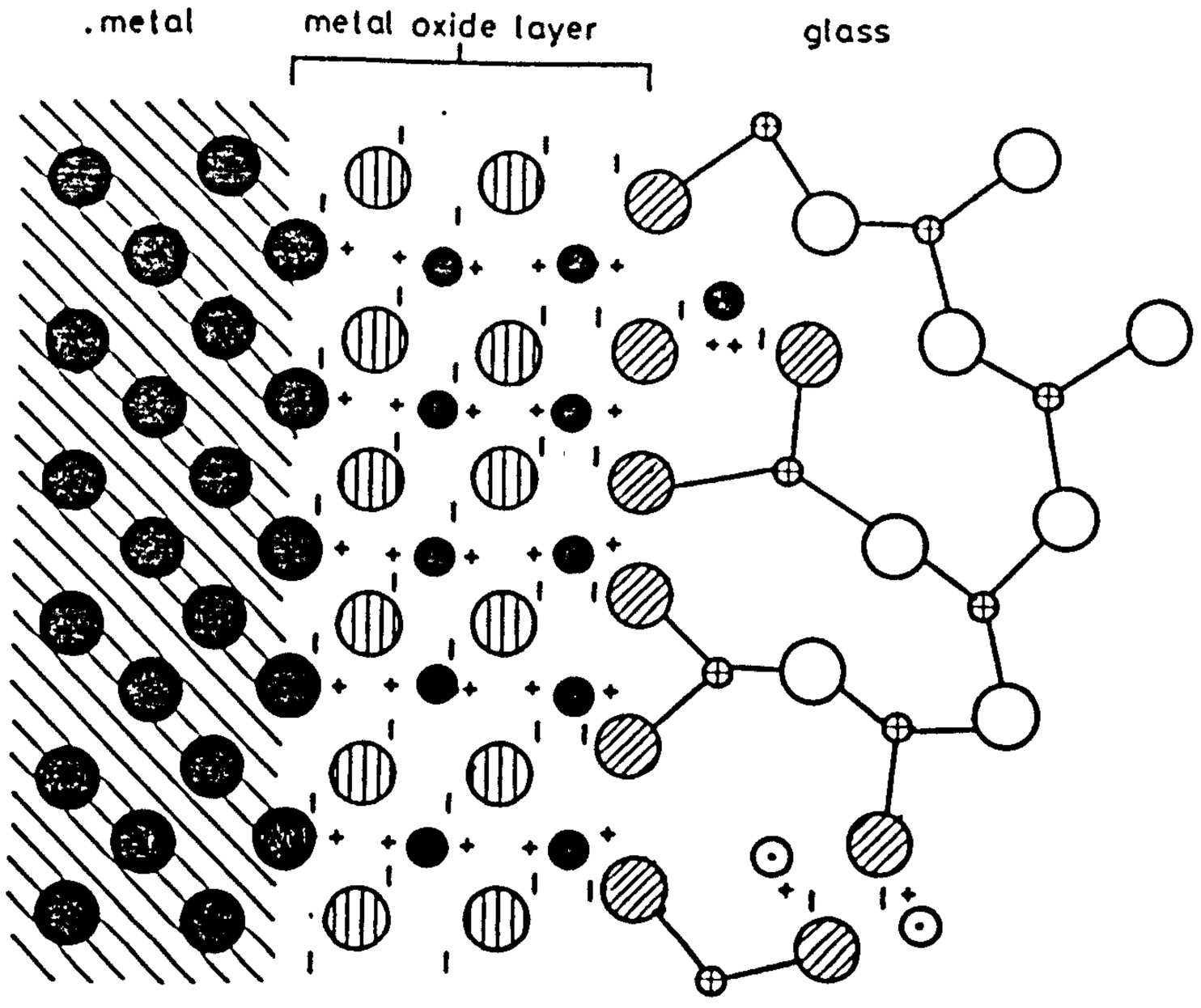

(a) discrete metal oxide layer,

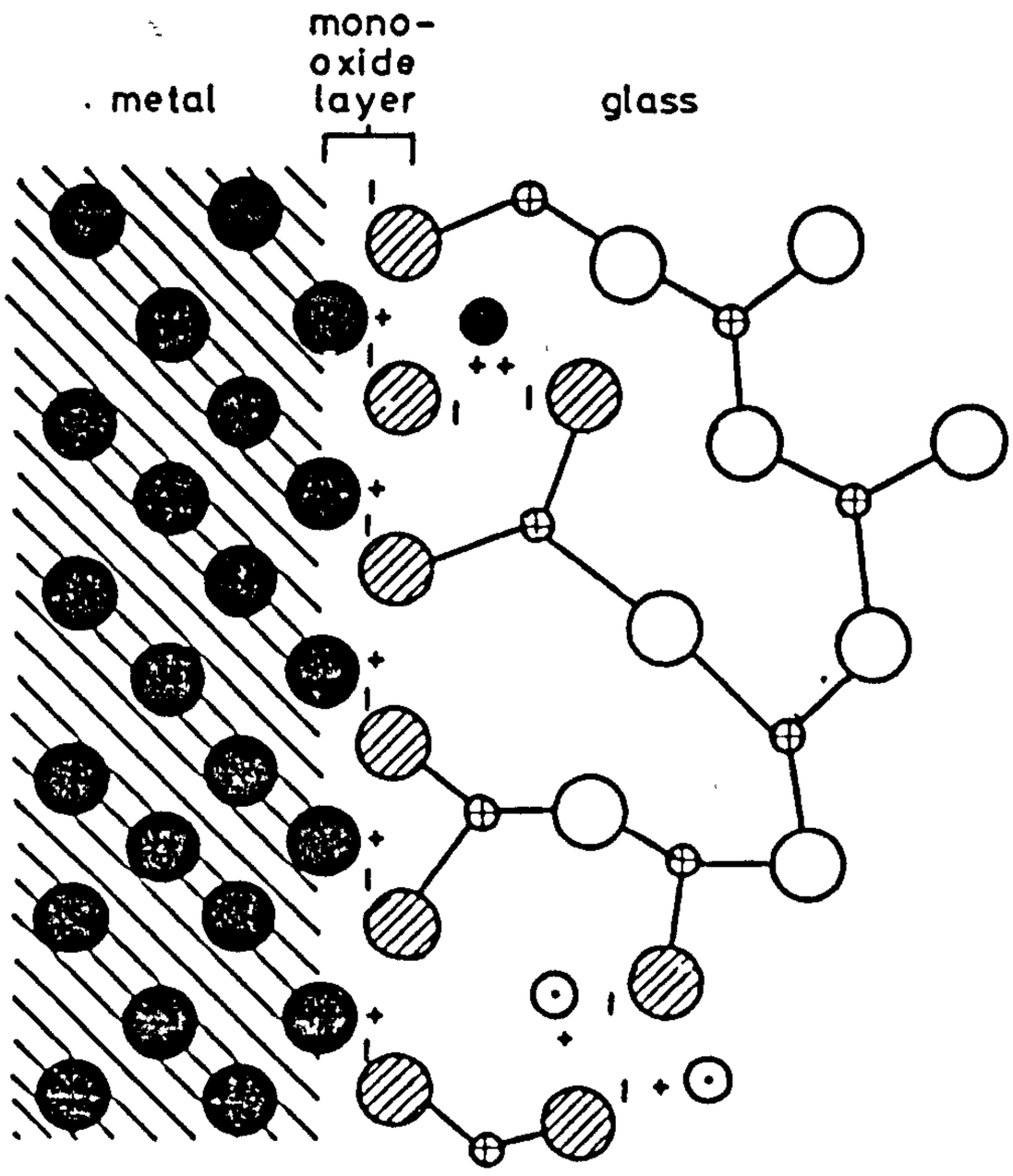

(b) mono-oxide layer,

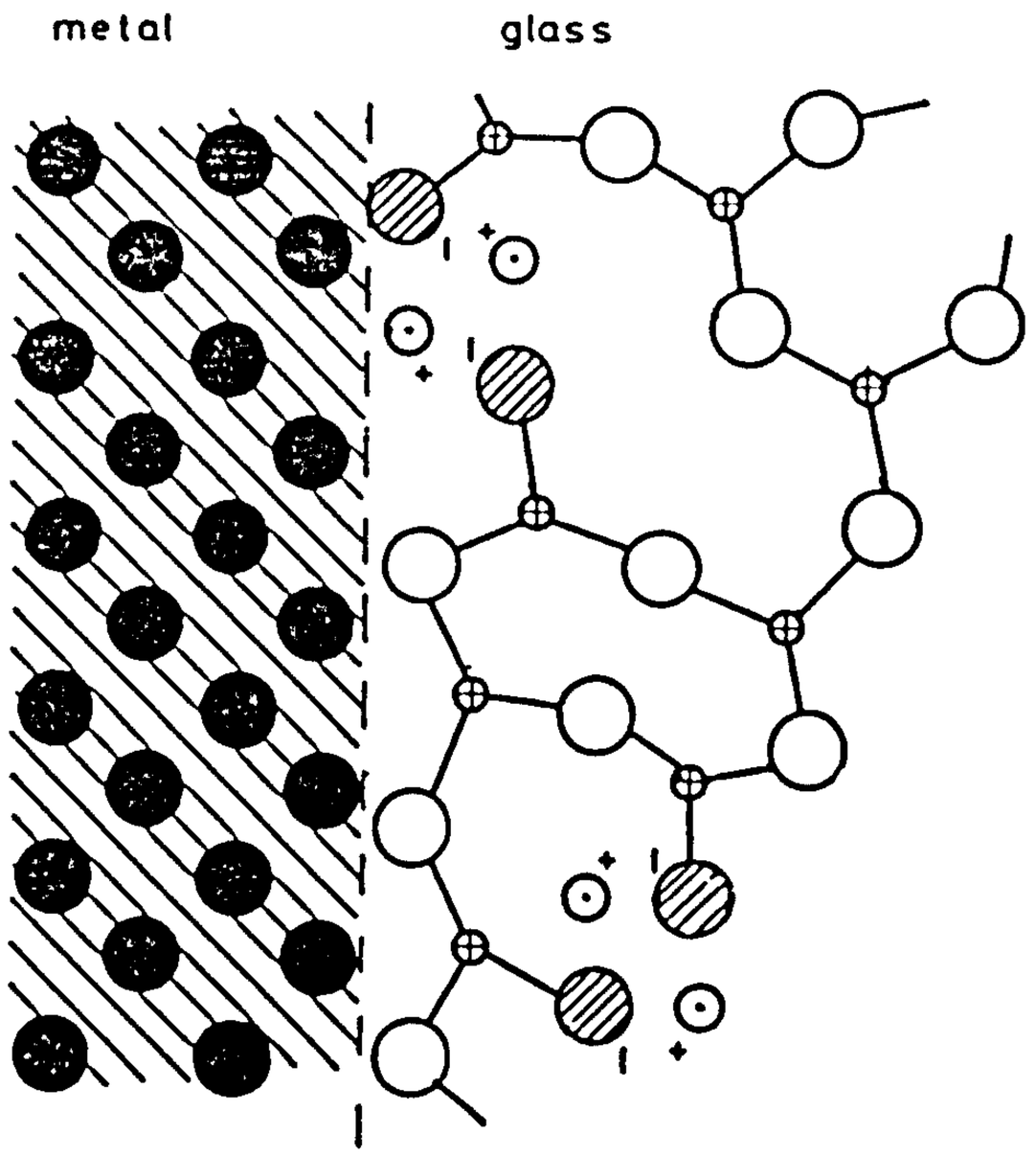

(c) Van-der-Waals bonding.

substrate metal atom

substrate metal ion (divalant)

alkali ion

silicon ion

non-bridging oxygen

oxygen ion (divalant)

bridging oxygen

electron cloud

Figure 2.2 Interface bonding between a glass and metal.

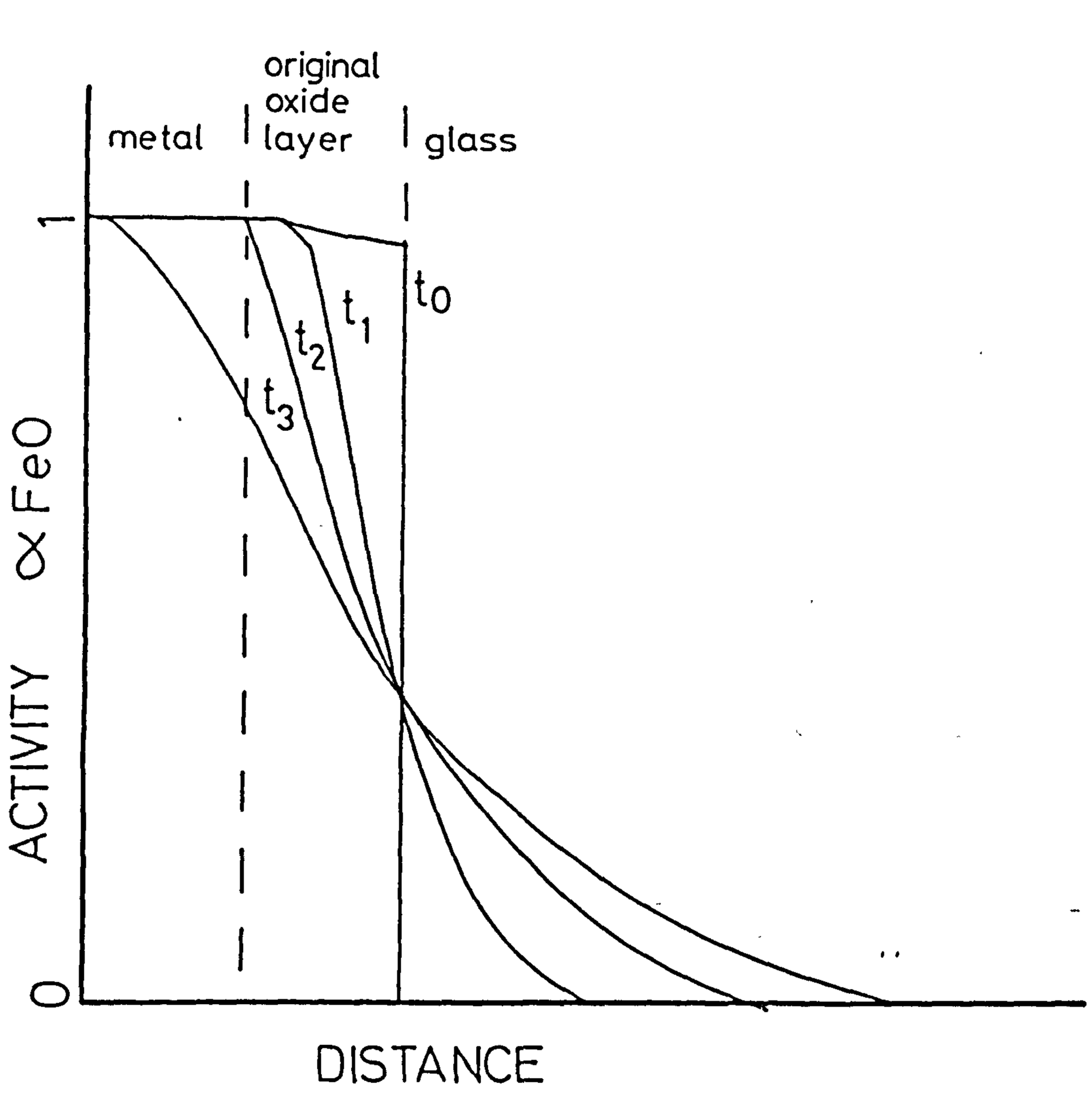

Figure 2.3 Activity of metal oxide across a glass-metal interface.

the metal oxide diffuses into the bulk glass. Between time t_1 and t_2 at least a mono-molecular layer of metal oxides exists, with electronic continuity or balance of bond energies across the interface.

If a discrete oxide layer is still present i.e. at t_1, then for good coating adherence this oxide must adhere well to the metal base and have considerable bulk mechanical strength. Often these requirements are not met and it is desirable to have only a mono-molecular layer of the metal oxide present between the metal and glass, i.e. at t_2. Under both these conditions γ_{sl} is lowered relative to γ_{sv} with a low contact angle and good wetting characteristics observed.

When the oxide is completely dissolved and the metal oxide no longer maintains its saturation level in the adjacent glass, equilibrium conditions are lost and the activity drops below one, i.e. at t_3. Strong chemical bonding is lost with only a weak Van der Waals attraction present. γ_{sl} is only slightly lowered due to screening provided by the oxygens at the glass surface and a large wetting angle or poor wetting characteristics occur.

If a new crystalline phase is precipitated at the interface in the glass saturated with the metal oxide, the glass composition remains in equilibrium with the new phase as well as with the metal oxide. Bonding will be maintained between the new phase and oxide or metal provided the additional requirement of an epitaxial match occurs.

2.4.4 Interfacial reactions

As most metal oxides have either low bulk mechanical strength or poor adhesion to the metal, the achievement of good coating adhesion

requires the limited case of a mono-molecular metal oxide at the interface. The practical problem is then of being able to maintain this situation. Initial saturation of the adjacent glass is a result of a separate preoxidation of the metal or oxidation during the early stages of firing. After complete solution of the oxide layer, equilibrium compositions and adherence is lost.

Saturation of the adjacent glass may be maintained and adherence retained if chemical reactions occur which oxidise the metal base. These provide a source metal cations at the interface allowing the adjacent glass to maintain saturation.

The possible reactions have been categorised by Pask [39] as gaseous oxidation, redox-reduction of cation valence, redox reduction of cations to a metallic state.

Gaseous oxidation may occur in oxidising atmospheres. Oxygen transport through the enamel is ionic and strongly dependent on glass composition. Water vapour in the atmosphere also strongly increases oxidation of the metal base under the glass, Ivanova [40]. However atmospheric oxidation is not significant.

The redox-reduction of cations is the most important mechanism by which the metal base is oxidised and is widely reported.

Consider an interface between a metal M^{o}_{I} and a molten glass containing a metal oxide $M_{II}2+O^{-2}$. A redox type of reaction may occur represented by

$$M^{o}_{I} + M^{2+}_{II}O^{2-}_{(gls)} = M^{2+}_{I}O^{2-}_{(gls)} + M^{o}_{II} \qquad 2.4$$

and the individual step reactions being

$$M^{o}_{I} + O^{2-}_{(gls)} = M^{2+}O^{2-}_{(int)} + 2e^{-} \qquad 2.5$$

$$2e^{-} + M^{2+}_{II}O^{2-}_{(gls)} = M^{o}_{II(s)} + O^{2-}_{(gls)} \qquad 2.6$$

$$M^{2+}_{I}O^{2-}_{(int)} = M^{2+}_{I}O^{2-}_{(gls)} \qquad 2.7$$

The free energy of such a reaction will be given by, see Smith (124):

$$\Delta G = \Delta G_o + RT \ln \frac{a(M_I O_{gls})\, a(M^o_{II\,s})}{a(M_{II} O_{gls})\, a(M^o_{I s})} \qquad 2.8$$

ΔG - Gibbs free energy

ΔG_o - Standard Gibbs free energy

R - Universal gas constant

T - Temperature

a - activity

Thermodynamically such a reaction is feasible if ΔG is negative, that is the energy of the system is reduced as it moves towards a state of chemical equilibrium. At equilibrium $\Delta G = 0$ and

$$\Delta G_o = -RT \ln \frac{a(M_I O_{gls})\, a(M^{\bullet}_{II s})}{a(M_{II} O_{gls})\, a(M^{\bullet}_{I s})} \qquad 2.9$$

ΔG_o , the standard free energy, represents the change in free energy for the reaction when both reactants and products are in their standard states. If ΔG_o is negative the reaction will readily proceed. However if ΔG_o is positive the reaction will only proceed under non-standard conditions when the activity quoted in equation (2.8) is sufficiently less than unity. ΔG overall is then negative.

When the free energy of formation of the oxide of metal M_I is a larger negative value than metal Me_{II}, reaction (2.4) will readily proceed to the right due to a decrease in the free energy, i.e. ΔG for the reaction is negative. The substrate metal Me_I will be oxidised by the reduction of Me^{2+}. Such a reaction will allow maintainance of saturation of the adjacent glass with $M_I O$ and the retention of a mono-molecular metal oxide layer and consequently good adhesion.

The data for free energies at formation of oxides in glasses is limited but considerable information is available for materials in their standard states [41]. Table 2.1 lists these values for several metal oxides at 1000°C. The validity of using such values for reactions in glasses has been shown by King [37] to be able to predict which reactions may occur, but it is doubtful if correct values for ΔG can be obtained as the metal oxides are part of the glass structure and not in standard states.

In a system with an iron base and a glass with a small percentage of CoO present among its constituents, the oxidation of metal iron by the reduction of Co^{2+} is feasible, the reaction having a negative G^{O} = -90.8 KJ $mole^{-1}$, the energy of the system is decreased. Such a reaction will readily proceed and is represented by

$$Fe + CoO_{(gls)} = FeO_{(gls)} + Co \qquad 2.10$$

As soon as the substrate cations enter the glass the metallic precipitates become alloys since these elements readily form solid solutions. The overall reaction is represented by

$$Fe + xCo^{2+} = xFe^{2+} + Fe_{(1-x)}\ Co_x \text{ alloy} \qquad 2.11$$

Such a reaction has been observed by many investigators, Bremann and Pask [42], King [37], and Borom and Pask [43].

The presence of such reducible oxides are known in enamelling technology as adherence oxides. They allow attainment and maintenance of equilibrium compositions at the interface by participating in the formation of metallic alloys whose composition is readily adjusted as the adjacent glass composition changes.

Table 2.1

Free energies of formation of metal oxides [41] [1000°C]

Oxide	Energy KJ mole^{-1}
$4Li + O_2 \rightarrow 2Li_2O$	-850.0
$4/3\ Al + O_2 \rightarrow 2/3\ Al_2O_3$	-842.1
$Ti + O_2 \rightarrow TiO_2$	-709.69
$Si + O_2 \rightarrow SiO_2$	-676.6
$4/3\ Cr + O_2 \rightarrow 2/3\ Cr_2O_3$	-533.4
$4Na + O_2 \rightarrow 2Na_2O$	-435.0
$2Zn + O_2 \rightarrow 2ZnO$	-409.5
$2Fe + O_2 \rightarrow 2FeO$	-376.4
$4/5\ P + O_2 \rightarrow 2/5\ P_2O_5$	-361.9
$4H + O_2 \rightarrow 2H_2O$	-351.9
$3/2\ Fe + O_2 \rightarrow 1/2\ Fe_3O_4$	-351.5
$4/3\ Fe + O_2 \rightarrow 2/3\ Fe_2O_3$	-324.5
$Sn + O_2 \rightarrow SnO_2$	-311.9
$2Co + O_2 \rightarrow 2CoO$	-285.6
$4K + O_2 \rightarrow 2K_2O$*	-248.3
$2Ni + O_2 \rightarrow 2NiO$	-185.9
$4Cu + O_2 \rightarrow 2Cu_2O$	-148.7
$2Cu + O_2 \rightarrow 2CuO$	-82.9

* estimated, K_2O decomposes above 827°C.

Thermodynamically it is possible for any oxide in the glass with a lower negative free energy of oxide formation than that of iron to act as an adherence oxide. In practise it is found that cobalt oxide is by far the most effective with nickel oxide also being a suitable oxide, on an iron substrate. Other metal oxides such as copper oxide do not act as adherence oxides. An additional requirement that the adherence oxide metal should form a continuous solid solution with the base metal can explain this difference, Borom and Pask [43].

As described above reaction 2.4 may still occur even though ΔG_o is positive. An example of this is a sodium silicate glass on a iron substrate, a possible reaction is:-

$$Fe + Na_2O_{(gls)} = FeO_{(gls)} + 2Na\uparrow \qquad 2.12$$

The free energy of the reaction is given by

$$\Delta G = \Delta G_o + RT \text{ LN } \frac{a(FeO_{(gls)})P^2(Na)}{a(Na_2O_{(gls)})} \qquad 2.13$$

At 1000°C ΔG_o is +5.8 KJ/mole, the activity content must be significantly less than unity for ΔG to become negative and the reaction to proceed.

This is possible with a low (FeO) and low partial pressure of sodium vapour at the interface. The reaction is observed to readily occur in a low total pressure and low partial oxygen pressure, Hoge [44].

Similar reactions are possible between oxides in the glass and substrate metal provided conditions exist which allow a significant change from standard conditions with the activity quotent in equation (2.8) reduced below unity. This is readily achieved if one of the products is gaseous and able to escape from the interface region. Again such reactions will allow maintenance of saturation and equilibrium conditions at the interface.

CHAPTER 3

Experimental Investigative Techniques

3.1 Measurement of coating adhesion

3.1.1 Introduction

In examining the interface between a glass-ceramic enamel and metal substrate it is desirable to be able to measure the degree of adhesion developed. Standard adhesion tests have been devised for traditional porcelain enamels. The adhesion tests for porcelain enamels on steel are given by A.S.T.M. C313 [45] and P.E.I. Bulletin T-29 [46]. Both involve deforming the enamelled metal substrate and measuring the area over which the enamel is removed. The adhesion is indicated by an adherence index which is the ratio of the area from which the enamel has been detached to the total area deformed. In such a test the actual parameter measured is a combination of enamel-metal adhesion and enamel bulk strength.

Many methods of testing enamel adhesion to metal are possible and such a list would include deformation by impact, bending or torsional twist, parallel shear, and tensile loading. However measured strength will depend on specimen dimension and testing procedure. A full investigation into enamel adhesion would require consideration of the stresses present, caused by the applied loads and the elastic and thermal expansion mismatch, as well as the individual fracture characteristics of the enamel, metal and interface.

The possibility of using a four point bend test or torsional twist to measure adhesion is discussed by Tsien et al [47]. A method based on a parallel shear test has been developed by Civian et al [48] and Chang and Beech [49]. Clearly these tests will given an estimation of adhesion dependent on the material properties.

A more satisfactory approach to describe coating adhesion may be to use fracture mechanics methods based on the energy required for crack propagation in the interface region. Berndt and McPherson used a method based on a contoured double cantilever beam technique [50] to measure adherence of plasma sprayed coatings. A fracture mechanics approach has also been used by Suga and Elssner [51] involving a 3 point bending technique. These methods require the introduction of a well defined notch at the interface. This would be difficult to achieve in the thin enamels examined in this project.

It was believed a tensile pull method would provide a simple measure of enamel to metal adhesion. Such a test will evaluate the force per unit area required to detach the enamel by a tensile force applied normal to the interface. Tensile tests have been developed to measure the adhesion of plasma sprayed coatings. A bar is adhered to the coating by means of an organic epoxy having a tensile strength greater than that of the coating, A.S.T.M. C633 [52]. Examples of the application of the tensile pull test to enamels is limited. King [37] used such a test to measure the adhesion of commercial enamels, but was limited by the strength of the adhesive. A tensile test has been developed to evaluate the bonding of dental porcelain to various metal alloys. See Sced and Mclean [53] and Fairhurst [54]. The tensile pull appears to be a viable test to measure enamel adhesion, at least to a qualitative degree. Although the actual tensile load to cause removal of the enamel will depend upon many other factors as well as the enamel-metal bond as discussed above. Three problems are encountered with a tensile pull test of adhesion:

- The requirement of an adhesive to bond a metal stud to the enamel with a strength exceeding that of the bond between the enamel and metal substrate.

- The need to eliminate non-tensile loads which give rise to cleavage forces on the enamel and as a result a non uniform load.

- The presence of a large scatter associated with repeated measurements of adhesion on identical coatings. This is a consequence of a failure being due to brittle fracture initiated at a critical sized flaw. Failure will depend on the probability that a flaw capable of initiating fracture at a specific load is present.

3.1.2 Tensile Pull Adhesion Method

The method developed involved adhering aluminium studs to the enamel and applying a tensile load until failure occurred either at the enamel-metal substrate interface or within the enamel body.

The adhesive used to adhere the stud to the enamel must be sufficiently strong in tension to exceed the bond strength between the enamel and metal substrate. Several commercial structural adhesives were tried based on cyanoacrylics, anaerobics and epoxy resins. Most adhesives failed before the enamel-metal bond. It was found that surface pretreatment with chromic acid and heat curing increased the strength of the adhesive bond of the epoxy to both the stud and enamel surfaces. Table 3.1 lists some typical failure values. It can be seen that an epoxy resin adhesive applied to pretreated surfaces and cured under heat provides the highest bond strength which in general exceeded the enamel metal substrate bond strength.

The epoxy finally selected was a one part, heat cured resin supplied by the Ciba-Geigy Company [55]. Both the aluminium stud surface and enamel surface were chemically pretreated. The surfaces

Table 3.1: Typical Strength of adhesives under tensile loading conditions

	Failure Load (MNm^{-2})		
	Cyanoacrylics	Anaerobics	Epoxies
no heat cure no pretreatment	3	8	6.5
heat cure no pretreatment	13	15	-
no heat cure pretreatment	-	10	6
heat cure pretreatment	-	26	> 50

Standard deviation ± 25%.

Table 3.2: Chromic Acid Pretreatment Solution

3.75 g	$Na_2Cr_2O_7$
7.5 cc	H_2SO_4
50 cc	H_2O

30 minutes at 60-65°C

Rinse in deionised water

Dry in warm air

were first degreased by soaking in acetone with ultrasonic agitation. A solution of chromic acid, Table 3.2, was made up and heated to 60-65°C. Into this the aluminium studs and coated enamel pieces were placed for 30 minutes, followed by several rinses in deionised water and drying in an oven at 60°C. The epoxy was applied as a thin layer to both the stud surface and enamel. Once brought into contact the epoxy required curing at 120°C for at least four hours.

The test procedure involved several steps. Glass powder pads of 8 mm diameter were screen printed onto a metal substrate and subjected to the same firing and heat-treatment schedules as for the enamelled substrates producing a glass-ceramic enamel. An aluminium stud of length 1 5 mm and diameter 8 mm had one end machined to a 7 mm diameter. This stud was adhered to the enamel pad with the epoxy as described above. The process was carried out with the use of accurately machined jigs, to ensure that the stud was perpendicular to the enamel surface and centrally placed on the enamel pad. Once adhesive had fully cured the jig was removed.

The measurement of tensile load was carried out using an Instron tensile loading apparatus. To ensure uniaxial loading two steps were taken. Firstly the enamel and stud had to be adhered to a block which could be attached to the base of the Instrom. Several enamelled pieces could be adhered to a single base block having several threaded holes for attachement to the Instron base. A jig was made that fitted onto the upper arm of the Instron and aligned accurately along the Instron axis. The stud was placed into this and epoxy adhesive applied to the metal substrate surface and base block. The cross arm of the Instron was lowered until the substrate made contact with the base block. Light pressure was applied and the adhesive (a rapid

cured one part epoxy resin) was semi-cured. The jig was raised and the base block moved such that another stud and enamelled piece could be adhered to the block. The epoxy was fully cured in an oven at 100°C over night.

Secondly, the tensile load applied when testing the bond strength of the enamel was applied via a universal joint and a 1 m long rod to insure, as close as possible, a purely tensile pull. The apparatus is shown in Figure 3.1 A cap was placed over the aluminium stud and held in place using a steel cross pin. The Instron crossbar was raised at a rate of 0.5 mm per minute, corresponding to a loading rate equal to 8 NS^{-1}. Failure occured within 2 minutes.

In a typical test the adhesion of the enamel applied under specific conditions was determined from five measurements. The tensile adhesion of the enamel was quoted as the mean of these five values. This was taken to be representive of the enamel to metal bond strength. The spread of the five measurements is large with a difference of typically 20 MNm^{-2} between the lowest and highest measured values, Table 3.3. To give an indication of the spread of values the standard deviation was quoted with each mean value of enamel adhesion.

The consistancy of the technique was established by measuring the enamel-metal adhesion for a coating on chrome iron fired at 960-970°C for 5 minutes, followed by a standard heat-treatment, see Section 4.3.3. Enamel adhesion was evaluated independently five times with 5 measurements taken in each case. The mean values, standard deviation and spread in values are listed in Table 3.3 The mean tensile load to cause removal of the enamel is seen to be reasonably

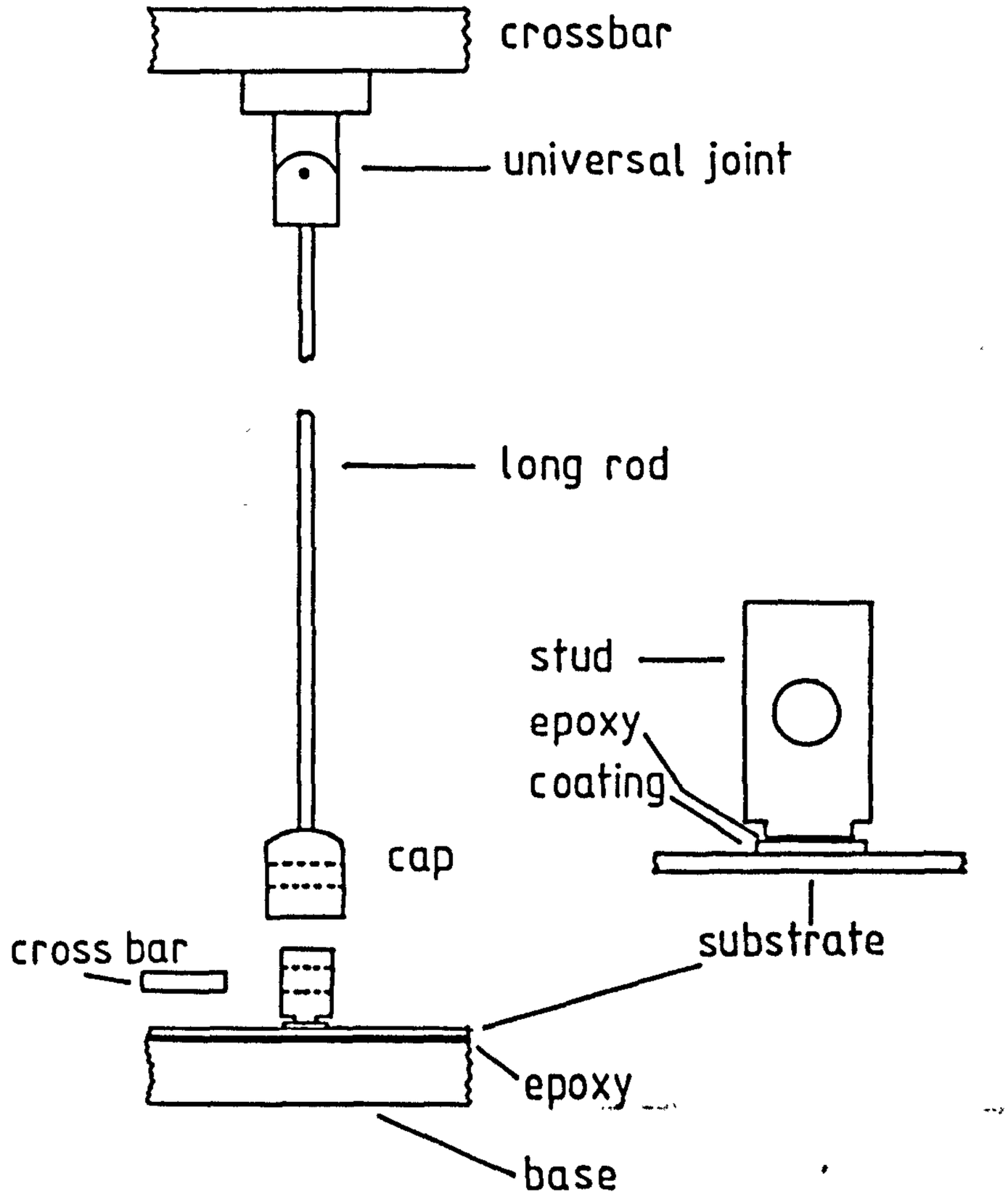

Figure 3.1 Tensile pull adhesion test apparatus.

consistant lying between 29 to 39 MNm^{-2}, and the spread of results is also consistant, having a standard deviation of $\pm$ 9 MNm^{-2}. In all the above measurements failure occurred between the enamel and metal substrate.

When using this technique to measure the enamel adhesion, particularly on mild steel, the failure occasionally occured at the epoxy-enamel interface. If this happened the value was incorporated into the mean and the number of epoxy failures out of the five measurements given in brackets. The mean value obtained is now lower than if the epoxy did not fail and the enamel adherence should be considered greater than this mean.

The type of failure was also noted and classified as:

- Adhesive failure: fracture ocurred along the enamel-metal substrate interface.
- Cohesive failure: fracture ocurred within the enamel bulk.
- Mixed failure: fracture ocurred both along the enamel-metal interface and within the enamel bulk.
- Epoxy failure, fracture ocurred along the epoxy interfaces or within the epoxy bulk.

Table 3.3: Adhesion as measured by the tensile loading method for a glass-ceramic enamel on chrome-iron. The enamel was fired for 5 minutes at 960-970°C followed by a standard heat-treatment.

Test	Mean tensile load to cause failure	Standard deviation	Upper value	Lower value
1	38.2	$\pm$ 10.8	51.9	26.5
2	29.4	$\pm$ 8.8	43.1	20.6
3	39.2	$\pm$ 8.8	57.8	29.4
4	34.3	$\pm$ 7.8	43.1	27.4
5	31.4	$\pm$ 7.8	40.2	20.6
	MNm^{-2}			

3.2 Scanning Electron Microscopy and Microanalysis

3.2.1 Introduction

Scanning electron microscopy is a well established analytical technique with the basic principles and instrument design extensively described in the literature, see Bowen and Hall [56], Maurice [57].

The S.E.M. offers a resolution between that of optical microscopy and transmission electron microscopy with observation of topographic features in the size range 10 to 10^2 nm. Interaction of the electron beam with the sample causes emission of several forms of energy which include: secondary electron emission (< 50 eV), back-scattered electrons (> 50 eV), cathodoluminescence, Auger electrons and characteristic X-rays, Figure 3.2. These provide the ability to obtain topographic imaging of submicron resolution and a large depth of focus, together with material characterisation.

Imaging of a solid specimen under the electron beam requires contrast between the various features. Contrast arises from a variety of mechanisms, Table 3.4. The most important being topography, atomic number differences, crystallinity and surface potential, see Newbury [58]. Topographic and atomic number contrast have been used extensively in this project to produce scanning electron micrographs.

Topographic contrast results from differences in both the number of electrons emitted from the sample and the trajectory of the emitted electrons. The electron detector subtends only a small solid angle and since the back scatter electrons are highly directional the electron detector has a poor collection efficiency and produces a harsh contrast with only those surfaces which face the detector providing a strong signal.

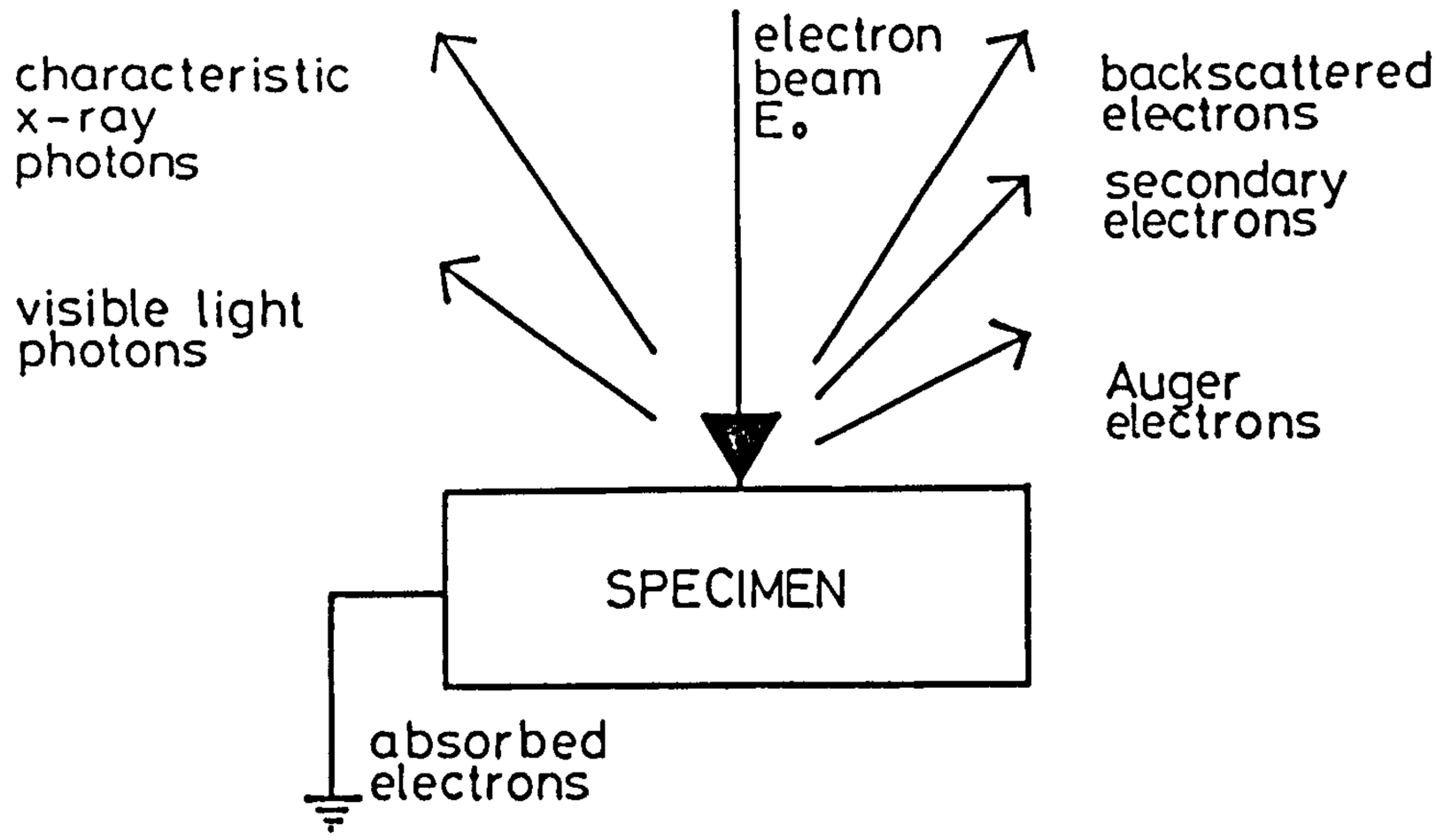

Figure 3.2 Signal emissions resulting from electron beam-sample interaction.

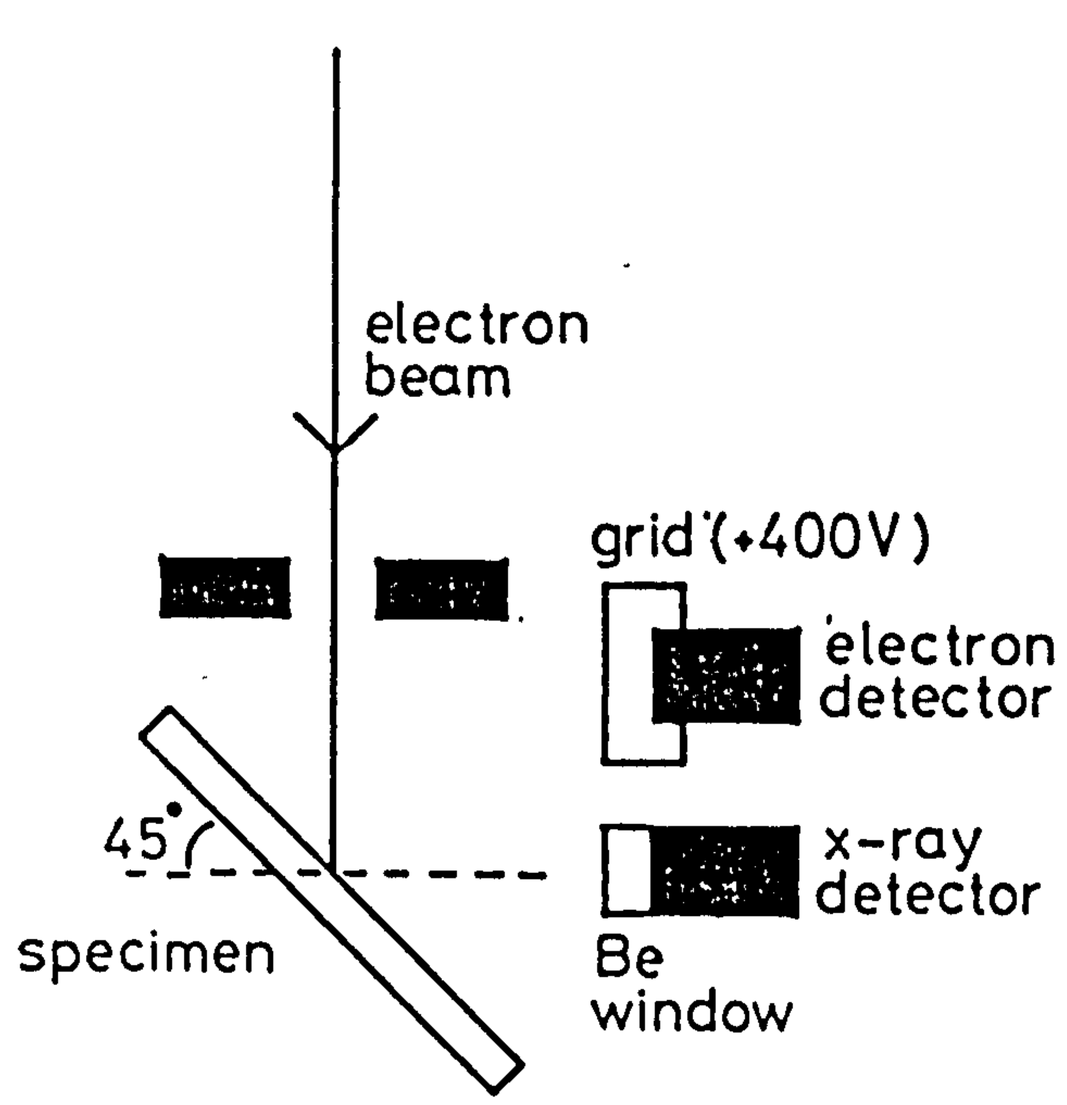

Figure 3.3 Sample position in scanning electron microscope.

Table 3.4: Primary Modes of Contrast

Mode	Information	Limits
Secondary electron (emission)	Microtexture Morphology	25 - 10 nm
Backscatter electrons (reflective)	Measure of Mean atomic number, chemical textural	50 - 200 nm
Cathodoluminescence	Sensitive measure of trace elements	~ 100 nm
Characteristic X-rays	Quantitative Chemical analysis	> 10^{-17} gramm
	Element mapping and distribution displays	100 nm
Specimen absorbed electrons (absorptive)	Surface topograph Atomic number variation	0.1 - 1 µm
Auger electrons	Light element analysis Element mapping	Submicron spatial resolution

By positively biasing the detector (+ 150 eV) to collect secondary electrons as well, an improved image with a softened contrast is obtained. The detector has a much larger effective solid angle for the collection of secondary electrons. These low energy

electrons are deflected significantly to follow curved paths to the detector. The result is an image similar to an optical image if the sample is viewed along the electron beam.

Atomic number contrast arises from differences, in the specimen, of atomic number (or compositional) contrast. As the electron beam travels in to the specimen it will undergo scattering due to collision processes with the ion nuclei and electrons. It is found, that the probability of a wide angle scattering is proportional to the square of atomic number and inversely to the square of the energy. After a number of wide angle scattering events the cumulative change in direction may cause the electron to leave the specimen surface. These are known as back scattered electrons and the fraction of the beam electrons which escape the specimen is known as the backscattering coefficient η. See Fontaine [59] for a more detailed description. The energy of these electrons leaving the surface after elastic and inelastic collisions have energies in excess of 50 eV.

It is possible to relate the backscattering coefficient η to atomic number by an expression given by Reuter [60].

$$\eta = -0.0254 + 0.016Z - 0.000186\ Z^2 + 8.31 \times 10^{-7}\ Z^3 \quad 3.1$$

It is generally believed the backscattering coefficient of a homogeneous alloy is given by the weighted sum of the individual backscattering coefficients. Hinrich [61].

$$\eta_{alloy} = \Sigma\ C_i \eta_i \quad 3.2$$

C_i Weight fraction of element i

η_i Backscattering coefficient of element i

This is unlikely to hold true for more complex compounds such as multicomponent oxides, but may indicate approximately the relative backscattering coefficient for various phases in a multiphase material. To have a large electron collection solid angle of the backscattered electrons a circular solid state detector is placed above and close to the specimen surface.

The generation of characteristic X-rays on interaction of the electron beam with the sample provides the ability for quantitative chemical microanalysis. For a review see Maurice [57]. The energy of the characteristic X-rays generated are related to the atomic number of the element by Moseleys law. In the energy dispersive spectrometer (EDX), the entire X-ray spectrum is collected by a suitable detector and displayed on a multi-channel analyser with each channel corresponding to a convenient energy range. The detector is a lithium drifted silicon solid state detector with a beryllium window in 10 μm thick to prevent contamination. Low energy X-rays are absorbed by this window inhibiting detection of elements with atomic number less than 11 (Na). The characteristics of a typical detector are given in Table 3.5.

The choice of operating voltage is important for X-ray analysis. The energy of the electrons must be sufficient to generate the characteristic X-rays. The ratio of the operating voltage E_o to the critical excitation potential E_c (the over voltage) must be at least 1.4 and typically 2-3 to generate a sufficient X-ray intensity for analysis. In general a 10 kV voltage provides optimum over-voltage for light elements by generating their K lines and very heavy elements by generating their L lines. A 20 kV voltage is ideal for medium to heavy elements by generating their K lines.

Table 3.5: Characteristics of the EDX Spectrometer [64]

Counting rate	10,000 counts S^{-1} nA^{-1} (wide spectrum)
Probe current	10 pA - 0.5 nA
Acquisition time	100 s
Element range	11 (Na) - 92 (U) (1-20 kV)
Resolution	150 eV (FWHM)
Peak to background ratio	10 - 100
Dead time	> 25 µs

The selection of beam current is also a critical factor X-ray intensity is directly proportional to the value of beam current and for good counting statistics the current must be sufficient to give a high count rate, but not damage the specimen.

3.2.2 Instrumentation

The scanning electron microscope used for this project was a Cambridge Instruments [62] 250 MK III Stereoscan model having a Lanthanium hexaboride ($La\ B_6$) filament in the electron gun. Secondary electron emission was observed using a Everhart-Thornley (E-T) detector with a positively applied bias of upto + 400 V. A silicon diffused p-type junction substrate produced by K.E. Developments [63] was used as the back-scattered electron detector, having a threshold sensitivity of 4 kV.

The microscope was equipped with an energy dispersive analyser supplied by Link Systems [64], model 860 series II. The Li drifted silicon X-ray energy detector had an interchangable window allowing replacement of the 8μm beryllium window with an ultra thin 1000 Å Formvar window. This enabled detection of elements with z < 11 (Na).

The spectrometer was linked to a microcomputer to give rapid on line identification of the elements present in a sample with full quantitative analytical capabilities.

3.2.3 Specimen Preparation

Examination of the specimen may require, as a first stage, sectioning and polishing. A flat surface is essential for good backscattered electron micrographs and quantitative microanalysis. The specimen, a bulk ceramic or coated metal substrate, was sliced using a diamond cutting wheel. Coated metal substrates were sectioned along a plane perpendicular to the interface plane exposing the interface region. Prior to polishing, the specimen was mounted in a supporting block of either electrically conductive carbon impregnated bakelite, or if the specimen is easily damaged, in a two part thermosetting resin. The first stages of polishing involved grinding with silicon carbide abrasive paper down to a 1000 grit size. Subsequent polishing used 6 μm, then 1 μm diamond paste on hard lapping cloths, finishing with ¼ μm diamond paste on a velvet polishing cloth.

Following polishing the specimen was cleaned by soaking in acetone with ultrasonics to remove residues, and dried in warm air.

To prevent localised charging under the electron beam, the surface of the sample must be made conductive. This is achieved by

depositing a thin layer (10-30 nm) of a conductive material. For backscattered imaging and microanalysis the specimens had a layer of carbon deposited onto their surface by sputtering carbon with an electrical arc. For topographic imaging the coating material was gold, which has a high secondary electron yield, placed over a previously deposited carbon layer to improve wetting.

The final polish and coating was carried out immediately prior to analysis. The specimens were subsequently stored in an evacuated desicator. If it was re-examined, the specimen was repolished with 1 and ¼ μm diamond paste and recoated with a conductive material before analysis.

3.2.4 Qualitative Microanalysis

The sample was positioned in the chamber such that the electron beam had an angle of 45° to the surface normal. The X-ray detector was placed in the plane of the axis of the tilted sample, Figure 3.3. To provide a sufficient voltage to generate characteristic X-rays from all of the detectable elements present, listed in Table 3.6, a voltage of 15 kV was used. A beam current at 6×10^{-8} A was selected with a beam diameter of 10 - 50nm. A counting rate of typically 2000 cps was obtained, for the whole spectrum, and a collection time of 100 seconds found sufficient to give good counting statistics.

The collected X-ray spectrum was displayed with energy along the base axis in channels of 20 eV range and the total number of counts per channel in the vertical axis. The energy of the characteristic K_α peaks could then be determined and related to atomic number allowing rapid identification of the particular elements present.

Table 3.6: Characteristic X-ray lines for elements of interest

Element	Z	Principal emission lines kV		
		K_α	K_β	L_α
O	8	0.525		
Al	13	1.486		
Si	14	1.739		
P	15	2.013	2.137(4)	
K	19	3.312	3.589(10)	
Cr	24	5.411	5.946(12)	0.573
Fe	26	6.398	7.057(13)	0.705
Co	27	6.924	7.648(13)	0.776
Ni	28	7.471	8.263(13)	0.851
Zn	30	8.630	9.570(13)	1.012

( ) intensity relative to K_α

3.2.5 Elemental distribution: X-ray area scanning

The characteristic X-ray peak corresponding to an element to be analysised was isolated. Its signal then used to modulate the brightness of the spot, on the CRT screen, scanned in synchronism with the electron probe. This allowed the collection of an image caused by variation of the X-ray emission from the scanned surface. In places of high concentration of the selected element the image is photographic white; in places of medium concentration, gray, and for low or negligible concentrations, black. By collecting separate

micrographs for each element present the distribution of the various elements was obtained.

Electron beam conditions and specimen orientation were identical to those described in Section 3.2.4. The image was collected over a period of 1000 seconds.

3.2.6 Element distribution: Line scans

The energy of a particular peak was selected, as for X-ray mapping, and its output used to modulate the vertical displacement on the CRT screen as the electron beam moves across a predetermined line displayed horizontally on the screen. This allowed the determination of an element distribution along a line on the specimen surface. By conducting several scans across the same line, the distribution of all detectable elements could be found. Beam and orientation conditions are identical to these in Section 3.2.4. A typical scan distance was 100 μm over a period of 500 seconds which gave a sampling period of 5 seconds per micron.

3.2.7 Quantitative X-ray Microanalysis

The X-ray spectrum collected under operating conditions described in Section 3.2.4, was identified into its characteristic X-ray peaks corresponding to the elements present. The intensity at the peak (e.g. a K_α line) was compared to that collected from a standard material under identical experimental conditions. These standards were either metals or oxide compounds. The characteristic peaks of various elements of interest were isolated from several standards and stored on the microcomputer attached to the

spectrometer.

On analysing a specimen, the X-ray spectrum was collected, the elements present identified and the characteristic peaks stripped from the spectrum. The continuous X-ray background radiation was removed and the integrated area of the remaining peak compared to that from the standard material. The measured relative intensity ratio, denoted K, was obtained

$$K_A = \frac{I_A}{I(A)}$$

K_A - Intensity ratio of element A

I_A - Intensity of characteristic X-ray line of element A in specimen

$I_{(A)}$ Intensity of characteristic X-ray line of element A in standard

In a first approximation the concentration of the element of interest, A, in the specimen is given by

$$C_A^o = \frac{K_A}{\sum_1 K_i}$$

C_A^o = approximate concentration of element A in specimen

K_i = intensity ratio of element i.

Howéver the value of C_A^o measured is not in general equal to be true concentration of element A, C_A. The value of C_A^o must be corrected for several effects, see Henoc [65]. The following corrections are used in the ZAF, correction method:

- Atomic number effect, Z
- Absorption of X-rays within the specimen, A
- Fluorescence, F.

The true concentration of A is then given as

$$C_A = C_A^{\circ} . K_Z . K_A . K_F$$

K_Z atomic number correction factor

K_A absorbtion correction factor

K_F fluorescence correction factor.

This must be repeated for each element present and was calculated on line, by a ZAF correction program on the microcomputer, using an iteration procedure.

To establish the accuracy of the technique for multiple component glasses a series of glasses were produced having varying amounts of Fe_2O_3 added. The as-mixed composition and that determined by quantitative microanalysis, described above, is given in Table 3.7. It is not possible to determine the concentration of Li_2O, so it is evaluated by assuming a constant ratio with SiO_2 expected from the as mixed composition. Good accuracy to within $\pm$ 1 oxide wt% is seen to exist for all detectable elements including those present in minor concentrations.

3.2.8. Windowless analysis

With a beryllium window, analysis is limited to elements with atomic number z > 11 (Na) as described previously. On replacement with an ultra thin window, qualitative microanalysis is possible down to boron, atomic number 5. This allows the detection of the characteristic X-ray lines of oxygen (K_α), Table 3.6. An attempt was made to do light element quantitative microanalysis to determine the oxygen concentration. However many problems exist in light element analysis, see Barbi [66].

Table 3.7: Composition of iron containing glasses

A - As mixed composition

B - Determined by quantitative energy dispersive analysis

Specimen		Oxide Wt%						
		Li_2O	Al_2O_3	SiO_2	P_2O_3	K_2O	ZnO	Fe_2O_3
1	A	12.0	4.5	77.0	2.0	2.5	2.5	0
	B	11.8	4.6	76.9	2.0	2.5	2.17	0
2	A	11.9	4.5	76.2	2.0	2.5	2.0	1.0
	B	11.7	4.2	74.9	2.3	2.7	2.9	1.33
3	A	11.4	4.3	73.3	1.9	2.4	1.9	4.7
	B	11.3	4.3	72.5	2.2	2.6	1.7	5.3
4	A	10.9	4.1	69.9	1.8	2.3	1.8	9.3
	B	10.8	4.0	69.3	1.7	2.5	2.3	9.5
5	A	9.7	3.7	63.9	1.7	2.1	1.7	17.0
	B	9.7	4.0	62.0	1.4	2.1	2.7	18.0
6	A	8.5	3.2	54.7	1.4	1.8	1.4	29.0
	B	8.1	3.3	52.0	1.3	1.8	0.8	32.7
7	A	7.4	2.8	47.7	1.2	1.6	1.2	38.0
	B	7.3	3.0	46.6	1.1	1.6	0.8	39.6
8	A	6.6	2.5	42.4	1.1	1.4	1.1	44.9
	B	6.8	2.5	43.8	0.9	1.4	0.8	43.8

- Separation between adjacent peaks of the characteristic X-rays for light elements is small, typically 130 eV, comparable to the resolution of the spectrometer.
- The background level is relatively high.
- To obtain satisfactory peak heights for the light elements a low electron beam accelerating voltage is required, typically 5-10 kV.

The operating conditions found most suitable were an accelerating voltage of 10 kV and a sampling period of 200 seconds with a counting rate of 400-500 counts per second. As oxygen was the only detectable light element present no problem with overlapping peaks was encountered.

To determine the concentration of oxygen present the oxygen K_α X-ray line was measured relative to that from standards collected under identical conditions. The concentrations of the major constituent elements Si, O, and Fe were determined this way using the characteristic X-ray K_α lines given in Table 3.6. No ZAF correction was applied, but the background, determined by measuring the level adjacent both sides of the peak of interest, was subtracted before evaluating the relative intensity ratio K. The standard used for silicon and oxygen was quartz (SiO_2). For iron and oxygen a magnetite standard (Fe_3O_4) was used. Both were polished as for the specimens and coated with carbon. To ensure deposition of similar thicknesses the specimens and standards were carbon coated together.

To establish the accuracy of this technique a series of glass of the same base composition with various additions of Fe_2O_3 added were analysed, Table 3.8. The minor element concentrations were assumed to have constant ratios with silicon. The charge imbalance

Table 3.8: Composition of iron containing glasses (Si, Fe and Li only)

A - As mixed composition

B - Determined by windowless quantitative energy dispersive analysis

Specimen		Oxide Wt% (normalised)		
		Li_2O	SiO_2	Fe_2O_3
1	A	12	77	0
	B	12.4	76.6	0
2	A	11.9	74.9	1.0
	B	14.5	73.3	1.7
3	A	11.4	73.3	4.8
	B	12.3	73.4	3.8
4	A	10.9	69.9	9.3
	B	11.6	70.4	8.0
5	A	10.0	63.9	17.0
	B	11.7	62.0	17.6
6	A	8.5	54.7	29.0
	B	7.0	55.9	32.0
7	A	7.4	47.7	38.0
	B	5.9	48.5	38.7
8	A	6.6	42.4	44.9
	B	5.1	46.3	42.0

was assumed to be met by the presence of lithium which cannot be determined even with the beryllium window removed. Good agreement was found with an accuracy of ± 2 at% for the oxygen level and ± 2 oxide Wt% for the evaluation of the amount of Li_2O present as deduced by charge imbalance. The estimation of the lithium concentration must be treated with caution, because of the indirect nature by which it is obtained, and the presence of iron ions capable of showing multiple valency.

The windowless analysis also provided a method by which an indication of the lithium distribution in the coating adjacent the coating-substrate interface could be obtained. First the concentrations of silicon, iron and oxygen were determined by windowless energy dispersive analysis, as described above, at points along a line perpendicular to the interface. The minor elements, aluminium, phosphor us, potassium and zinc were assumed to have a constant ratio with silicon, identical to that in the bulk glass. Any charge imbalance was compensated by the presence of lithium ions.

3.2.9 Problems with glasses and interfaces

Mobile elements, typically the alkali elements, exhibit electrical effects. They are generally present as positive ions and can be attracted to the negatively charged electrons of the beam under the surface of the specimen. This did not appear to be a problem with potassium in the glasses analysed. A linear count rate was obtained as a function of time under the conditions used. Due to the inability to determine the lithium concentration directly it was not possible to say if it was affected by the electron probe.

The volume from which X-ray emission occurs is largely determined by electron penetration and far exceeds the probe diameter. It is useful to estimate this volume because quantitative analysis is accurate only if all the volume of X-ray emission is within a homogeneous region of the specimen. When analysing precipitates or phases in a matrix consisting of several phase types the minimum analysable size of one phase is approximately the X-ray emission volume. Reed [67] has published a nomagram of the relation.

$$PR \simeq K\ (E_o - E_c)$$

E_o accelerating voltage of electrons (KV)

E_c absorbtion energy of X-ray edge for element analysed (KV)

P density (g cm^{-3})

R diameter of X-ray emission volume (μm)

For Fe K_α radiation in a sample having a density 2.2 g cm^{-3}, typical of a glass, and an accelerating voltage of 15 kV the value for R is about 1.5 μm. It can be seen that the volume from which X-rays are generated is quite significant and must be considered when interpreting quantitative X-ray analysis results.

Problems will exist with a phase boundary or interface. Due to differences in hardness, the surface relief may change at the boundary. This will adversely effect the intensity of the X-ray emissions and hence the determined concentrations. By using hard lapping cloths and continuously rotating the surface during polishing any relief effects were reduced to a minimum.

3.3 X-ray Diffraction

Identification of crystal phases was undertaken using a Philips powder diffractometer [68]. This is an established technique and well documented by Klug and Alexander [69]. The essential conditions for diffraction from a crystalline solid are given by the Bragg equation

$$n\lambda = 2d \sin\theta$$

λ Incident X-ray wavelength

d crystal d-spacing

θ angle of incident or reflected rays with respect to a normal to the surface

n order of reflection.

A powdered sample, crushed by impact and passed through a number 200 sieve, is placed into a holder in the diffractometer. A beam of x-rays generated from a copper target (CuK_α = 1.5417 $\mathring{A}$) was diffracted by the sample. As the sample rotated at a rate of 1^o 2θ per minute, the intensity of the diffracted beam measured at an angle 2θ allowed the diffraction peaks to be obtained. The data yields values for the inter-planar spacings, d, and comparison with the standard J.C.P.D.S.[1] powder files enabled identification of the crystalline species present. This technique was used to establish the crystal phases present in bulk ceramic and enamel samples.

To determine the crystal phases present at the interface between an enamel and metal substrate the interface was first exposed. Adhesive tape was placed over the enamel, which was then subjected to several blows with a hammer. The enamel shattered and could be removed on peeling away the tape. The exposed ceramic surface was analysed in the powder diffractometer.

1 Joint Committee for Powder Diffraction Standards

3.4 Measurements of the Thermal Expansion Coefficient

The coefficient of thermal expansion was measured with a fused silica dilatometer. The apparatus consisted of a fused silica specimen holder and a linear variable differential transducer (LVDT), Figure 3.4, with the expansion of the specimen measured relative to that of silica. The sample, in the form of a rectangular rod, 5 x 5 mm^2 cross-section and length 30 mm was placed as shown in Figure 3.4. As the specimen expands on heating it pushed up a silica push rod whose displacement was measured using an LVDT, converting the displacement to an electrical output. The electrical signal produced was proportional to its linear displacement and had a sensitivity of 4.32 mV per micron displacement. The temperature of the specimen was measured by an adjacent thermocouple and displayed, along with displacement, on a chart recorder. Silica is used due to its very low thermal expansion coefficient compared to most glasses and ceramics. However a correction must be applied to obtain the absolute value of expansion.

The coefficient of thermal expansion α is given by

$$\alpha = \frac{L - L_o}{L_o(T-T_o)}$$

L_o - specimen length at room temperature T_o
L - specimen length at a temperature T.

By measuring the displacement between room temperature and a temperature T, increasing at regular intervals, a series of values for α were obtained for successively increasing temperatures. The specimen was heated from room temperature at a rate of 1.78^oC per minute.

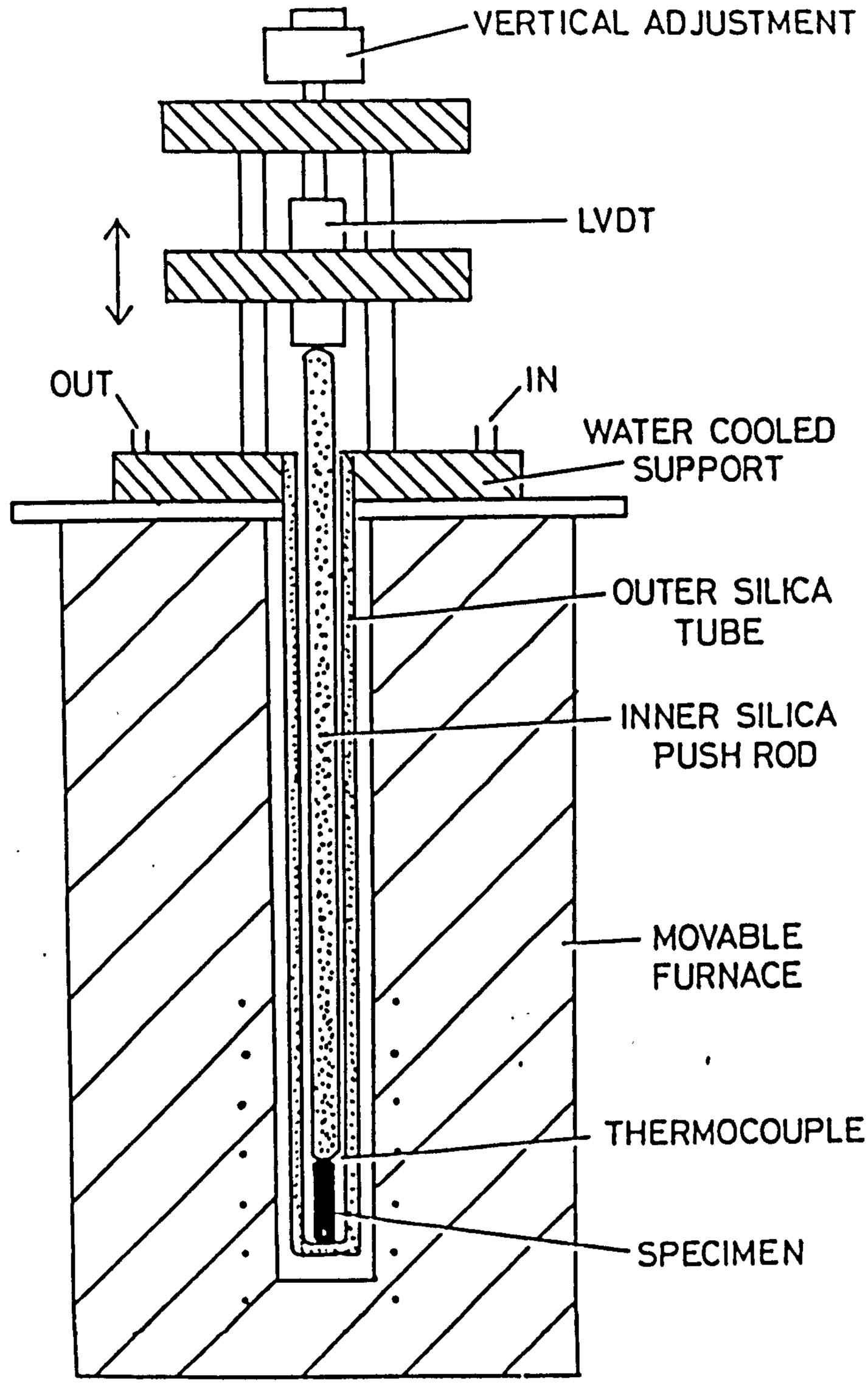

Figure 3.4 Fused silica dilatometer.

3.5 Differential Thermal Analysis

When a material passes from one state to another, energy in the form of heat is either absorbed or evolved. Differential thermal analysis (DTA) is a technique to measure this. For a glass-ceramic DTA can be used to measure the temperature at which crystal phases first appear, indicated by exothermic peaks, and the temperature at which the crystal phases remelt, indicated by endothermic peaks. Other material characteristics may also often be determined such as the transformation temperature given by a slight endothermic dip.

Thermocouples were placed in close contact with the small platinum crucibles containing two finely powdered and compressed powders. One was the specimen of interest and the other, an inert powder, the reference material. Aluminium oxide is an ideal material and used in this apparatus. The thermocouples are connected so that their e.m.f.s are opposed. The net e.m.f. represents the temperature difference between the specimen and inert reference material.

The two materials were heated at a constant rate of 5^{o}C per minute. In the steady state both will be at a constant temperature and no e.m.f. developed across the thermocouples. When the temperature reaches some point where crystallisation occurs, the exothermic transition will result in the sample acquiring an extra amount of heat so its temperature will increase relative to the standard. An e.m.f. is then developed across the thermocouples. The reverse is true for melting of a crystal phase.

The differential temperature was plotted against the temperature of the reference material with exothermic effects indicated by peaks and endothermic effects by dips in the curve.

3.6 Thermogravimetric analysis

Thermogravimetric analysis, TGA, is the quantitative measure of the changes of weight occurring in a material as it undergoes heating or cooling. The apparatus used was a Stanton Redcroft TG 750 thermobalance [70]. A small sample, up to 1g, was lowered into the microfurnace and the weight change recorded as a function of time at a constant temperature, or the weight change on heating at a specified rate recorded, depending upon the experiment being conducted.

CHAPTER 4

Experimental Preparative Techniques

4.1 Materials

4.1.1 Composition

Glass-ceramics based on the lithium-aluminosilicate system were used to provide the glass-ceramic enamels. Materials derived from these compositions are able to produce a highly crystalline body with phases having large coefficients of thermal expansion matching closely those of high expansion metals.

The glass compositions used to coat a 17% chrome-iron (Glass A) and a low carbon mild steel (Glass B) are shown in Table 4.1. The structural role of each oxide is lised in Table 4.2. The high silica content favours the formation of a lithium disilicate ($Li_2O.2SiO_2$) phase together with a quartz phase (SiO_2). Phosphorus oxide (P_2O_5) was added as a nucleating agent. The ability of P_2O_5 to act as an efficient nucleating agent is well documented, see McMillan [71], and it is believed to be related to the formation of lithium orthophosphate (Li_3PO_4) crystallites which act as heterogeneous nuclei, Headley [72]. Aluminium oxide stabilises the residual glass phase and improves the chemical durability of the glass-ceramic. Zinc oxide (ZnO) and Potassium oxide (K_2O) are important in determining the type of crystalline silica phase appearing. Both K_2O and ZnO favour the development of quartz as the silica phase, see Partridge [73]. Mild steel has a larger coefficient of thermal expansion compared to chrome-iron. Consequently the glass-ceramic used to coat mild steel requires a greater coefficient of thermal expansion than glass-ceramic A. The two glass-compositions are very similar, but glass B has a

higher amount of zinc oxide which has the effect of increasing the amount of quartz relative to lithium disilicate in the glass-ceramic. This increases the thermal expansion coefficient of glass-ceramic B relative to A since quartz has a larger coefficient of thermal expansion than lithium disilicate, (132 x 10^{-7} and 110 x $10^{-7}{}^{o}C^{-1}$ respectively over the range 20-300^{o}C).

Table 4.1: Glass Compositions

	Wt% Oxide					
Metal	Li_2O	Al_2O_3	SiO_2	P_2O5	K_2O	ZnO
			Glass A			
17% Cr-Fe	12	4.9	78.2	2.0	2.4	0.3
			Glass B			
Mild steel	12	4.5	77.0	2.0	2.5	2.0

Table 4.2: Role of Oxides in Glass

Oxide	Structural role	Functional role
SiO_2	Glass former	Crystal phase formation
P_2O_5	Glass former	Nucleating agent
Al_2O_3	Intermediate	Stabilises residual glass
ZnO	Intermediate	Preferential development of quartz
K_2O	Modifier	Preferential development of quartz
Li_2O	Modifier	Crystal phase formation

Two metal types were coated with the appropriate lithium-aluminosilicate glass-ceramics enamels, a 17% Chrome-iron and a low carbon mild steel. Their compositions are given in Table 4.3. The Chrome-iron was supplied by Krupp Stahl Werke [74] and had a thickness of 0.71 mm. The mild steel was an enamelling grade low carbon mild steel (C < 0.1 Wt%) supplied by Vitrostall [75]. It was a cold rimmed steel having a thickness of 0.92 mm. The presence of minor impurity components in the metals is of importance in determining the properties of the metal and also the quality of the enamel layer, as discussed by Thomas [76]. For example, a low carbon content is essential to prevent excessive evolution of gaseous CO and CO_2 at enamelling temperatures.

Table 4.3: Metal Composition

Element	Metal	
	17% Chrome-iron	Mild Steel
	Chemical analysis (wt%)	
Carbon	0.03	0.01
Aluminium	-	0.02
Silicon	0.32	0.01
Manganese	0.36	0.32
Sulphur	-	0.01
Phosphorus	0.028	0.01
Chromium	16.07	0.015
Nickel	0.14	0.15
Copper	-	0.03
Vanadium	0.15	0.01

4.1.2 Glass Preparation

The parent glass, required composition as given in Table 4.1 , was prepared. The glass batch was made up using 'Analar' grade reagents, consisting of the oxides SiO_2, P_2O_5, Al_2O_3 and ZnO together with the carbonates Li_2CO_3 and K_2CO_3. The mass of carbonate added was that calculated to give the required oxide mass on decomposition.

After tumble-mixing for 24 hours the batch was melted in a platinum 10% rhodium crucible in an electrically heated furnace for 3 hours at 1350°C. The melt was cast into deionised water, the resulting glass frit thoroughly mixed and remelted as above. The melt was finally cast into a glass slab or quenched to a frit in deionised water as required. A clear, bubble free glass was obtained and no crystal phases could be detected by X-ray diffraction techniques. Quantitative energy dispersive X-ray analysis (EDX) indicated that no significant loss occurred during melting, with the final glass having a composition close to that expected, Table 4.4.

The bulk glass was annealed by placing in a furnace at 400°C for one hour and then cooling slowly to room temperature before removal.

Table 4.4: Composition of Prepared Glasses

wt%

	Li_2O	Al_2O	SiO_2	P_2O_3	K_2O	ZnO
Glass A	11.9	5.1	76.8	2.0	2.9	1.0
(Nominal	12.0	4.9	78.2	2.0	2.4	03:)
Glass B	11.8	4.5	76.9	2.0	2.4	2.1
(Nominal	12.0	4.5	77	2.0	2.5	2.0)

Values accurate to ± 0.1 wt%

4.1.3. Glass and Glass-Ceramic Characteristics

Both glasses readily undergo crystallisation on heating. Differential thermal analysis of the glasses, ground to a powder and passed through a 200 sieve, is shown in Figure 4.1. Two crystal phases are seen to appear indicated by the presence of the exothermic peaks. The first peak, at 665°C for glass A and 660°C for glass B, is due to the formation of crystalline lithium disilicate ($Li_2O.2SiO_2$). Determined by x-ray diffraction of the powdered glass quenched just past this temperature. The second peak, occurring at 825°C for glass A and 820°C for glass B, is due to the appearance of β-quartz (SiO_2). An endothermic dip occurs at 970°C for glass A and 960°C for glass B, and is due to the melting of the lithium disilicate phase.

It is desirable to produce, during the controlled crystallization or heat-treatment, a glass-ceramic with the required properties, in particular a thermal expansion curve which can be matched to the metal being coated. For glass A, used to coat chrome-iron, this necessitates a heat-treatment consisting of a nucleation hold at 600°C for 30 minutes followed by a growth stage at 800°C for 3 hours. Glass B, used to coat mild steel, required a nucleation hold at 580°C for 1 hour followed by a growth stage at 820°C for 3 hours. These are listed in Table 4.5 To avoid the setting up of destructive thermal stresses the glass was heated from room temperature to the nucleation stage and then on to the growth stage at a rate of 5°C per minute. On completion of the growth stage the crystallised glass was gradually* cooled in the furnace to room temperature before removal. Properties of the bulk glass-ceramics were then examined.

* The furnace was switched off and allowed to cool at its natural rate.

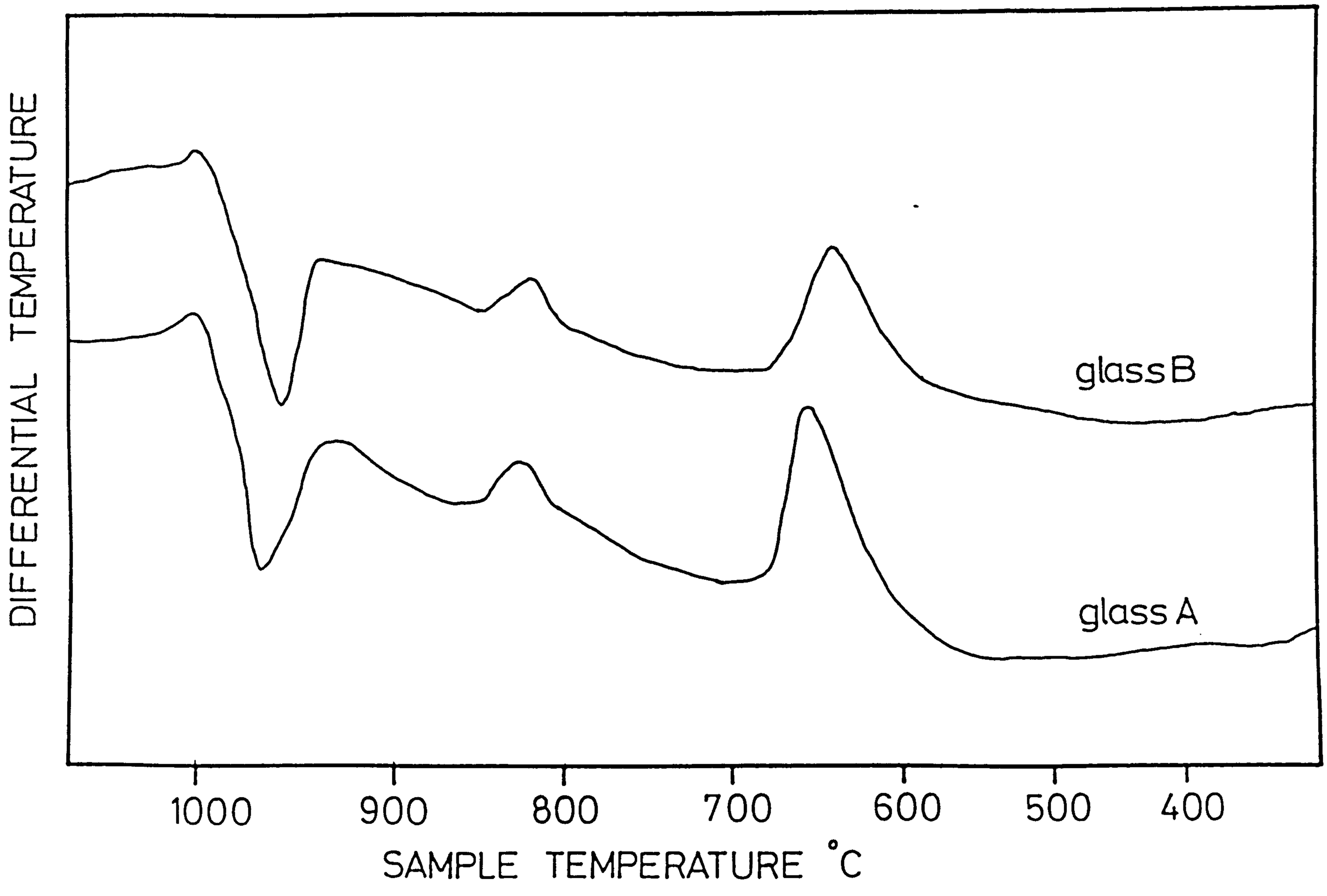

Figure 4.1 DTA curves for glass A and glass B.

Table 4.5: Heat Treatment Schedules

	Nucleation Stage	Growth Stage
Glass A	30 minutes	3 hours
	600°C	800°C
Glass B	1 hour	3 hours
	580°C	820°C

The crystal phases present after heat-treatment were determined by X-ray diffraction.

Glass-ceramic A, derived from the parent glass A, contains, as the major crystal phases, lithium disilicate ($Li_2O.2SiO_2$) and β-quartz (SiO_2). A small proportion of cristobalite is also present.

Glass-ceramic B, derived from the parent glass has the crystal phases lithium disilicate ($Li_2O.2SiO_2$) and β-quartz as the major phases and cristobalite present as a minor phase. However the amount of quartz has increased, with respect to the amount of lithium disilicate, in comparison with the glass-ceramic A.

In both glass-ceramics a very fine microstructure was developed by the heat-treatment. The typical microstructure for glass-ceramic A is shown in Figure 5.1.12(c).A dark contrast elongated phase identified as lithium disilicate can be seen, with a light matrix containing a small bright contrast phase identified as quartz. Both crystal phases have submicron dimensions.

The thermal expansion curves of glass A, glass-ceramic A and the 17% chrome-iron are shown in Figure 4.2. The parent glass exhibits an increase in its slope at 420°C associated with the transformation temperature (T_g) and shows a maximum at 445°C, the dilatometric softening (M_g) temperature. Values for the coefficient of thermal expansion are listed in Table 4.6 as measured from 50°C to the specified temperature. Between 50-400°C the coefficient of thermal expansion coefficient of the glass A is 77 x 10^{-7}°C^{-1}. The glass-ceramic shows an increase in its thermal expansion and dilatometric softening temperature. It begins to deform in the dilatometer at 725°C, and has a thermal expansion coefficient between 50-400°C of 105 x 10^{-7}°C^{-1}. A good match between the thermal expansion curves of the bulk glass-ceramic and chrome-iron substrate exists. Assuming the glass-ceramic enamel to show the same thermal expansion characteristics as the bulk material, the residual stresses present along the interface will be small and compressive. It is difficult to evaluate the stresses set up at the interface due to the lack of information, particularly in deciding at which temperature the glass-ceramic can be regarded as a rigid body.

Table 4.6: Thermal Expansion Coefficients for Glass A and glass-ceramic A

ΔT	Glass A	Glass-ceramic A	17% Chrome-iron
50-100	64	103	100
50-200	73	118	106
50-300	75	107	108
50-400	77	105	108
50-500	-	103	108
50-600	-	105	109
50-700	-	-	
°C		x 10^{7}°C^{-1}	(±1 x 10^{7} °C^{-1})

The thermal expansion curves for glass B, glass-ceramic B, and mild steel are shown in Figure 4.3. The glass shows a slight increase in slope at 420°C, associated with the transformation temperature, and a dilatometric softening temperature of 465°C. A value of 79 x 10^{-7}°C^{-1} is obtained for the thermal expansion coefficient for the temperature interval 50-400°C. On conversion to a glass-ceramic an increase in the thermal expansion and in the dilatometric softening point occurs. The dilatometric softening temperature is 745°C and the value for the thermal expansion coefficient between 50-400°C, Table 4.7, is 132 x 10^{-7}°C^{-1}. A bend occurs in the expansion curve at 425°C, but the exact cause of this is unknown. It does not represent a phase inversion of the phases present and is most likely related to the residual glass phase. The expansion curve for mild steel is also shown. An inflection occurs at 900°C associated with the transformation of α-iron (body centre cubic) to γ-iron (face centre cubic). This is significant in that on cooling the iron will expand between 900-800°C and may introduce tensile stresses in the enamel if it is rigid, between this temperature interval.

Table 4.7: Thermal Expansion Coefficient for Glass B and Glass-ceramic B

ΔT °C	Glass B	Glass-ceramic B	Mild Steel
50-100	83	84	115
50-200	84	119	115
50-300	84	133	119
50-400	79	132	124
50-500	-	115	128
50-600	-	109	125
50-700	-	108.	116

x 10^{7}°C^{-1} ($\pm 1 \times 10^{7}$ °C^{-1})

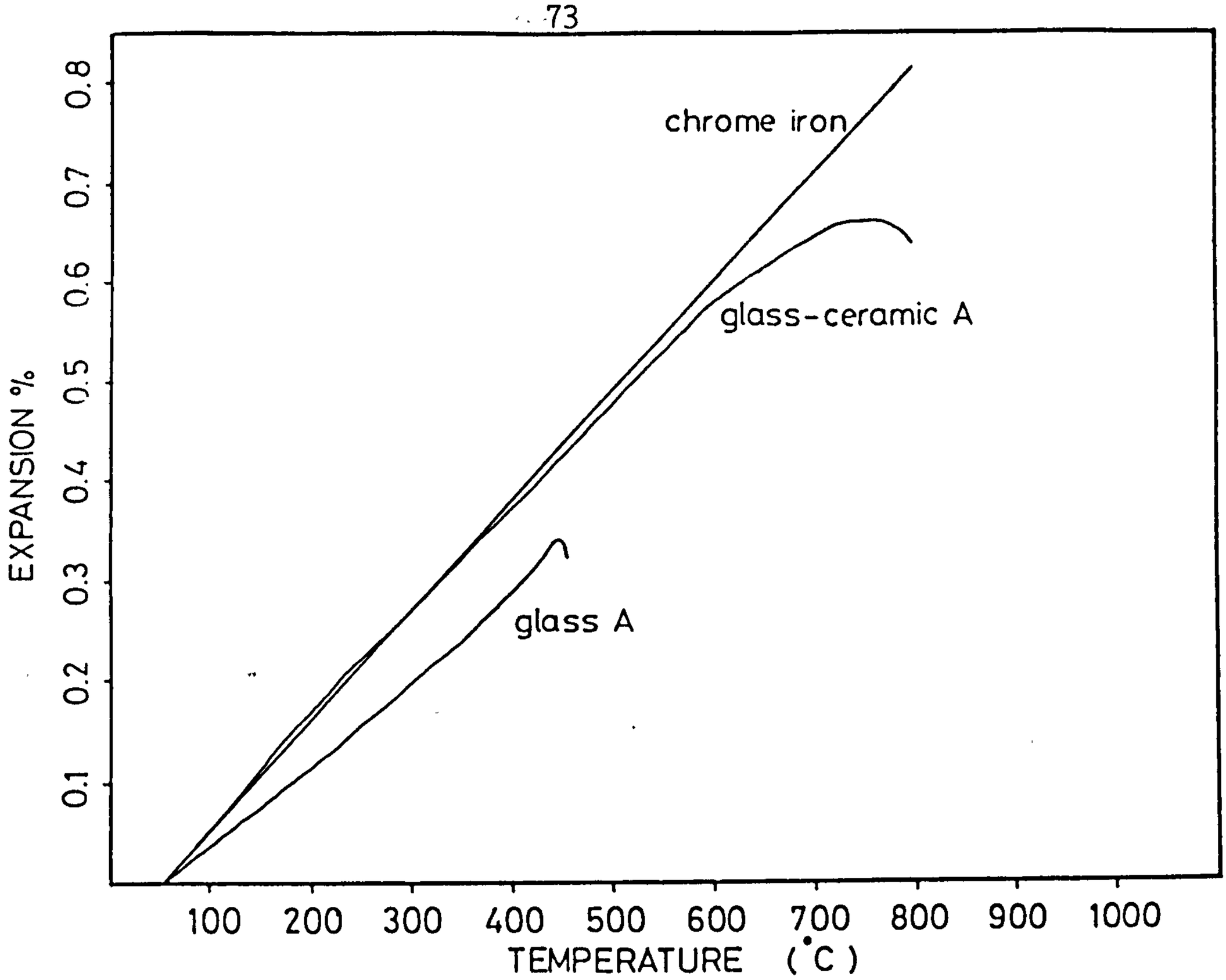

Figure 4.2 Thermal expansion of glass A, glass-ceramic A and 17% chrome-iron.

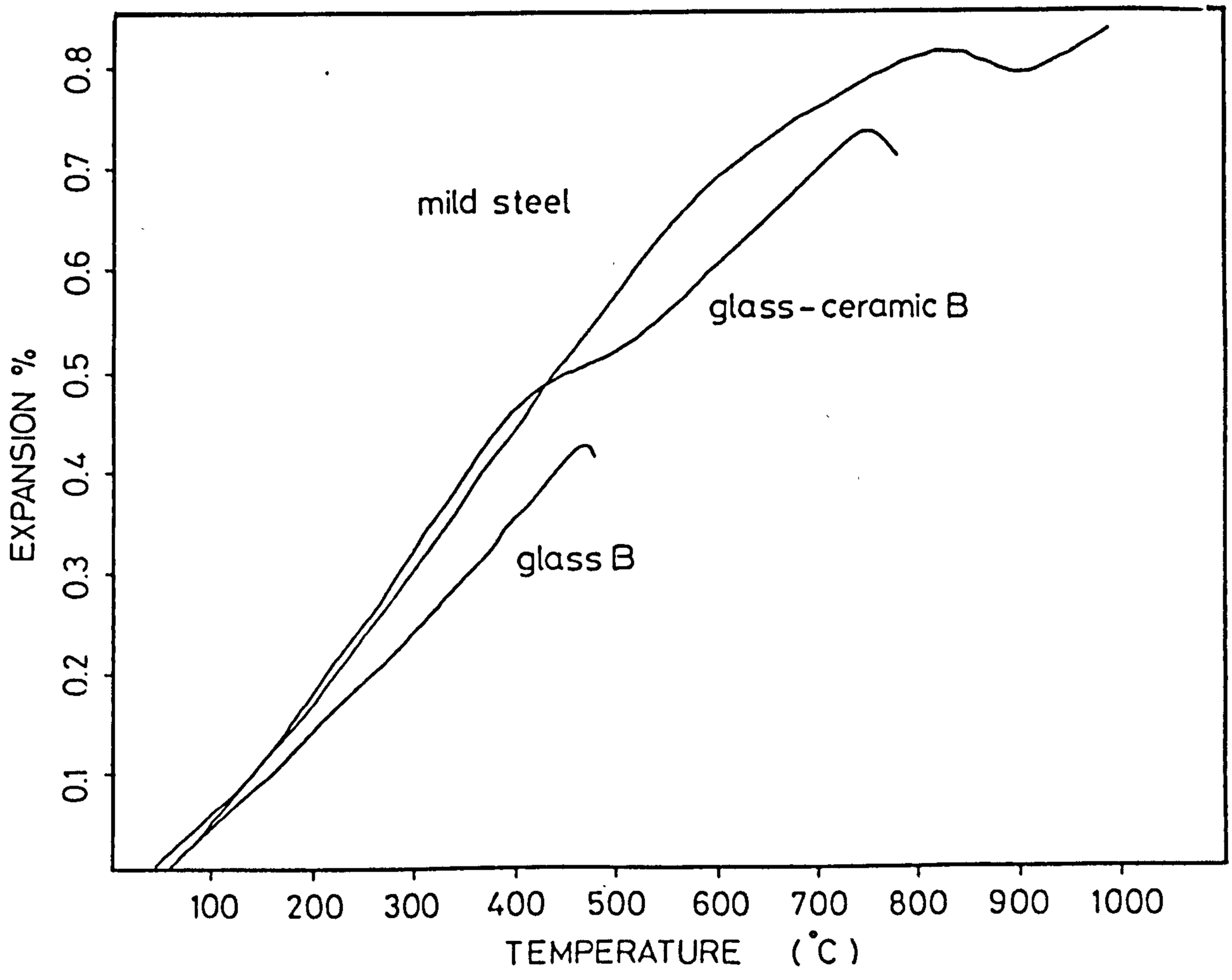

Figure 4.3 Thermal expansion of glass B, glass-ceramic B and mild steel.

The properties of a typical lithium-alumino-zinc-silicate glass-ceramic, similar in composition to glass-ceramic A are listed in Table 1.3.

4.2 Coating Techniques

4.2.1. Glass powder formation

Glass-frit of the required glass composition produced as described in Section 4.1.2 was ball milled to a fine powder. Milling was done in an alumina container approximately half full with alumina balls of various sizes. The glass frit, or charge, was added such that the mill was three quarters full, and the mill tumbled for 3 hours to break up the glass frit. A solvent was then added to the charge, the amount being twice that volume of glass frit initially added. It was found that water resulted in lumping of the powder in the final slurry. The use of an organic solvent, methanol, gave a much more uniform distribution of the powder in the slurry. Milling was continued for a further 33 hours on addition of the methanol.

After milling, the slurry was poured into an open top plastic tray and allowed to dry. The dried powder was sieved through a 200 mesh. Powder particle size distribution will be influenced by many factors such as mill ball size, solvent type and content, milling time and speed. Figure 4.4 shows the particle size distribution obtained for the milling method above, as determined by a laser particle size analyser.

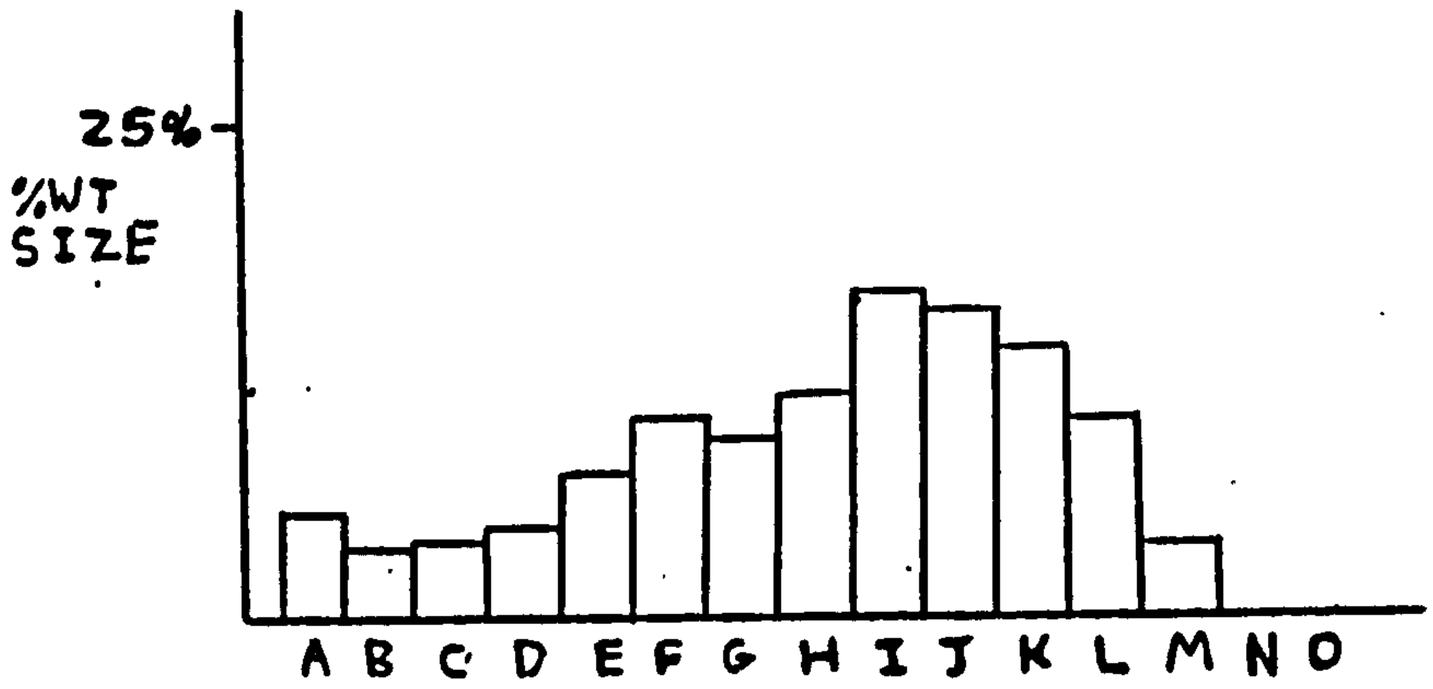

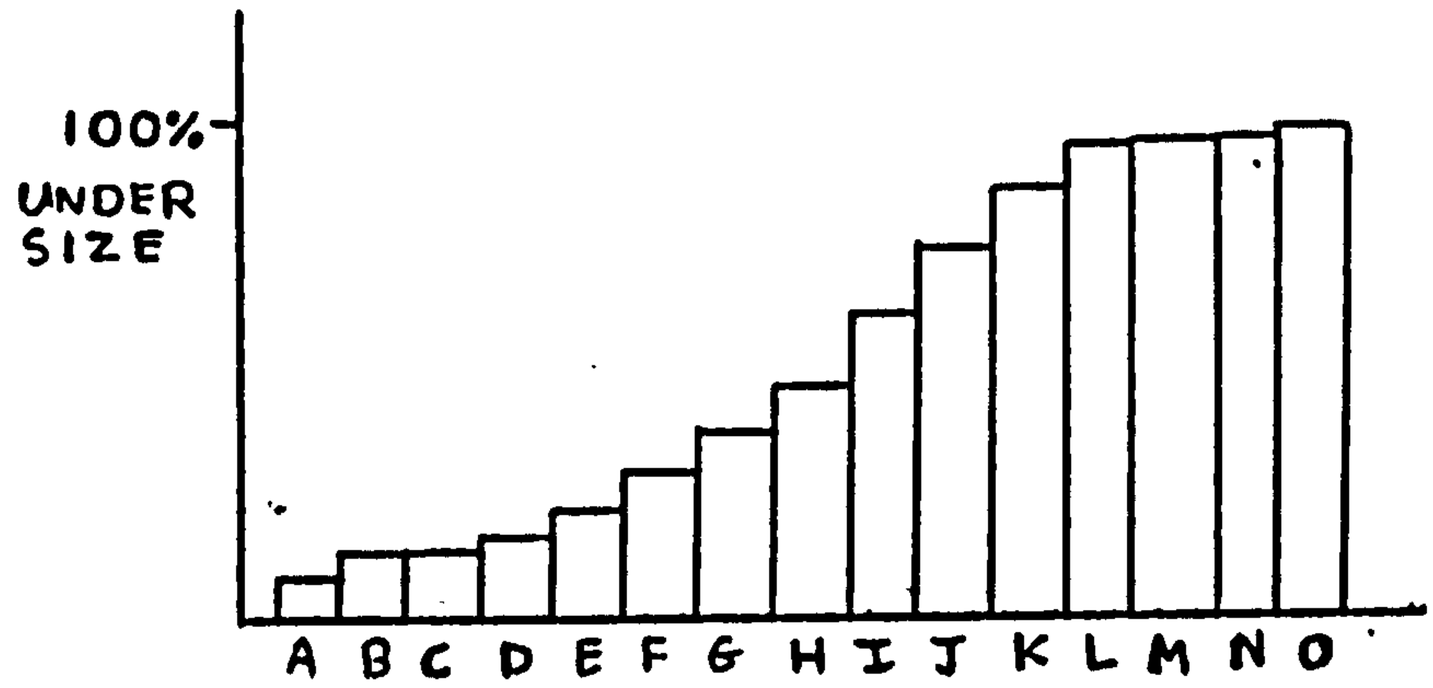

	SIZE BAND UPPER	LOWER	CUMULATIVE WT BELOW	WEIGHT IN BAND	CUMULATIVE WT ABOVE	LIGHT ENERGY COMPUTED	MEASURED
A	188.0	37.2	100.0	0.0	0.0	53	6
B	37.2	53.5	100.0	0.0	0.0	94	77
C	53.5	37.6	99.9	0.1	0.0	152	141
D	37.6	28.1	97.6	2.3	0.1	234	230
E	28.1	21.5	88.4	9.2	2.4	358	360
F	21.5	16.7	75.3	13.1	11.6	524	526
G	16.7	13.0	60.1	15.2	24.7	736	735
H	13.0	10.1	44.5	15.5	39.9	948	952
I	10.1	7.9	34.1	10.4	55.5	1139	1144
J	7.9	6.2	26.1	8.0	65.9	1303	1304
K	6.2	4.8	17.1	9.0	73.9	1443	1448
L	4.8	3.8	11.2	5.9	82.9	1598	1611
M	3.8	3.0	8.4	2.8	88.8	1758	1738
N	3.0	2.4	6.1	2.3	91.6	1900	1888
O	2.4	1.9	4.0	2.1	93.9	2047	2047

Figure 4.4 Glass powder size distribution after milling.

4.2.2 Metal pretreatment and oxidation

The metal surfaces required a thorough degreasing to remove surface oils and contaminants followed by a preoxidation stage. The treatments used were suggested by GEC Stafford from experience they had in coating these metals.

The chrome-iron was degreased by soaking in acetone with ultrasonic agitation for 5 minutes followed by several rinses in deionised water. Abrasion of the metal surface, if required, was then carried out using alumina grit (~ 250 μm) and blasting the metal surface for a few seconds at a 40 p.s.i. pressure. After abrasion the metal surface was again degreased in acetone with ultrasonic agitation and rinsed in deionised water. The chrome-iron was oxidised, if required, in wet hydrogen at 900°C for 6 hours. The atmosphere, produced by passing hydrogen through water, was oxidising with respect to chromium but reducing for iron resulting in the formation of a chromium oxide (Cr_2O_3) layer as opposed to a chrome-iron spinel. X-ray diffraction patterns from an unoxidised chrome-iron surface and an oxidised surface are displayed in Figure 4.5, clearly showing the development of a chromium oxide (Cr_2O_3) layer. The total measured oxide weight gain of 0.53 ($\pm$ 0.02) mg cm^{-2} corresponds to an oxide thickness of 1.01 μm if fully dense. Figure 4.6 shows a backscattered electron micrograph of the unoxidised, but abraded metal surface. Particles of alumina grit are embedded in the surface and these are not removed by the subsequent cleaning stage prior to oxidation. The surface after oxidation is shown in Figure 4.6, it is seen to be completely covered by chromium oxide (Cr_2O_3) and has a highly irregular surface. EDX analysis of the surface gives the composition shown in Table 4.8. Iron is present, and the oxide scale is believed

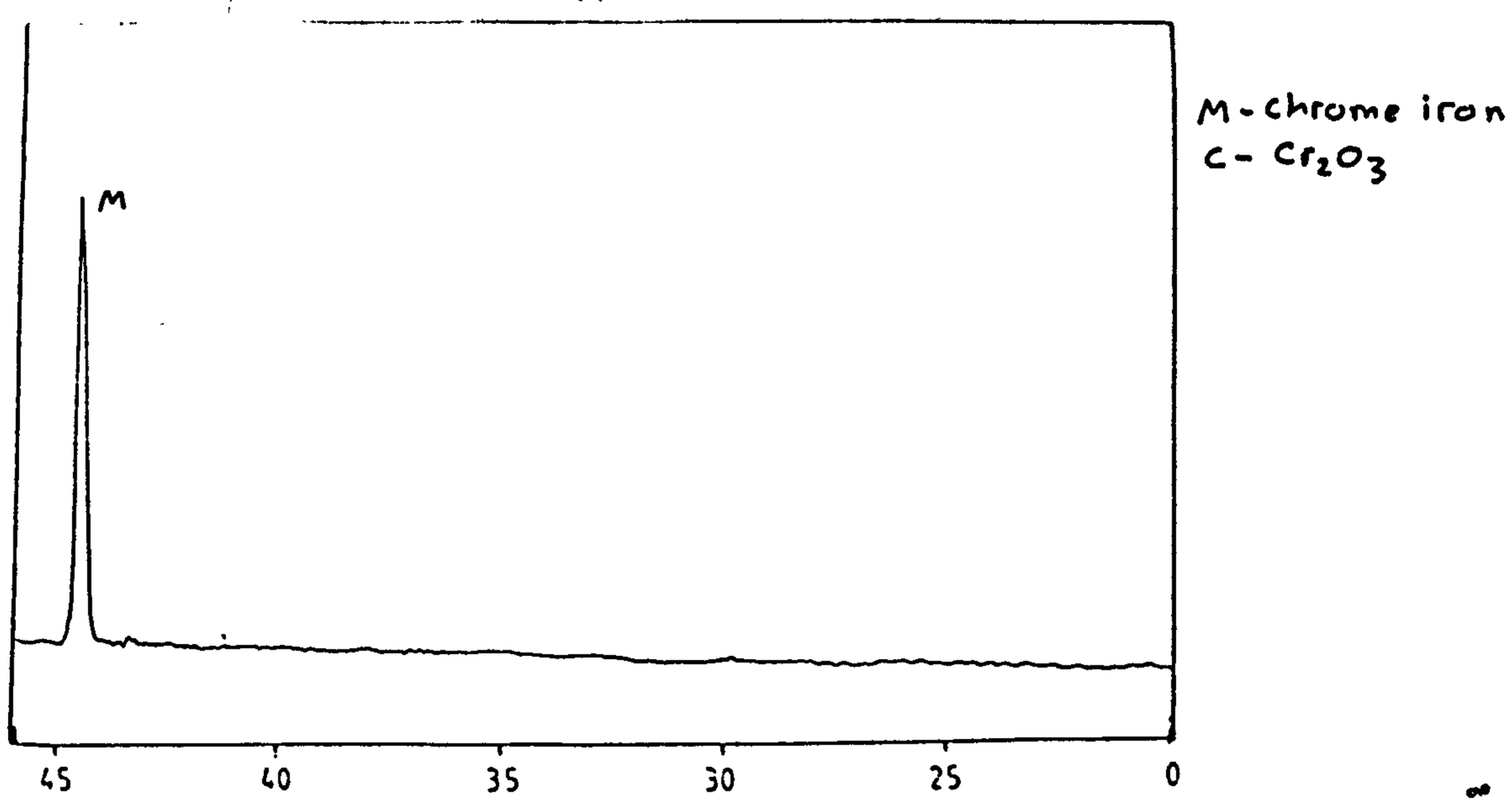

(a) unoxidised metal surface.

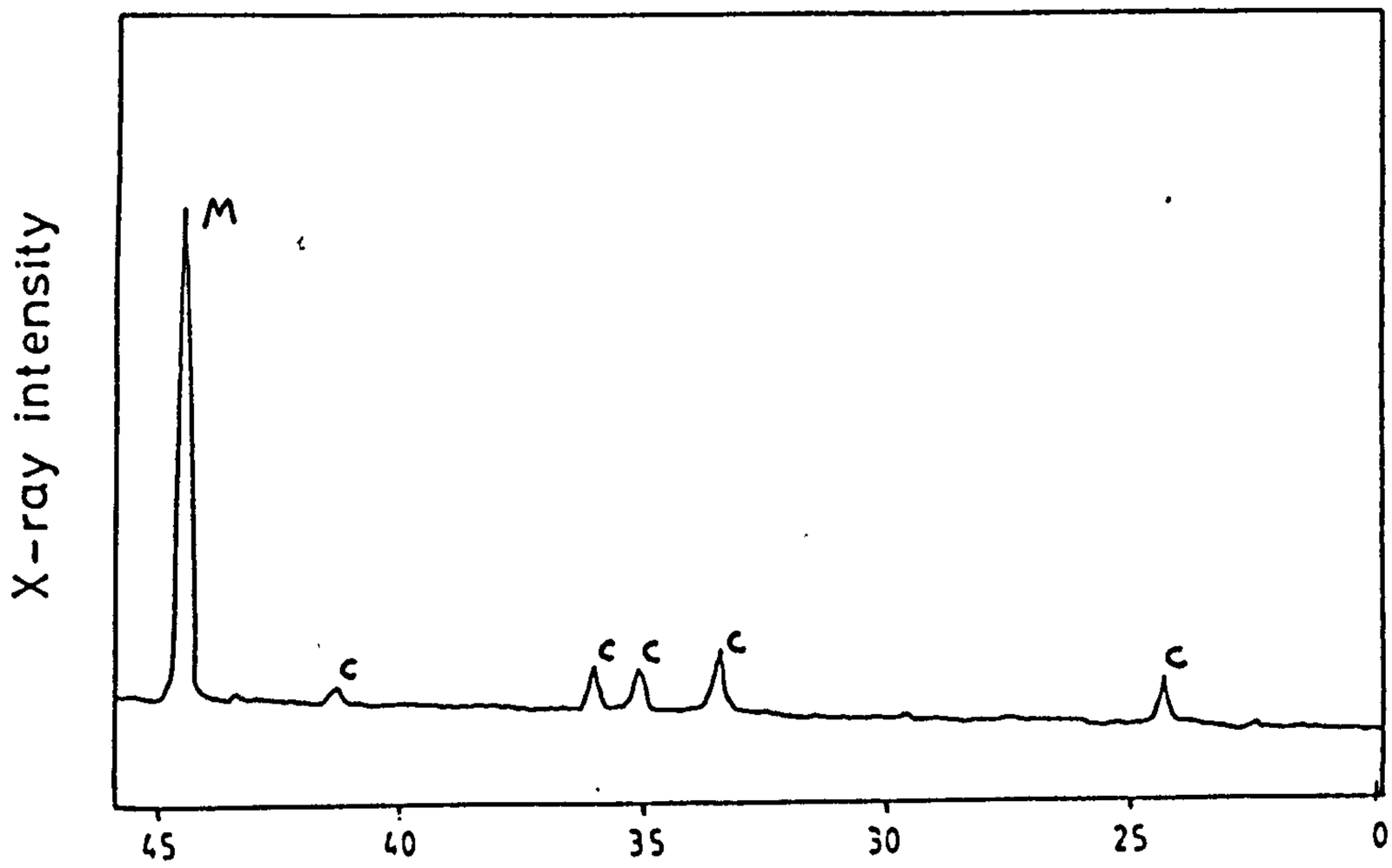

(b) oxidised in wet hydrogen.

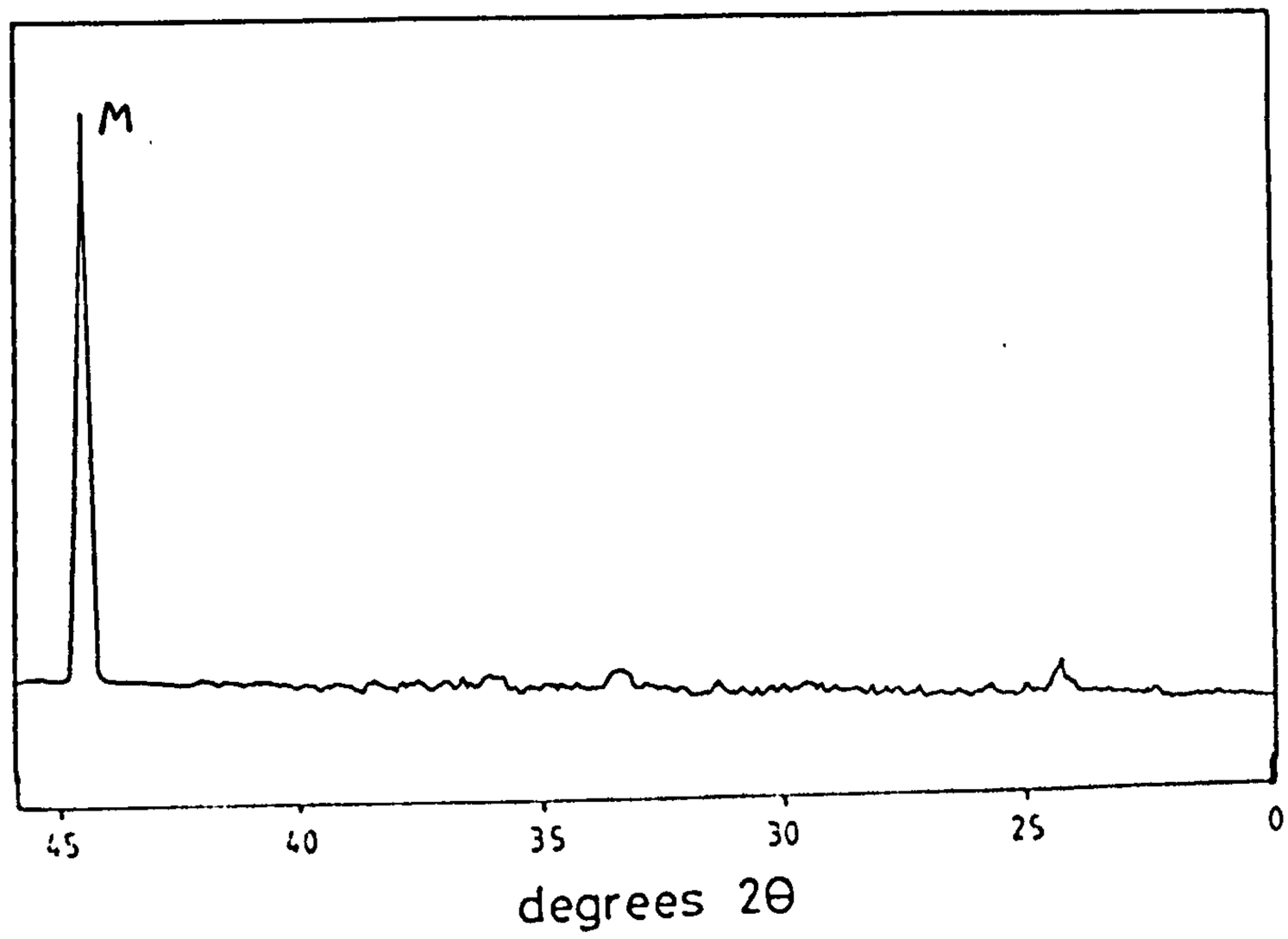

(c) oxidised in air at 970°C for 5 minutes.

Figure 4.5 XRD patterns of a unoxidised and preoxidised 17% chrome-iron surface.

Figure 4.6. Electron micrographs of chrome-iron surface

(a) abraded but not oxidised

(b) preoxidised in wet hydrogen

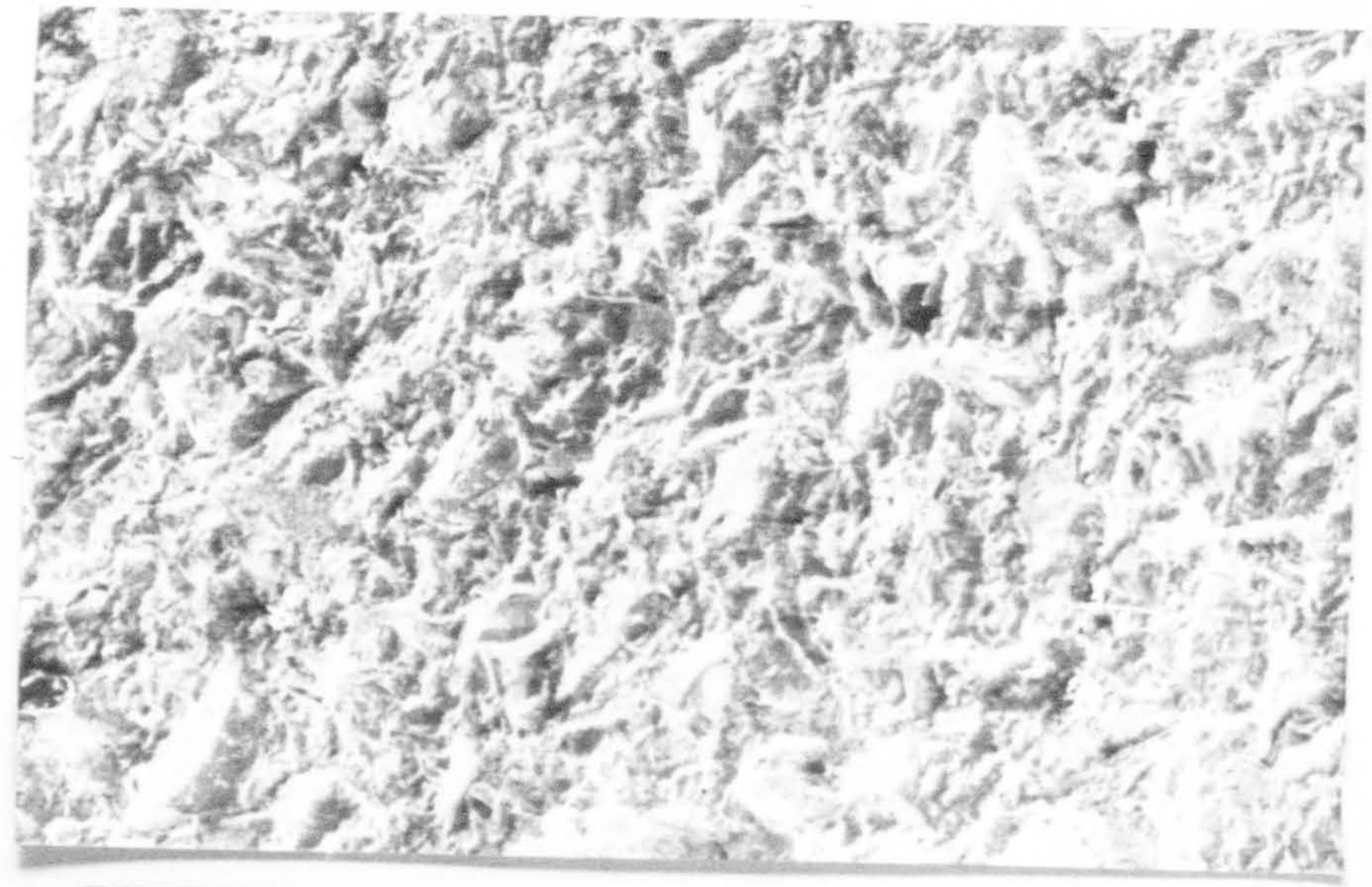

100 µm

4 µm

chrome-iron surface abraded
and preoxidised in wet hydrogen

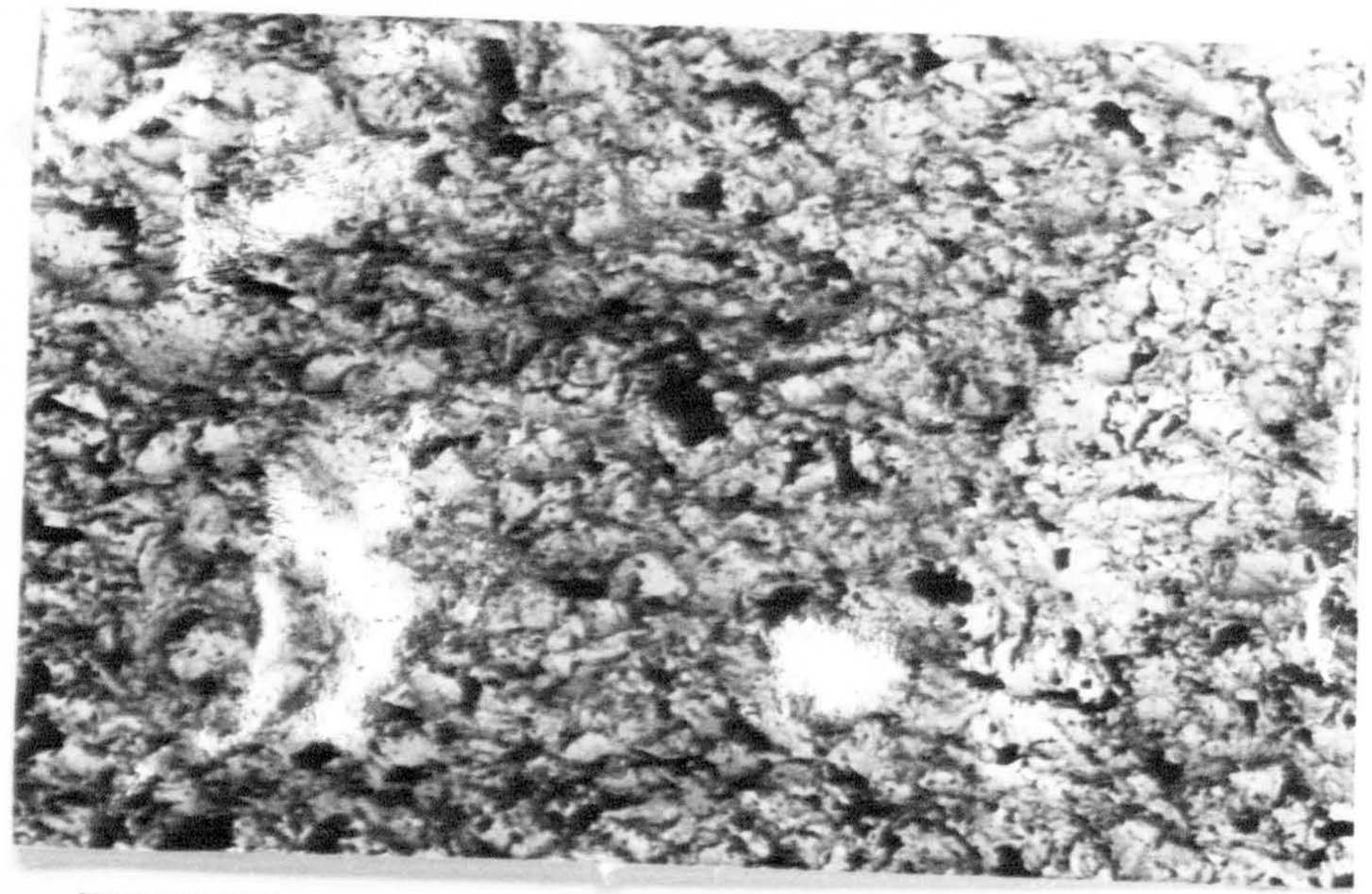

100 µm

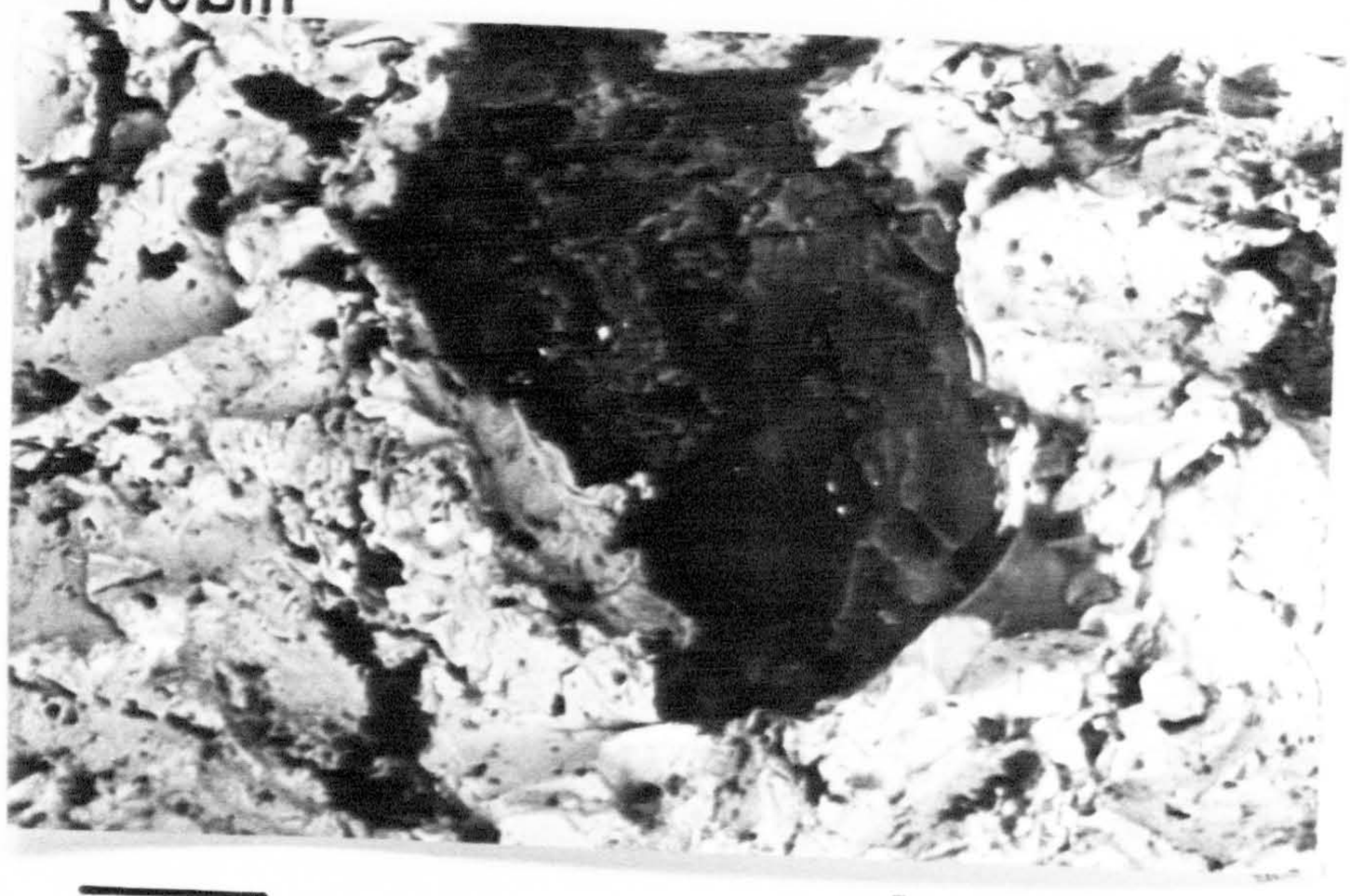

4 µm

chrome-iron surface abraded
with alumina grit

A - embedded alumina grit

Table 4.8 Composition of oxide scale on chrome-iron oxidised in wet hydrogen. (Oxygen calculated)

EDX analytical conditions		Oxide composition atomic % (±0.1 at%)							
		Al	Si	P	K	Cr	Fe	Zn	O
20 kV	$100\mu m^2$	2.5	0.6	0	0	29.4	7.2	0	60.1
	$1\mu m^2$	0.5	0.9	0	0	29.3	8.9	0	60.1
10 kV	$100\mu m^2$	2.4	0.3	0	0	32.9	4.0	0	60.0
	$1\mu m^2$	0.1	0.3	0	0	32.3	4.0	4,0	59.2

to be essentially chromium oxide (Cr_2O_3) with a small quantity of ferric oxide (Fe_2O_3) in solid solution. The composition is approximately 10 wt% Fe_2O_3, 90 wt% Cr_2O_3.

The mild steel was degreased in two steps, first, using an acetone soak with ultrasonic agitation then subsequently soaking in a 7.5 W/V NaOH solution (pH 13) for 15 minutes at room temperature, again with ultrasonic agitation. The sodium hydroxide is involved in saporification of residual oil and grease producing a soap which is soluble and removed from the metal surface. The metal was rinsed several times with deionised water, dried at 150^{o}C in air and stored in an evacuated desiccator. No abrasion of the surface was given or pretreatments such as acid pickling or nickel dipping used.

The mild steel substrates were preoxidised by placing in an open ended furnace for various times and temperatures. Oxidation of mild steel is a much more critical process than for the chrome-iron and it was carefully examined.

Mild steel substrate pieces of dimensions 20 x 20 mm^2 were subject to various preoxidations in air, followed by rapid quenching on a cold metal surface. The phases of iron oxide present on the surface were determined by x-ray diffraction. The x-ray diffraction patterns collected from metal surfaces oxidised at 650 and 750^{o}C for 15 minutes in air are shown in figure 4.7. For comparison the unoxidised metal is also shown. At 500^{o}C a black tarnish was developed with magnetite (Fe_3O_4) present. At higher temperatures a thicker, powdery black oxide was formed, which was easily detached. The oxides of iron present are a mixture of magnetite (Fe_3O_4) and Wustite (FeO) with increasing amounts of Wustite at higher temperatures. Iron forms three stable oxides, Wustite (FeO), magnetite (Fe_3O_4) and hematite (Fe_2O_3). Below 570^{o}C Wustite

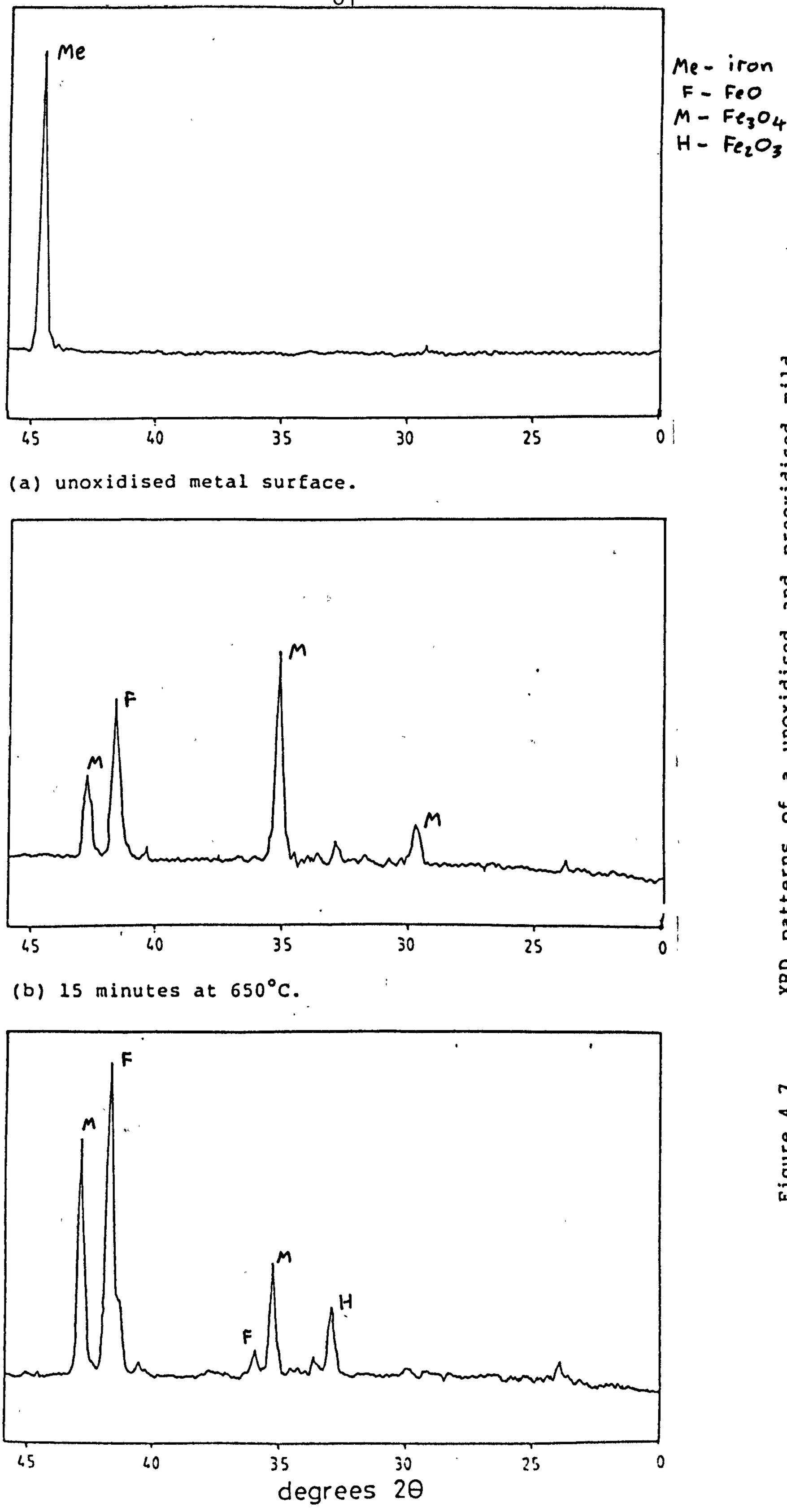

(a) unoxidised metal surface.

(b) 15 minutes at 650°C.

(c) 15 minutes at 750°C.

Figure 4.7 XRD patterns of a unoxidised and preoxidised mild steel surface.

is unstable and may partly revert to the more stable forms on quenching to room temperature. The oxide scale formed above 570°C[1] is composed of three oxide layers, although essentially wustite. At 700°C FeO is formed adjacent to the metal, Fe_3O_4 and Fe_2O_3 as outer layers, with Fe_2O_3 the outer most. The relative thickness of the three oxide layers is about 100/10/1, Hanffe [77]. The mass of iron oxide as determined by weighing of the metal pieces prior and after oxidation is given in Table 4.9. To complement this, thermo-gravimetric measurements were performed on small pieces of mild steel, typical mass 50 mg, and surface area of 1 cm^2, subjected to identical pretreatment as for the enamelled pieces. This allowed oxide weight gain to be determined as a function of time at temperatures 500, 550, 600, 650, 700, 800 and 900°C. The curves obtained are parabolic and a plot of oxide weight gain per unit area against $(time)^{\frac{1}{2}}$ yields a linear relation at each temperature, Figure 4.8. Oxidation of mild steel is a rate controlled process depending on the diffusion of iron ions through the oxide already formed. Parabolic weight gain is described by:

$$\Delta M^2 = Kpt$$

ΔM - Metal oxide weight gain g cm^{-2}

Kp - Parabolic rate constant g^2 cm^{-4} s^{-1}

t - Oxidation time s

The temperature dependence of oxidation processes are found to obey a Arrhenius equation, such that:

$$Kp = K_O\, e^{-Q/RT}$$

Using the data in figure 4.8, it is possible to evaluate Q and K_O. The oxide weight gain at a particular temperature and time can be

[1] In air at atmospheric pressure.

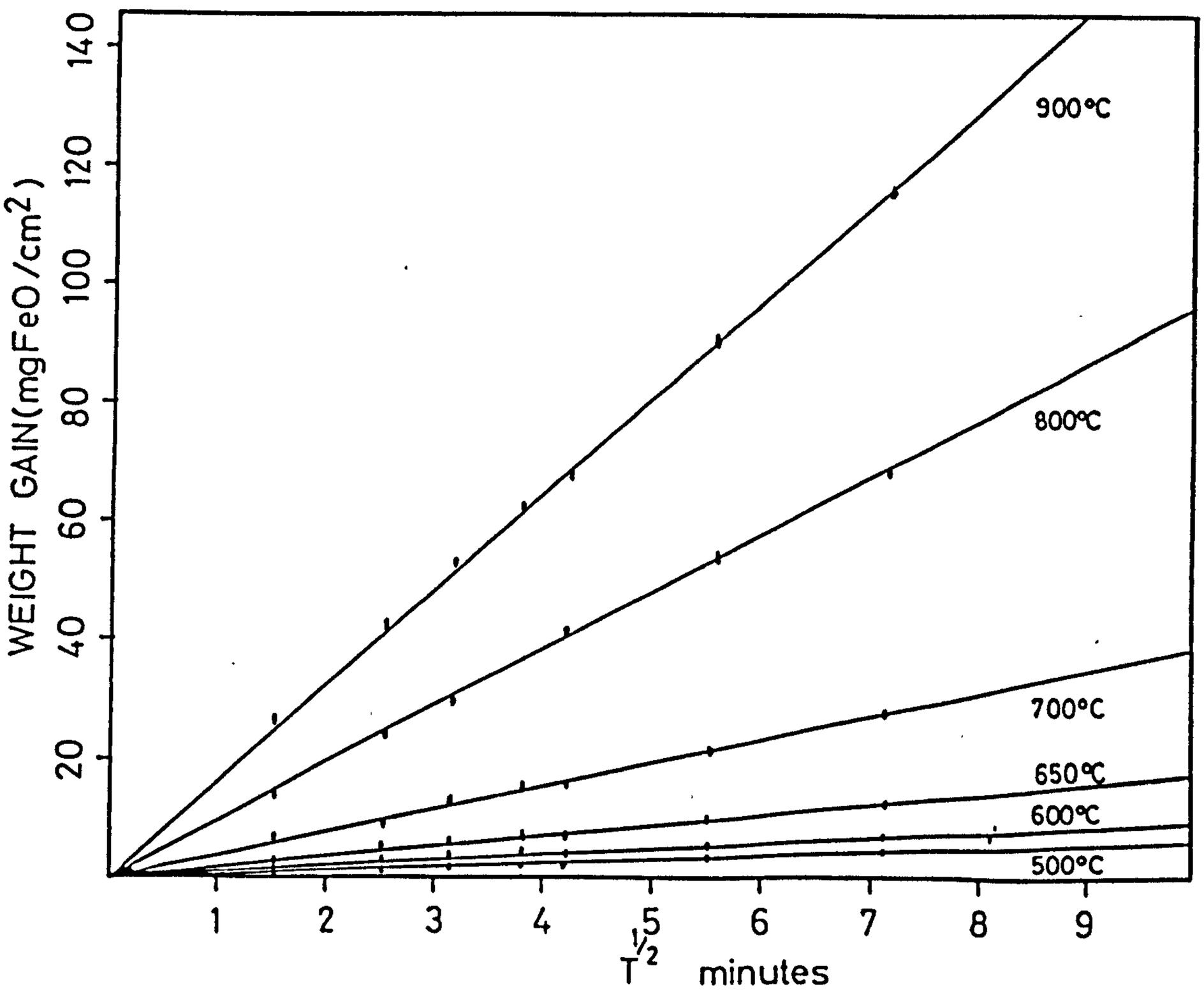

Figure 4.8 Iron oxide weight gain with time at 500, 600, 650, 700, 800 and 900°C. (In atmospheric air)

Table 4.9: Oxidation of Mild Steel

Weight of oxide found after 15 minutes at stated tempeature

Temperature	Oxide Weight Gain
500	0.9 ±0·1
550	0.9 ±0·1
600	5.3 ±0·1
650	9.0 ±0·1
700	14.8 ±0·1
800	29.7 ±0·1
900	64.1 ±0·1
°C	mg cm^{-2}

Table 4.10: Weight of Oxide determined by Equation 4.1

Temperature	Oxide Weight Gain
600	4.9 ±0·2
650	8.2 ±0·2
700	13.2 ±0·2
800	29.8 ±0·2
900	58.5 ±0·2
°C	mg cm^{-2}

expressed by:

$$\Delta M^2 = 7.36 \exp[-1.698 \times 10^4/T]t \qquad 4.1$$

ΔM - Oxide weight gain mg cm^{-2}

T - Temperature ^oK

t - Oxidation time s

The calculated oxide weight gain determined using this equation are listed in Table 4.10.

4.2.3 Screen Printing Technique

The glass powder produced by ball milling as described in 4.3.1 was mixed with an organic binder to produce an ink. The organic binder, supplied by Blythe Colours Ltd [78], was added to the glass powder to give a fairly viscous fluid. A ratio of two parts glass powder to one part binder produced the required constituency. Metal strips, dimensions 50 x 17 mm^2, of the required metal were prepared as previously described. The glass powder was screen printed onto the metal substrate surface using a printer supplied by Dek Instruments Ltd [79]. The screen had a pattern of three circular pads such that three pads of glass powder; 8 mm in diameter, were printed onto the metal surface. After printing the ink was dried by placing the coated metal substrate in an oven at 150^oC for 15 minutes. A total of three coats were applied with drying between each coat. The final result was a metal substrate having 3 glass powder pads bound with the organic binder which could withstand handling.

It is important to remove the binder before firing. This is an organic compound and will produce on heating a reducing atmosphere which may be detremental to processes during firing of the enamel. The results of thermogravimetric measurements on 5 mg of powder plus binder heated from room temperature at a rate of 5°C per minute are shown in Figure 4.9. The binder can be seen to be removed at about 250°C.

Chrome-iron was screen printed with an ink prepared from glass A, so that on firing and heat-treatment a enamel coating of glass-ceramic A is produced. Likewise mild steel was coated with an ink prepared from glass B.

4.2.4 Firing condition

The coated metal substrates were fired in a mullite tube furnace, shown in Figure 4.10, which had sealable ends. The specimen was placed on a refractory tile and pushed into the central region of the furnace. Its exact position was in the furnace hot zone, a region found to be 13 cm in length where the temperature had a maximum and varied by less than $\pm$ 5°C along its length. A thermocouple placed just above the specimen was used to record the specimen temperature. If an inert atmosphere was required the furnace tube ends were sealed and an inert gas, oxygen free nitrogen, passed through. The nitrogen was passed in at the opposite end to which the specimens were inserted or removed.

In a typical firing schedule, the furnace was heated to the required firing temperature and allowed to stabilise. If necessary nitrogen was then passed through the tube at a rate of 2 litres per minute. One of the furnace ends was removed, the specimen rapidly

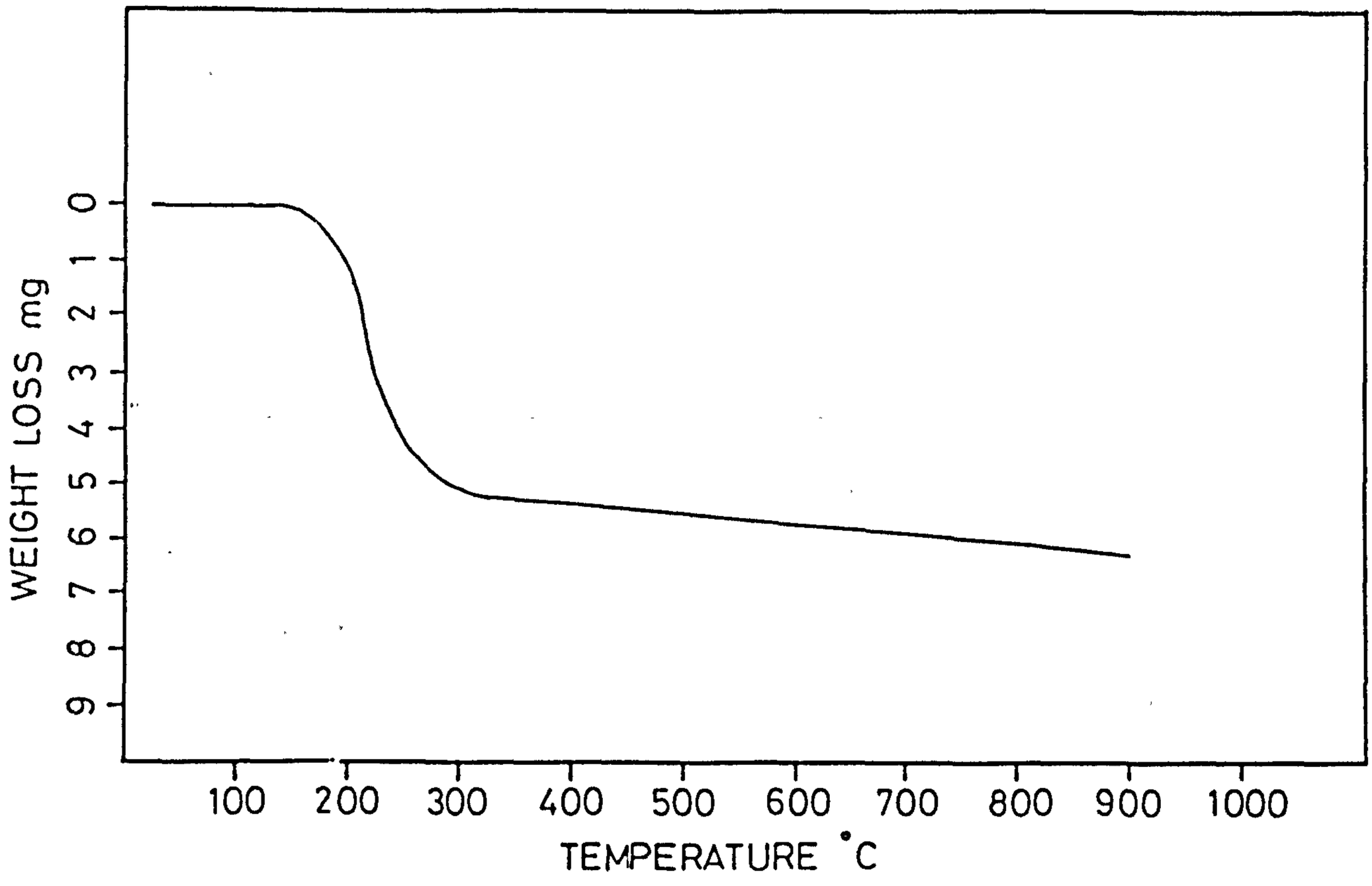

Figure 4.9 Thermogravimetric measurement on powder plus binder.

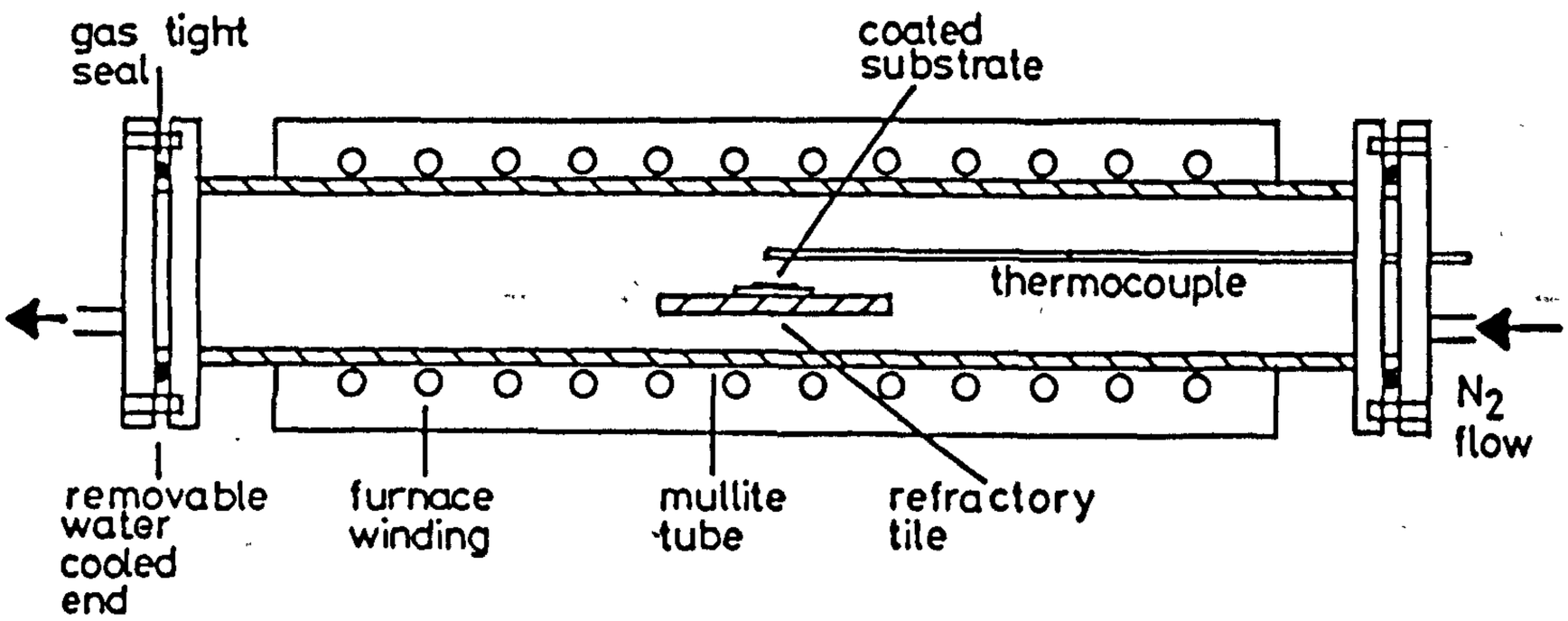

Figure 4.10 Tube furnace used to fire and heat-treat the coatings.

pushed into the furnace hot zone and the end resealed. If an air atmosphere was used the end was left open. The furnace temperature as recorded by the thermocouple over the specimen dropped by about 50°C and gradually recovered to stabilise at the initial temperature. The specimens remained in the furnace for the required firing time as recorded from the point the specimen first entered the furnace. On completion of firing the temperature at this time was noted, the furnace end removed and the specimen quickly withdrawn from the furnace. The coated metal substrate was rapidly cooled by placing on a cold metal surface.

In the coating of chrome-iron the glass powder coating needed to be fired at a furnace temperature of 970°C in an atmosphere of air. The firing time was varied over a wide range from a few seconds to many hours. With a firing time of 5 minutes at 970°C the pretreatment was varied by omitting abrasion with alumina grit and/or altering the preoxidation stage. Table 4.11 lists the variations in parameters for the enamelling of chrome-iron. All the chrome-iron firings are represented by a label C. In each case some of the enamelled metal substrates were kept in the rapidly cooled state and referred to as a fired only coating. The remainder were subjected to a heat-treatment cycle described in the next section.

In the coating of mild steel the enamel was fired at various temperatures between 930 to 990°C for firing times ranging from 30 seconds to 20 minutes. To prevent excessive oxidation of mild steel an atmosphere of oxygen free nitrogen was required. The metal was given a preoxidation of 15 minutes at 650°C. Table 4.12 lists the firing parameters. All the mild steel enamelled metal substrates were labelled M. Again in each case some of the enamelled pieces were kept in the rapidly cooled condition and the remainder subjected to heat-treatment.

Table 4.11: Firing conditions for enamels on chrome-iron

Label	Preoxidation Conditions	Firing Temperature °C	Firing Time Minutes
C1	alumina	906	0.5
C2	abrasion	920	1
C3	preoxidised	940	2
C4	in wet	968	4
C5	hydrogen	969	5
C6		967	20
C7		967	40
C8		967	60
C9		967	120
C10		967	180
C11		968	360
C12		969	540
C13		967	1440
C14		968	2880
C15		967	4320
	oxidised in wet hydrogen		
C16	abraded	970	5
C17	not abraded	970	5
	oxidised in air at 650°C		
C18	abraded	970	5
C19	not abraded	970	5
	no preoxidation		
C20	abraded	967	5
C21	not abraded	967	5

Table 4.12: Firing conditions for enamels on mild steel

Label	Preoxidation Conditions	Firing Temperature °C	Firing Time Minutes
M3	15 minutes	920	0.5
M4	650°C	950	1
M5		956	2
M6		956	3
M7		963	4
M8		960	5
M9		970	5
M10		976	6
M11		966	7
M12		970	8
M13		967	15
M14		970	20
M15		930	5
M16		950	5
M17		980	5
M18		990	5
M19	0.25 wt%	970	5
M20	CoO	970	8
M21	added	970	15
M22	0.25 wt%	970	5
M23	NiO	970	5
M24	added	970	15

4.2.5 Heat-treatment

If the sample required subsequent heat-treatment it was placed in the tube furnace at room temperature. The temperature was gradually increased at 5°C per minute up to the nucleation temperature where it was held for the required time then increased at 5°C per minute up to the growth temperature, and held for the growth period. The furnace was then allowed to drop to room temperature at its natural cooling rate.

For chrome-iron substrates coated with glass A, the heat-treat schedule was identical to that given in Section 4.1.1 for bulk glass A. Consisting of a nucleation stage of 30 minutes at 600°C followed by a growth stage of 3 hours at 800°C. The heat-treatment was carried out in an air atmosphere.

For mild steel substrates coated with glass B, the heat-treatment was identical to that in Section 4.1.1 for bulk glass B, a nucleation stage of 1 hour at 580°C followed by a growth stage of 3 hours at 820°C. The heat-treatment required an atmosphere of oxygen free nitrogen.

The labels used for the heat-treated coated substrates are identical to those for the quenched or glassy coatings but followed by a H. For example, a heat-treated coating on chrome-iron having a firing schedule of 6 minutes at 969°C is labled C5H.

4.3 Firing of bulk glass on oxide discs

To compare with the enamelled metal substrates, bulk glass discs were placed in contact with discs of various oxides and heated at the firing temperature.

A 1" disc of glass A, 20 mm thick, was fired on a disc of chromium oxide for a period of 10 days at 970°C. The chromium oxide disk was prepared by compacting 'Analar' grade powder in a press to produce a 1" diameter 10 mm long pellet. This was sintered at 1300°C for 2 days then gradually cooled. The sides of both the glass and oxide discs were polished with diamond paste to a 1 μm finish.

Discs of glass B, 1" in diameter, were fired on iron oxide discs and unoxidised metal. Discs of ferrous oxide (FeO) were prepared by decomposing ferrous oxalate powder ($FeC(OOH)_2$) in an alumina tube, heating gradually to 1000°C under an atmosphere of pure argon and holding for 4 hours. The temperature was reduced to room temperature, still under argon, before removal. The resulting black powder was compressed into a 1" disc and sintered at 970°C in air for 2 hours followed by quenching in liquid nitrogen. The disc was black, non-magnetic and its X-ray diffraction pattern identical to that from wustite in the J.C.P.D.S. file 6-0615. Discs of ferric oxide (Fe_2O_3) were prepared by compressing reagent grade Fe_2O_3 powder into 1" discs and sintering at 800°C in air for one hour. The resulting disc was reddish brown and the X-ray diffraction pattern identical to that for hematite (Fe_2O_3) given in the J.C.P.D.S. file 33-664. Mild steel 1" square was given identical pretreatment to that used for the coating on mild steel, a degrease in acetone and 7.5% W/V NaOH solution as

described in Section 4.2.2. The glass disks, after placing on the iron oxide disks or metal piece, were fired in a furnace at 970°C under a nitrogen atmosphere. The temperature initially dropped to 900°C but reached 970°C after 30 minutes, the firing was then continued for a further 1 hour, followed by rapid quenching on a metal slab. Table 4.13 labels the various glass-oxide couples.

Table 4.13: Glass oxide couples

Label	Oxide disk and glass	Firing	
		Temperature °C	Time
D1	Cr_2O_3	970	10 days
	Glass A		
D2	Mild steel metal	962	1 hour
	Glass B		
D3	FeO	970	1 hour
	Glass B		
D4	Fe_2O_3	967	1 hour
	Glass B		

4.4 Bulk glass containing substrate oxides

Bulk glass batches were melted containing increasing amounts of Cr_2O_3, Fe_2O_3 or FeO. The parent bulk glass of composition A or B was prepared as described in Section 4.1.2 with the glass fritted after the second melting.

Increasing amounts of 'Analar' grade chromium oxide (Cr_2O_3) powder was mixed with glass grit A by tumbling. The mixture was then melted at 1350°C for 3 hours in a platinum 10% rhodium crucible in

an electrically heated furnace. The melt was quenched in deionised water, thoroughly mixed and remelted, and finally cast into a slab which was annealed at 400°C for 1 hour. Table 4.14 gives the composition of the chromium containing glasses.

Glasses of composition B containing ferric oxide (Fe_2O_3) were prepared by melting increasing amounts of reagent grade calcined ferric oxide with glass frit in the same manner as above.

It was found to be difficult to prepare bulk glasses containing ferrous oxide (FeO). The problem was in retaining the iron as Fe^{2+} in the glass. Attempts to produce ferrous oxide containing glasses by melting glass frit with ferrous oxalate in air and by flushing a furnace with nitrogen proved unsuccessful, principally due to the oxidation of ferrous oxalate before it entered the glass. Ferrous oxide containing glasses were eventually produced by melting under an oxygen free nitrogen atmosphere in a sealed tube furnace, but only small quantities could be obtained, typically 20 grams. The glass was melted for 1 hour at 1400°C, quenched then broken by impact, and remelted after mixing for a further 1 hour. After pouring, the glass was annealed at 400°C for 1 hour.

The composition of the iron containing glasses is given in Table 4.15. Comparison between the as mixed composition and that determined by analysis, Table 3.6, shows that little loss of the oxides is occurring during preparation of the ferric oxide containing glasses. Some loss of ferrous oxide occured during melting and the final glass composition for the ferrous oxide containing glasses is that determined by quantitative energy dispersive X-ray analysis (EDX).

Table 4.14: Bulk glass A containing chromium oxide

	Wt% oxide (±0.1%)						
Label	Li_2O	Al_2O_3	SiO_2	P_2O_5	K_2O	ZnO	Cr_2O_3
E1	11.9	4.8	78.0	2.0	2.3	2.0	0.2
E2	11.9	4.8	77.9	2.0	2.3	2.0	0.3
E3	11.9	4.8	77.7	1.9	2.3	1.9	0.6
E4	11.8	4.8	77.2	1.9	2.3	1.9	1.1
E5	11.7	4.7	76.3	1.9	2.3	1.9	2.3
E6	11.5	4.7	75.4	1.9	2.3	1.9	3.4
E7	11.4	4.6	74.6	1.9	2.2	1.9	4.5
E8	11.1	4.5	72.0	1.8	2.2	1.8	7.4
E9	10.3	4.2	67.4	1.7	2.0	1.7	13.7

Table 4.15: Bulk glass B containing iron oxides

Wt% oxide(±0.1%)

Ferric oxide (Fe_2O_3)

Label	Li_2O	Al_2O_3	SiO_2	P_2O_5	K_2O	ZnO	Fe_2O_3
F1	11.8	4.4	76.2	1.9	2.4	1.9	1.0
F2	11.4	4.2	73.2	1.9	2.3	1.9	4.8
F3	10.8	4.0	69.8	1.8	2.2	1.8	9.2
F4	9.9	3.7	63.9	1.6	2.0	1.6	16.9
F5	8.5	3.1	54.6	1.4	1.7	1.4	29.0
F6	7.4	2.7	47.7	1.2	1.5	1.2	38.0
F7	6.6	2.4	42.3	1.1	1.3	1.1	44.9

Ferrous oxide (FeO)

Label	Li_2O	Al_2O_3	SiO_2	P_2O_5	K_2O	ZnO	FeO
G1	11.1	4.2	71.3	2.3	2.2	2.6	6.0
G2	10.5	3.8	67.4	2.0	2.1	2.0	12.0
G3	9.6	3.6	61.8	1.7	2.0	1.8	19.2
G4	8.9	3.2	57.3	1.6	1.9	1.6	25.1

CHAPTER 5

Results

5.1 Coating on Chrome-iron

5.1.1 Introduction

A chrome-iron substrate, abraded with alumina grit and preoxidised in wet hydrogen, was coated by firing at 969°C for 6 minutes (C5). This is referred to as the "standard" firing condition. The resulting enamel coating had completely fused, wetted well and developed good adhesion to the substrate. Initial investigations concentrated on this coating with it being examined, after firing:

- in the quenched condition (C5)
- on completion of a heat-treatment (C5H)

The effects of variations in the firing conditions were examined. In particular crystallisation during firing, interfacial reactions, and alterations in the metal pretreatment studied.

5.1.2 Enamel coating on chrome-iron quenched after firing C5

Microstructure:

The microstructure of a coating quenched after firing for 6 minutes at 969°C (C5) is shown in Figure 5.1.1, a backscattered electron micrograph. The initial glass powder has fused to form a continuous coating approximately 80µm thick.

The interface between the coating and substrate is irregular but sharply defined. Along the interface there is a 1µm thick layer. It

Figure 5.1.1 Backscattered electron micrographs of a coating on chrome-iron subjected to a firing C5.

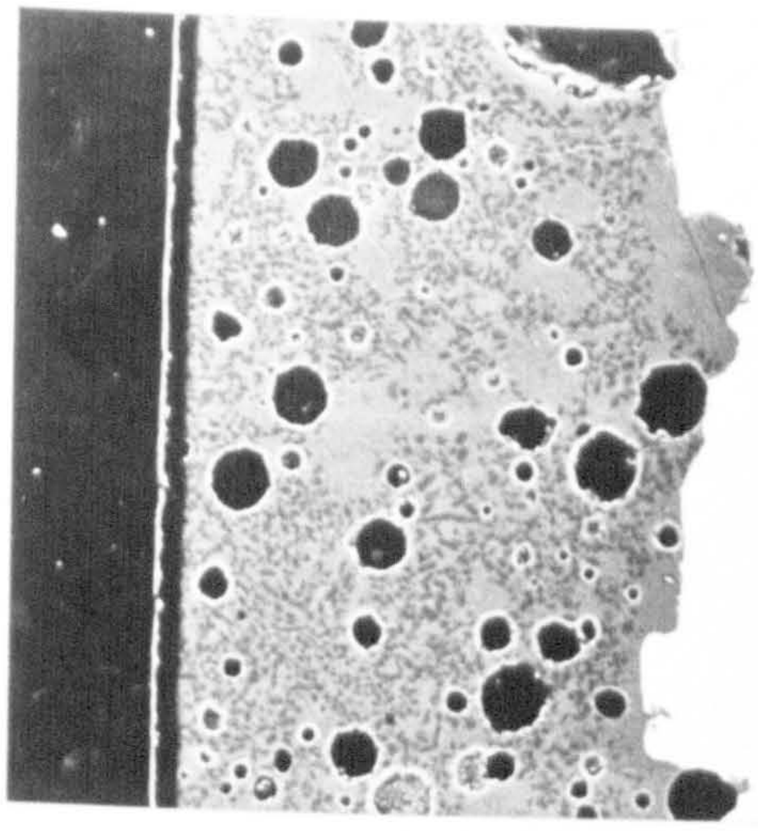

40µm

coating

chrome-iron

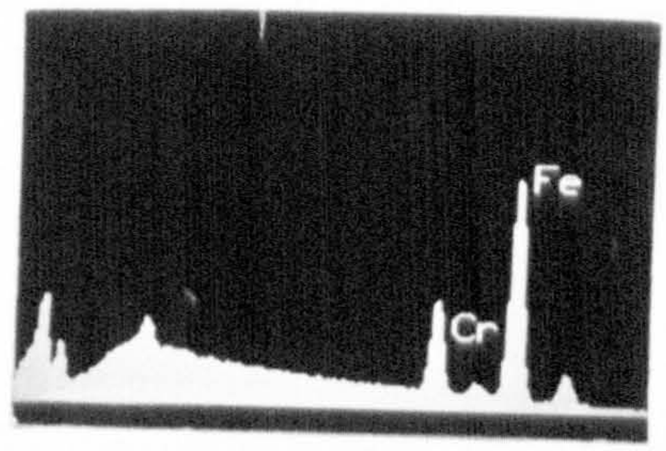

A substrate

lithium disilicate

glassy region

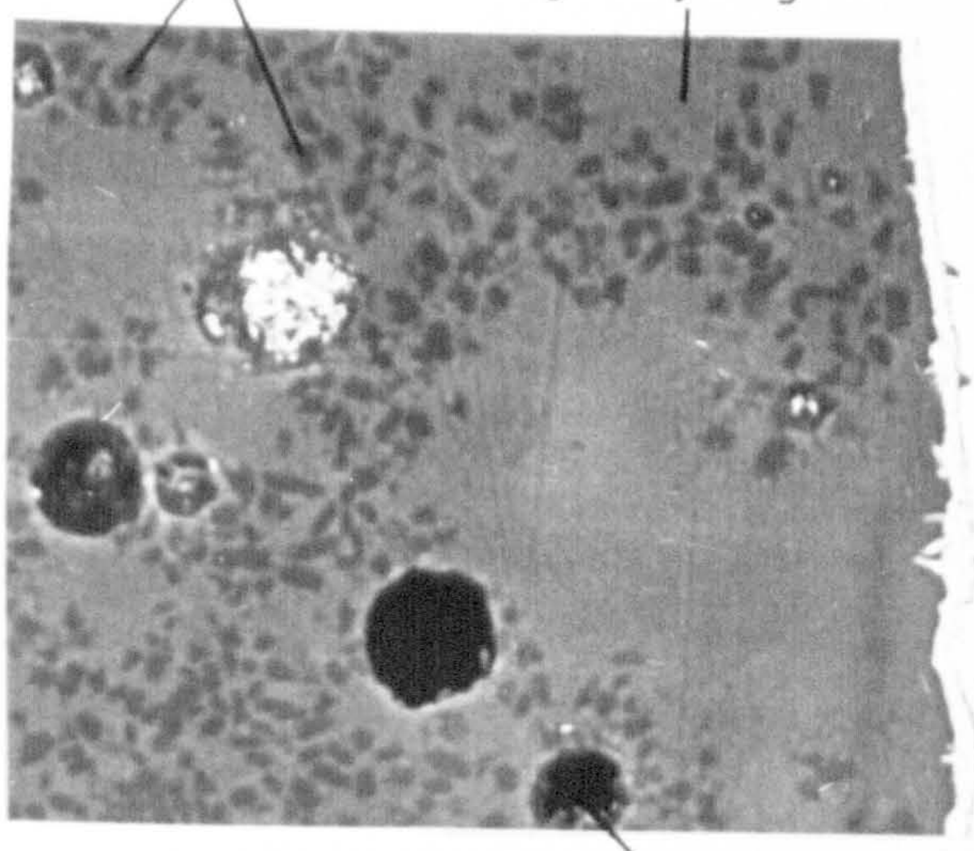

10µm

pore

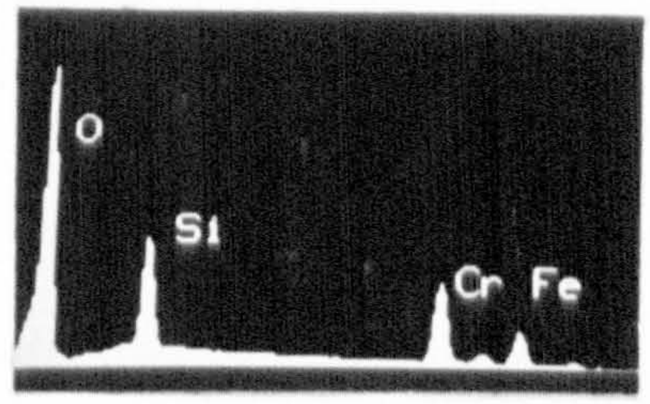

B silica layer

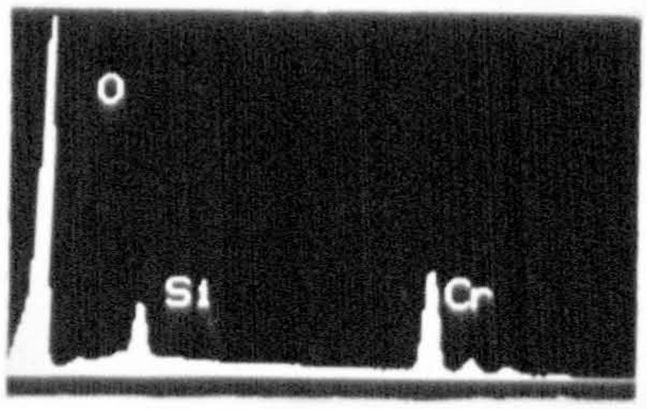

C chromium oxide

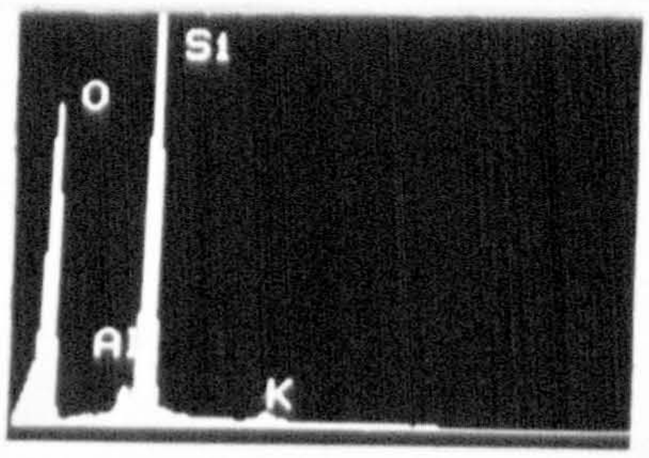

D adjacent coating

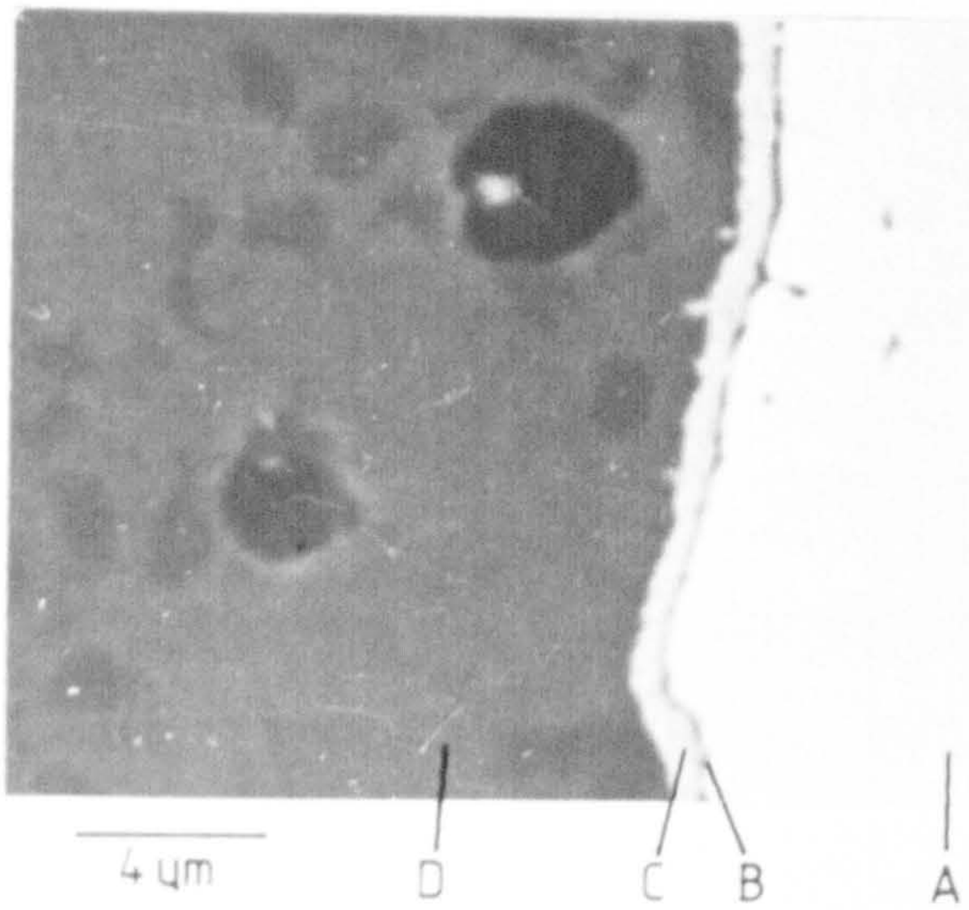

4 µm

D C B A

has a high chromium content as determined by EDX microanalysis, and small amounts of silicon and iron. The backscattered micrograph shows the layer to have a darker contrast than the adjacent alloy indicating a lower mean atomic number. This suggests an oxide rather than a metal. By dissolving the substrate alloy in dilute acid the oxide layer was exposed. X-ray diffraction identified this layer as chromium oxide (Cr_2O_3), the characteristic peaks of which are accompanied by those associated with the crystal phases in the underlying coating, Figure 5.1.2.

Also noticeable is the presence of a dark band, of submicron thickness, between the chromium oxide and alloy. Its composition cannot be accurately determined by X-ray microanalysis due to the limited spatial resolution of the technique. However analysis of this region indicates a high silicon content and the presence of iron and chromium. The very dark contrast of the band reflects the low mean atomic number and it is unlikely to contain large amounts of the heavier metal elements. Indications are that the band is a layer of silica (SiO_2) either amorphous or crystalline. As a consequence of abrasion, pieces of alumina grit are occasionally embedded in the alloy at the interface.

It is apparent that a substantial degree of crystallisation has occurred on completion of the firing stage and before heat-treatment. The microstructure is non-uniform, consisting of featureless regions surrounded by areas containing a dark contrast phase, 1-2μm diameter, in a lighter contrast matrix, Figure 5.1.3. Etching in a dilute (2% V/v) hydroflouric acid solution for 30 seconds reveals a second phase of slightly smaller dimensions, Figure 5.1.3. This phase is intermingled with the darker contrast phase. Both surround the featureless regions. X-ray diffraction, Figure 5.1.4(a), of a coating

fired under identical conditions, removed by impact and ground to a powder detects two crystalline phases: Lithium disilicate ($Li_2O.2SiO_2$), β-quartz (SiO_2).

Lithium disilicate wo uld be expected to exhibit a darker backscatter contrast due to its lower mean atomic number when compared to quartz. Therefore the darker contrast phase is lithium disilicate and the lighter contrast phase α-quartz. Problems exist in differentiating between these two phases by x-ray microanalysis because of the inability to detect lithium directly.

It is observed that potassium is preferentially concentrated in the featureless regions. This is clearly shown by x-ray spectra collected over 4 x 4 μm^2 areas from a featureless region and a region containing both crystal phases, Figure 5.1.3. No such variation is noticed for other detectable elements. The evaluated potassium concentrations, determined by quantitative EDX analysis is 1.83 at% in the featureless regions and 1.20 at% for the crystallised regions. Analysis of a larger area containing both of these regions yields a concentration of 1.46 at%. It appears that during the firing process, potassium is moving into the featureless regions from the crystallising regions. It is not possible to say, by the analytical methods available, if a similar situation exists for lithium.

Element distribution:

Profiles of the detectable elements across the interface are given in Figure 5.1.5(a). They were obtained from line scans (section 3.2.6). The principle features are described below:

- Aluminium (also zinc and phosphorus) are essentially constant within the coating. They drop to background at the coating chromium oxide boundary.

- Silicon has a constant concentration in the coating. It drops rapidly to background at the coating - chromium oxide boundary.

- Potassium shows a varying profile. It has a decreased concentration in areas where crystallisation is occurring. On reaching the coating - chromium oxide boundary it drops rapidly to background.

- Iron is detected at an appreciable level only in the alloy substrate. It drops to background at the alloy - chromium oxide boundary. The absence of a plateau where the chromium exhibits a peak suggests iron is not a major component of the oxide layer.

- Chromium shows a depletion in the adjacent alloy extending to 8μm. A peak is observed at the interface associated with the chromium oxide layer. Its level then rapidly drops to background at the coating-chromium oxide boundary. Very little chromium enters the adjacent coating.

A full quantitative EDX determination of the element distribution is displayed in Figure 5.1.6. The profiles for silicon, chromium, and iron are shown. Concentrations are expressed in normalised atomic percent. Lithium must be included to evaluate the normalised atomic percentage concentrations. A constant ratio of lithium to silicon, as expected from the parent glass A composition was assumed in all calculations. Both chromium and iron are taken to be present in the trivalent state.

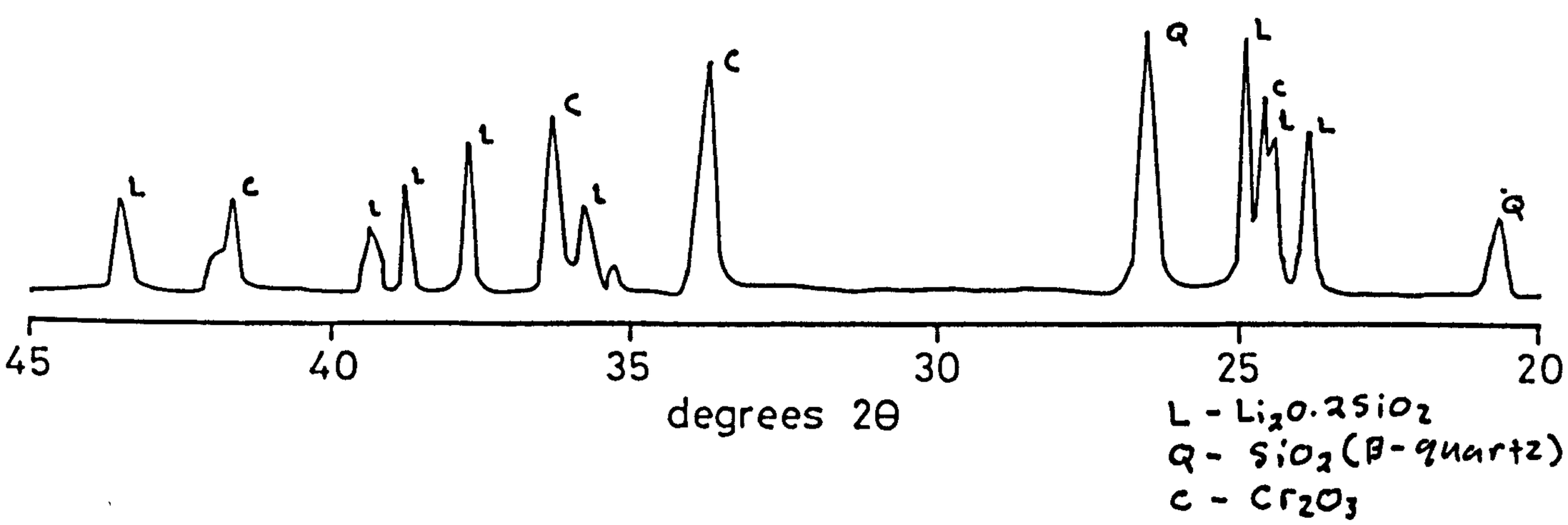

Figure 5.1.2 XRD pattern collected from exposed chromium oxide layer.

Figure 5.1.3 Backscattered and secondary electron micrographs of fired only coating etched in HF acid.

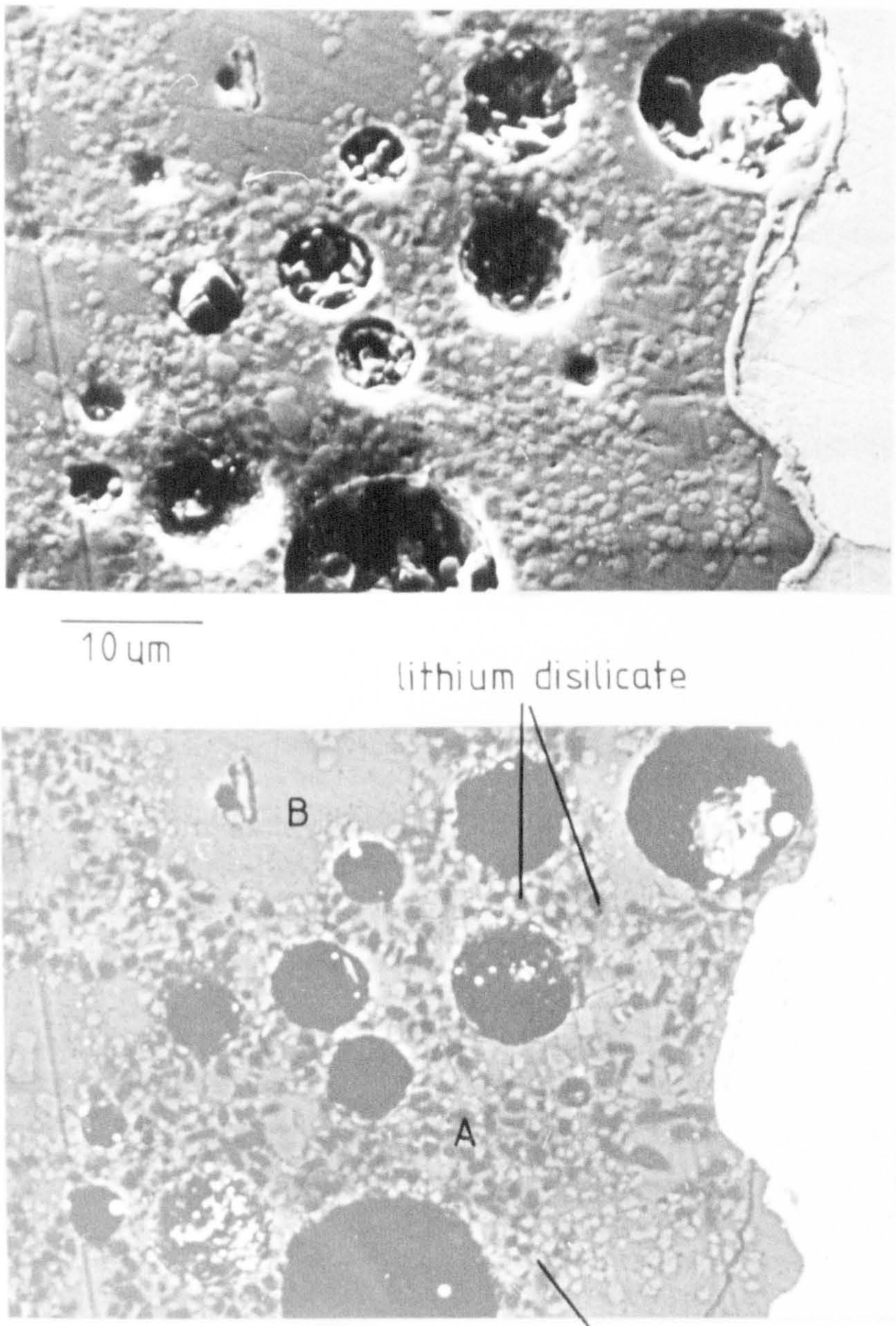

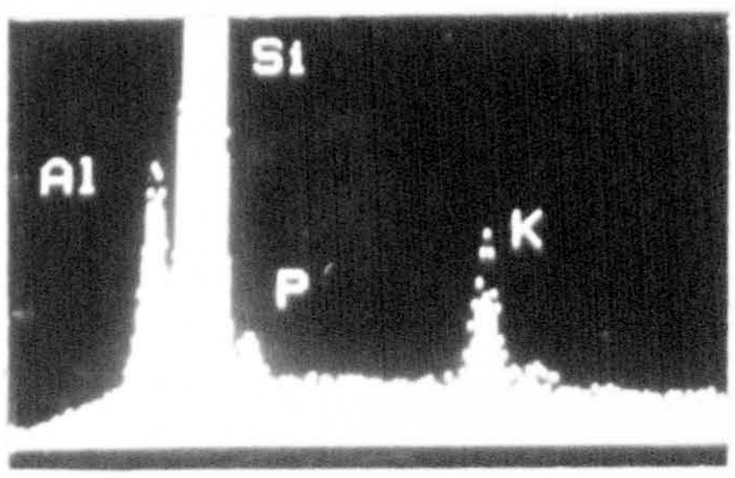

crystalline region A

glassy region B

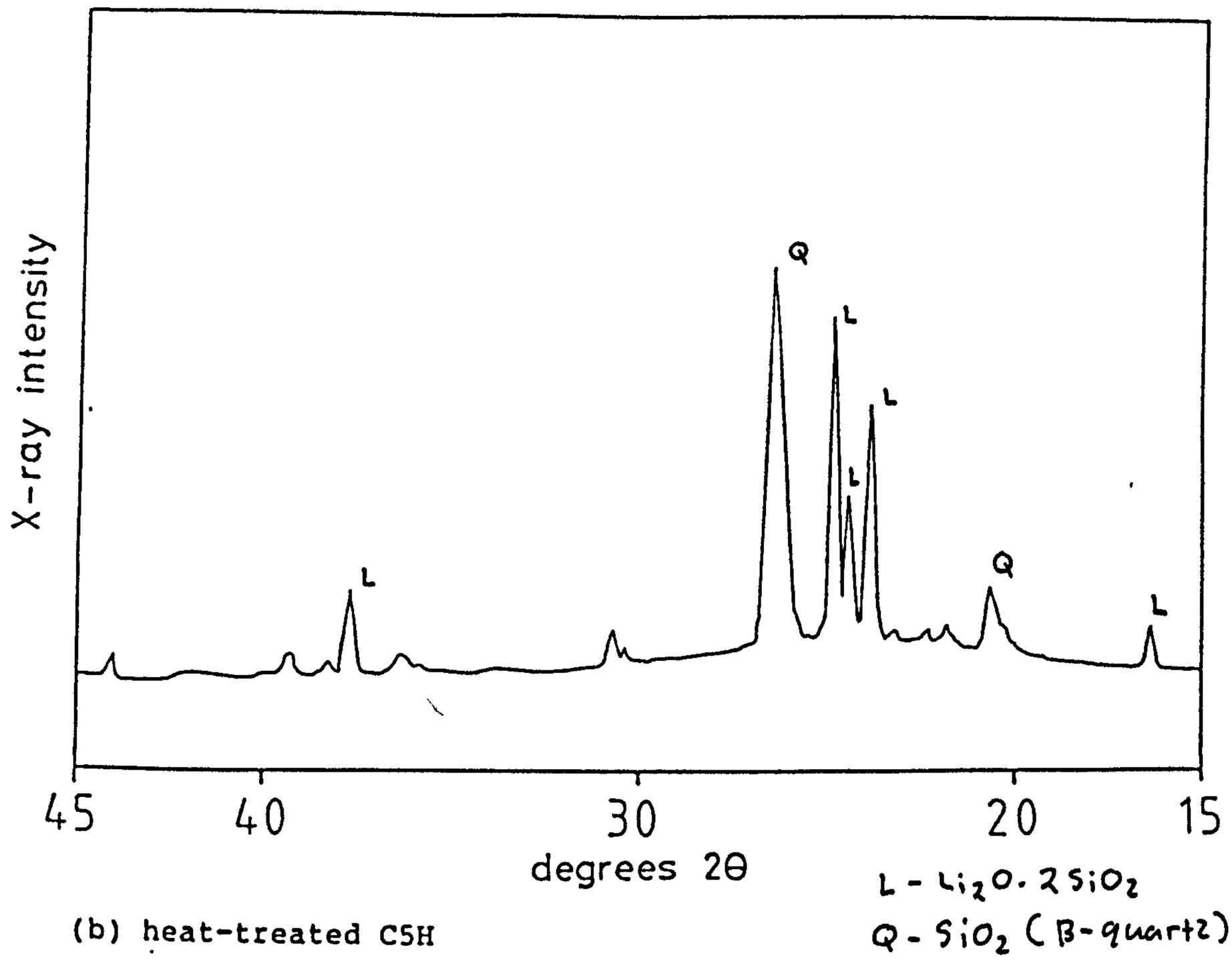

(b) heat-treated C5H

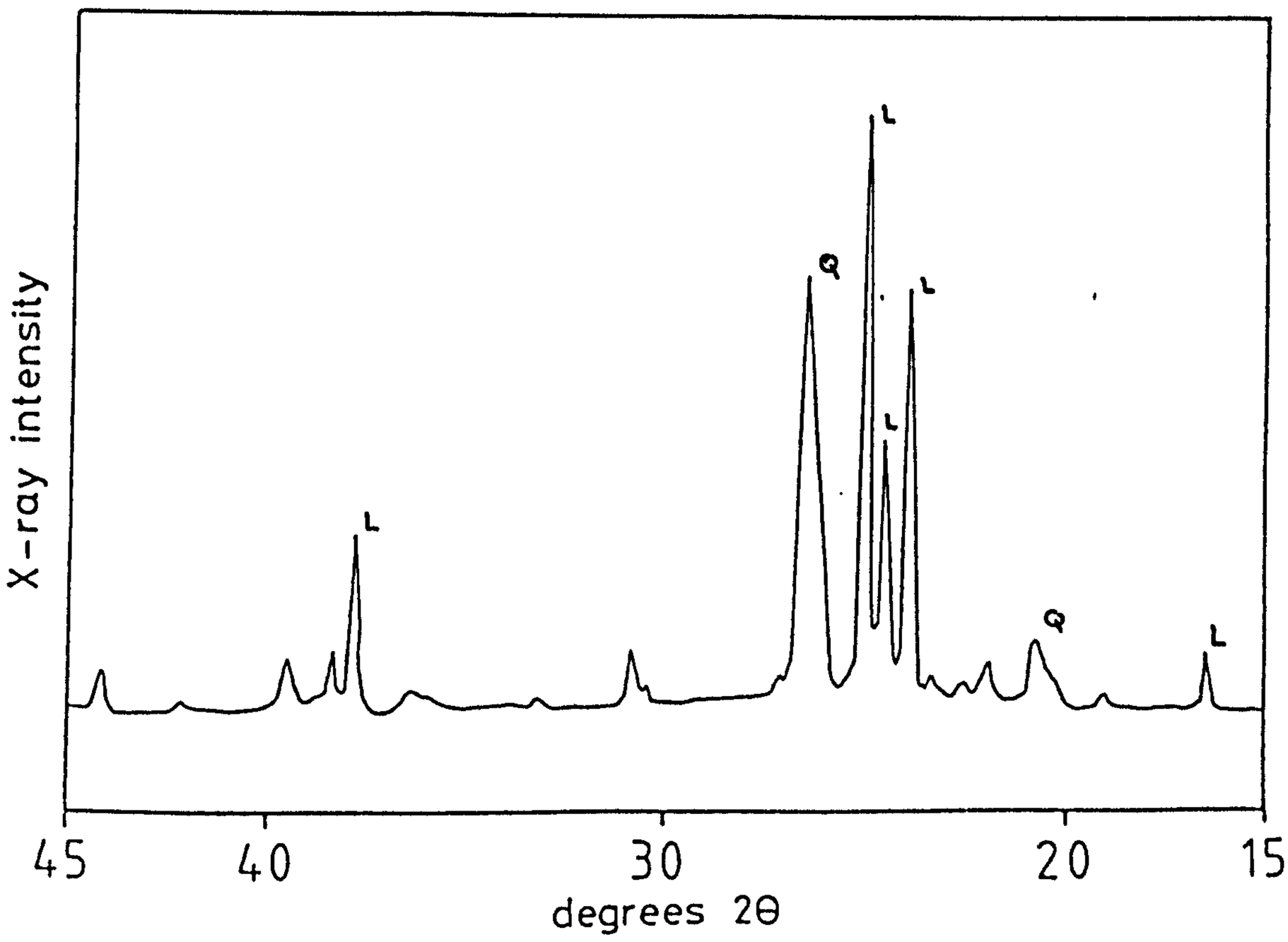

(a) fired only C5

Figure 5.1.4 XRD pattern collected from removed coating ground to a powder.

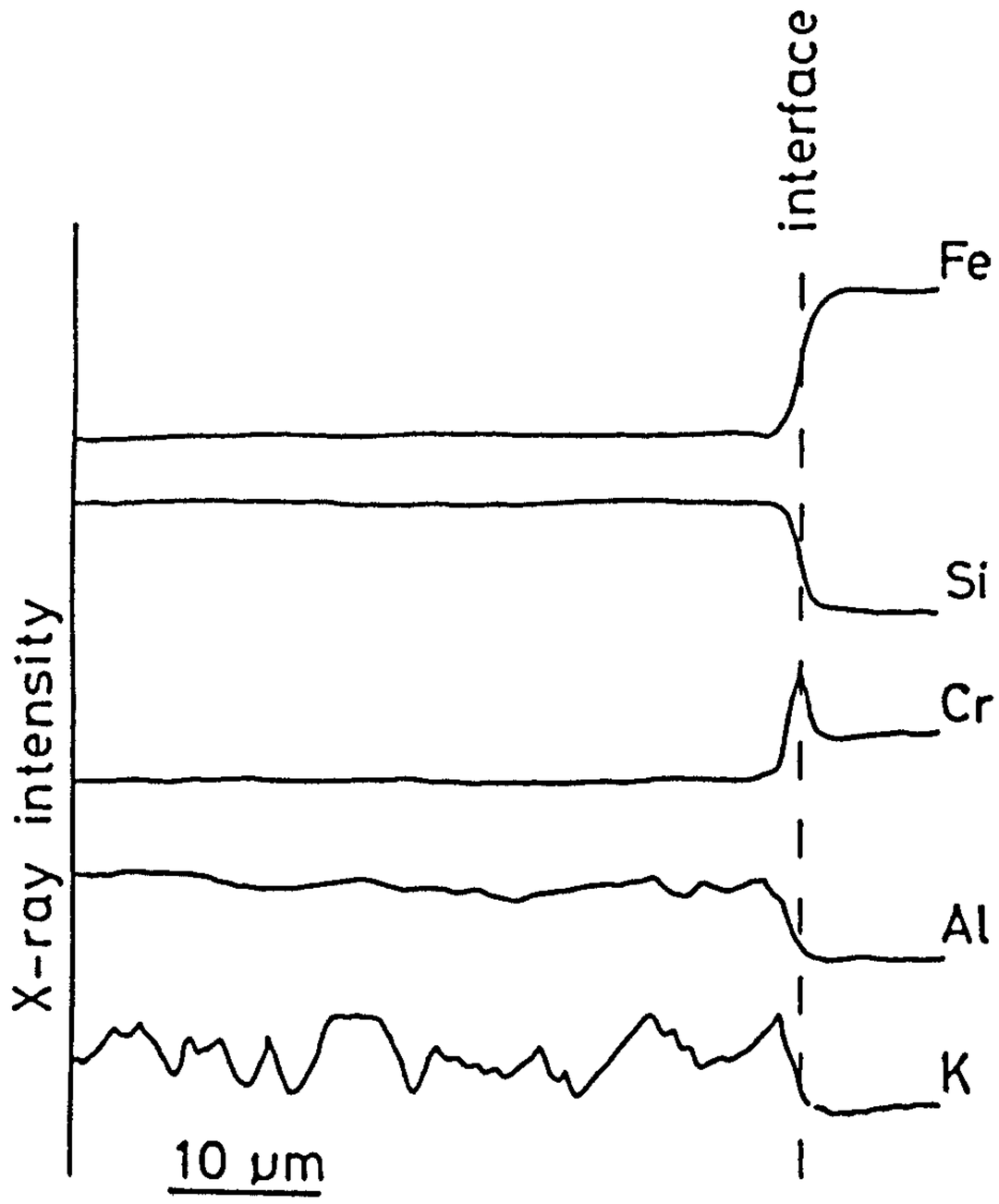

(a) fired only C5

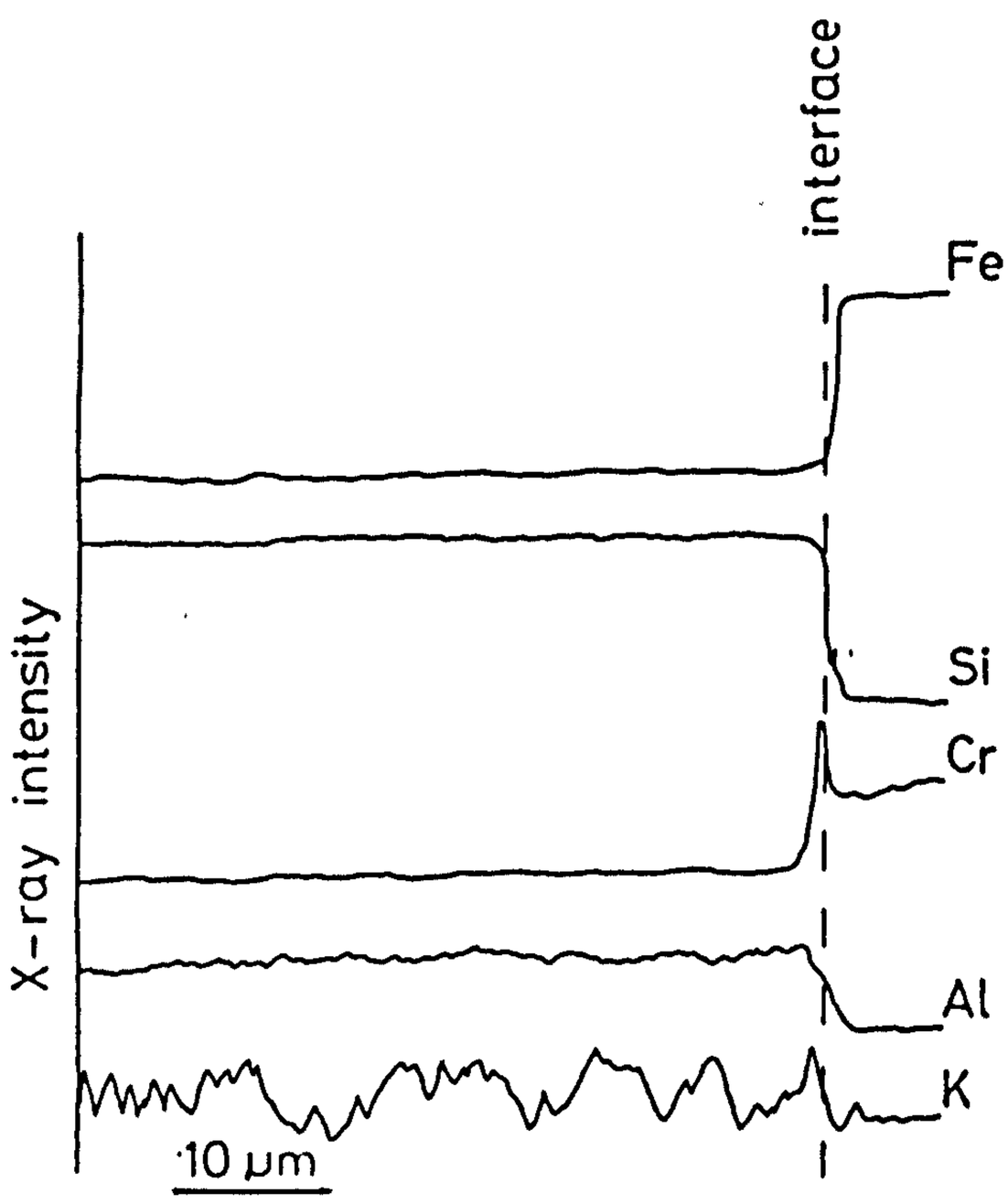

(b) heat-treated C5H

Figure 5.1.5 Element distribution collected from linescans conducted across the interface.

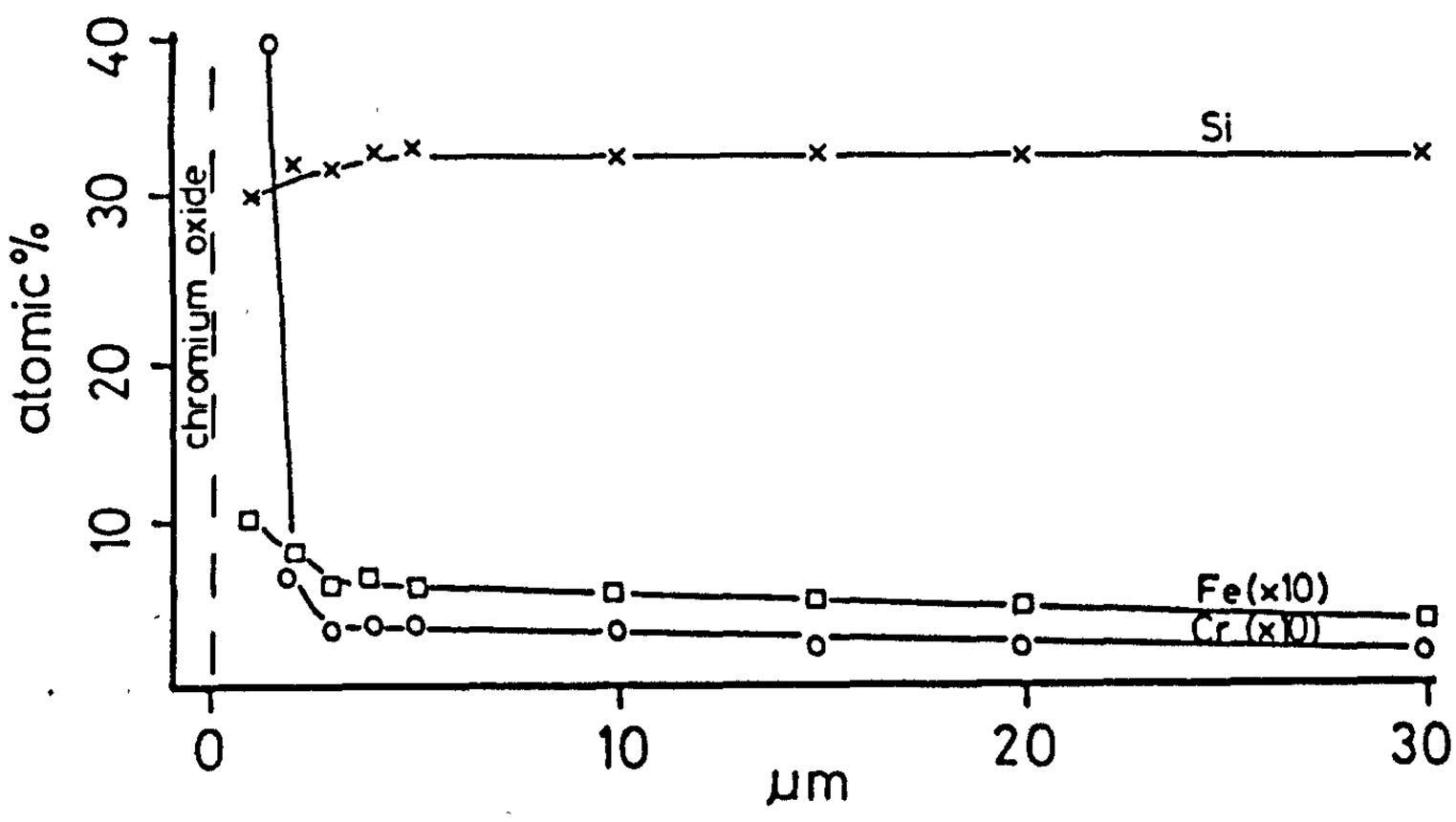

Figure 5.1.6 Quantitative element distribution across the interface of a fired only coating, C5.

- Chromium attains a concentration of 0.3 at% at 3μm from the coating - chromium oxide boundary. The limited resolution of the EDX technique prevents an assessment of the decrease. Higher levels of chromium are detected up to 2μm adjacent the interface. This is a result of the electron beam spreading into the chromium oxide layer. At further distances the chromium level gradually decreases. It reaches a concentration of 0.2 at% by 20μm.

- Iron is present in the adjacent coating at very low concentrations, but in greater levels than chromium. At 3 μm the concentration is 0.7 at%. It decreases to 0.4 at% by 20μm.

These profiles agree with the line scans. A sharp interface, exists along the coating - substrate boundary. Very little chromium or iron is diffusing into the adjacent coating.

5.1.3 Enamel coating on chrome-iron heat-treated after firing. C5H

Microstructure:

The microstructure of a coating fired at 969°C for 6 minutes and then subjected to a heat-treatment schedule of 30 minutes at 600°C and 3 hours at 800°C, (C5H), is shown in Figure 5.1.7. There is no noticeable change in the interfacial boundary structure. A well defined interface still exists with a discrete chromium oxide layer, 1μm thick, present between the alloy and coating. As indicated by the dark layer adjacent to the alloy, silica remains as a thin layer between the chromium oxide and alloy.

The coating shows almost complete crystallisation with two crystal phases and a small residual glass fraction. X-ray diffraction of a coating, produced under identical conditions, removed by impact and ground to a fine powder indicates the presence of lithium disilicate and β-quartz, Figure 5.1.4(b). Comparison with the x-ray pattern collected from the quenched coating, illustrates that the amount of lithium disilicate relative to quartz has increased. As mentioned above the dark contrast phase in the electron micrographs is lithium disilicate and the lighter contrast phase, now clearly visible, β-quartz. The microstructure is not homogeneous, two distinct regions can be identified. The majority of the microstructure consists of randomly oriented small spherical crystals of lithium disilicate and β-quartz, approximately 1μm in size. Region A in Figure 5.1.8. In other regions, the dark contrast phase is elongated with the light contrast, β-quartz phase, still present in a spherical form, Region B in Figure 5.1.8. Analysis by transmission electron microscopy using selected area diffraction techniques shows the elongated phase to be crystalline. As only lithium disilicate and β-quartz can be detected by x-ray diffraction, the dark contrast elongated phase must be lithium disilicate. Quantitative EDX analysis of selected regions shows potassium to be concentrated into areas containing the elongated lithium disilicate phase, Figure 5.1.8. For region A, containing the spherical lithium disilicate phase the concentration of potassium is 0.88 at% and for region B with the elongated phase 1.27 at%. No such variation is observed for other detectable elements.

The crystallisation of the coating occurs up to the chromium oxide-coating boundary and is similar to that observed in the bulk of the coating. Both lithium disilicate and β-quartz are present

Figure 5.1.7 Backscattered electron micrographs of a coating on chrome-iron fired and heat-treated, C5H.

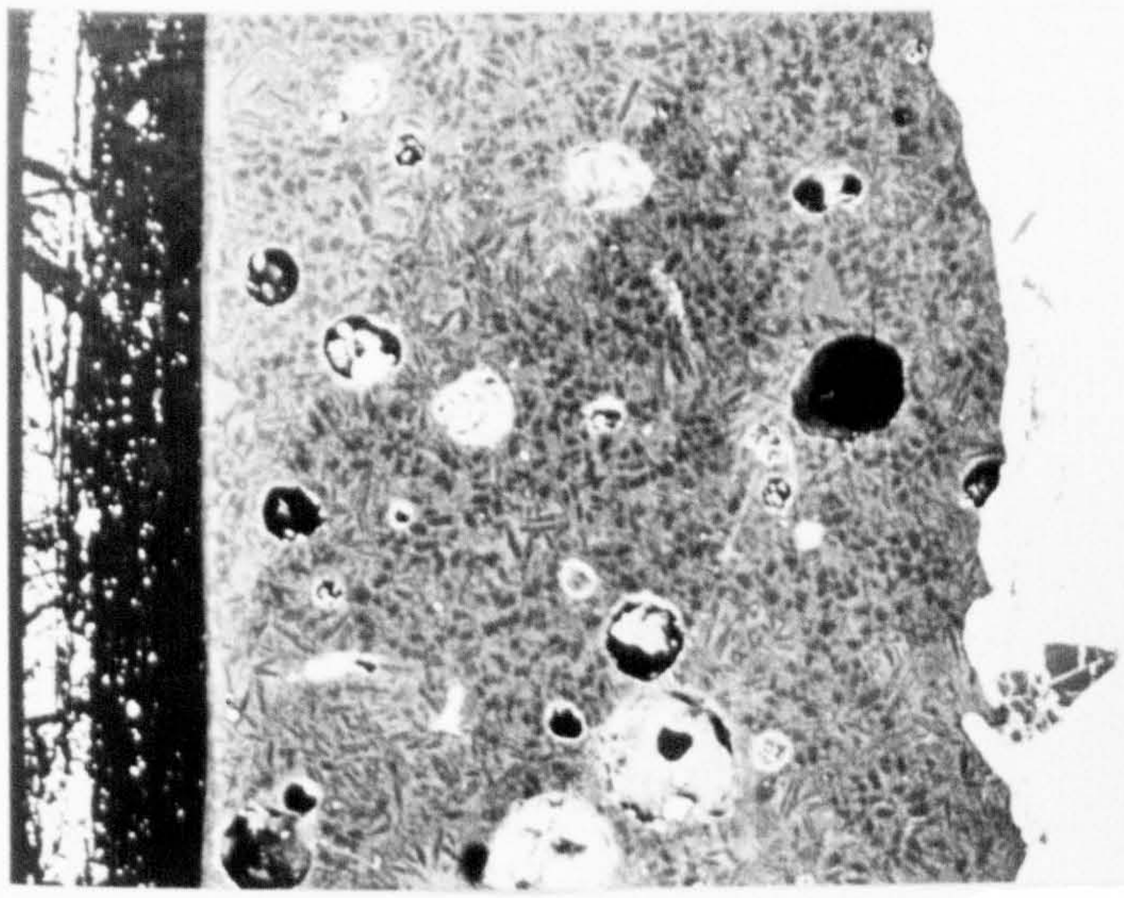

40 µm coating

CHROME IRON

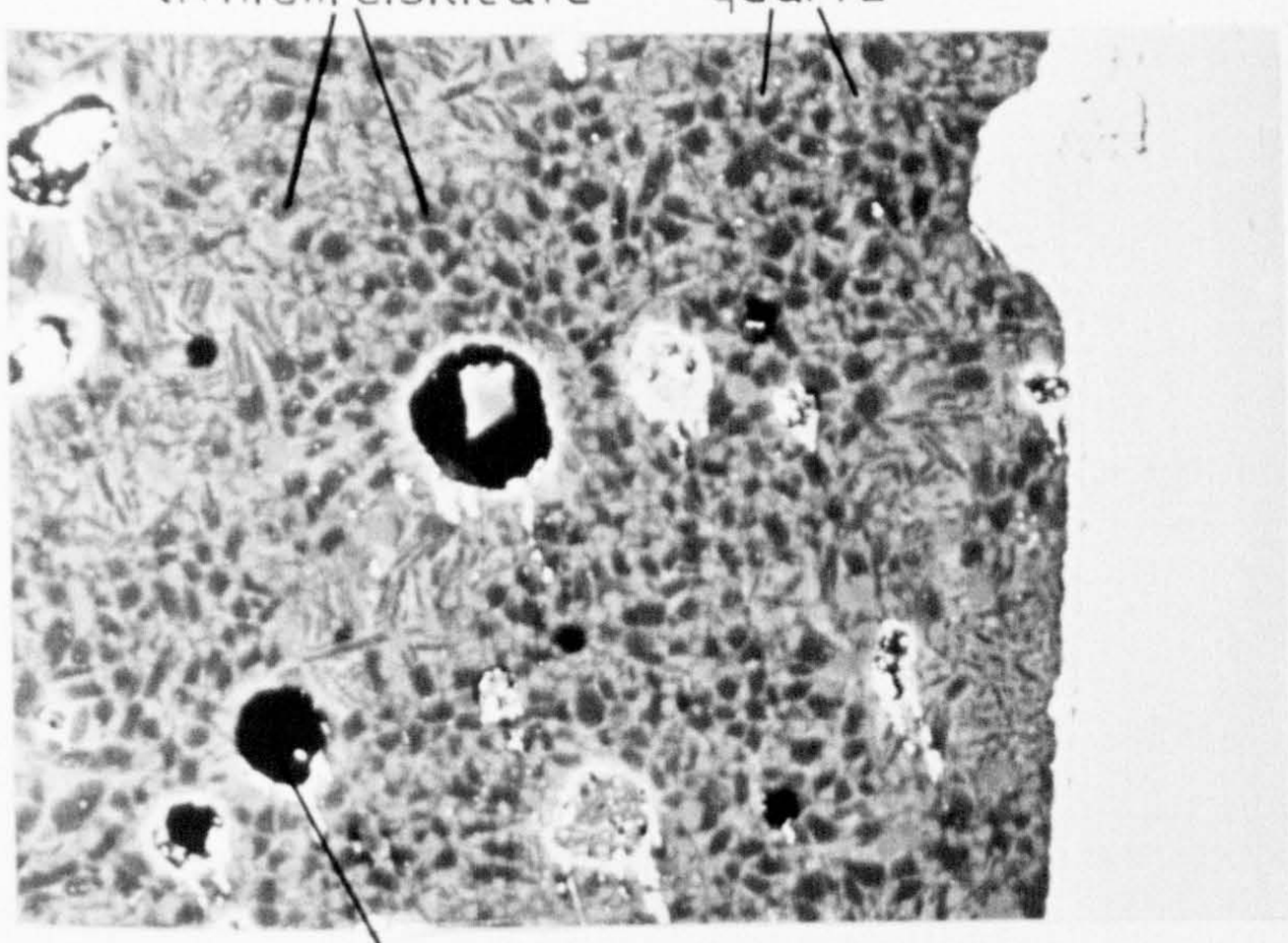

10 µm

etched in 2% HF

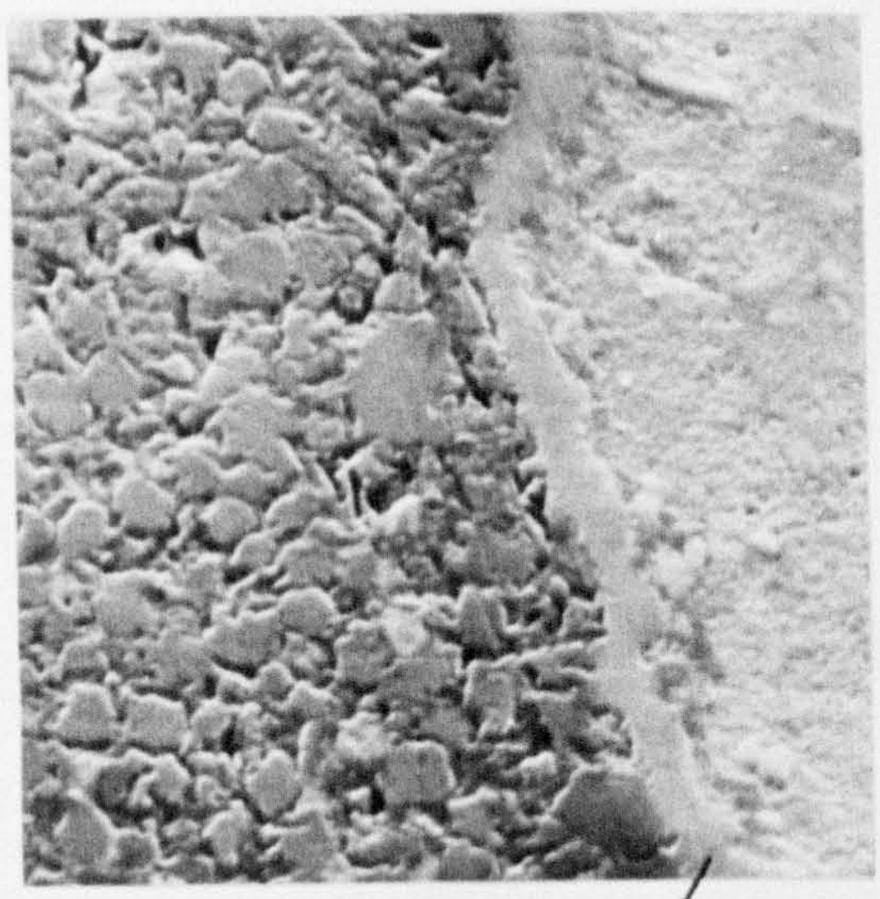

4 µm

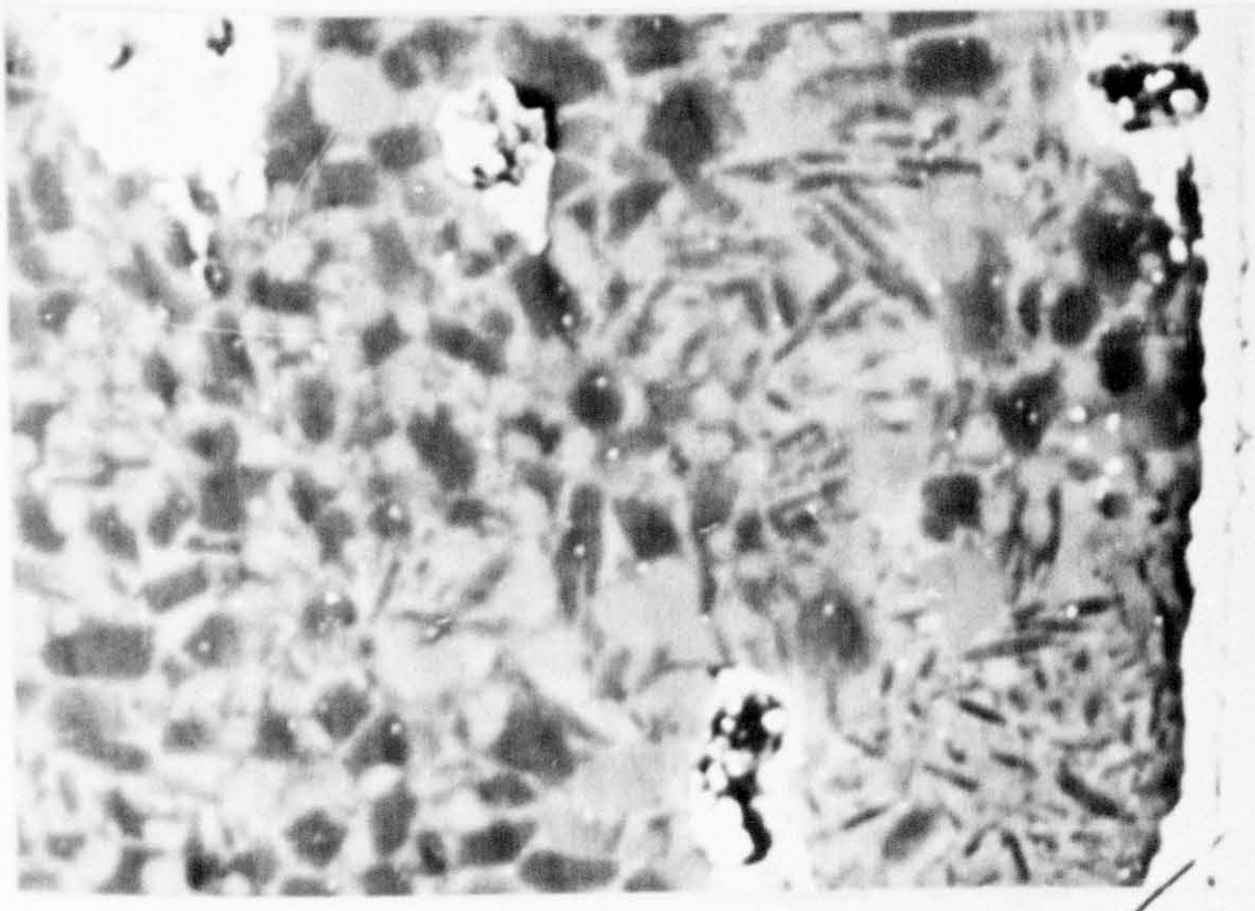

4 µm

Figure 5.1.8 Different microstructure forms of heat-treated coating, M9H.

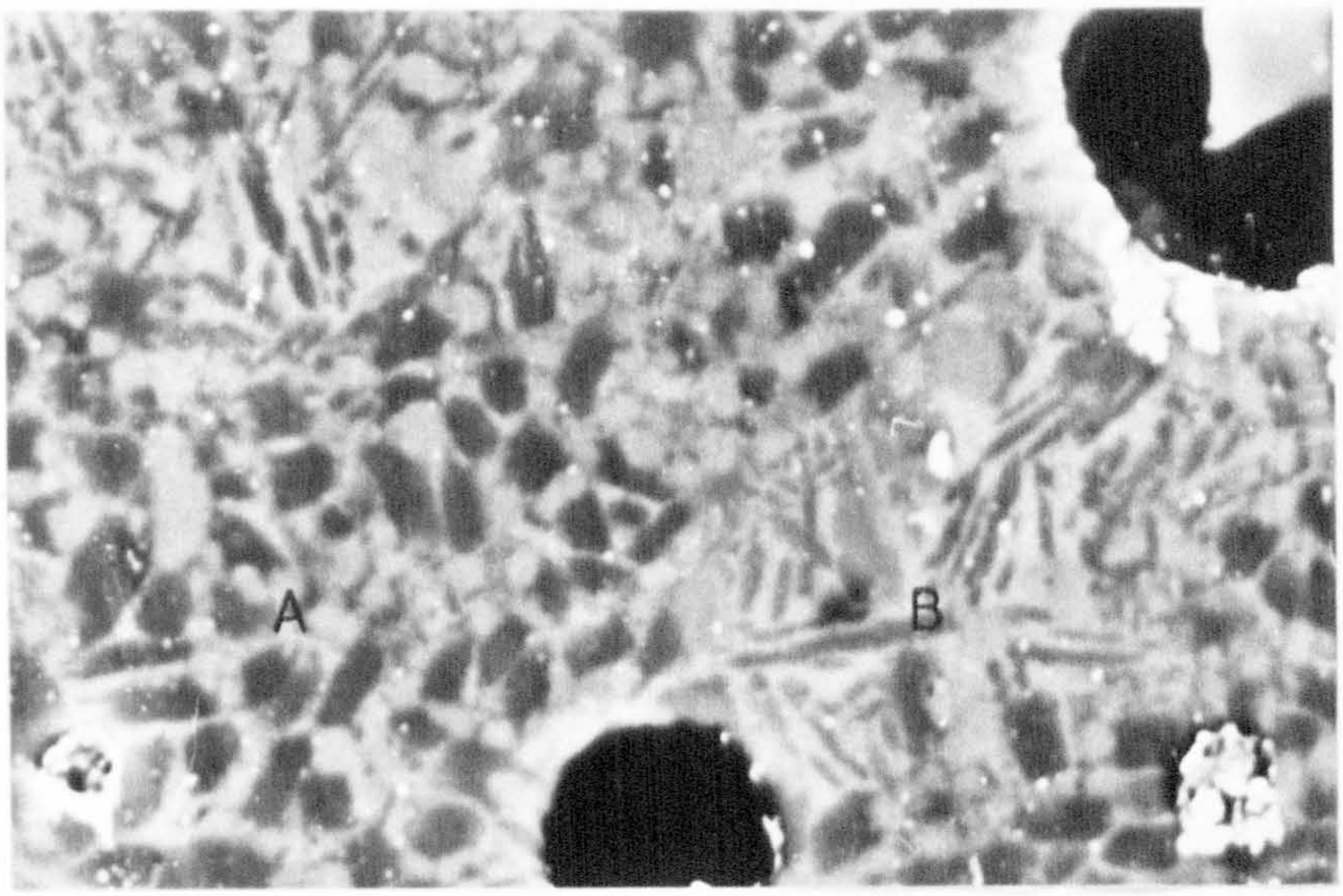

4 µm

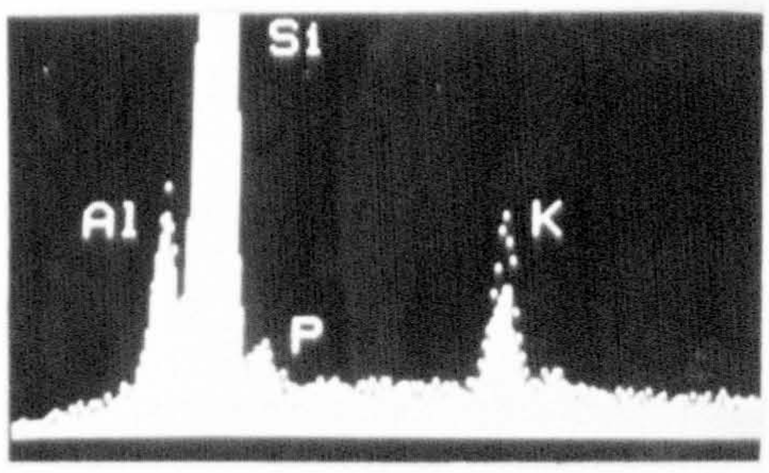

——— region A

..... region B

immediately adjacent to the interface. The presence of the chromium oxide surface does not preferentially nucleate any particular phase, nor does the small amount of chromium oxide and iron oxide in solution influence the microstructure in any notiecable way.

Element distribution:

Distribution of the detectable elements collected from line scans across the interface [Section 3.2.6] are displayed in Figure 5.1.5(b). They remain essentially unaltered from the quenched coating. The main features are:

- Chromium exihibits a peak corresponding to the oxide layer. It drops rapidly to background at the coating - chromium oxide boundary.

- Iron is present in measurable amounts only in the alloy.

- Potassium shows a variation in concentration associated with the different microstructure types.

A quantitative EDX analysis [Section 3.2.7] produces an element concentration profile almost identical to that for the quenched coating. By 3 μm chromium and iron are present at very low levels. They were measured at 0.23 at% Cr and 0.4 at% Fe.

5.1.4 Microstructural development during firing

Significant crystallisation is observed on completion of the firing process. An investigation was undertaken to study the

microstructural development during firing. The coated, but unfired, substrate was placed into the tube furnace initially at 970°C. After a firing time of 30 seconds, 1, 2 and 4 minutes the substrate was withdrawn and quenched. When placing the substrate in the furnace the temperature dropped and the shortest firing times did not allow a full recovery of temperature to the initial value. Table 4.11 lists the firing times and removal temperatures. The firing period was also greatly extended to many hours, well in excess of that used in the "standard" firing condition. These are again listed in Table 4.11. In all cases the substrate had been abraded and preoxidised in wet hydrogen.

Figure 5.1.9(a) shows the coating after a short firing time of 30 seconds and a removal temperature of 906°C, (C1). The coating is still in particle form with some necking at the points of contact. Crystallisation is seen to originate at particle surfaces. X-ray diffraction detects a significant amount of β-quartz together with minor quantities of lithium metasilicate ($Li_2O.SiO_2$) and lithium disilicate ($Li_2O.2SiO_2$), Figure 5.1.10(a). In the very early stages of firing, surface nucleation and growth of β-quartz predominates.

After a firing time of 1 minute and a removal temperature of 920°C (C2) there is considerable necking between particles. Extensive crystallisation has occured. Only the centres of the larger particles remain uncrystallised. Two crystal phase can be identified in backscattered electron contrast, both having submicron dimensions. See Figure 5.1.9(b). X-ray diffraction detects β-quartz and lithium disilicate as the major, and only, crystal phases present, Figure 5.1.10(b). Lithium metasilicate is not detected.

A high level of fusion is achieved after a firing time of 2 minutes and a removal temperature of 940°C (C3). The microstructure

still has a two crystal phase structure with a fine grained appearance and very few uncrystallised areas. Considerably more contact is made with the substrate.

Between 2 and 4 minutes a major change in microstructure form is apparent. Figure 4.1.9(d) shows the coating fired for 4 minutes and with a removal temperature of 968°C. Fusion is complete and a continuous coating has formed with residual porosity. The porosity results from the entrapment of gases. Contact is now made completely along the coating-substrate interface. The crystal phases occupy a much reduced area, while the mean crystal dimension has increased. Lithium disilicate and β-quartz are still present as major phases, Figure 5.1.10(d). Both form a network around featureless glass regions. A coarsening process operates between 2 to 4 minutes in which the average grain size increases and the number of grains decreases. For such a process to occur the smaller grains must be taken into solution while the larger grains grow. This will occur more readily if the temperature is close to the liquidus of the crystal phase. The liquidus of lithium disilicate in this glass composition is measured at 970°C, (Section 4.1.3). The increased removal temperature between the firings at times of 2 and 4 minutes is believed to cause the change in microstructure. With a removal temperature of 968°C the coarsening process will be rapid. The liquidus of β-quartz is much higher and above 1100°C for this glass composition. Consequently the coarsening process will proceed at a lower rate. This may explain the smaller crystal size of β-quartz.

The process continues for extended firing periods. Figure 5.1.9(e) shows a coating fired for 40 minutes and figure 5.1.9(f) for 3 hours. Both have a removal temperature of 967°C. Also apparent for extended firing times is the appearance of α-crystobalite at the

expense of β-quartz. A gradual polymorphic transformation of silica is occurring, Figure 5.1.10(e) and (f). The transformation is reconstructive and occurs slowly.

For comparison the crystallisation of bulk glass A was examined. Sections 1 x 2 x 7 cm^3, were subjected to various thermal treatments listed in table 5.1.1. Firing for 6 minutes at 967°C followed by rapid quenching results in the development of α-cristobalite and lithium disilicate. β-quartz is also present but as a minor phase. See Figure 5.1.11(a). Lithium disilicate appears as an elongated dark contrast phase in Figure 5.1.12(a). It has a typical length of 2-10μm. Cristobalite remians unresolved from the matrix.

Subsequent heat-treatment results in a large increase in the amount of β-quartz, see Figure 5.1.11(b). β-quartz is now a major phase. Its appearance is associated with a dispersed dark contrast phase in the light contrast matrix. Porosity is also observed. The β-quartz can be formed from the uncrystallised glass matrix or by transformation of the α-cristobalite. Conversion of α-cristobalite to β-quartz results in a 16% volume decrease. This would explain the observed presence of porosity.

If the bulk glass is heat-treated and not given a firing treatment before hand and only β-quartz and lithium disilicate appear. Figure 5.1.11(c). The microstructure is much finer and more interconnecting as shown in Figure 5.1.12(c).

In summary the crystallisation occuring during the vitreous enamelling process produces a coarser microstructure. It is strongly influenced by the surface of the initial glass powder and length of the firing period. In particular the glass surface preferentially nucleates β-quartz during firing. The equilibrium polymorph of silica in bulk glass at the firing temperature (970°C) appears to be α-cristobalite.

Figure 5.1.9 Backscattered electron micrographs of coatings subjected to increasing firing times.

(a)
C1
30 seconds
906°C

4 um

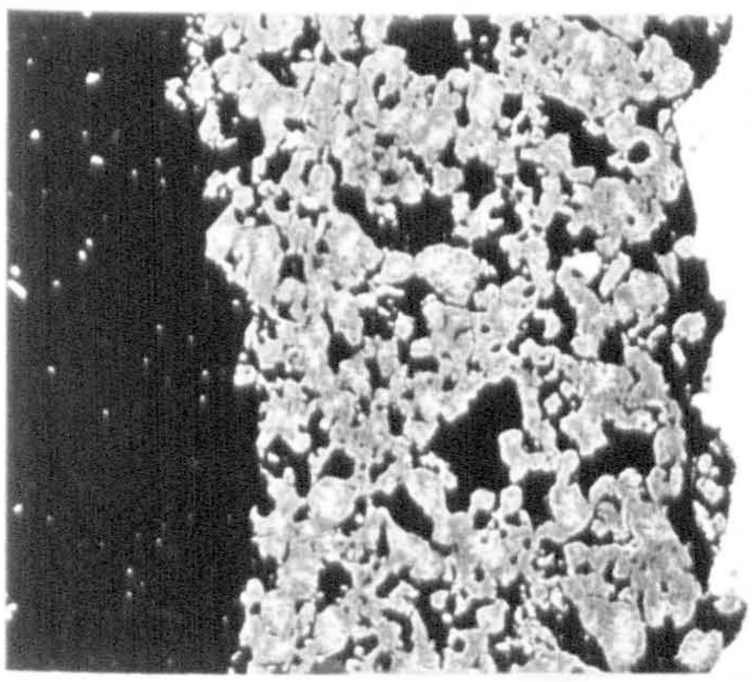

(b)
C2
1 minute
920°C

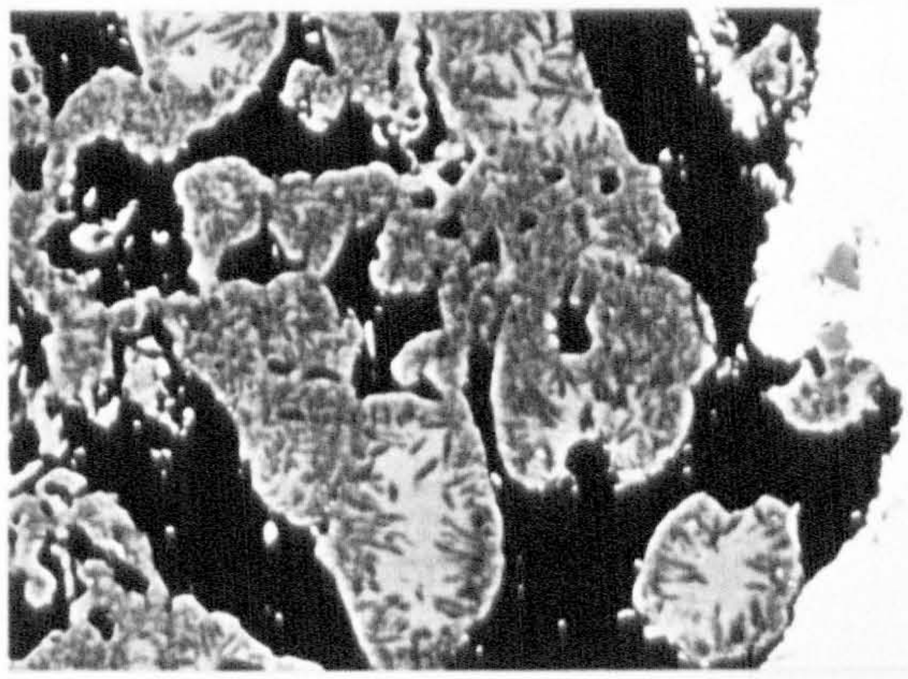

40 um

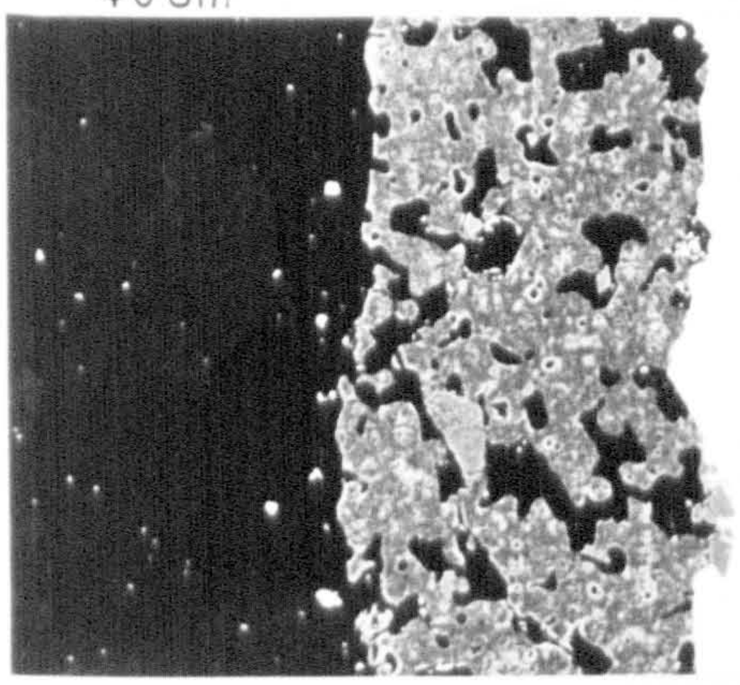

(c)
C3
2 minutes
940°C

10 um

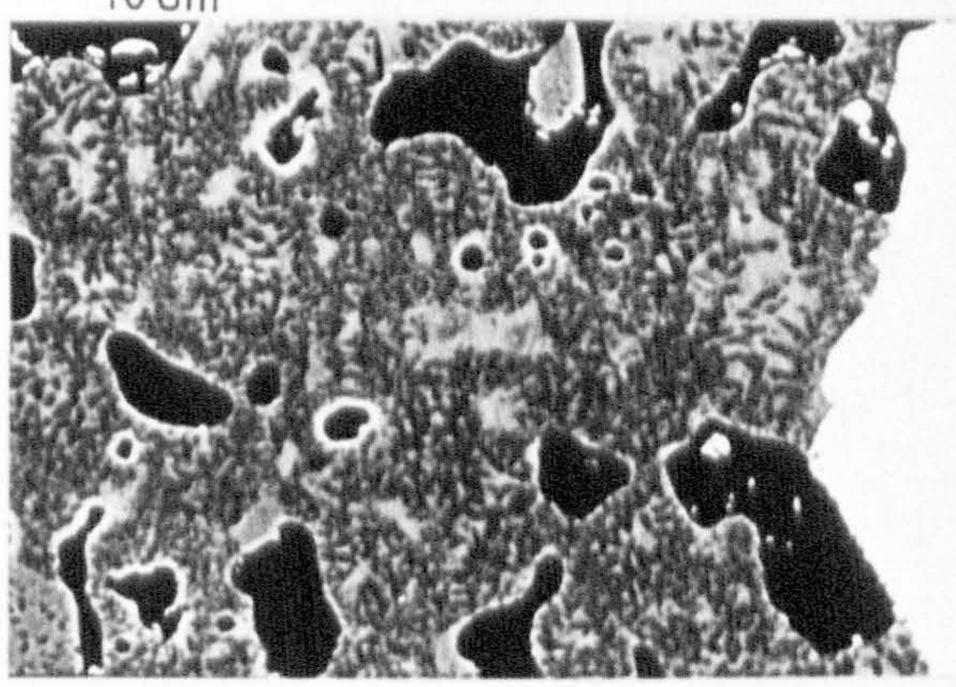

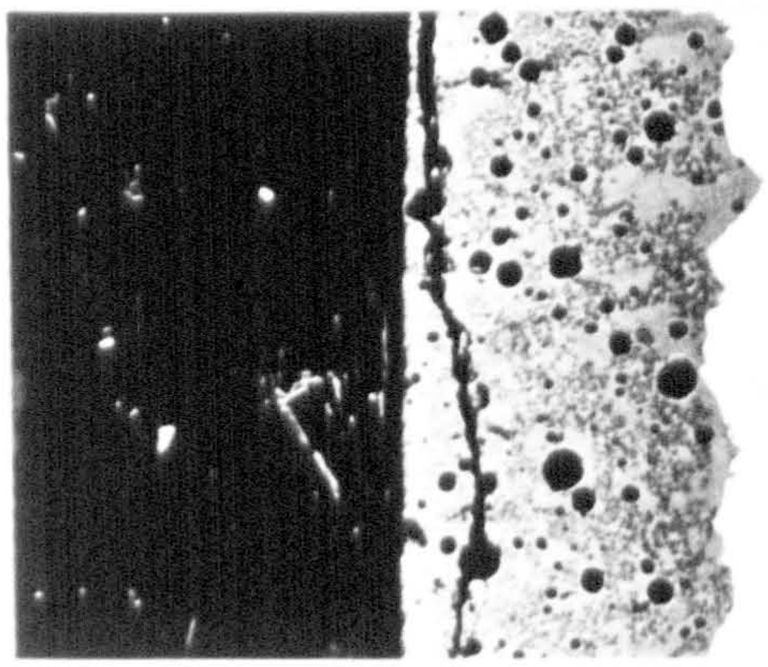

(d)
C4
4 minutes
968°C

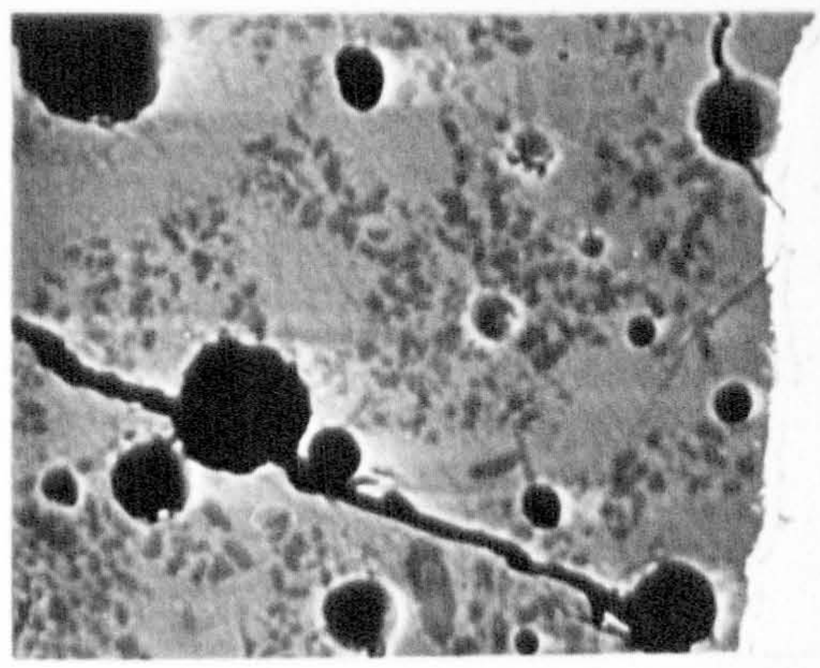

Resin coating metal

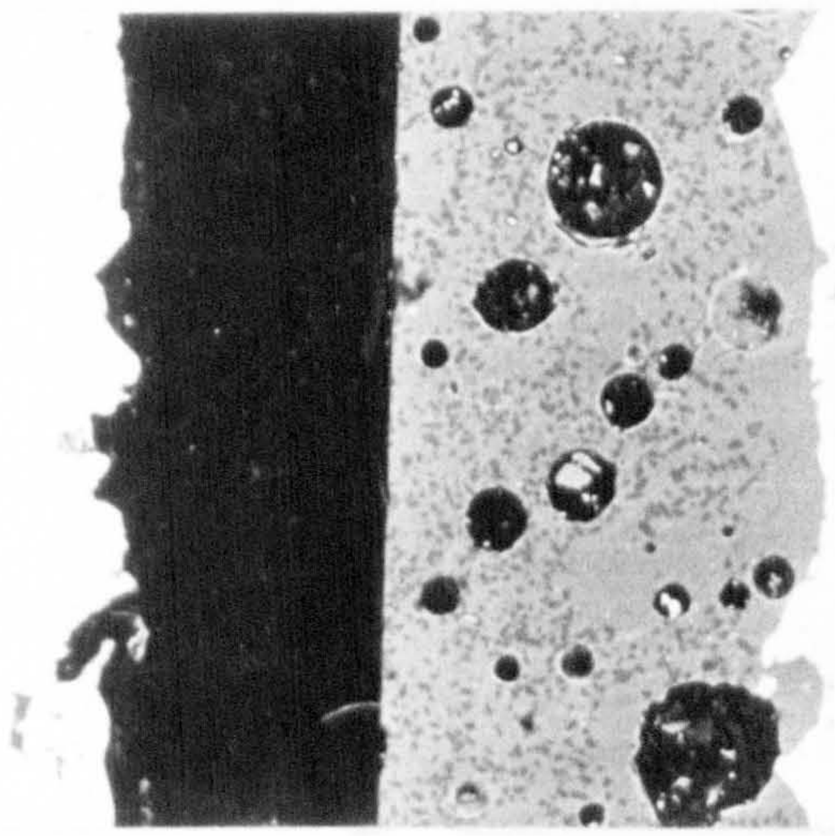

(e)
C7
40 minutes
967°C

40 um

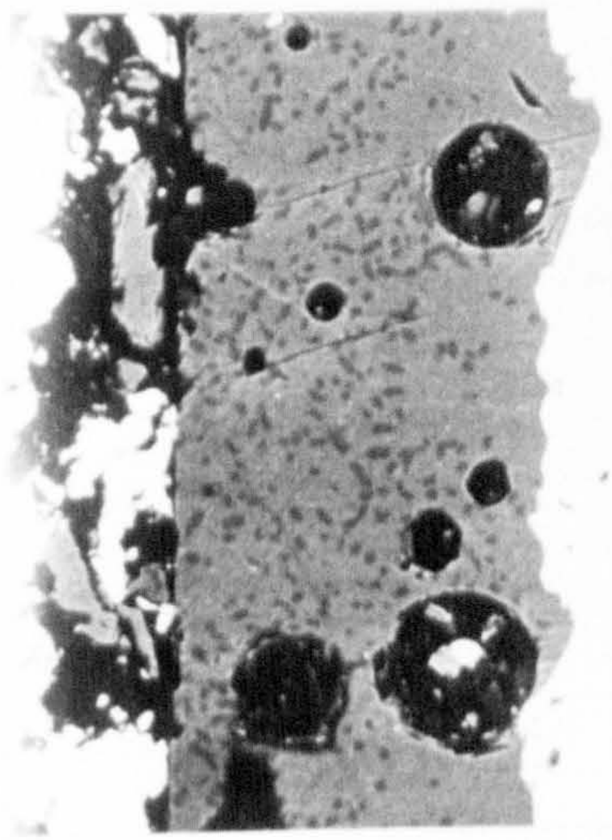

(f)
C10
3 hours
967°C

coating substrate

L - Lithium disilicate
M - Lithium metasilicate
Q - β-quartz
C - cristobalite

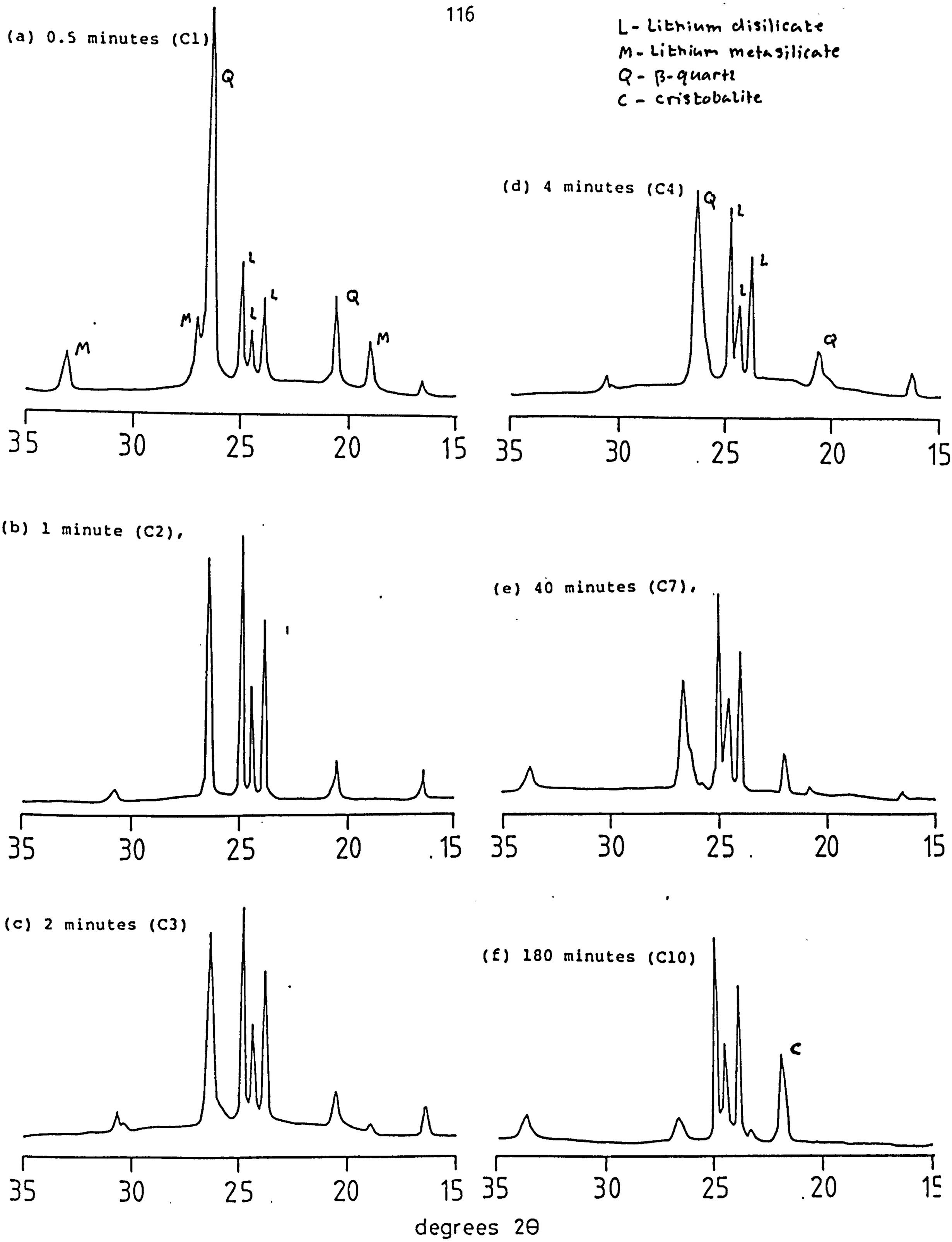

Figure 5.1.10 XRD patterns collected from coatings subjected to increasing firing time.

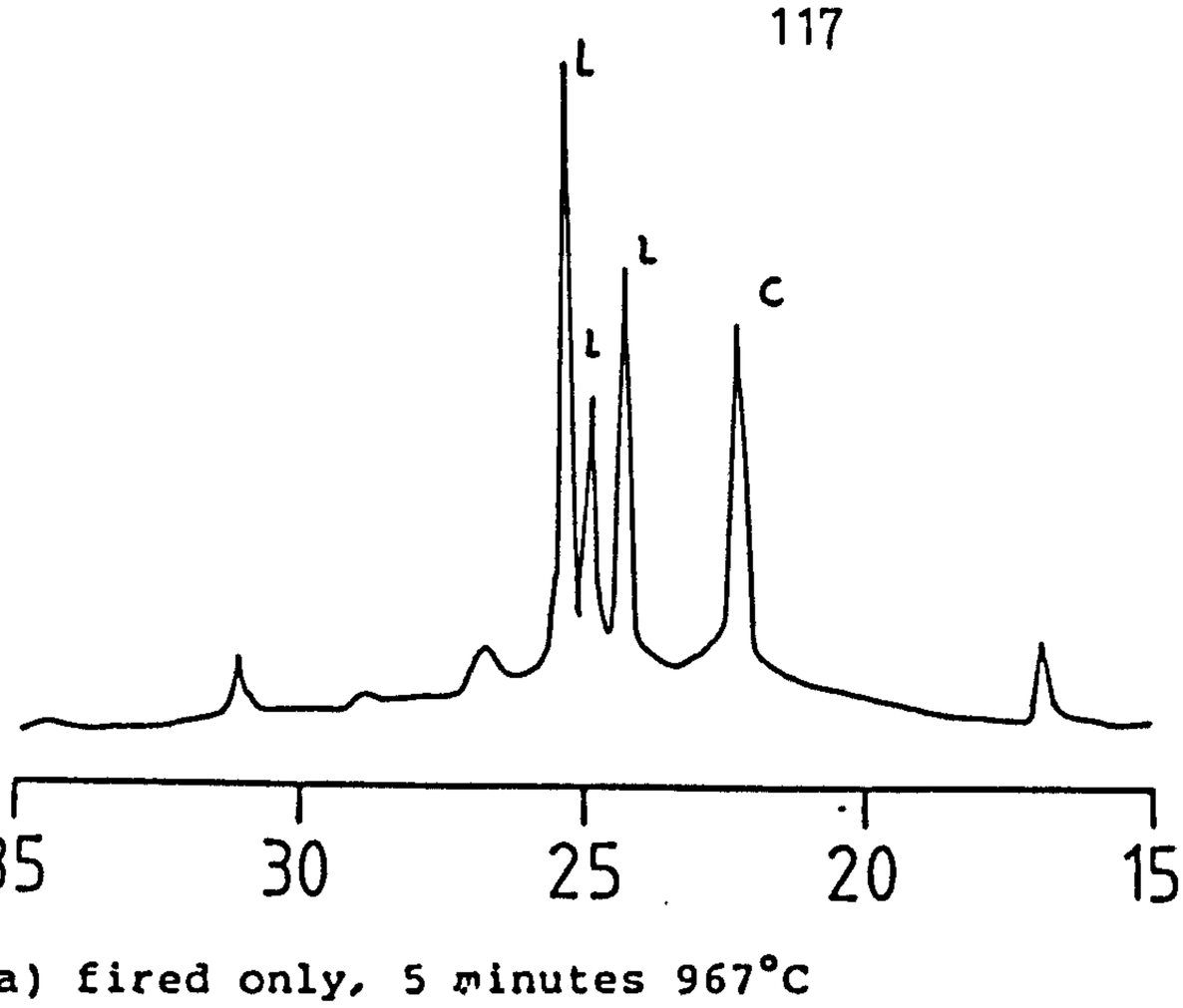

(a) fired only, 5 minutes 967°C

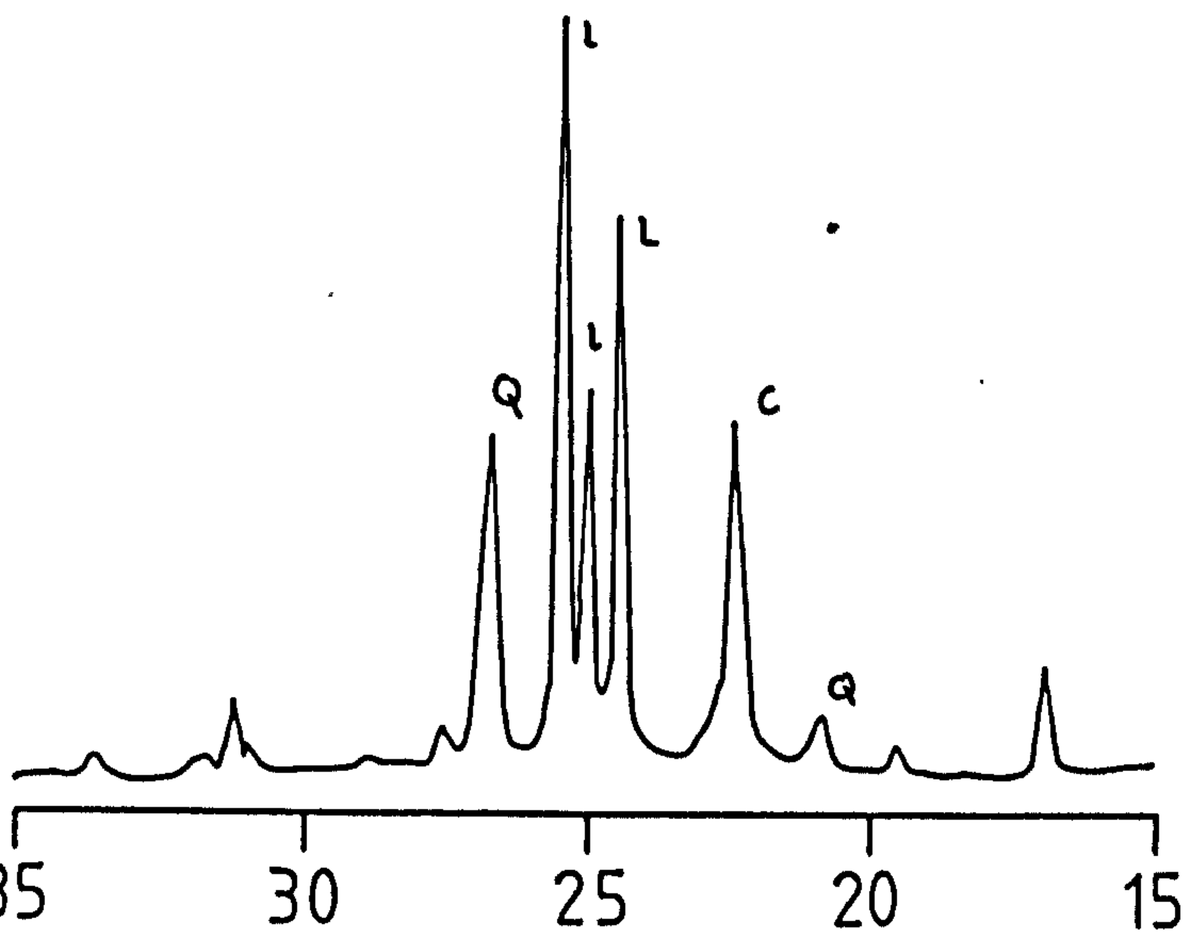

(b) fired and heat-treated

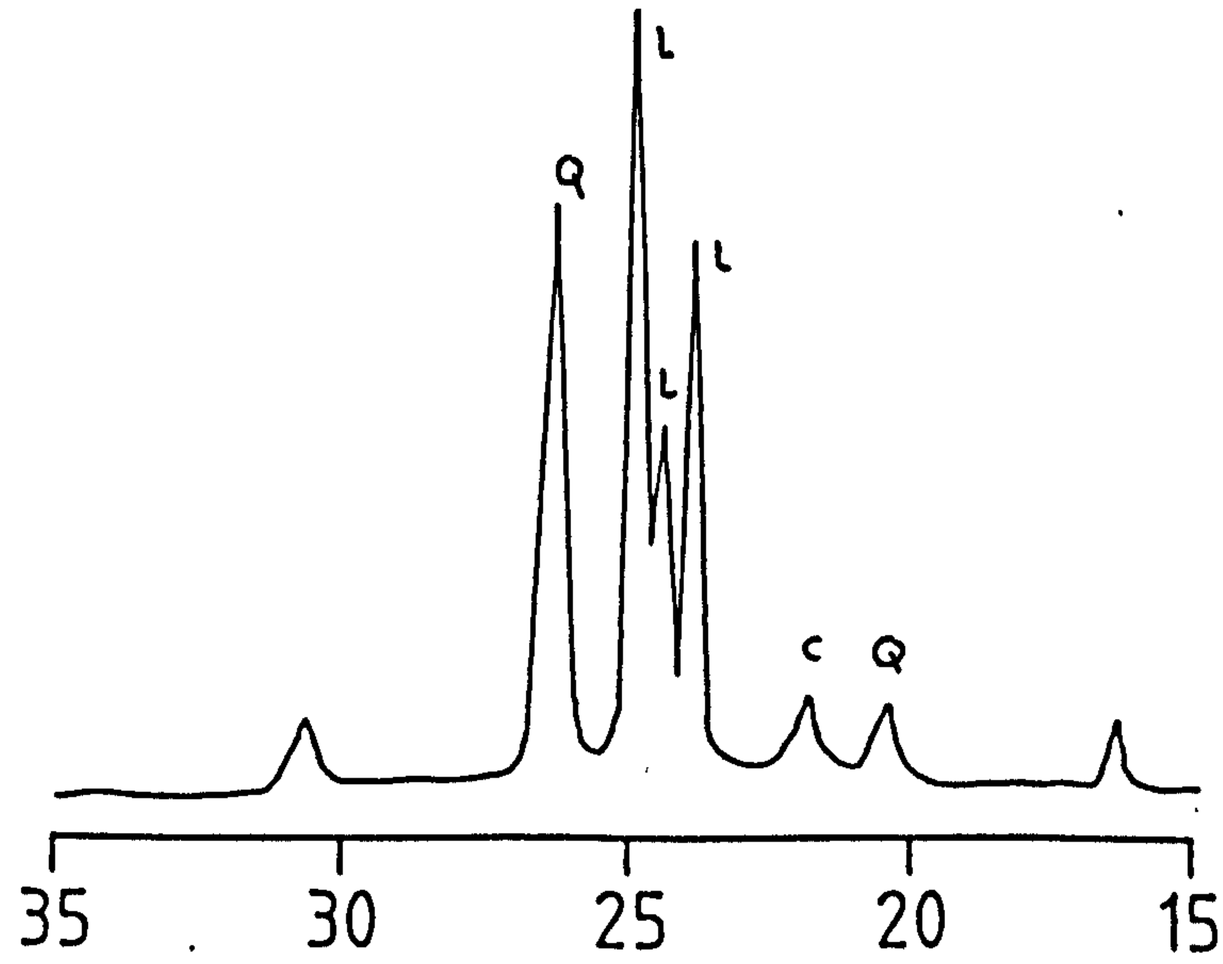

(c) heat-treated only.

Figure 5.1.11 XRD patters collected from bulk glass A subjected to various thermal treatments

Figure 5.1.12 Backscattered electron micrographs of bulk glass A subjected to various thermal treatments.

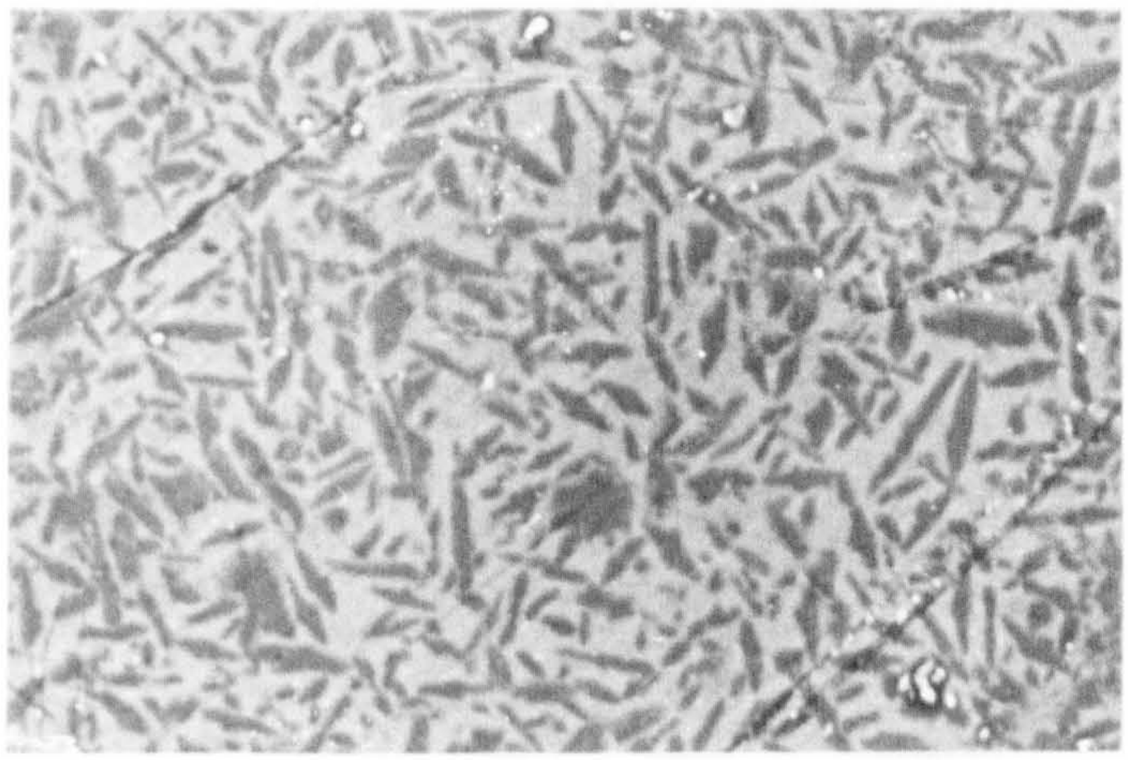

10 µm

fired only

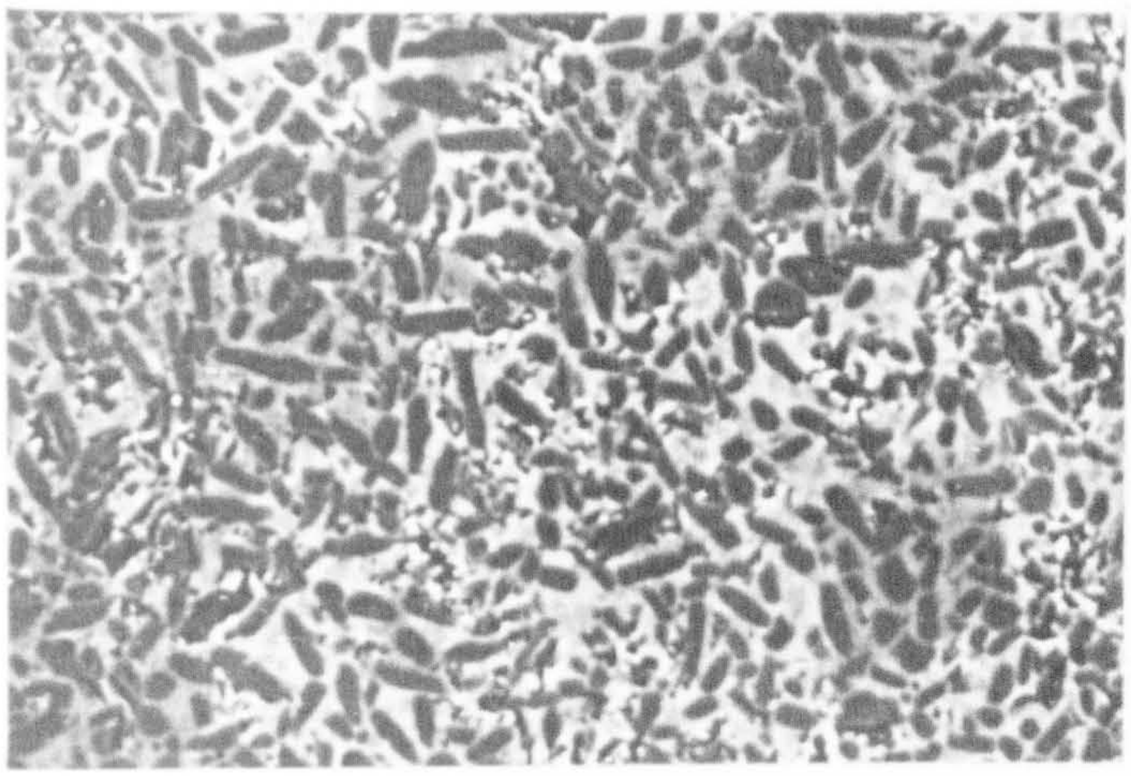

10 µm

fired and heat-treated

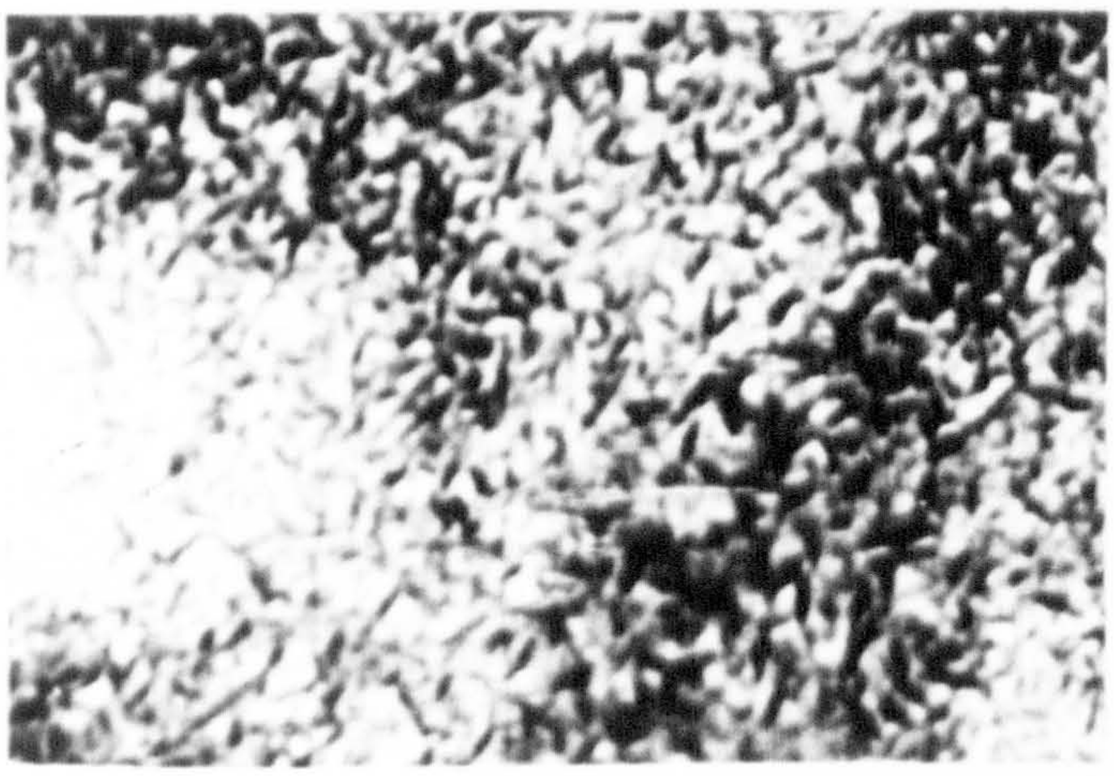

4 µm

heat-treated only

Table 5.1.1: Thermal treatment of bulk glass A

Firing Conditions minutes	°C	Subsequent treatment	Crystal phases present
6	967	Quenched	Lithium disilicate Cristobalite Minor amounts of quartz
6	967	Heat-treated	Lithium disilicate Cristobalite β-quartz
no firing		Heat-treated	Lithium disilicate β-quartz

5.1.5 Reaction between the substrate and coating

For greatly extended firing periods, in excess of 1 hour, a new phase is observed between the chromium oxide and coating. See Figure 5.1.13, which shows the interfacial microstructure of a coating fired for 6 hours (C11). The thickness of the new phase gradually increases with firing time. It first becomes noticeable after 1 hour, existing in isolated areas adjacent to the chromium oxide layer. For longer times it forms a continuous layer between the chromium oxide and coating. But it remains less than 1μm thick for up to 6 hours. By 48 hours the phase has grown to 6μm and the chromium oxide layer is almost completely depeleted. The measured thickness of the new phase for increasing firing times is listed in Table 5.1.2. When plotted as a linear function of time a good fit is obtained, figure 5.1.14. Growth of this layer is governed by a phase boundary reaction and not by diffusion through the layer, which would give a parabolic dependence on time. The linear growth rate is measured at 0.136μm per

hour. This predicts, for a "standard" firing period of 5 minutes, that the layer would have attained a thickness of 0.014μm. If present at normal firing periods it will be undetectable by the techniques used.

The results from x-ray microanalysis of the new phase are given in Table 5.1.3 and show it to be a chromium silicate. To estimate the oxygen concentration light element EDX analysis was used. The determined atomic % concentrations are listed in Table 5.1.3. To maintain charge neutrality (assuming chromium as trivalent) 10 Li^+ ions are required. This indicates the compound is a lithium chromium silicate of composition $Li_5Cr_7Si_{10}O_{33}$. A bulk glass and chromium oxide disc were heated at 970°C for 10 days as described in Section 4.4. The glass has diffused intergranularly into the oxide disk, see Figure 5.1.15. It reacts to form lithium chromium silicate. The interface was exposed by grinding away the glass. Analysis by x-ray diffraction detects chromium oxide and additional peaks. These are listed in Table 5.1.4. They correspond to $LiCr(SiO_3)_2$ as given by the J.C.P.D.S. file. The higher measured chromium to silicon ratio in Table 5.1.3 can be explained by assuming there is some solid solution with chromium oxide. This corresponds to 5 $LiCrSi_2O_6$:1 Cr_2O_3. This is not accompanied by any significant change in lattice parameters.

Table 5.1.2: Thickness of lithium chromium silicate layer

Firing time hours	Thickness μm
1	0.5
2	0.5
3	0.5
6	0.19 ± 0.3
9	1.4 ± 0.5
24	3.5 ± 0.8
48	6.5 ± 1
72	6.5 ± 1

Table 5.1.3: Composition of lithium chromium silicate layer.
Detectable elements only

	Element at% (±0.1%)						
Detector window in	Al	Si	P	K	Zn	Cr	Fe
	2.5	54.1	0	0	0.3	41.3	1.7

	Element at% (±2%)			
Detector window removed	Si	Fe	Cr	O
	20	0	14	66

Table 5.1.4: X-ray pattern collected from Cr_2O_3 - glass A interface

Phase	measured			J.C.P.D.S. file	
	2θ	d	T/I_o	d	I/I_o
Cr_2O_3	24.3	3.65	70	3.63	75
	33.5	2.67	100	2.66	100
	36.0	2.49	69	2.49	95
	41.3	2.18	31	2.17	40
	39.6	2.27	15	2.26	12
	44.0	2.06	6	2.06	10
	50.0	1.82	37	1.81	40
	54.6	1.68	90	1.67	90
$LiCr(SiO_3)_2$	20.0	4.43	41	4.39	30
	20.7	4.31	41	4.28	30
	25.4	3.50	41	3.47	35
	30.1	2.97	100	2.95	100
	31.6	2.83	75	2.82	75
	37.6	2.39	38	2.41	40
	42.3	2.13	25	2.13	25
	43.0	2.10	25	2.09	20
	56.6	1.62	35		

Figure 5.1.13 Coating on Chrome-iron preoxidised in wet hydrogen and fired for 6 hours at 970°C, (C11).

Figure 5.1.15 Glass A heated at 970°C for 10 days on a chromium oxide disc.

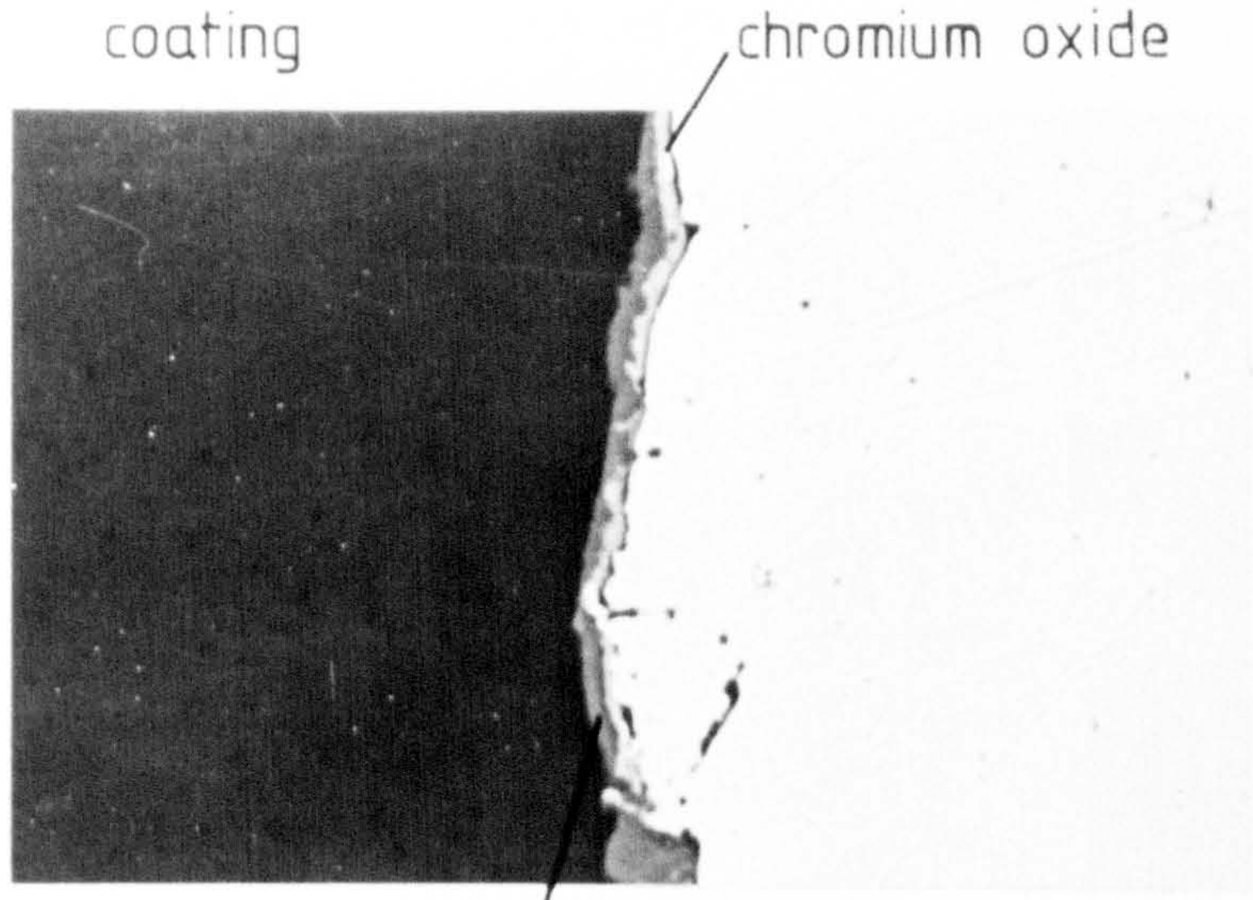
coating
chromium oxide
lithium chromium silicate
substrate

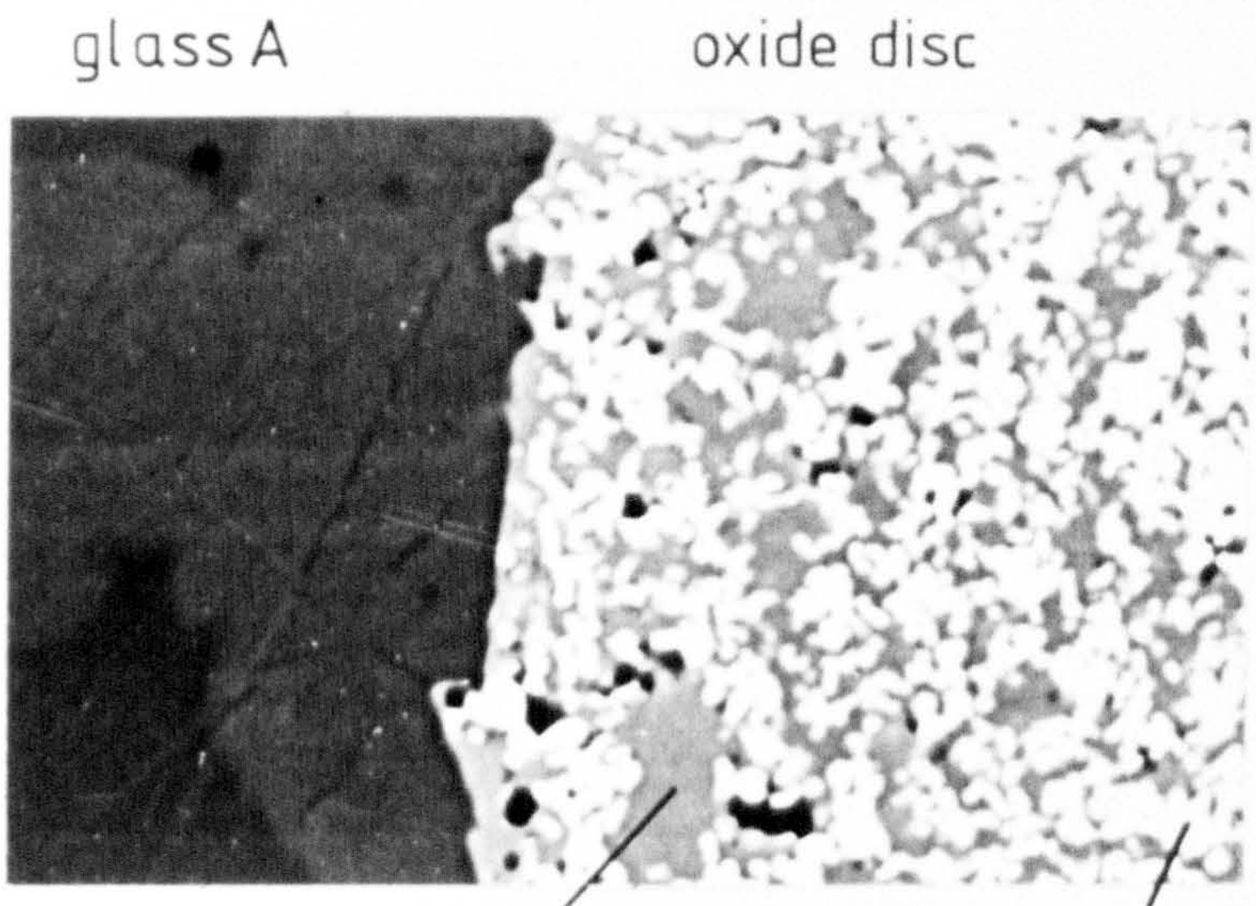
glass A
oxide disc
lithium chromium silicate
chromium oxide

4 µm

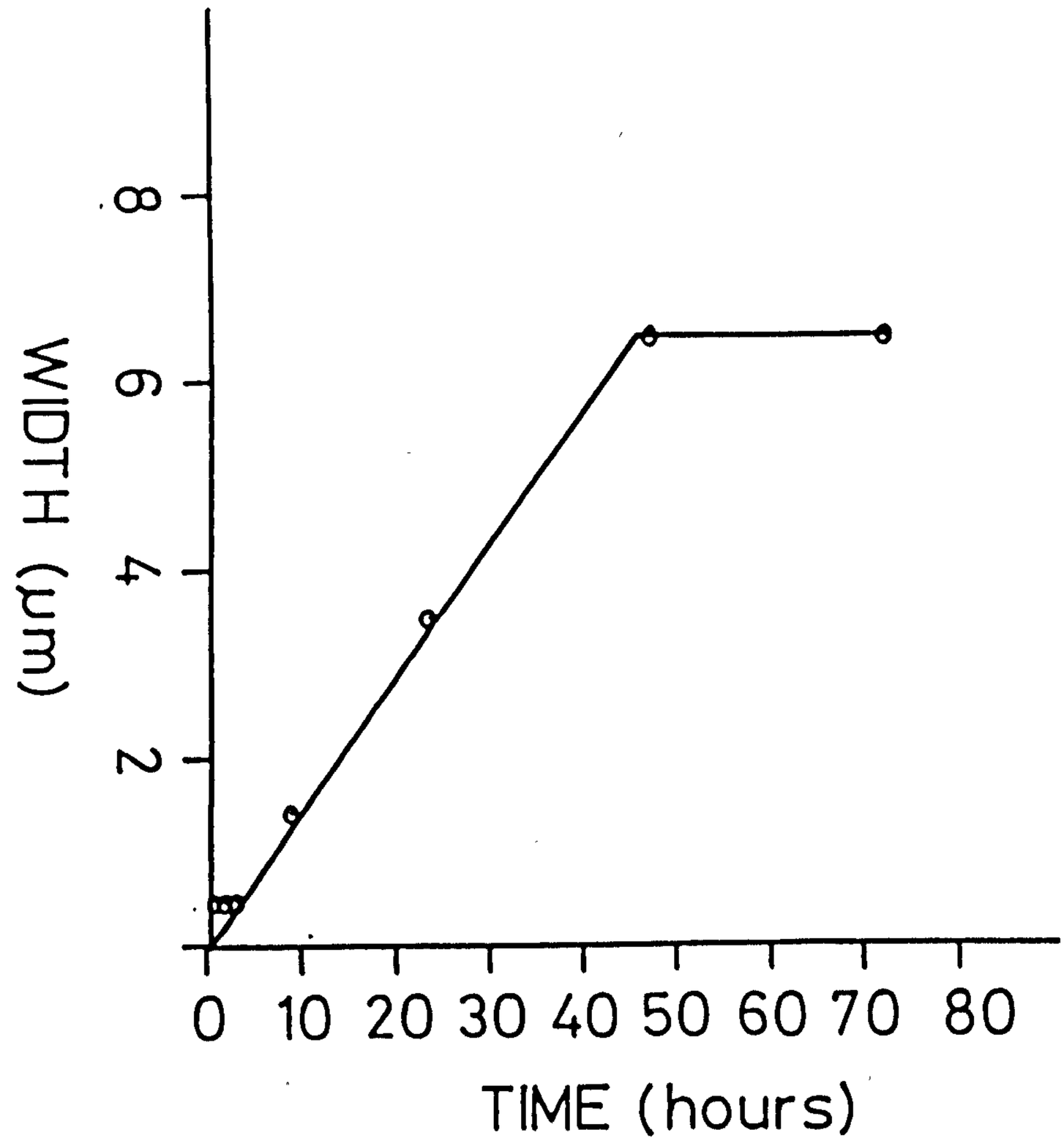

Figure 5.1.14 Width of lithium chromium silicate layer for increasing firing times.

5.1.6 Influence of firing time on interdiffusion

The distributions of the detectable elements in the coating adjacent to the interface were determined by quantitative EDX analysis (Section 3.2.7) for a range of firing periods up to 24 hours. The results are discussed with reference to those coatings fired for 5 minutes, (C5), Figure 5.1.6., 40 minutes (C7), Figure 5.1.16(a), 2 hours, (C9), Figure 5.1.16(b) and 24 hours, (C13), Figure 5.1.16(c). Profiles for chromium, iron and silicon are shown and expressed in normalised at% values. All firing periods produce very similar elemental distributions in the coating. The chromium level drops rapidly from a peak value corresponding to the chromium oxide layer (or lithium chromium silicate layer for greatly extended periods) to a concentration of 0.3 at% by 3μm into the coating (or from the lithium chromium silicate - coating boundary).

Chromium concentrations adjacent to the interface should represent the saturation level in this glass composition. This requires the oxide solution rate to exceed the rate of diffusion away from the interface. The concentrations at 3μm are taken to be representitive of the chromium level at the interface. Here contributions from the chromium containing phases due to electron beam spreading is negligible. It is apparent that the chromium concentration remains essentially constant at 0.3 at% irrespective of the firing time. This means that the solution rate dues exceed diffusion away from the interface. The very low chromium level represents a saturation of chromium oxide in the adjacent coating. Confirmation comes from the observation that chromium has a concentration of 0.23 at% at the interface between the bulk glass and chromium oxide disc fired for 10 days at 970°C.

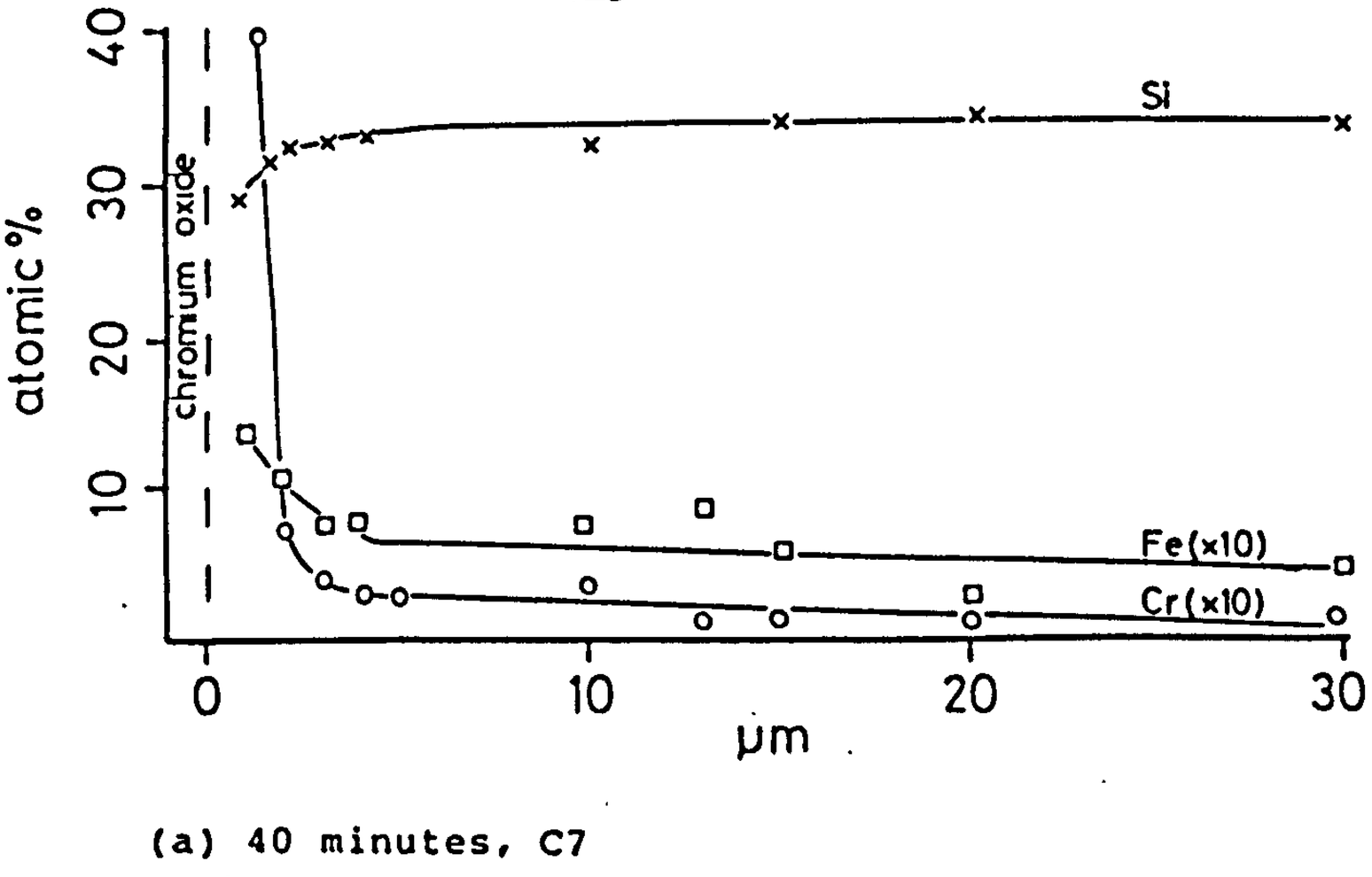

(a) 40 minutes, C7

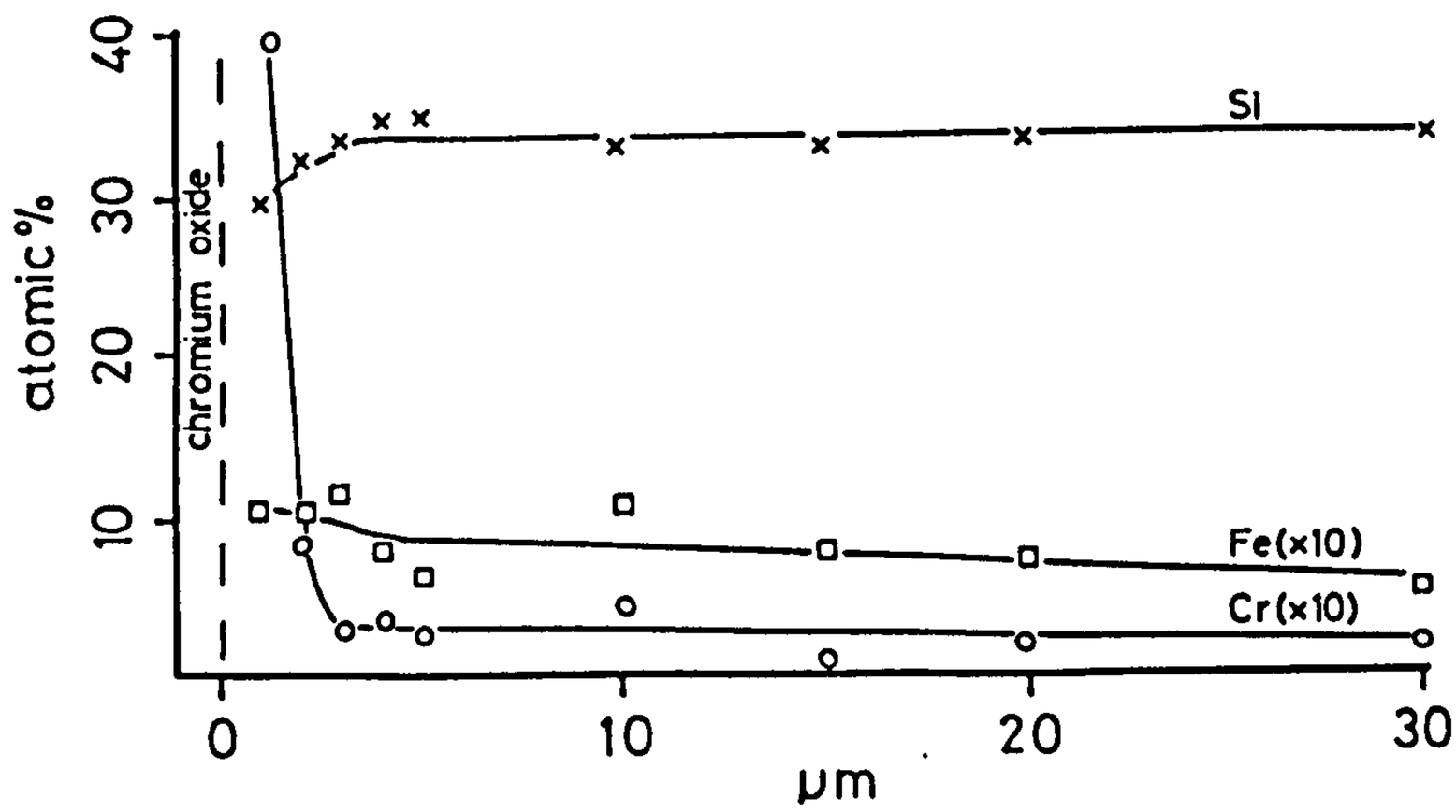

(b) 2 hours, C9

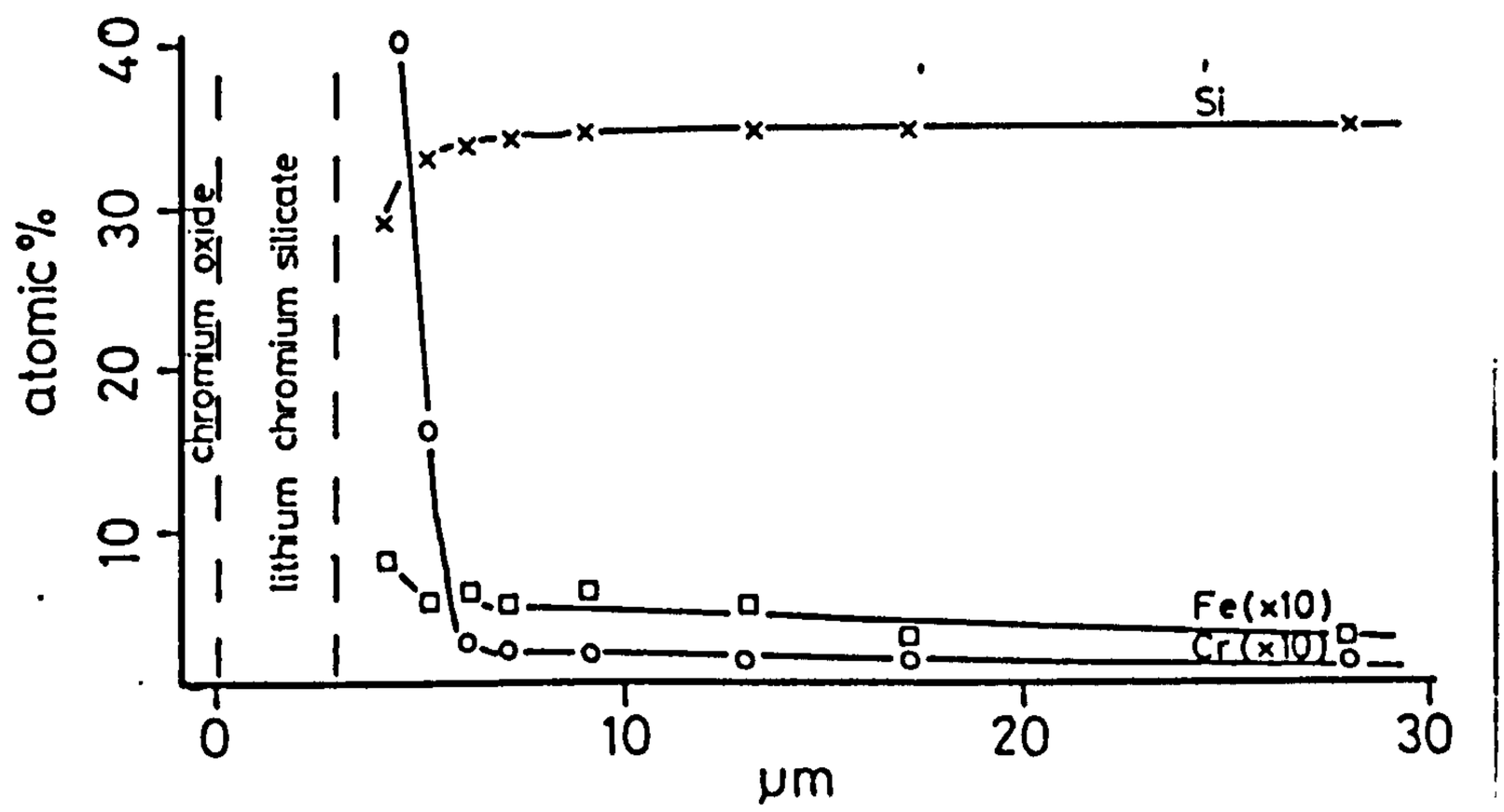

(c) 24 hours, C13

Figure 5.1.16 Quantitative element distribution across the interface of coatings fired for increasing times.

Iron is present in the coating at greater concentrations than chromium, but still at low levels, typically 1 at% by 3μm adjacent the interface. There is no peaking at the interface, consistent with the oxide layer being essentially a chromium oxide and not a spinel. Both iron and chromium have diffused in excess of 30μm from the interface. Potassium shows significant variation related to the microstructural form. No clear trends were observed for the other detectable elements, apart from scatter about mean levels.

5.1.7 Variation in metal pretreatment

The enamel coatings examined so far have been on chrome-iron substrates abraded with alumina grit then preoxidised in an atmosphere of wet hydrogen. Using "standard" firing and heat-treatment condit ions satisfactory coatings were obtained (C5 and C5H). These exhibited good wetting characteristics. The interface structure is very stable to considerable variation in firing time. To establish if the conditions above are essential for good wetting and adhesion, the preparation of the chrome-iron substrate was altered.

The abrasion with alumina grit was omitted before preoxidation in wet hydrogen. A layer of chromium oxide was formed on the alloy surface and identified by x-ray diffraction. Subsequent enamelling was carred out under "standard" firing conditions. This was followed by a "standard" heat-treatment (C17H).

The substrate with and without initial abrasion was preoxidised in an air atmosphere at 650°C for 15 minutes. Oxidation was very slight resulting in a blue tarnish. No oxide could be detected by x-ray diffraction techniques and no weight gain was detected. The substrate was enamelled under "standard" firing condition but in an atmosphere of oxygen free nitrogen. A "standard" heat-treatment in

air was then given (C18H and C19H).

The substrate in the abraded and unabraded condition, but without any preoxidation, was also enamelled. Firing was carred out in air using the "standard" firing conditions. The coating was heat-treated in the usual way (C20H and C21H).

The abrasion, preoxidation and firing parameters are summarised in Table 5.1.5. In all cases the enamel wetted the substrate well. A smooth, white and thin enamel layer resulted. The interfacial microstructure for various pretreated substrates are described below:-

Preoxidised in wet hydrogen - C5H and C17H:

The microstructural appearance is described fully in Section 5.1.3 for the abraded substrate (C5H). On omission of the abrasion a smooth interface is observed. See Figure 5.1.17(a). All the feature for the abraded substrate are present. The interface is well defined. A discrete chromium oxide layer exists between the alloy and coating. The oxide layer is separated from the alloy by a submicron thick silica layer.

Preoxidised in air - C18H and C19H:

A well defined boundary exist at the interface without the presence of a discrete metal oxide layer. See Figure 5.1.17(b). The abraded substrate has a much more irregular interface, but is otherwise identical to the unabraded substrate. Two submicron features are observed along the interface. A small spherical phase of bright contrast appears adjacent to but detached from the alloy. Another phase, slightly darker in contrast, is attached to the

Table 5.1.5: Influence of pretreatment and preoxidation

Lable	Pretreatment	Preoxidation	Coating adhesion	Composition* of exposed coating surface Element at% (±0.1%)							
				Al	Si	P	K	Zn	Fe	Cr	O
C5H	abraded	Wet hydrogen	34.5 ±3 (1)	1.81	16.9	0.4	1.5	0.9	1.9	14.7	63
C17H	not abraded	Wet hydrogen	19.1 ±8 (0)	0.8	7.0	0.3	0.5	0.3	2.0	30.0	64
C18H	abraded	Air	53 ±3 (2)	3.2	19.7	0.4	0.6	0.1	4.2	8.4	64
C19H	not abraded	Air	27 ±8 (0)	1.0	15.5	0.3	0.4	0.4	1.8	17.9	63
C20H	abraded	No preoxidation	54 ±8 (3)	3.4	18.6	0.4	1.4	0.4	2.4	10.6	63
C21H	not abraded	No preoxidation	17 ±8 (0)	0.8	14.1	0.4	0.4	0.1	2.7	19.2	62

*excluding Li and its associated O

Figure 5.1.17 Backscattered electron micrographs for coats on chrome-iron substrates given different pretreatments and preoxidations.

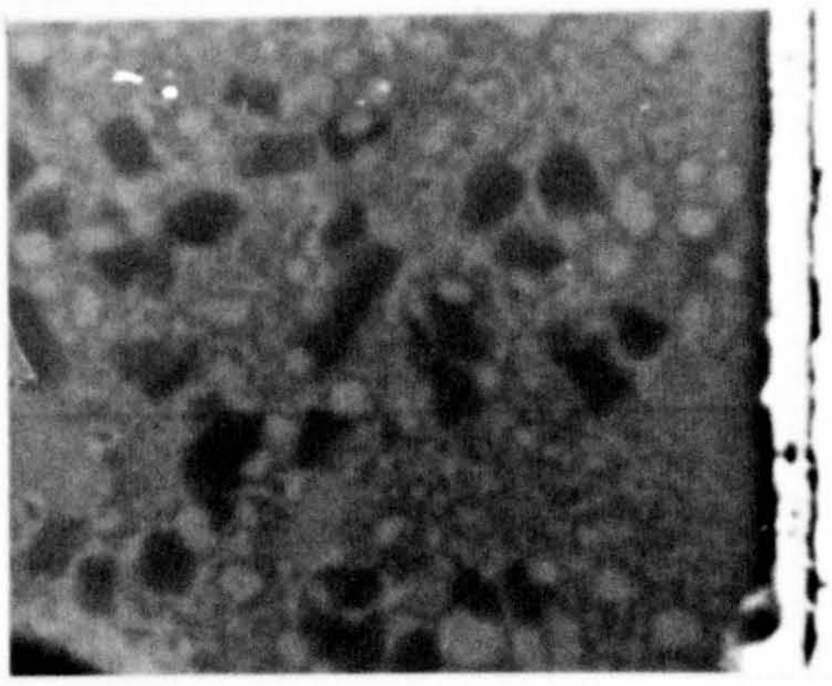

(a) preoxidised in wet hydrogen C17

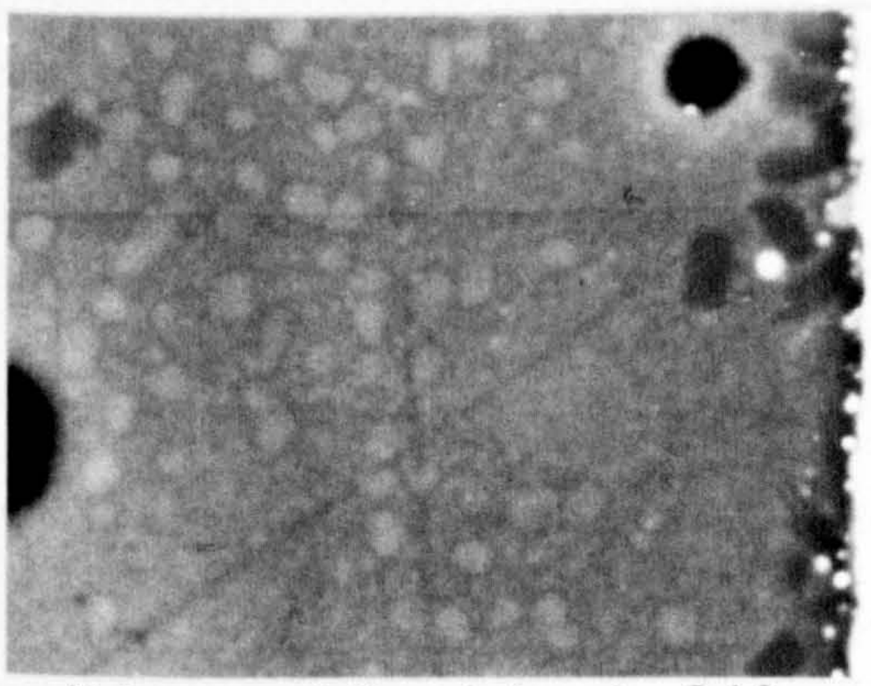

(b) preoxidised in air C19

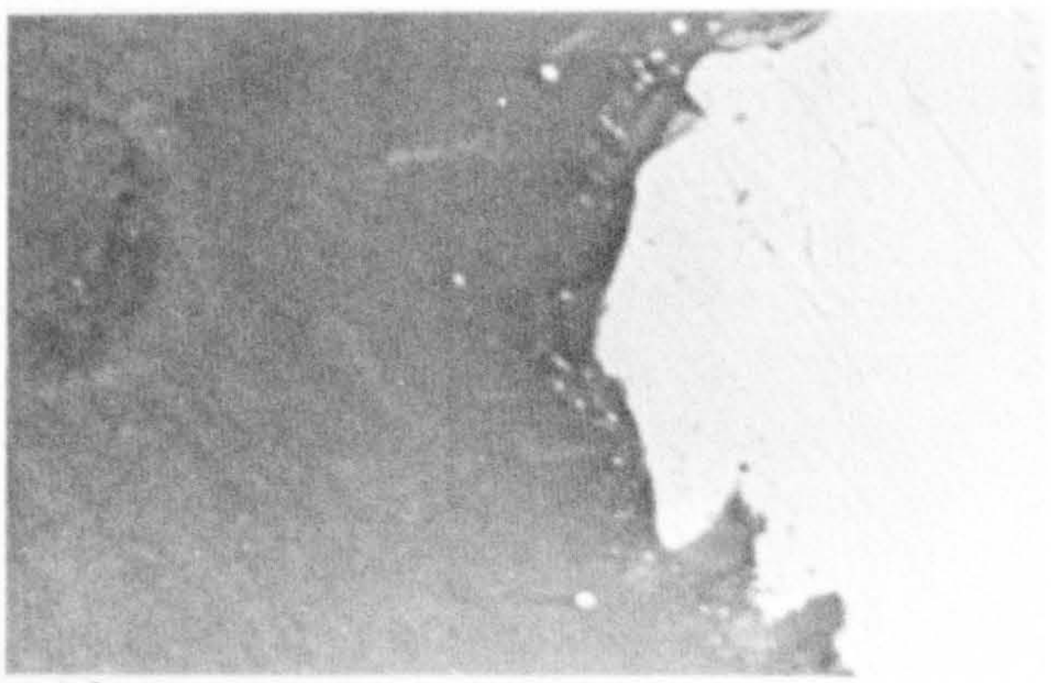

C18

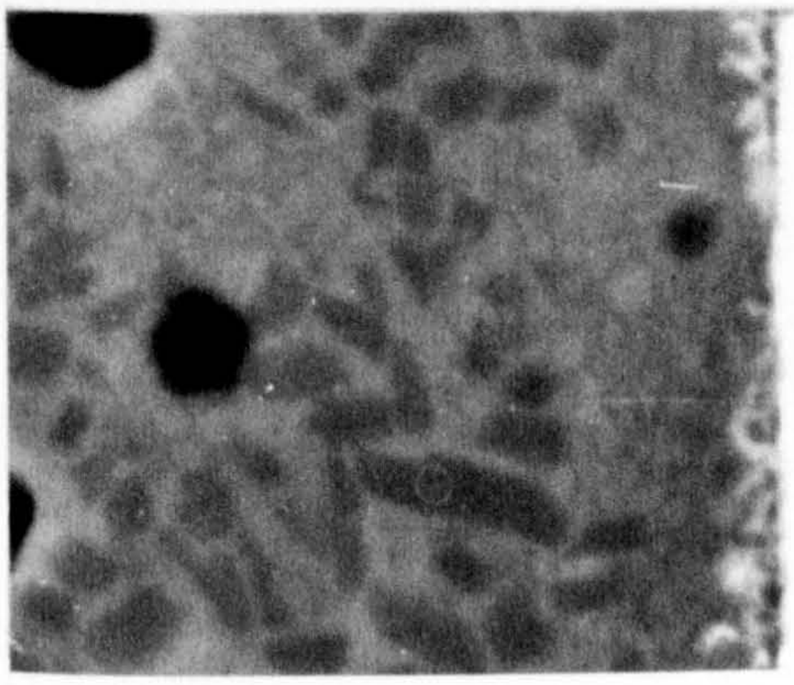

(c) no preoxidation C21

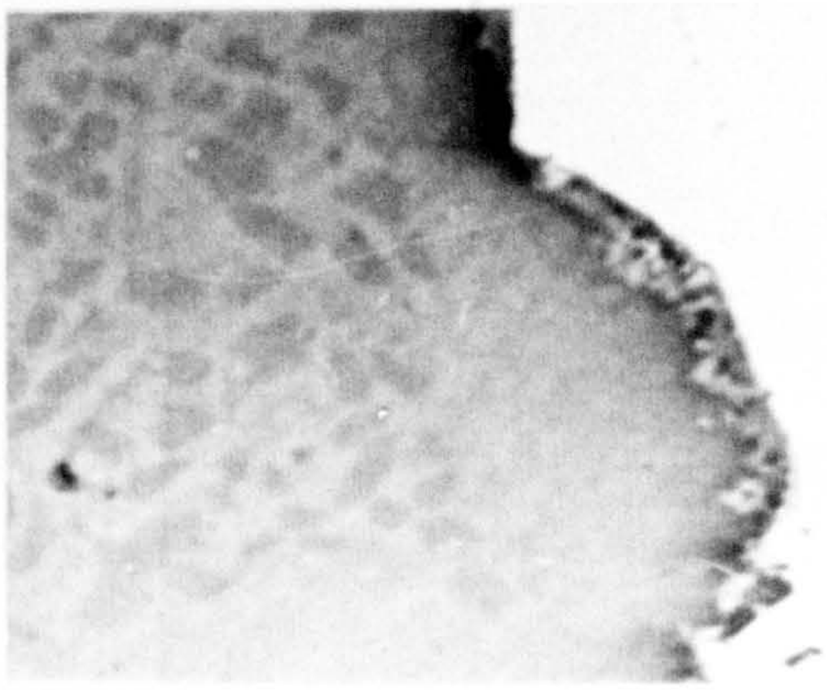

C20

4 µm

interface. The small sizes prevent identification by EDX analysis. An indication of the mean atomic number is possible from backscatter contrast. The small spherical phase has a contrast similar to the alloy. This suggests it is metallic. The other phase has a slightly darker contrast but is still brigher than the coating. It is likely to be an oxide of the substrate alloy. X-ray maps collected using CrK_2 and FeK_2 radiation are shown in Figure 5.1.18(a). Iron and chromium remain essentially within the alloy.

Not preoxidised - C20H and C21H:

A sharp boundary is present at the interface. See Figure 5.1.17(c). Again no discrete oxide layer exists. Abrasion results in a more irregular interface but no change in the interfacial features. A dispersed phase is attached to the alloy and extends 2μm into the coating. It has a light backscatter contrast but is darker than the alloy. This suggests it is an oxide of the substrate alloy. Figure 5.1.18(b) shows the x-ray maps for CrK_2 and FeK_2 radiation. Iron remains within the alloy. Chromium extends beyond the alloy boundary into the coating. It corresponds to the presence of the dispersed phase. The indications are that this phase is mostly chromium oxide.

The distribution of chromium, iron and potassium in the coating adjacent the interface are displayed in Figures 5.1.19(a) to (c) for each pretreated substrate. These have been determined by quantitative EDX analysis. There is very little difference between them. In all cases chromium and iron are present in very low concentrations. Chromium reaches a concentration of typically 0.3 at%. Iron has a similar or slightly greater concentration. Potassium shows some variation. But its level is influenced markedly by the coating

Figure 5.1.18 X-ray maps of $Fe_{k\alpha}$ and $Cr_{k\alpha}$.

(a) preoxidised in air C 19

(b) no preoxidation C 21

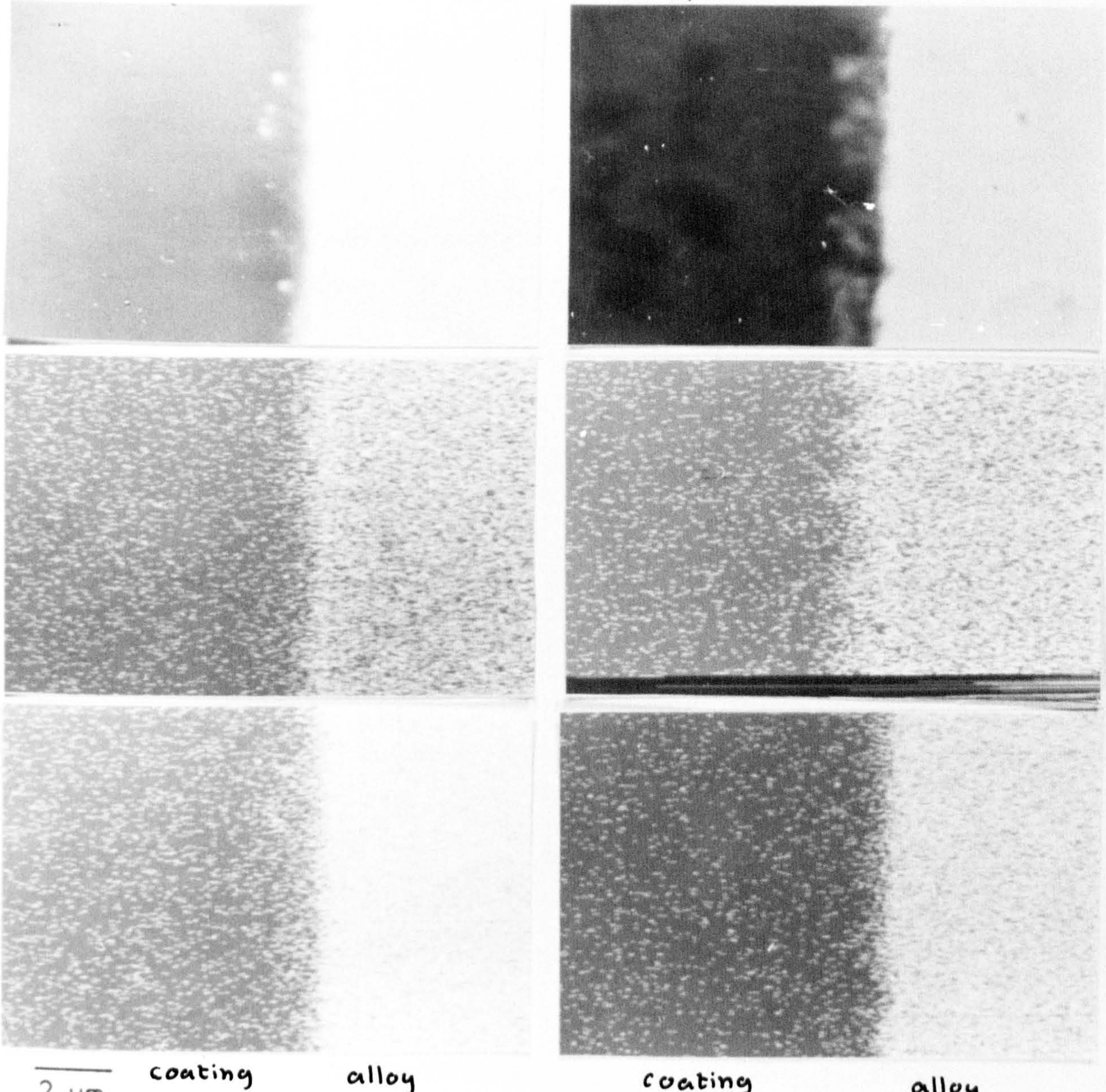

$Cr_{K\alpha}$

$Fe_{K\alpha}$

2 µm

coating

alloy

coating

alloy

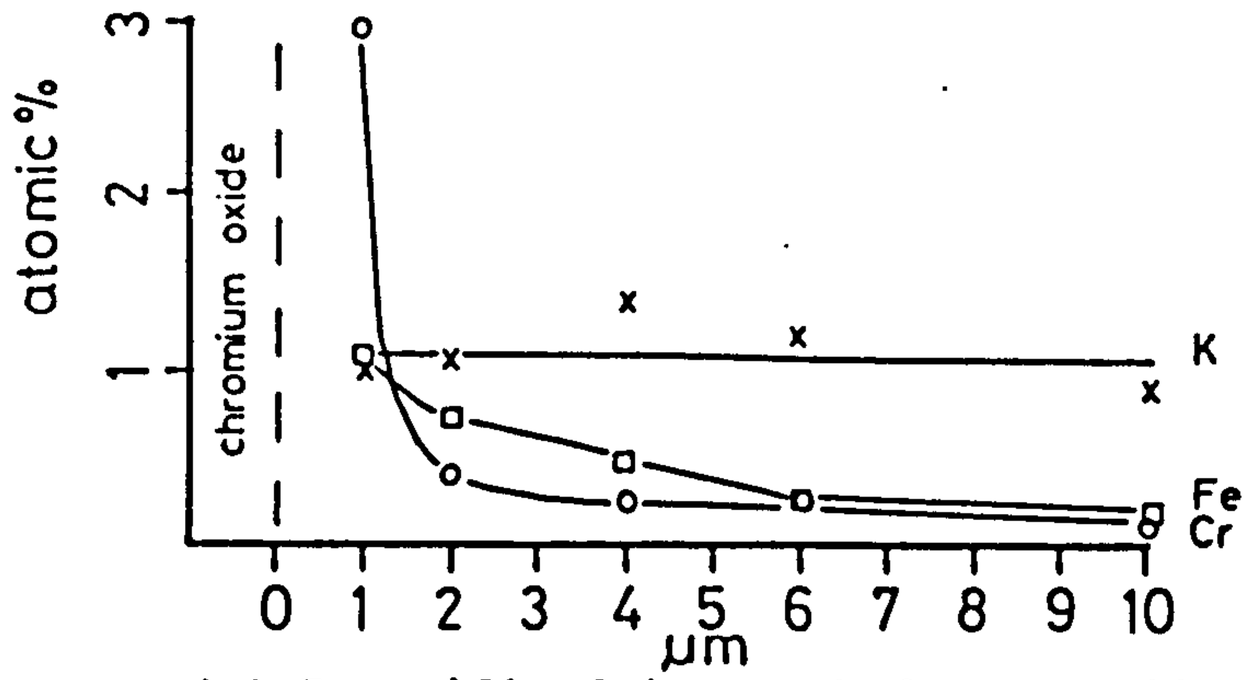

(a) Preoxidised in wet hydrogen, C17H.

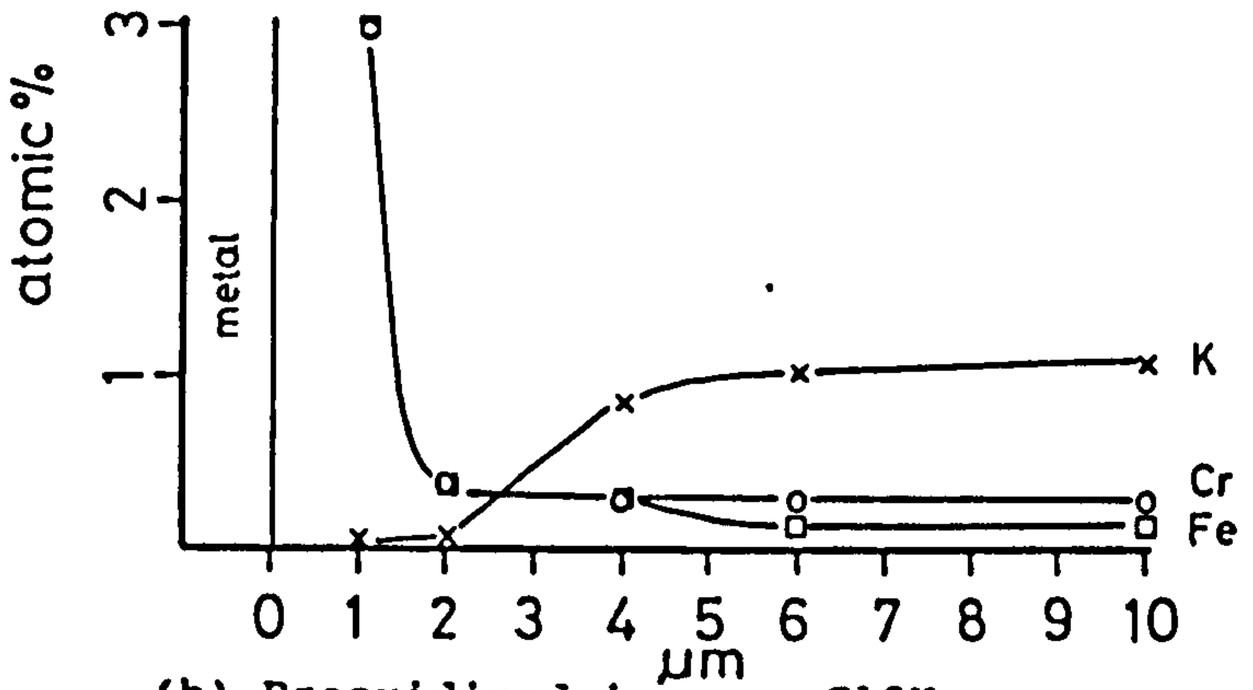

(b) Preoxidised in air, C18H.

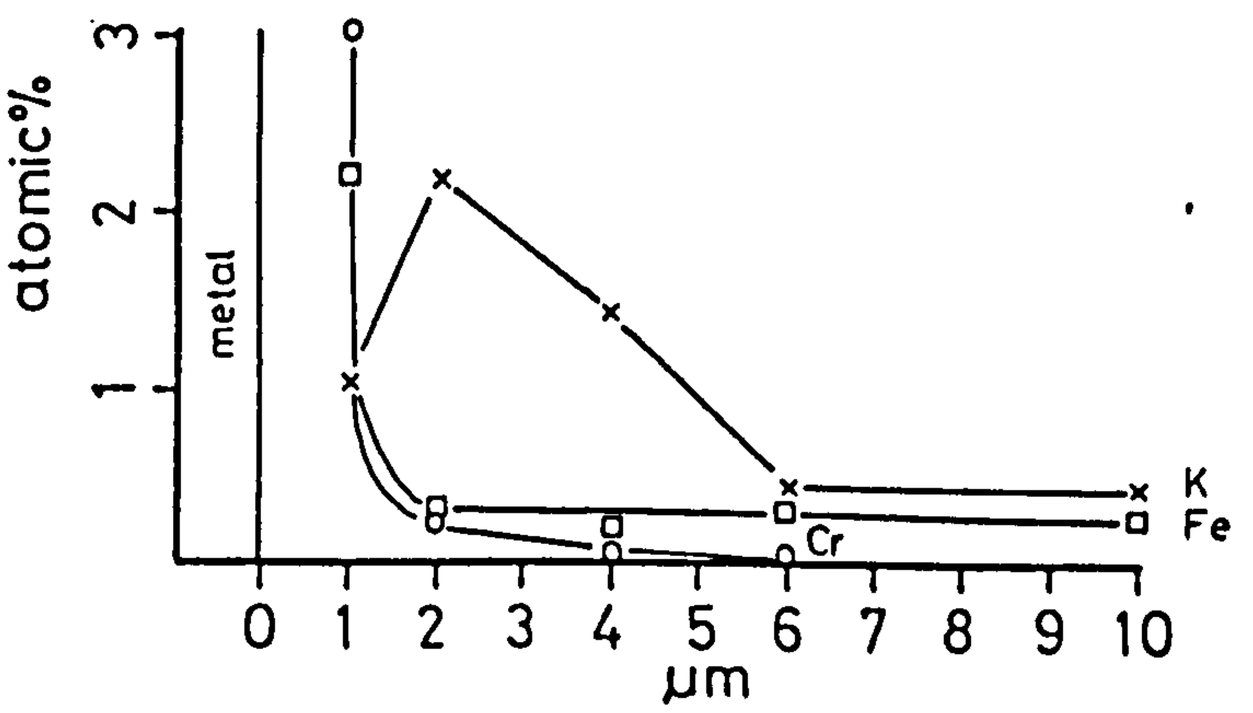

(c) not preoxidised, C20H.

Figure 5.1.19 Quantitative element distributions across the interfaces of coatings on various pretreated chrome-iron substrates.

microstructure. It is not possible to say it variations observed near the interface are due to interactions or local microstructure.

5.1.8 Tensile adhesion of the enamel coatings

The tensile adhesion strength of the enamel coatings was measured using the tensile pull test described in Section 3.1.2. The measured values are listed in Table 5.1.5. The adhesion of the coatings on the various pretreated substrates are described below:-

Preoxidised in wet hydrogen, abraded - C5 and C5H

For the heat-treated coating (C5H) the tensile adhesion strength was measured on several separate occasions as discussed in Section 3.1.2. The mean value of these measurements is 34.5 ±3 MNm^{-2}. If the coating was rapidly cooled after firing (C5) the tensile adhesion is found to be 33.4 ± 8 MNm^{-2}. The adhesion of the coating to the substrate is not noticeably affected by the subsequent crystallisation produced on heat-treatment. It is excellent for both the fired only partially crystallised coating, and the fully crystallised coating.

Failure was similar in both cases. In every measurement only part of the enamel coating was removed. Usually from the central region. In no measurement did the epoxy fail. The exposed coating surface has a black speckled appearance. The exposed substrate is metallic, irregular and with small pieces of enamel coating remaining attached. A backscatter electron micrograph of the exposed coating surface is shown in Figure 5.1.20(a). Two distinct contrast areas are observed. A dark area corresponding to the enamel coating and a

lighter area of high chromium content. Quantitative EDX analysis over a large area of the exposed coating surface containing both contrast features is given in Table 5.1.5. Chromium is present in high concentrations, far in excess of that expected from the saturation level of chromium in the coating. Iron is present in only minor quantities. It appears that chromium oxide is attached to some areas of the removed coating, corresponding to the light contrast areas. Examination of the exposed substrate shows the majority of the surface is metallic with a composition of 13 at% Cr and 87 at% Fe. It is clear from these results that failure is mixed, being partly adhesive and partly cohesive. Failure is occurring by fracture along the chromium oxide-alloy boundary and also within the adjacent coating. Substantial amounts of chromium oxide remains attached to the removed coating.

Preoxidised in wet hydrogen, not abraded - C17H

On omission of abrasion the measured coating adhesion is greatly reduced, with a mean value 19.1 ± 8 MNm^{-2}. The coating is completely removed and the exposed ceramic surface has a smooth light green appearance. The exposed substrate appears metallic and smooth, with no residual coating or chromium oxide remaining. Analysis over a large area of the exposed coating surface detects essentially only chromium, see Table 5.1.5. The chromium oxide layer remains attached to the removed coating. Failure is now adhesive and fracture occurs along the chromium oxide-alloy boundary.

Preoxidised in air, abraded - C18H

Excellent coating adhesion is obtained with a mean value of 53 ± 3 MNm^{-2}. Two of the five measurements failed in the epoxy. The other three showed mixed failure. The coating is only partially removed and small pieces of coating remained attached to the substrate. The exposed coating surface has a green coloration, similar to the oxide on the uncoated metal. Areas of high chromium content are present on the exposed coating as shown in Figure 5.1.20(b). Quantitative EDX analysis over a large area detects a high concentration of chromium, Table 5.1.5. These results indicate chromium oxide is present on the exposed coating surface over intermittent areas. Failure occurs by fracture along the coating-alloy boundary and within the coating.

Preoxidised in air, not abraded - C19H

If abrasion is omitted, the coating adhesion drops to 27 ± 8 MNm^{-2}. The coating is completely removed, exposing a bright metallic substrate surface. The exposed ceramic has a uniform backscatter contrast. Quantitative EDX analysis indicates a high chromium content. Failure is now adhesive with fracture occuring along the coating-alloy boundary.

No preoxidation, abraded - C20H

Excellent coating adhesion was measured, with a mean value of 54 ± 8 MNm^{-2}. Three measurements failed in the epoxy. The other two showed mixed failure with only partial removal of the coating. The

exposed surface again has a green coloration with two contrast areas observed in backscatter imaging, Figure 5.1.20(c). The bright areas have a high chromium content. Quantitative EDX analysis over a large surface area, detects a high concentration of chromium. Failure occurs by fracture along the coating-alloy boundary and within the coating.

No preoxidation, not abraded - C21H

On omission of abrasion the coating adhesion again drops markedly to a mean value of 17 ± 8 MNm^{-2}. The coating is completely removed. Adhesive failure occurs, with fracture along the coating-alloy boundary. A high chromium concentration is detected on the exposed coating surface. This surface had a uniform backscatter contrast.

Coating adhesion is seen to be critically dependent on the initial abrasion with alumina grit. It is not influenced by the subsequent preoxidation. Good adhesion is related to failure being mixed with the fracture path travelling along the coating-alloy or chromium oxide-alloy boundary and also through the adjacent coating.

A discrete chromium oxide layer can be identified only at the interface for a coated substrate preoxidised in wet hydrogen. There is strong evidence that crystalline chromium oxide is also present at the interfaces of the other coatings. Quantitative EDX analysis detects significant concentrations of chromium on the fracture surface of the removed coating. The very low saturation concentrations precludes the high level of chromium being due to that incorporated into the adjacent coating. It must be a result of chromium oxide or a high chromium containing phase at the interface. This phase corresponds to the bright contrast dispersed phase shown in the electron micrographs of the coating-substrate interfaces.

Figure 5.1.20 Backscattered electron micrographs of exposed coating surfaces,

a

40 µm

preoxidised in
wet hydrogen
C5H

b

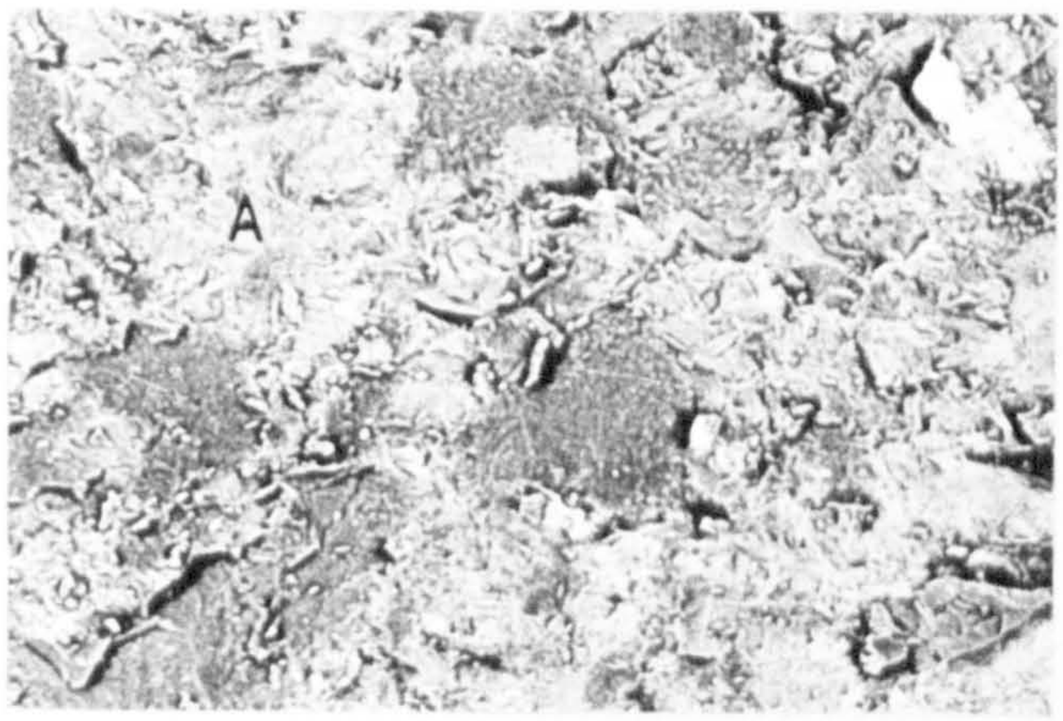

40 µm

preoxidised in
air
C18H

c

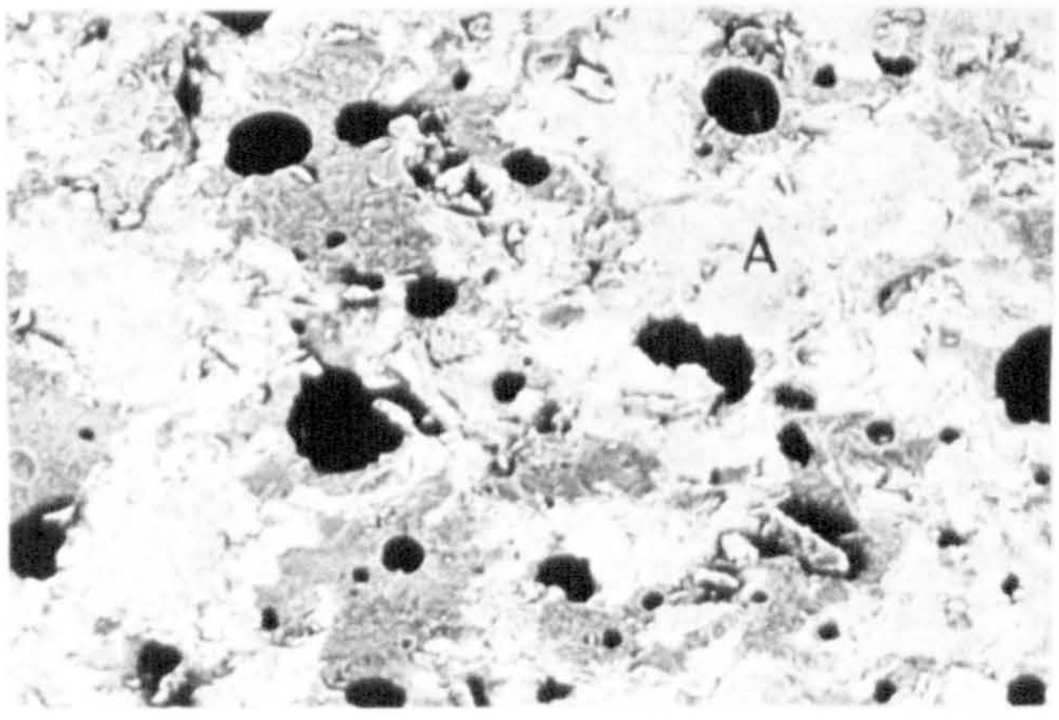

40 µm

not
preoxidised
C20H

A-chromium rich region

5.2 Coatings on mild steel

5.2.1 Wetting ability of glass B on mild steel

The wetting of mild steel by glass B is dependent on the degree of preoxidation and firing conditions. A series of experiments were undertaken to establish the requirements for good wetting.

Some coated, but unfired, mild steel substrates were preoxidised at 500°C for 15 minutes in air. These were then fired using temperatures ranging from 915° to 990°C for a time of 5 minutes in an atmosphere of oxygen free nitrogen. This was followed by quenching on a steel plate. The appearance of the enamel coatings are listed in Table 5.2.1. Between 945 to 955°C the glass has fused and appears to wet the substrate with a low contact angle. However the viscosity is too high for the fused enamel to flow. At a temperature of 960°C or above wetting does not occur although viscosity has decreased sufficiently for flow to be possible. The glass either moves to the periphery or draws up to a hemispherical half bead.

The preoxidation was then altered. Temperatures of 600, 650 and 700°C were used for times of 5, 15 and 30 minutes. Firing was conducted at 965-970°C for 5 minutes under an oxygen free nitrogen atmosphere. Table 5.2.2 lists the appearance of the coatings. For a preoxidation of 15 minutes at 650°C and all times at 700°C the coating has fully fused, flowed and wetted the substrate.

It is important for the enamel coating to flow and wet the substrate surface. The "standard" enamelling procedure adopted to achieve this is:-

- Preoxidise in air, a mild steel substrate coated with the glass powder, for 15 minutes at 650°C.

Table 5.2.1: Influence of Preoxidation.

Preoxidation: 5 minutes at 500°C

Firing time: 5 minutes

Removal temperature °C	Appearance
915	Powdery, dull, good wetting
928	" " "
930	" " "
946	Partially fused, dull, good wetting
947	Fused, dull, good wetting
955	" " "
965	Fused, shiney, non-spreading
985	" " "
990	" " "

Table 5.2.2: Influence of preoxidation

Firing: 5 minutes at 965°C

Preoxidation		Appearance
minutes	°C	
5	600	Fused, shiney, non-spreading
15	600	" " "
30	600	" " "
5	650	" " "
15	650	Fused, shiney, good wetting
30	650	" " "
5	700	" " "
15	700	" " "
30	700	" " "

- Fire at 965-970°C for 5 minutes in an oxygen free nitrogen atmosphere (M9).
- Heat-treat (if required) at 580°C for 1 hour followed by 820°C for 3 hours, in an oxygen free nitrogen atmosphere (M9H).

The preoxidation used, described above, enabled wetting and spreading with the least amount of iron oxide formed during preoxidation. This minimises the residual iron oxide present at the fired enamel coating-mild steel interface. For an uncoated mild steel substrate the preoxidation above results in 8.24 mg $\bar{cm}^2$ (or 14µm $\bar{cm}^2$) of iron oxide (Equation 4.1), assuming only ferrous oxide is formed.

After firing, the quenched enamel coating is seen to be fully fused, smooth and shiney. It has a deep blue colouration. See Figure 5.2.1(a). On completing a heat-treatment the enamel coating acquires a dull white appearance. The outer edge is light brown, Figure 5.2.1(b).

5.2.2 Enamel coating on mild steel quenched after firing

Microstructure:

The interface region of an enamel coating quenched after the "standard" firing condition (M9) is shown in Figure 5.2.2. Complete fusion has occurred to produce a continuous coating with a thickness of 180µm. The interface between the coating and mild steel has a smooth, well defined boundary. Isolated pockets of iron oxide exist along the interface. They represent the remains of the initial preoxidised iron oxide layer. An additional phase has grown dendritically from the mild steel-coating and iron oxide-coating

a

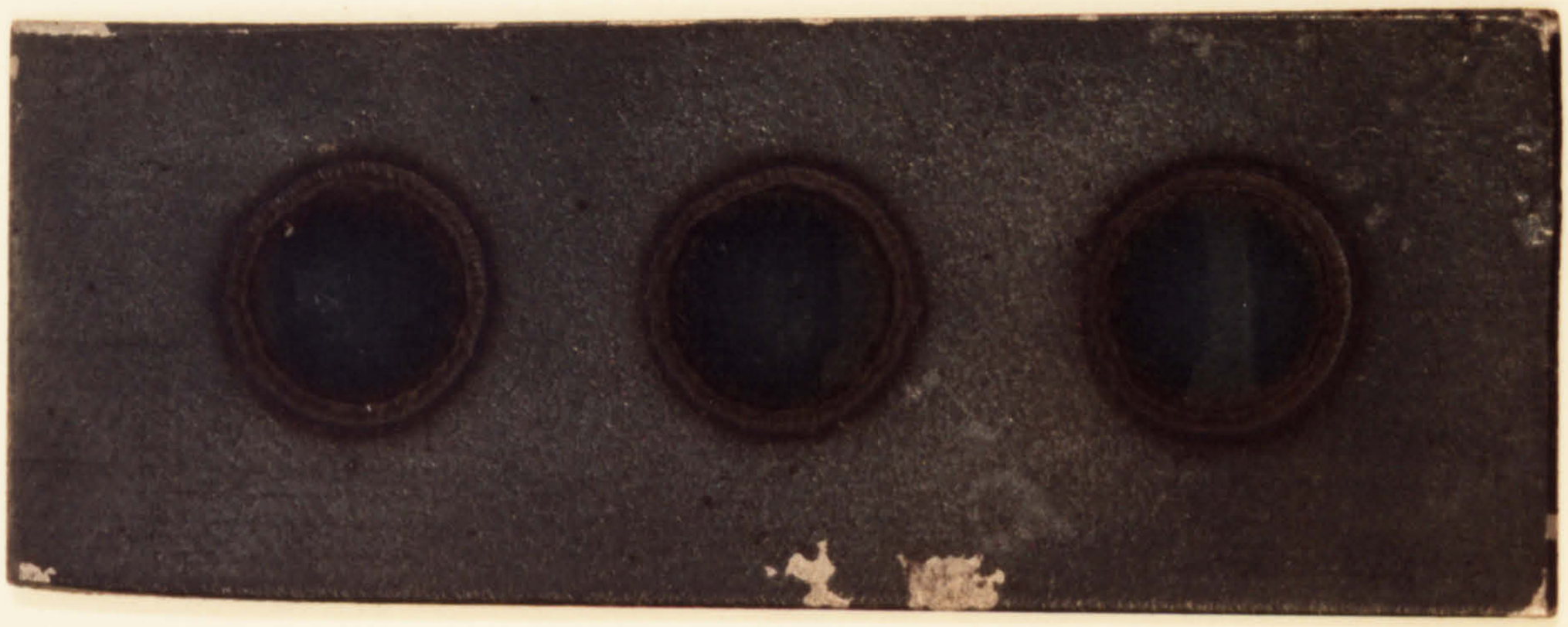

b

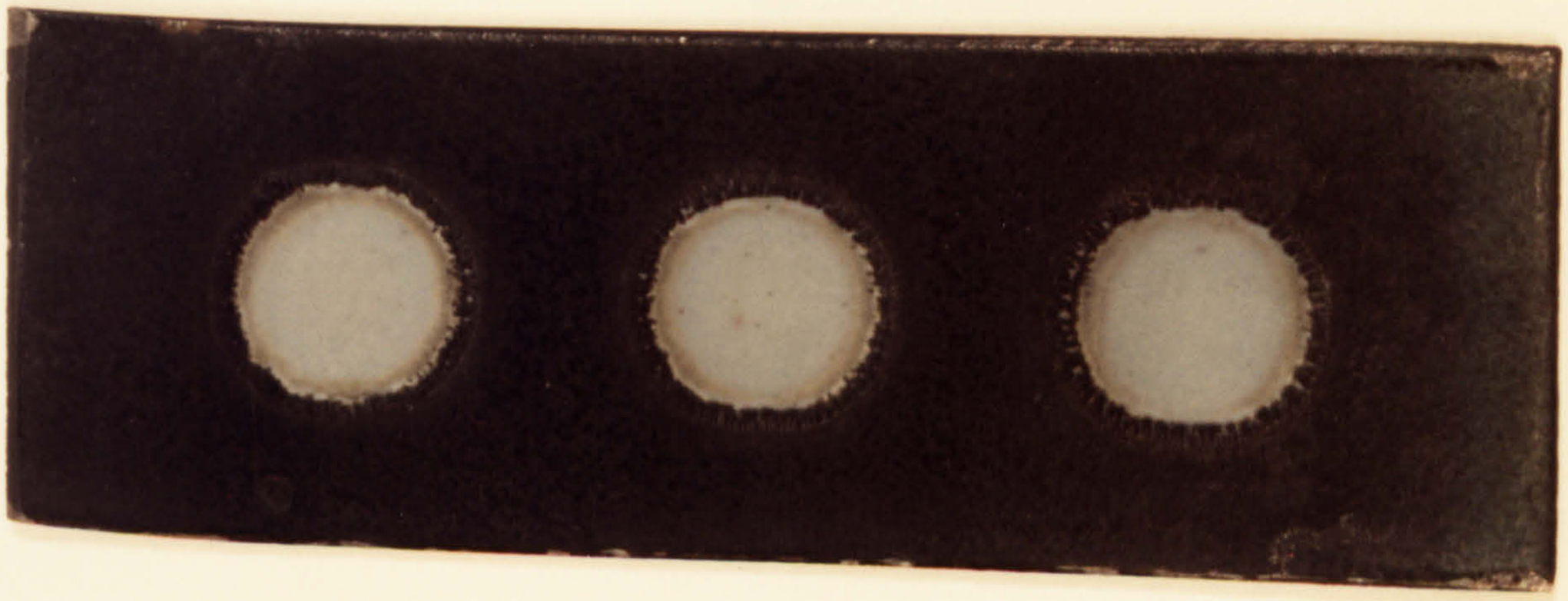

Figure 5.2.1 Appearance of coating on mild steel.

(a) fired only coating

(b) heat-treated coating.

Figure 5.2.2 Backscattered electron micrographs of a coating on mild steel subjected to a firing only, M9.

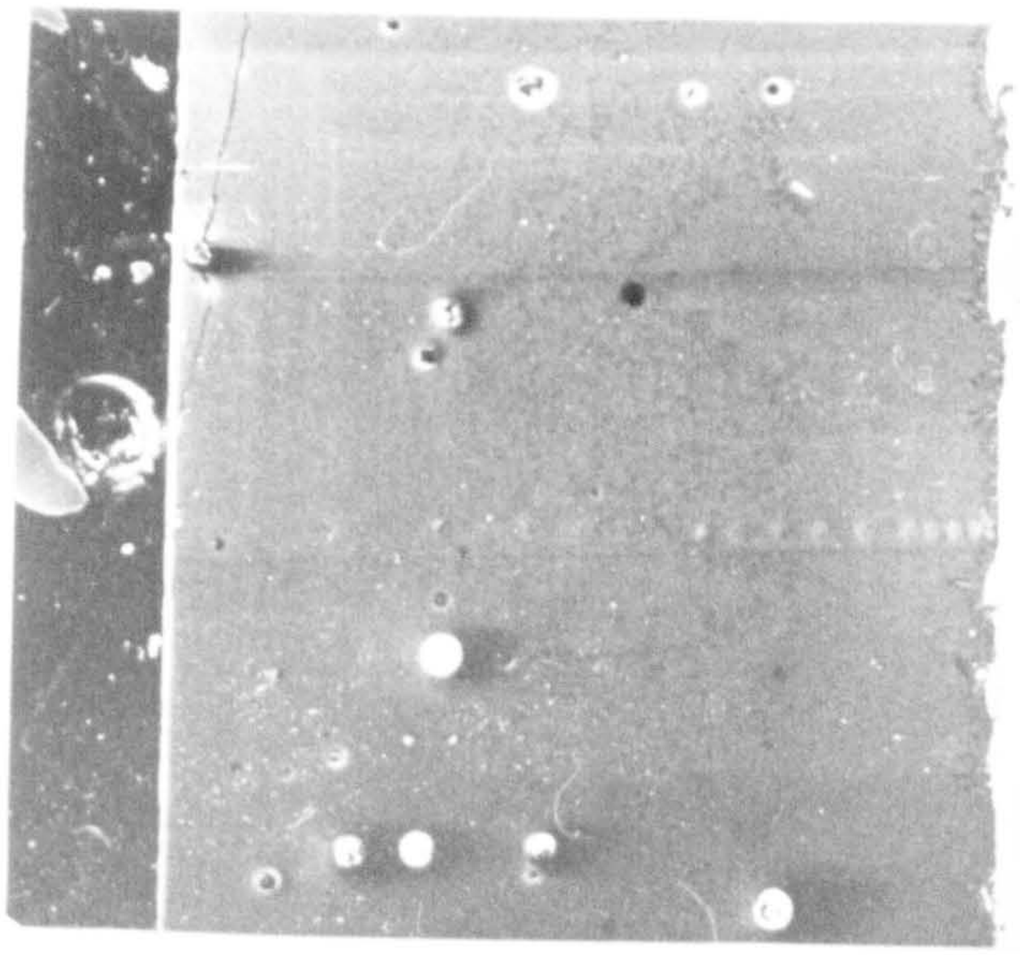

40 µm

coating

mild steel

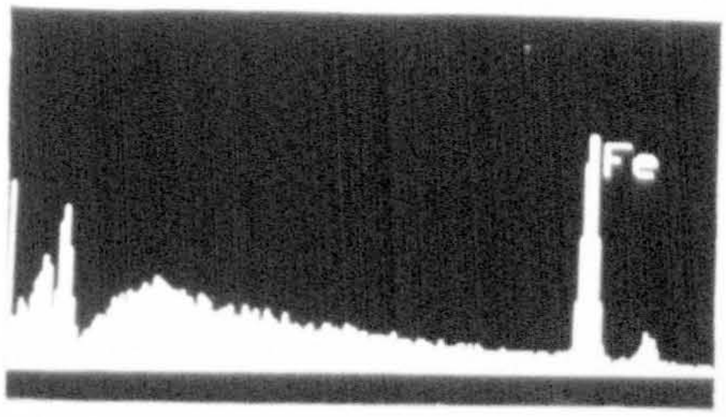

A substrate

quartz

glassy region

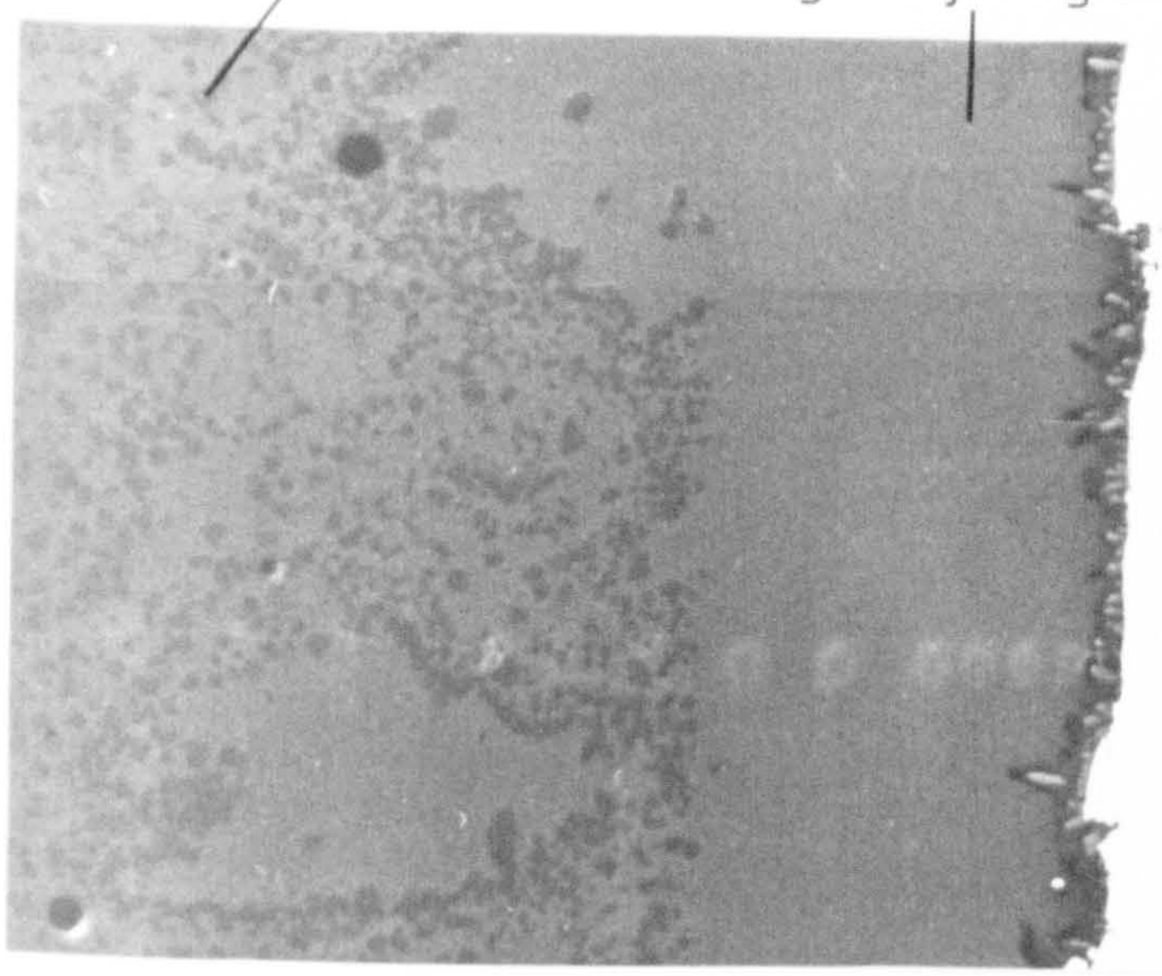

20 µm

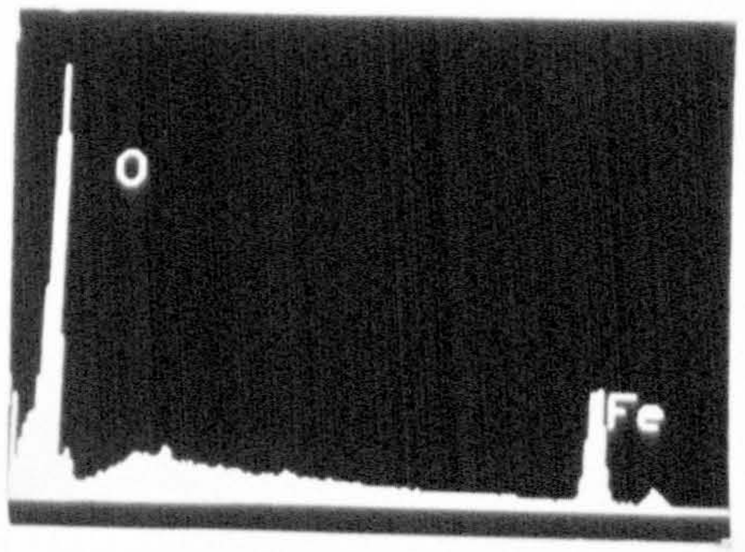

B ferrous oxide

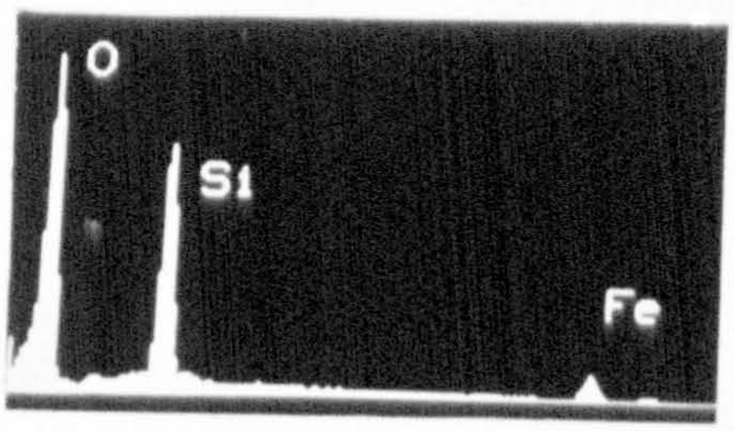

C dendrite

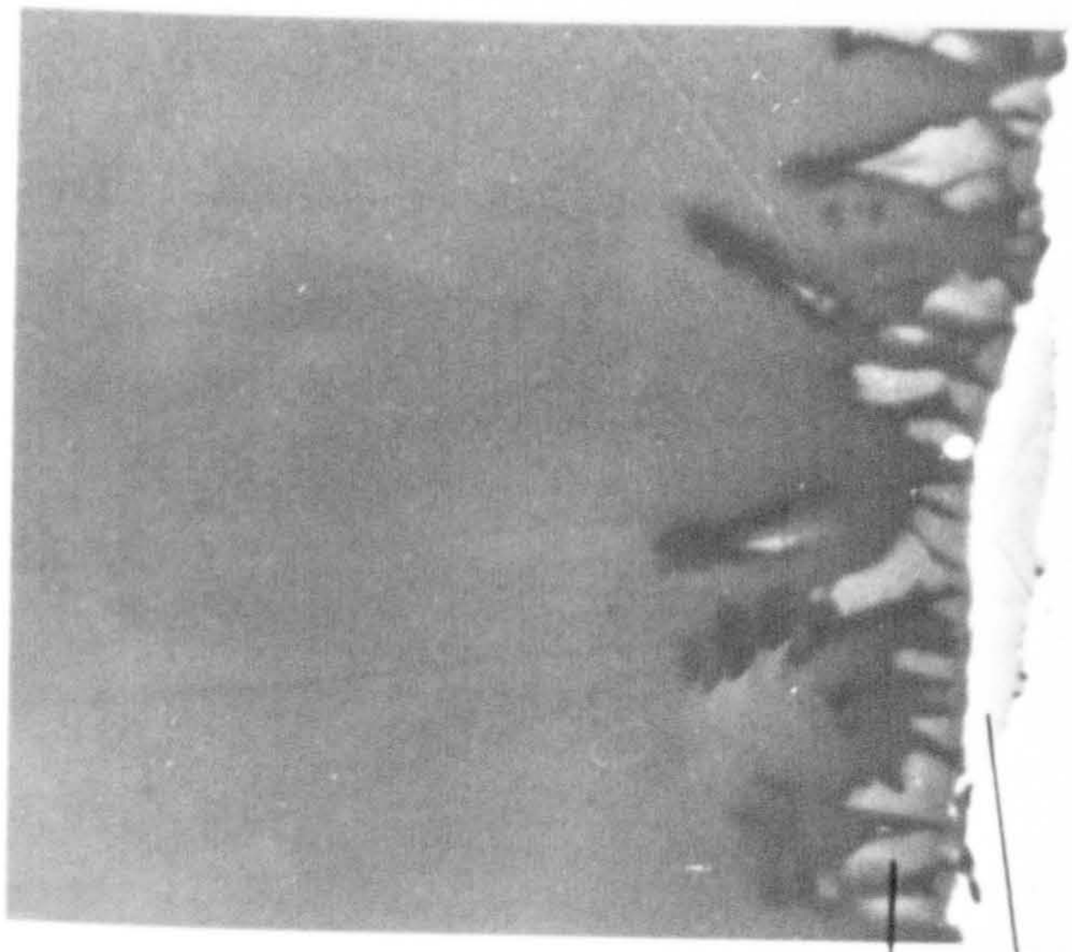

4 µm

C B A

boundary. It extends 5μm into the coating. Quantitative EDX analysis with the detector window in place shows the dendrite phase to consist of iron, zinc and silicon. Table 5.2.3 gives the normalised at% concentrations of the detectable elements. The backscatter contrast of the dendrite is darker than the residual iron oxide. This suggests it is a complex oxide. As shown latter the dendrite is a lithium-iron-zinc-silicate. The dendrite tip is of a darker backscatter contrast, consistent with it being deficient in iron and zinc.

An inhomogeneous bulk microstructure exists. Only one crystal phase is visible when using backscatter electron contrast. Etching in hydrofluoric acid does not reveal a second phase. At 40μm a boundary parallel to the interface is noticeable. There is a region extending from 40μm to the interface where this crystal phase is absent. The X-ray diffraction pattern at a coating ground to a powder is shown in Figure 5.2.3(a). Only β-quartz is present, identified as the crystal phase in the bulk enamel coating.

The coating was completely removed and the exposed coating surface examined by x-ray diffraction. A single peak at 42.2° 2θ is present, Figure 5.2.4(a). This corresponds to a d-spacing at 2.14 Å.

Table 5.2.3: Composition of dendrite phase
(excluding Li and O)

Region	Element at% (±0.1%)					
	Al	Si	P	K	Zn	Fe
Dendrite body	2.6	50.3	2.1	0.6	3.7	40.6
Dendrite tip	4.1	73.1	1.6	1.6	1.4	18.1
Adjacent glass	5.2	67.3	1.4	1.2	1.2	23.6

detectable elements only

x-ray patterns were also collected from an uncoated substrate fired as above and a ferrous oxide disc. The ferrous oxide disc was prepared as described in Section 4.3. The peaks are listed in Table 5.2.4 along with those given by the J.C.P.D.S. file for Wustite (file number 6-615).

The nature of the residual iron oxide needs to be established to interpret the x-ray data. On oxidising mild steel at 650°C ferrous oxide would be expected to form, (Section 4.2.2). On cooling to room temperature the oxide appears as a mixture of Wustite (FeO) and magnetite (Fe_3O_4). During firing this oxide may transform to mostly wustite, the stable high temperature form. Analysis by windowless quantitative EDX gives a composition of $Fe_{0.9}O$ for the residual iron oxide.

It was assumed that the residual iron oxide was exclusively wustite. The single x-ray peak for the exposed coating surface corresponds to the (200) plane of wustite. Absence of the other peaks can be explained if the iron oxide is showing a strong preferred orientation. The (200) plane of the residual oxide is aligned parallel to the interface.

Element distribution:

The profiles of the detectable elements were determined by conducting line scans across the interface. These are displayed in Figure 5.2.5(a) and described below:

- aluminium and phosphorus remain essentially constant in the coating then drop rapidly to back ground at the interface.

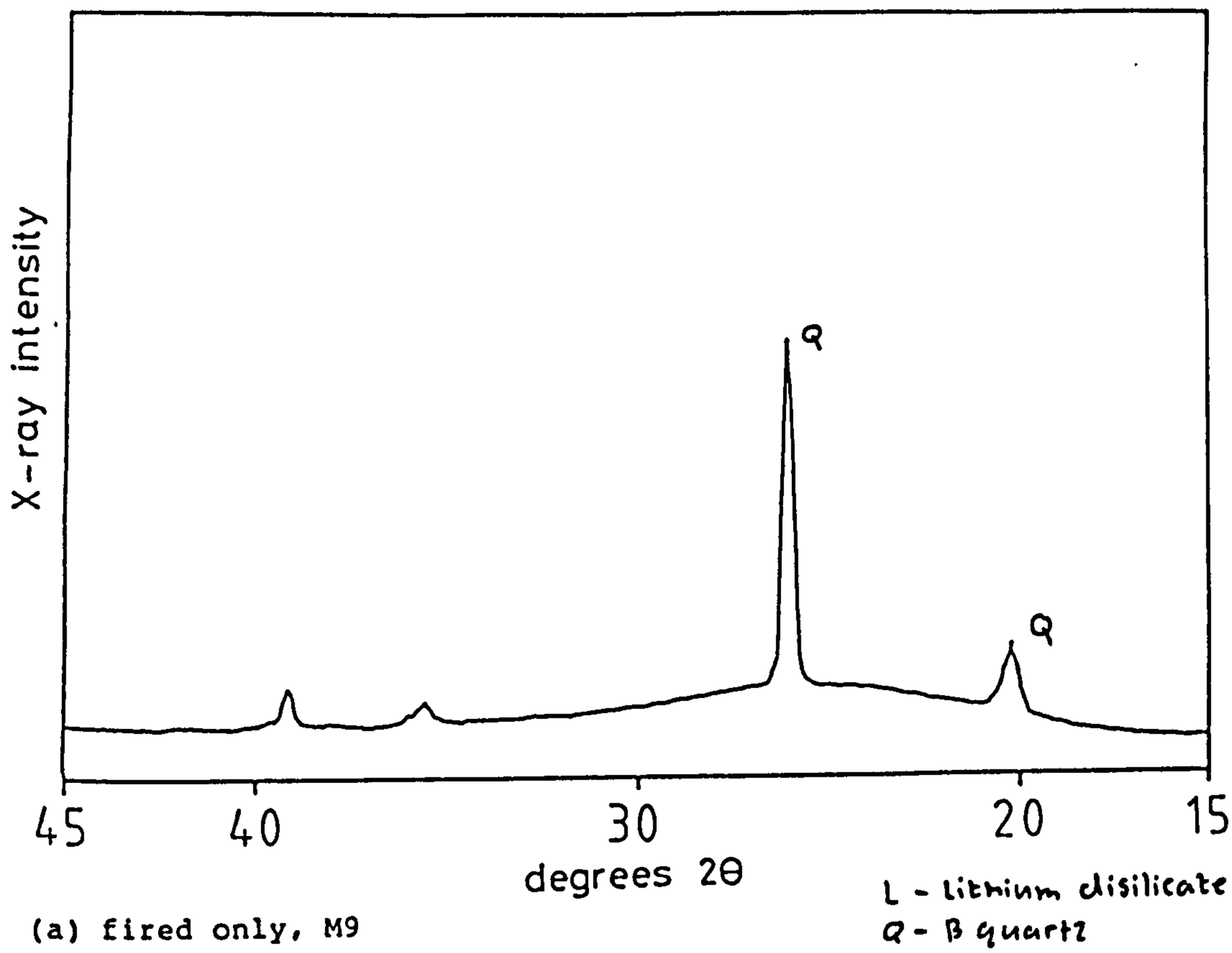

(a) fired only, M9

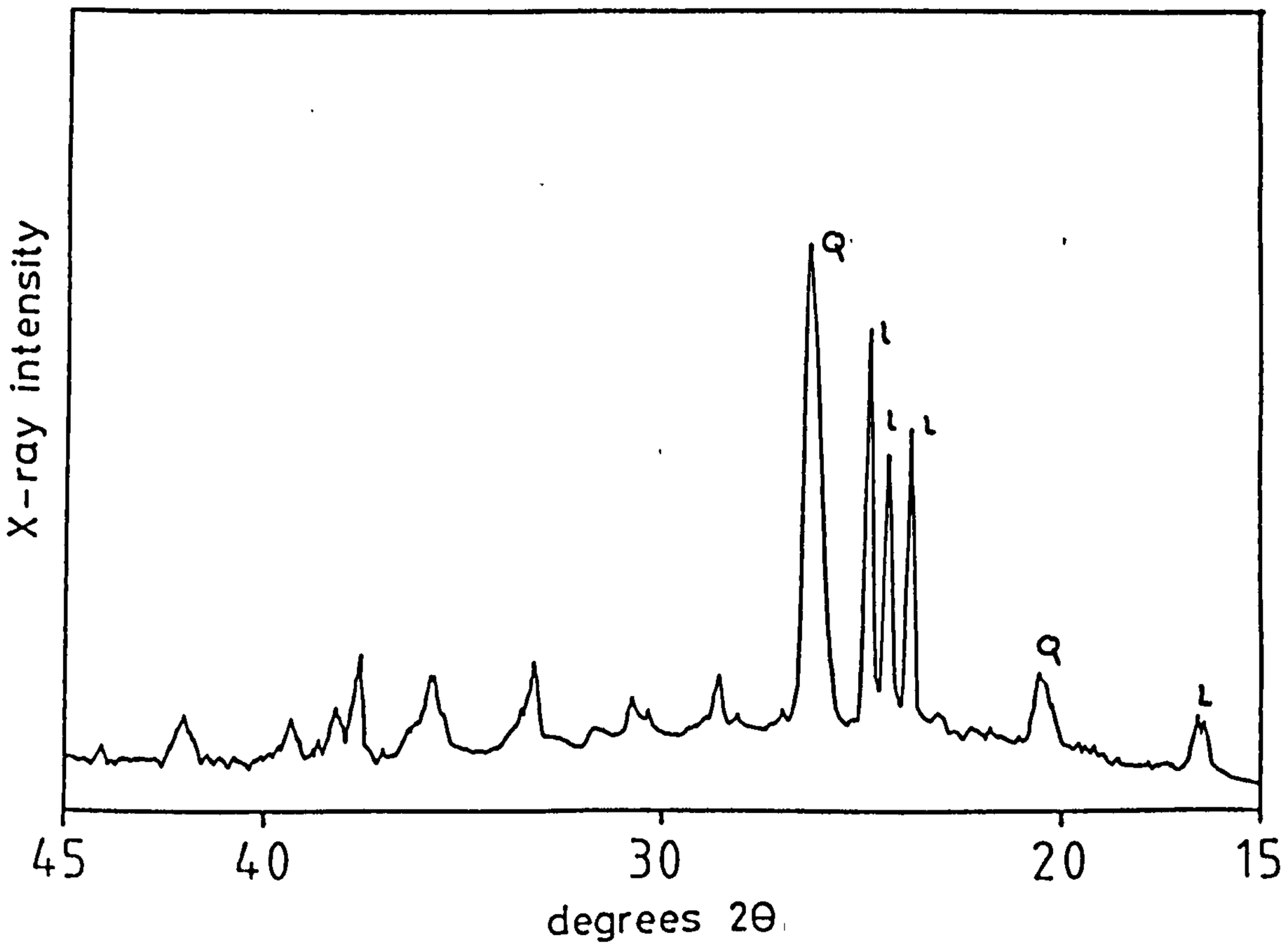

(b) heat-treated, M9H.

Figure 5.2.3 XRD patterns collected from removed coating.

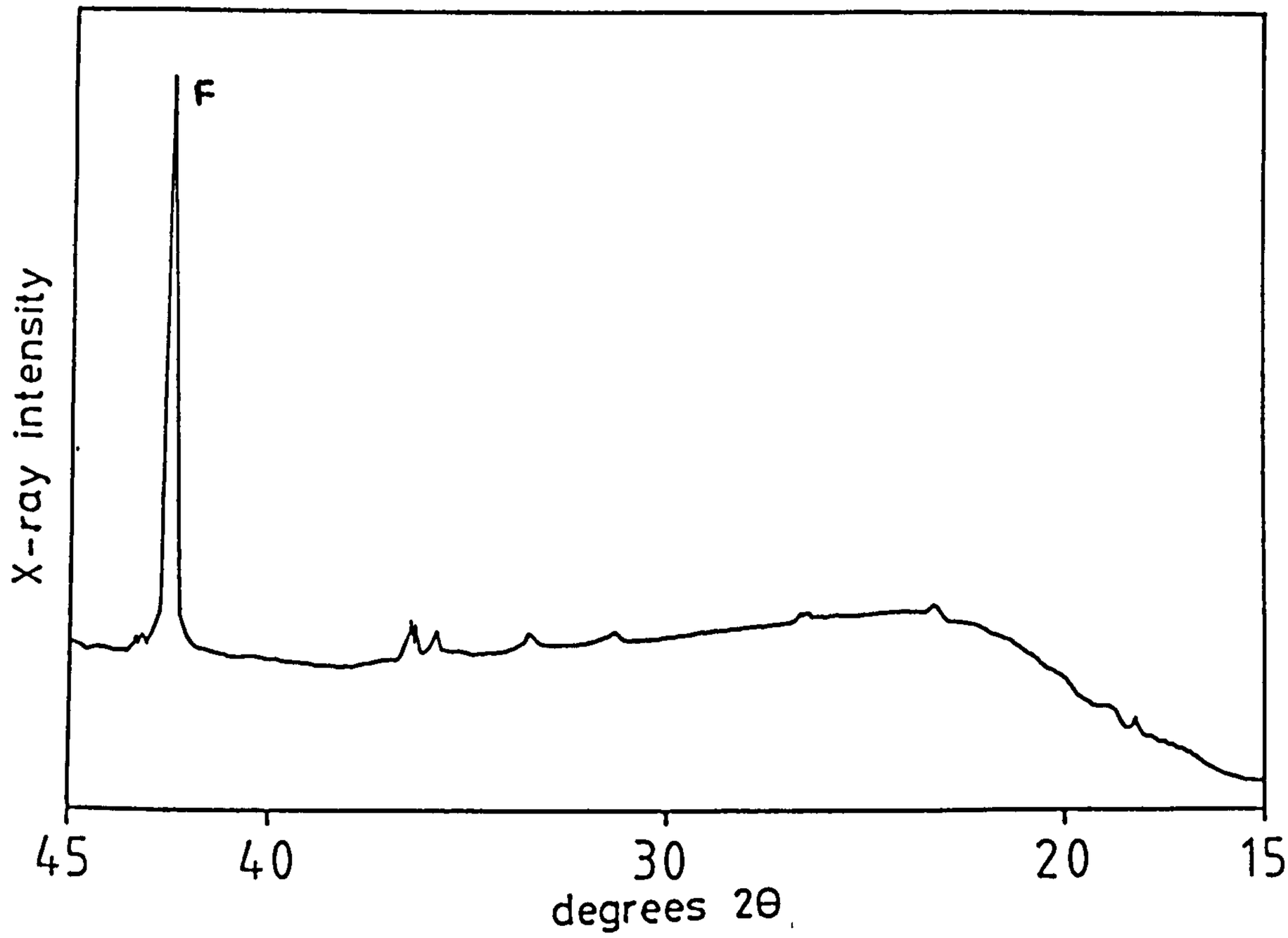

(a) fired only coating, M9.

F. ferrous oxide

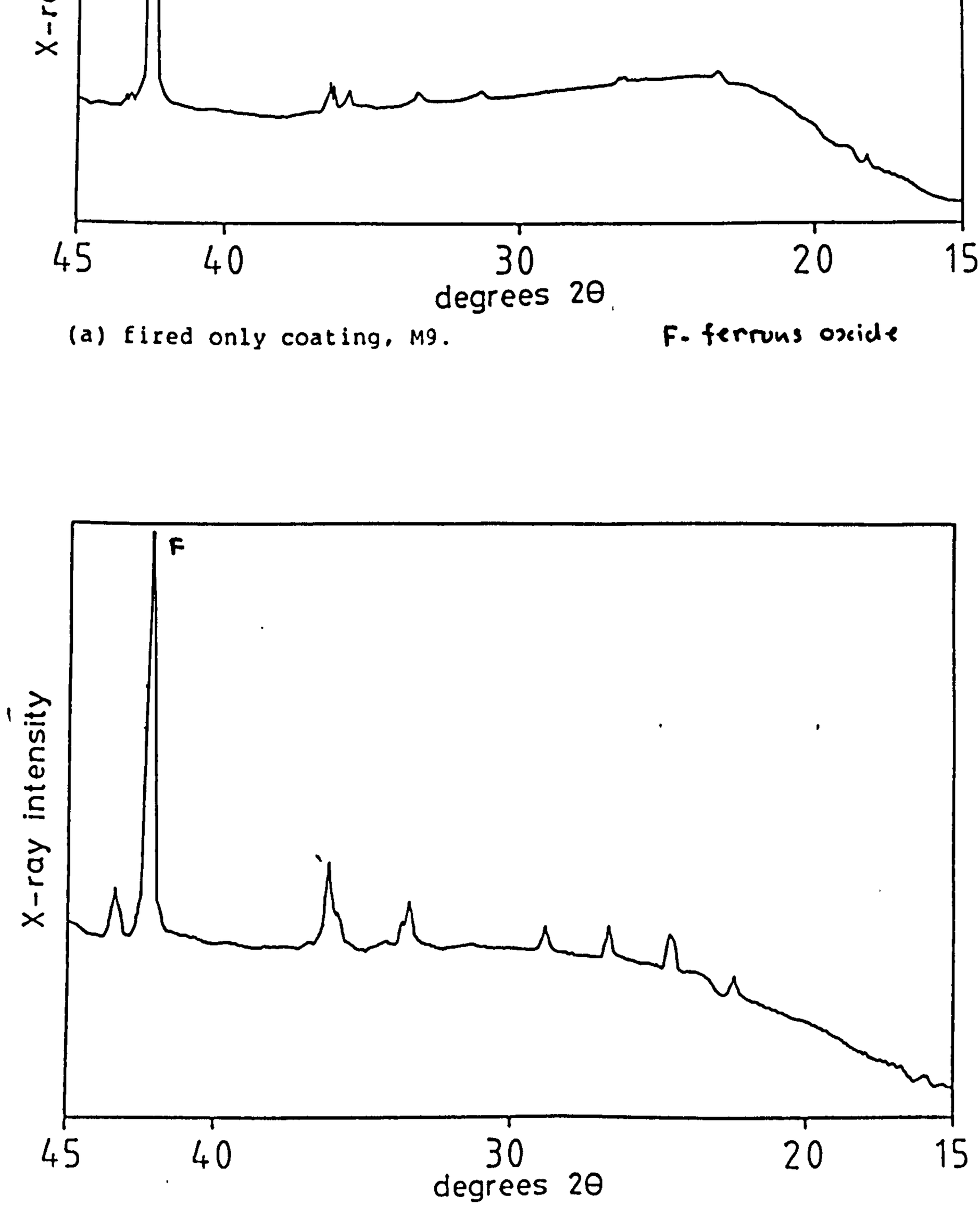

(b) heat-treated coating, M9H.

Figure 5.2.4 XRD patterns collected from the exposed coating surface,

- Silicon decreases on approaching the interface, but shows a slight peak at about 5μm. It then drops rapidly to background at the coating-iron oxide or coating-mild steel boundary.

Table 5.2.4: XRD Patterns

Sample	2θ	d(A)	I/I_o	
Exposed ceramic surface	42.2	2.14	100	
Uncoated substrate, pre-	35.5	2.53	38	
oxidised and fired under	42.0	2.15	100	
standard conditions	(43.1	2.08	29 α-Fe)	
Ferrous oxide disk	36.2	2.48	80	
	42.0	2.15	100	
				hkl
Wustite	36.0	2.49	80	111
J.C.P.D.S file	42.0	2.15	100	200
6-615	60.76	1.523	60	220
	72.73	1.299	25	311

- Iron shows considerable diffusion into the coating, extending to at least 100μm. A dip is seen at the interface associated with the tip of the dendritic phase. The level increases at the interface, to reach a value corresponding to the mild steel. Close to the maximum level a slight plateau is observed. This is where the profile crosses an iron oxide pocket.

- Zinc is barely resolved from background in the bulk coating. It

exhibits a peak at the interface in the region where the dendritic phase is present.

- Potassium shows a reduction in concentration. It starts at about 40μm and has dropped to background levels at the interface.

To evaluate the element concentrations in the adjacent coating a full quantitative EDX analysis was performed. The presence of lithium is accounted for by assuming a constant Li/Si ratio of 0.630, (the bulk glass B composition). Concentration profiles of silicon, iron and potassium are given in figure 5.2.6. They are summarised below:-

- Iron attains a concentration of 7.6 at% Fe (25 wt% FeO) adjacent the interface. It remains at this level to a distance of 20 μm into the coating. The concentration drops gradually to reach 4 at% Fe (15 wt% FeO) when β-quartz firsts appears. Iron is still present close to the outer coating surface at a concentration of 0.5 at% Fe (1.5 Wt% FeO).

- Potassium shows the expected concentration in the coating bulk. On reaching 40 μm the level drops to 0.4 at% K (or 1 Wt% K_2O) and remains at this level up to the interface.

During firing a loss of potassium appears to occur in the area adjacent to the interface extending to 40 μm. This coinsides with the region where crystallisation is absent.

These results do not provide information on the lithium distribution. Lithium would be expected to be highly mobile at the

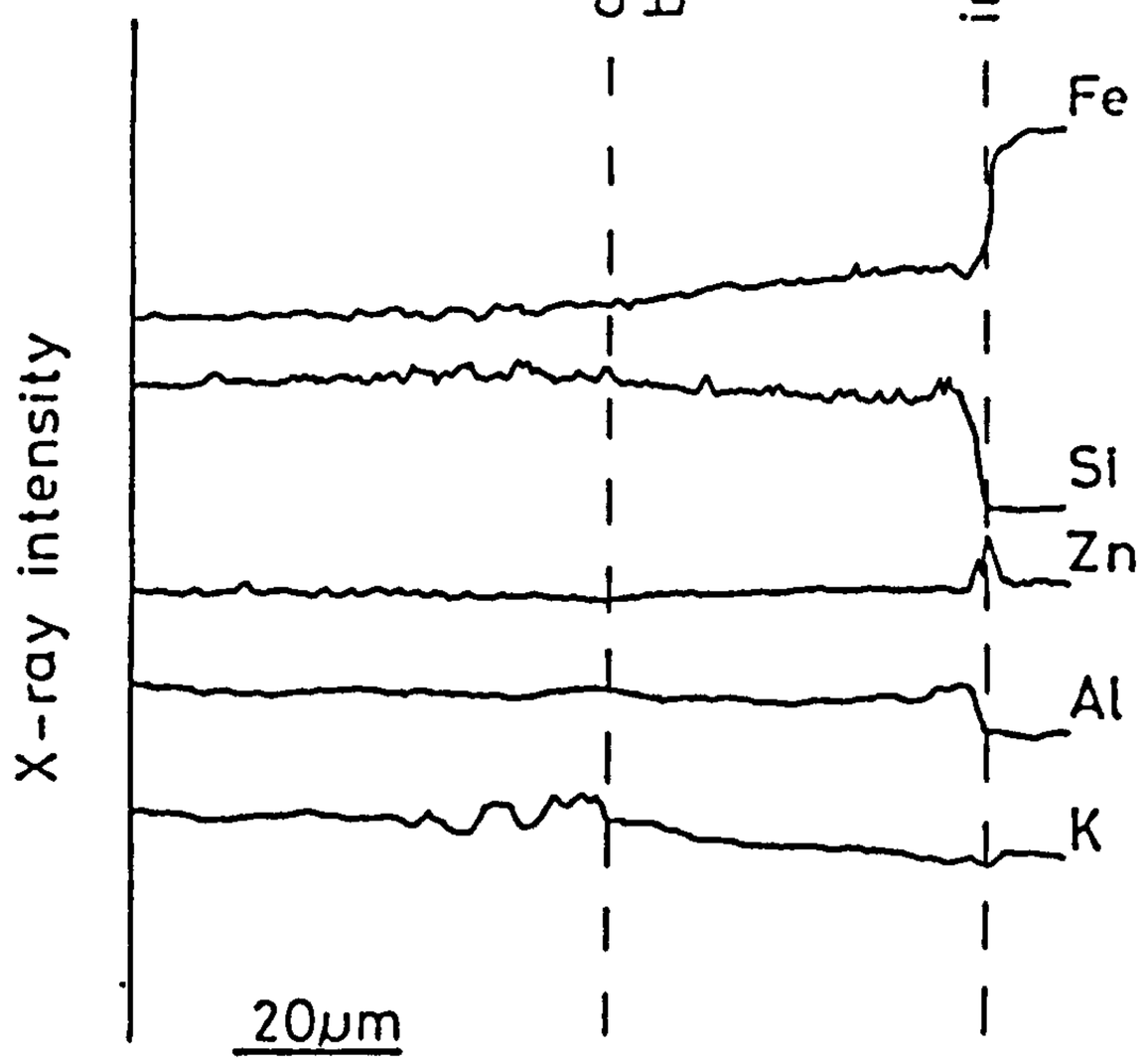

(a) fired only, M9

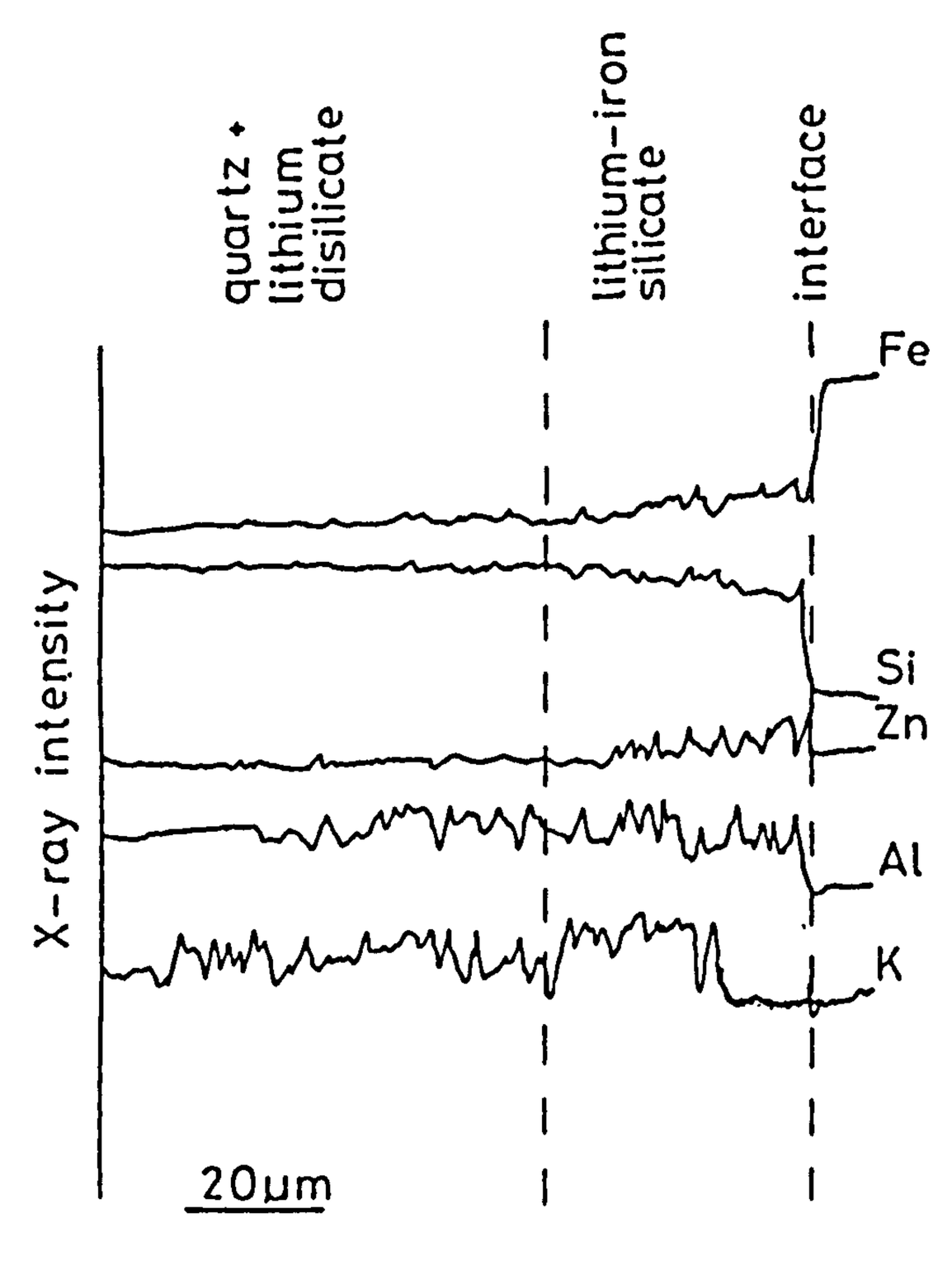

(b) heat-treated, M9H.

Figure 5.2.5 Element distribution collected from line scans conducted across the interface.

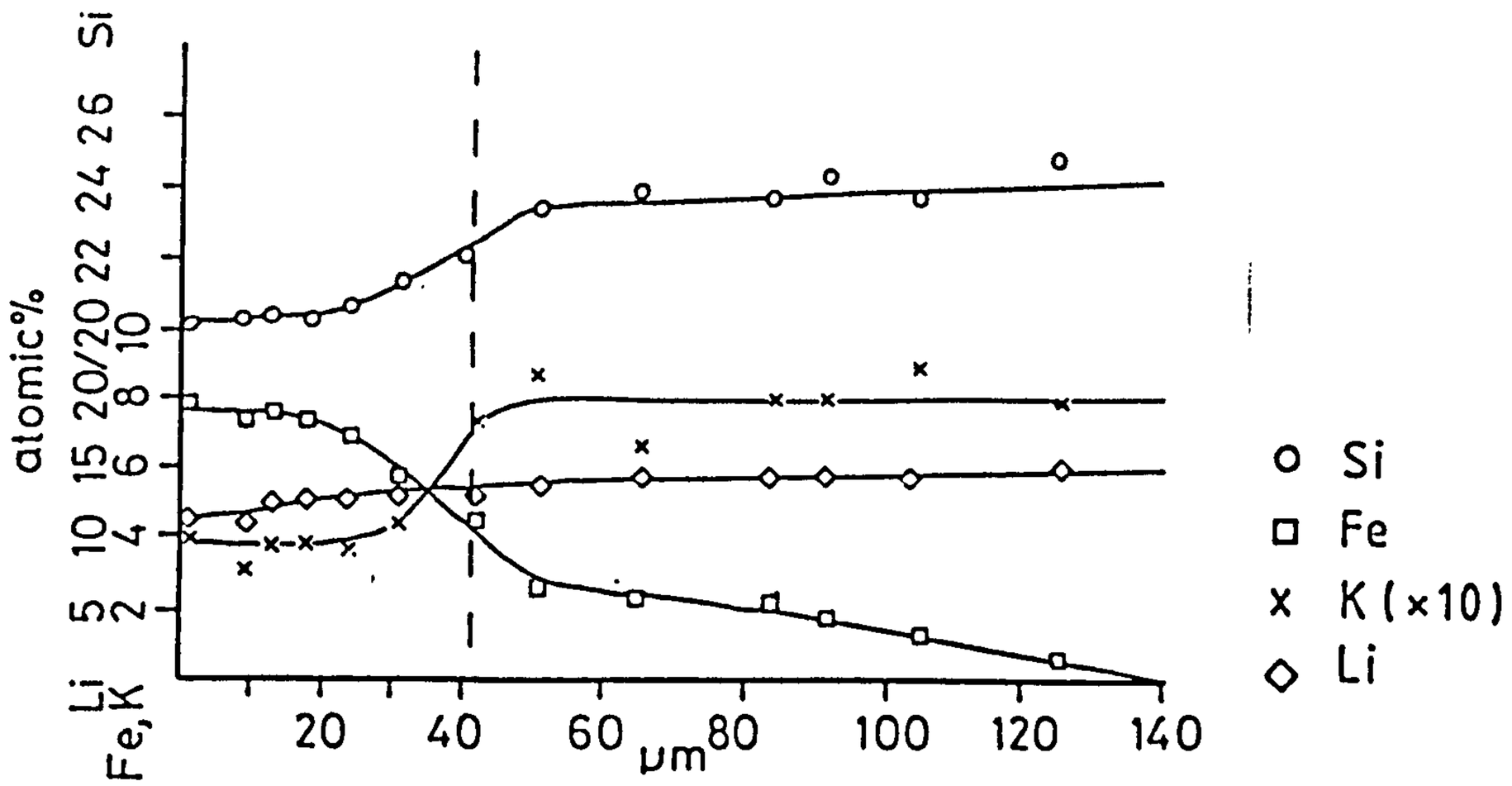

Figure 5.2.6 Quantitative element distribution across the interface of a fired only coating, M9.

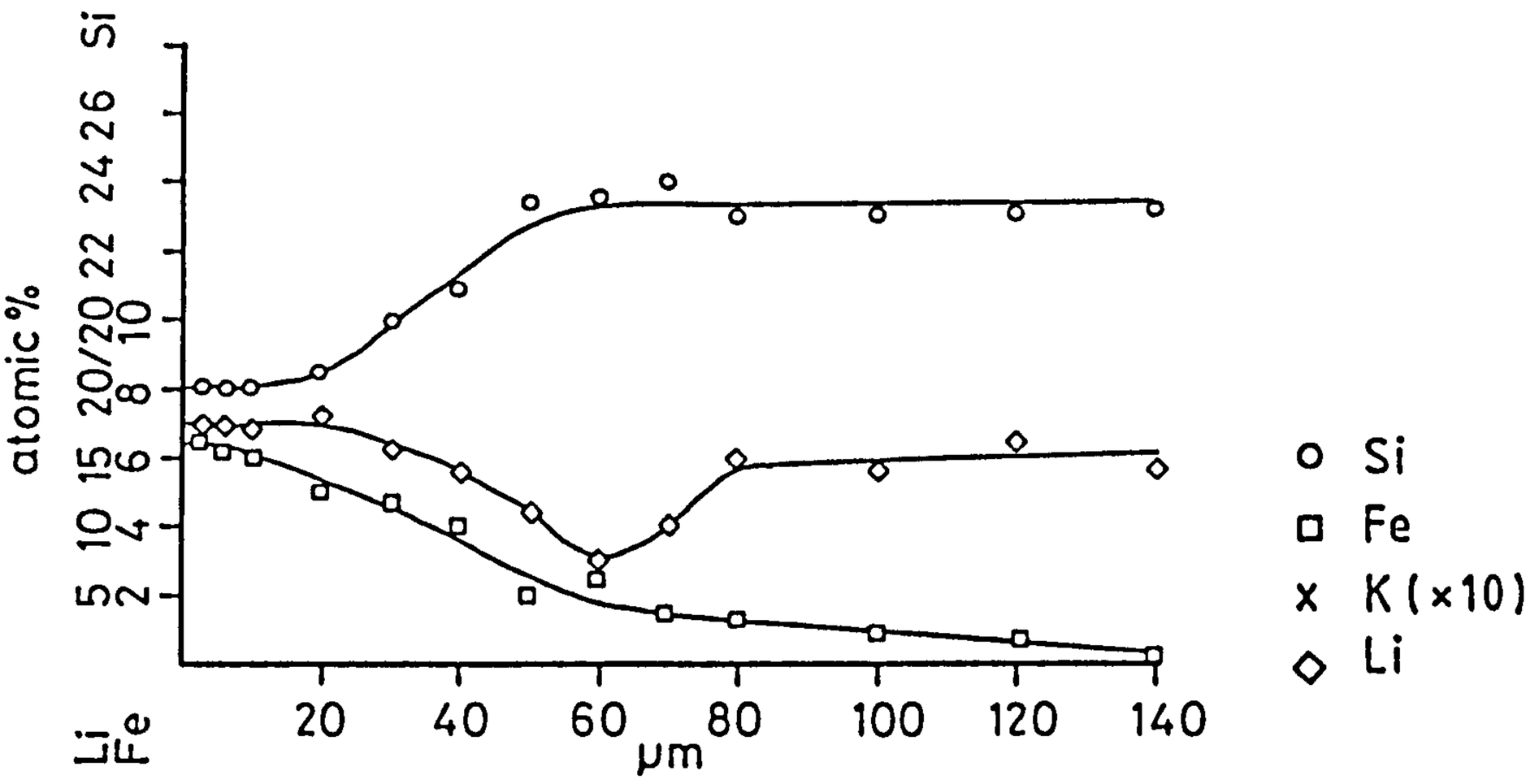

(a) "windowless" EDX

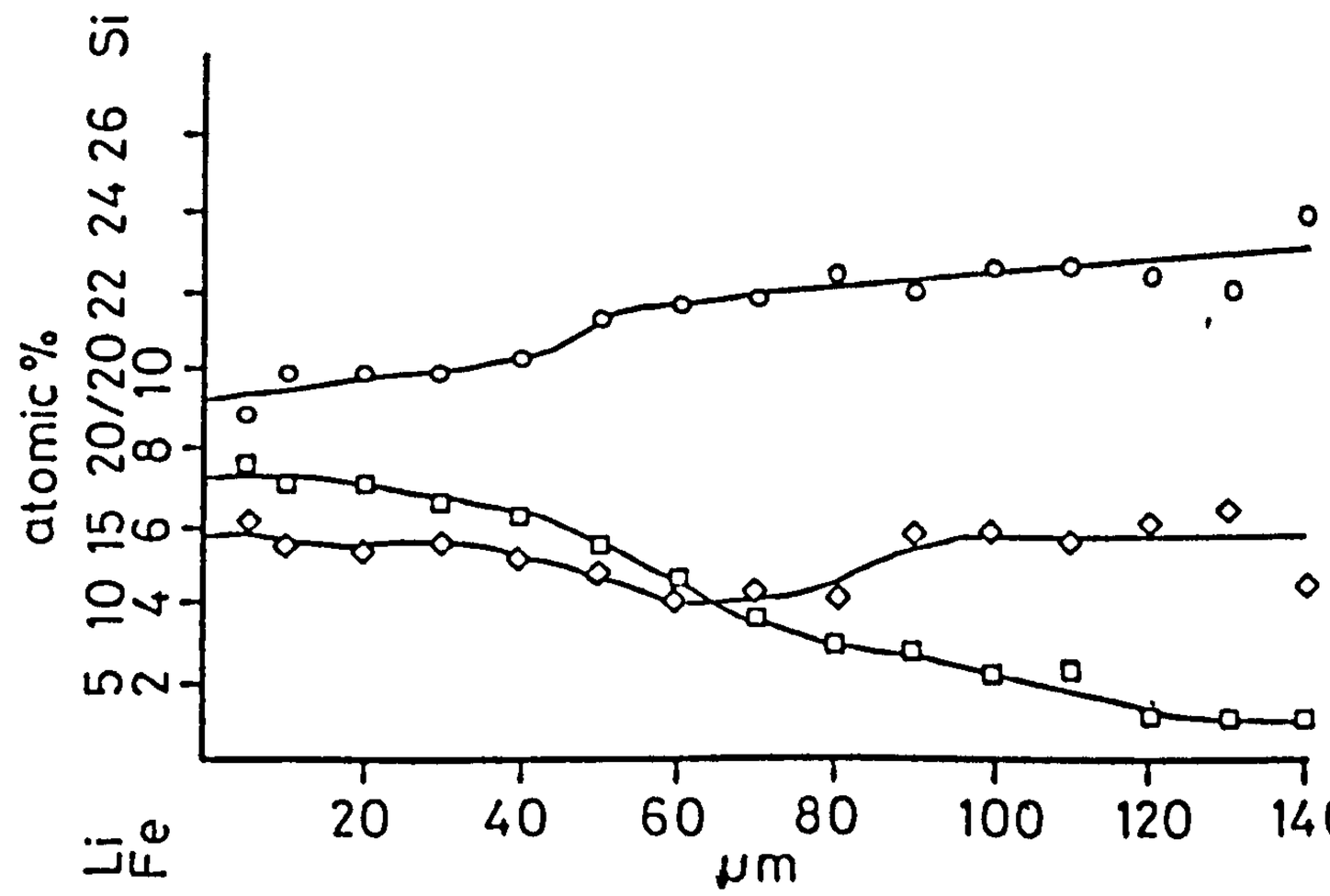

(b) L.I.M.A.

Figure 5.2.7 Quantitative element distribution across the interface of a fired only coating, M9.

firing temperature. An attempt was made to infer the lithium distribution by windowless quantitative EDX analysis. This is described in Section 3.2.8. The use of a constant ratio of the minor elements to silicon to estimate their concentration seems a reasonable assumption. Table 5.2.5 lists the determined element concentrations at various distances from the interface. The iron concentration and its associated oxygen has been subtracted. Within experimental scatter and noting the loss of potassium the minor elements maintain constant concentrations.

Knowledge of the iron valency is essential. A spectroscopic thiocyanate analytical technique for determining the Fe^{2+} and Fe^{3+} ratio is described in appendix 4. The Fe^{2+} concentration is measured at 83% of the total iron content. This result together with the deep blue colouration of the enamel suggest iron is present essentially as Fe^{2+}. Approximating the total iron detected by windowless EDX analysis to be Fe^{2+} a lithium profile can be calculated from the need to maintain charge neutrality. The profile is shown in Figure 5.2.7(a). This should be compared with Figure 5.2.6. The lithium concentration at the interface, predicted using a constant Li/Si ratio, is 10 at% Li. But that obtained from charge neutrality is 17 at% Li. Lithium appears to show an increased concentration in the interface region, with a dip at 60 μm. Similar results are obtained for the other coatings M16 and M17.

Clearly many faults can be found in such an indirect method. An alternative technique was sought which could measure the lithium concentration directly. Laser induced mass spectroscopic analysis (LIMA) was used. This is described in Appendix 4. The resulting lithium profile is shown in Figure 5.2.7(b). It appears to substantiate the increase of lithium in the interface region. The

limited accuracy of both techniques do not allow a full quantitative determination of its extent. The dissolution of iron oxide appears not to be a simple solution by the glass but also involves an interdiffusion between iron oxide (FeO) and lithium oxide (Li_2O).

Table 5.2.5: Measured concentration after removal of iron (excluding Li and O)

Regions	Element at% (±0.1%)				
µm	Al	Si	P	K	Zn
1-11	6.3	88.9	1.6	2.3	1.8
14-27	6.6	85.6	2.2	2.4	2.9
32-41	5.6	87.1	2.0	3.4	1.6
47-56	6.1	85.6	2.0	4.5	1.9
60-77	5.3	87.8	1.7	3.9	1.7
81-91	5.9	86.6	2.2	4.5	0.7
95-105	5.8	86.7	2.4	4.1	1.9
110-150	5.5	82.5	2.1	3.5	0.7
expected bulk glass B	5.8	87.8	1.9	3.6	1.7

5.2.3 Enamel coating on mild steel heat-treated after firing

Microstructure:

The microstructure of the coating is shown in Figure 5.2.8. Extensive crystallisation has occured during heat-treatment. Grannular crystals of micron dimensions make up the bulk enamel microstructure. The original dendritic growth has extended to form a

Figure 5.2.8 Backscattered electron micrographs of a coating on mild steel fired and heat-treated, M9H.

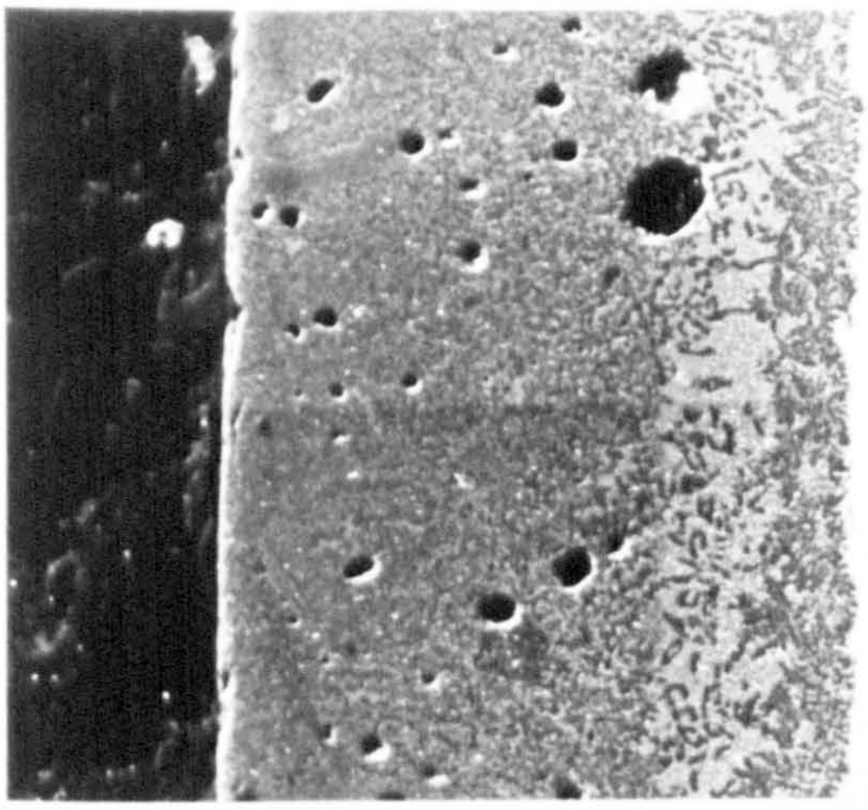

40 um

coating

mild steel

lithium disilicate
+ quartz

lithium iron
silicate

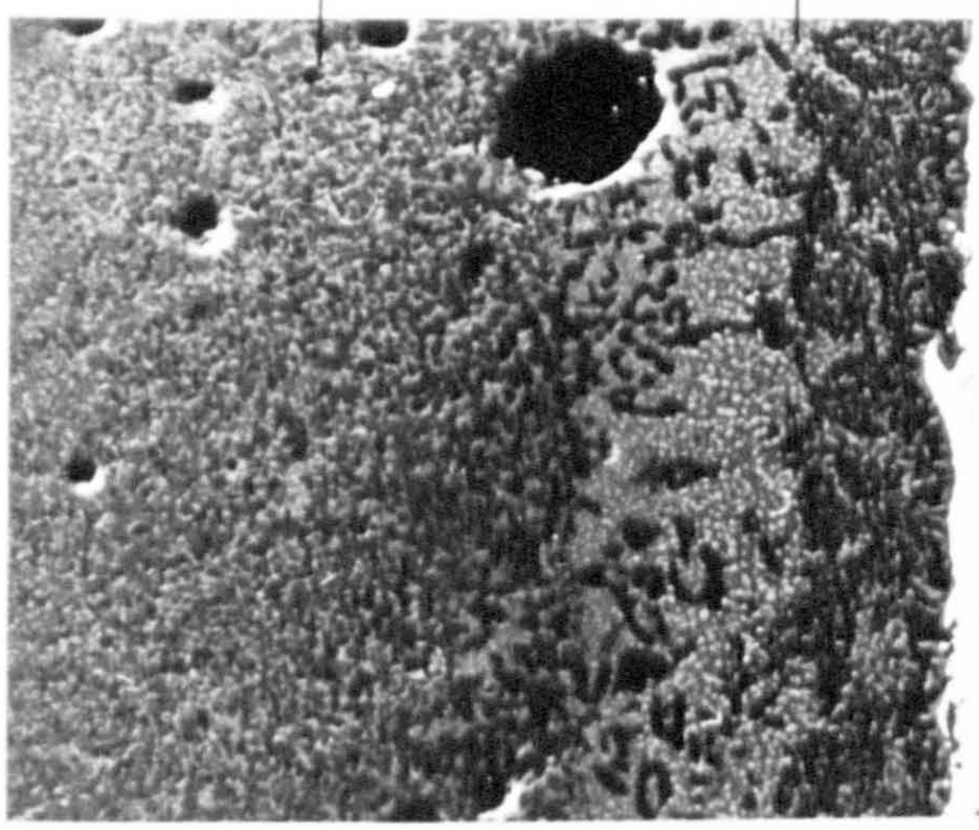

20 um

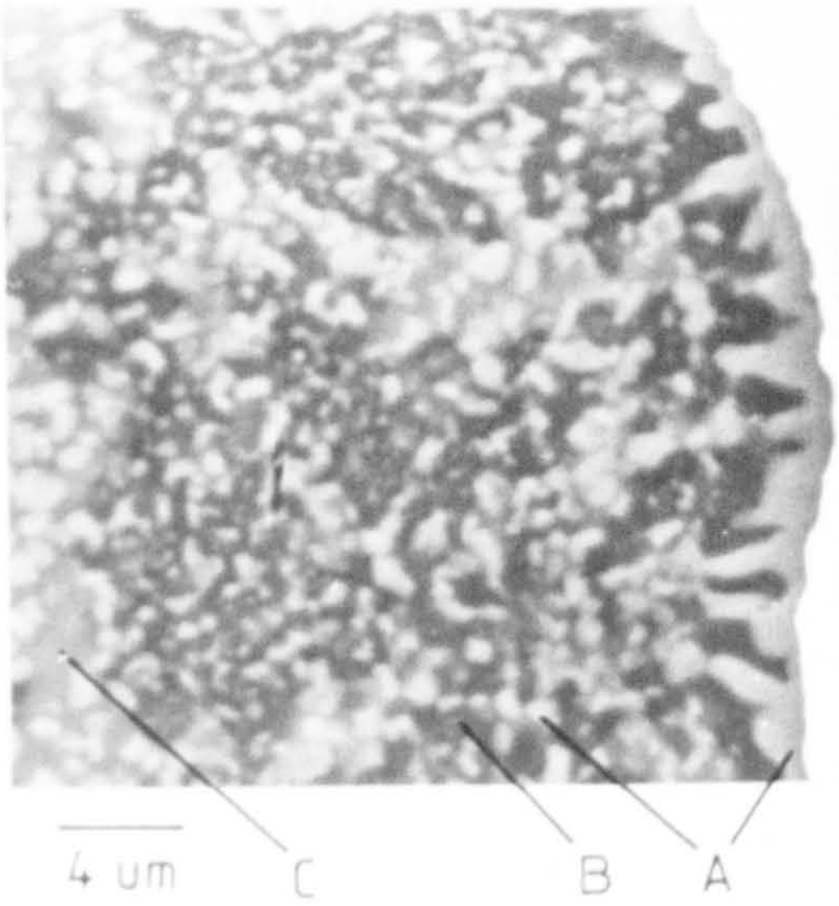

4 um

C

B

A

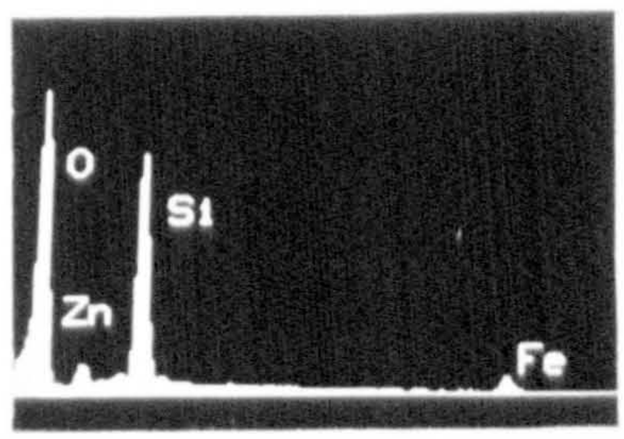

A lithium iron silicate

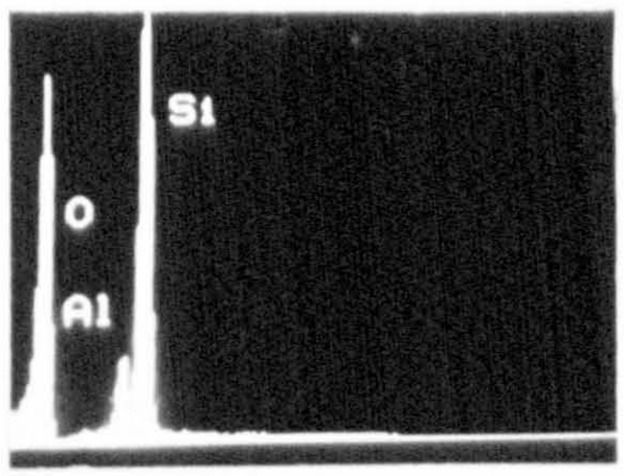

B dark matrix

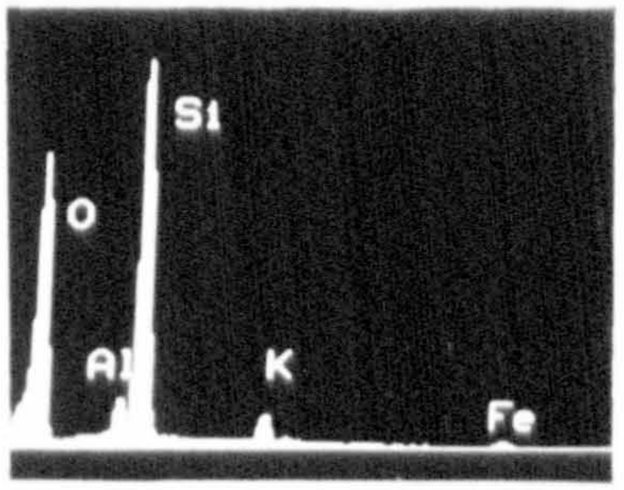

C light matrix

continuous layer along the coating-mild steel or coating-iron oxide boundary. Micron size crystals of a similar bright backscatter contrast appear in the interface region. Three zones are apparent:

0-20 μm: Bright contrast crystals appear in a predominantly dark contrast matrix.

20-40 μm: Bright contrast crystals appear in a predominantly light contrast matrix.

> 40 μm: The bright contrast crystals merge with the bulk coating microstructure.

The x-ray pattern of a coating removed and ground to a powder is shown in Figure 5.2.3(b). It reveals β-quartz and lithium disilicate as the major crystal phases. In the bulk microstructure the lighter contrast phase is β-quartz and the darker lithium disilicate. A few additional peaks, not accountable by the above two phases, are observed. These are due to residual iron oxide and the bright contrast interface phase. The x-ray pattern collected from the exposed coating surface is displayed in Figure 5.2.4(b). A large peak at 42.2° 2θ (d = 2.14 Å) is present. A few additional peaks relating to the interfacial crystal phase could be seen.

An extensive quantitative EDX analysis was conducted to identify the interfacial phases.

Bright contrast crystal phase:

The bright contrast phase was examined in 10 positions extending 1 to 30 μm from the interface. The resulting mean concentrations are given in Table 5.2.6(a). This phase is composed of iron, zinc and silicon. With the detector window removed, substantial amounts of

oxygen were observed, Table 5.2.6(b) . The silicon to oxygen ratio is 4. These results suggest the phase is an iron zinc-orthosilicate. It is necessary to know if lithium is also present. The minor concentrations of aluminium, phosphorus and potassium were assumed to be a consequence of electron beam spreading into the matrix. Combining (a) and (b) in Table 5.2.6 an estimate of lithium concentration is calculated from the requirement to keep charge neutrality. The normalised concentrations are given in Table 5.2.6(c). Iron has been assumed present exclusively in the divalent state. From these observations it is possible to say the phase is a lithium-iron-zinc-orthosilicate. The compositions in Table 5.2.6 yield the formula:

$$Li_2O\ Fe_{0.86}\ Zn_{0.14}\ O.SiO_2$$

For comparison the composition was calculated with the minor elements included. This yields the formula:-

$$0.77\ (Li_2O).\ 0.02\ (Al_2O_3).\ 0.03\ (P_2O_5).\ 0.02\ (K_2O).\ 1\ (Zn,\ Fe\ O).1\ (SiO_2).$$

Dark contrast matrix phase:

The dark matrix phase is a silicate with a low iron content. Only minor amounts of phosphorus, zinc and potassium are present. It is not possible to say what proportion of the detected iron and zinc is due to electron beam spreading. Assuming the measured values are the actual concentrations, a very low lithium content is evaluated.

Table 5.2.6: Composition of interfacial crystal phases

(Bright contrast crystal phase)

(a) detector window in place

Element at% (±0·1%)

Al	Si	P	K	Zn	Fe
2.0	46.5	2.7	2.0	6.5	40.2

(b) detector window removed

Element at% (± 2%)

Si	Fe	O
17.4	12.4	70.0

(c) combined composition

Si	Fe+Zn	O	Li
12.4	12.5	50.0	25.2

Table 5.2.7: Composition of interfacial matrix phase

(a) detector window in place

Element at% (±0·1%)

	Al	Si	P	K	Zn	Fe
Dark matrix	7.7	75.7	1.1	1.7	1.7	1 2,
Light matrix	5.4	61.4	0.3	10.0	1.9	2 1,

(b) detector window removed

Element at% (±2%)

	Si	Fe	O
Dark matrix	29.3	0.7	70.0
Light matrix	26.4	5.0	68.5

(c) combined composition

	Al	Si	P	K	Zn	Fe	O	Li
Dark matrix	2.7	26.5	0.4	0.6	0.6	4.2	63.8	1.2
Light matrix	2.1	23.6	0.1	3.8	0.7	8.0	61.2	0.3

Table 5.2.8: Position of peaks on x-ray pattern collected from exposed glass-ferrous oxide disk interface

Angle 2θ	d A	I/I_o	
	Lithium iron silicate		
24.4	3.64	42	
26.4	3.37	50	(possibly due to quartz)
28.6	3.12	38	
33.3	2.69	46	
35.9	2.50	100	
49.6	1.84	25	
	Ferrous oxide		
36.3	2.47	69	
42.2	2.14	100	

Light contrast matrix phase

The light matrix phase is a silicate with relatively high iron content. Phosphorus and zinc occur in minor quantities. Potassium has a high concentration and appears to be preferentially located in this phase. Lithium is calculated to be present in negligble concentrations.

An attempt was made to identify the phases by x-ray diffraction. Bulk glass B was placed on a ferrous oxide disc and held at 970°C for 1 hour (D3), (See Section 4.5). The interface was exposed by grinding away the ferrous oxide. Figure 2.2.9 shows the collected x-ray pattern. Ferrous oxide is detected plus several additional peaks due to the lithium iron-zinc-silicate phase. These are listed in Table 5.2.8. X-ray diffraction data on lithium-iron-silicate phases is very limited. No standard patterns in the J.C.P.D.S. file corresponded to the peaks in Table 5.2.8.

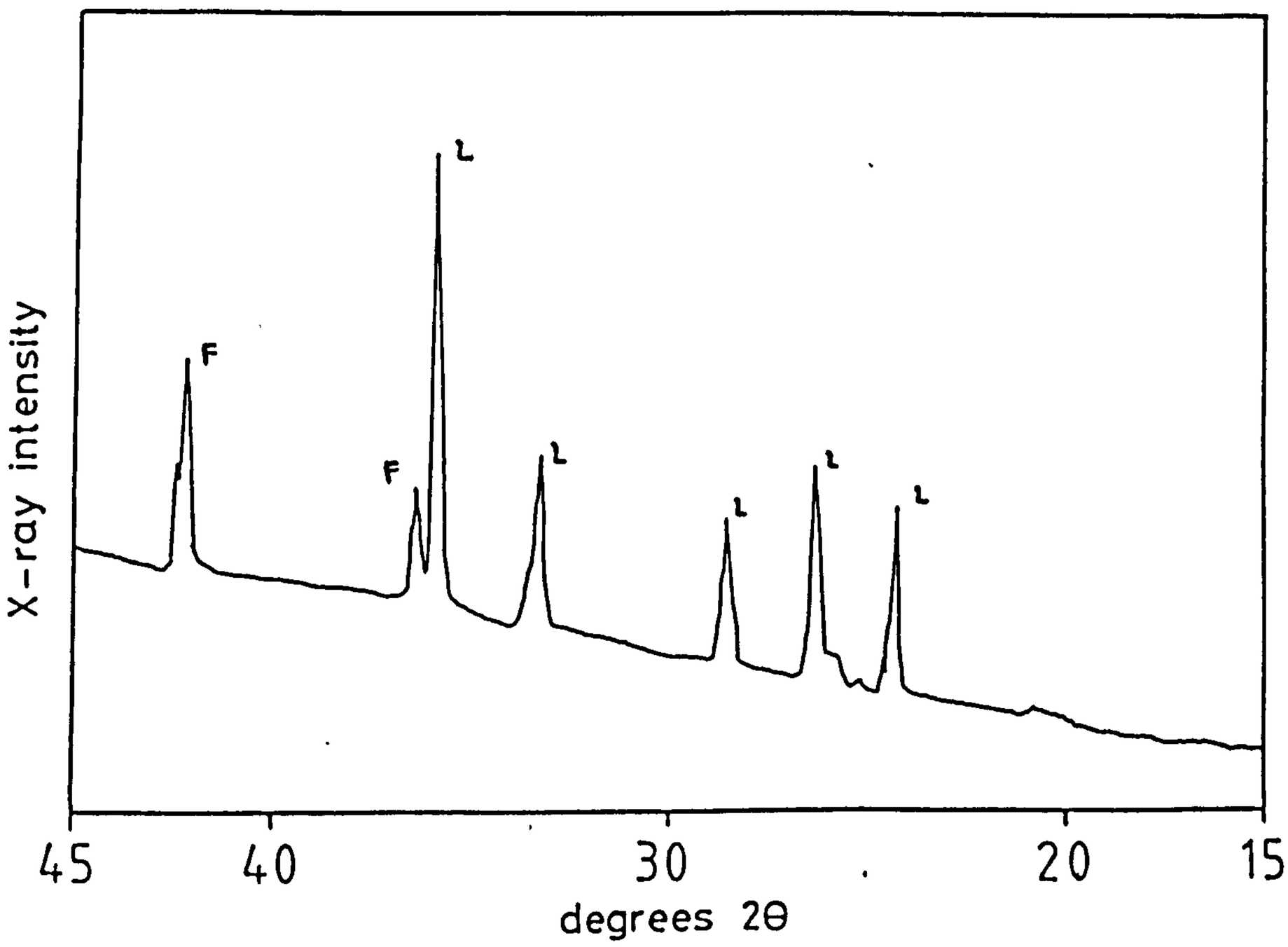

Figure 5.2.9 XRD patterns collected from a exposed glass B ferrous oxide interface.

F - ferrous oxide

L - lithium iron silicate

$Li_2O.FeO.SiO_2$

Element distributions:

The distribution of elements across the interface are illustrated in Figure 5.2.5(b). These profiles were collected using linescans. A large redistribution has occured during heat-treatment. This is especially pronounced in the region extending to 40 µm:-

- Silicon fluctuates markedly in the interface region. Peaks correspond to the matrix phase.

- Iron also fluctuates markedly with peaks corresponding to the lithium-iron-zinc-silicate crystals. At the coating-mild steel boundary the level rapidly increases to a constant value in the substrate.

- Aluminium has a profile which resembles that of silicon suggesting it resides in the matrix.

- Zinc is concentrated in the interface region and related to it being incorporated in the lithium-iron-zinc-silicate crystals.

- Potassium shows an apparent increased concentration in the light contrast matrix. It peaks in the region between 20-40 µm where the light matrix is present. Adjacent to the interface where the dark matrix occurs, the level drops.

Shown in Table 5.2.9 are the concentrations determined by EDX analysis over 8 x 8 µm regions. Both crystals and matrix phases are incorporated within these areas. Iron and its associated oxygen has

been removed. The lithium presence is ignored. With no movement of the detectable elements, concentrations should remain similar to the bulk glass. This is not the case of potassium. An increase is observed in the region between 20-40 μm. Potassium must diffuse over relatively large distances in excess of the areas analysised.

Table 5.2.9: Measured concentration after removal of iron (excluding Li and O)

Region	Element at% (±0·1%)				
μm	Al	Si	P	K	Zn
2-10	6.0	82.8	2.6	1.7	4.8
10-18	6.0	83.7	1.4	2.8	3.7
18-26	5.1	86.4	1.7	8.2	3.1
26-34	5.1	82.2	1.7	9.0	1.7
34-47	5.6	81.1	1.7	9.9	1.7
42-50	6.1	87.4	2.0	1.7	2.0
50-58	5.8	87.8	1.3	3.2	1.5
58-66	5.8	86.9	1.9	3.6	1.7
expected bulk glass B	5.8	87.8	1.9	3.6	1.7

5.2.4 Oxide formation under screen printed powder

The mild steel was preoxidised for 15 minutes at 650°C in air. This was shown to produce an oxide layer of ferrous oxide 8 mg cm^{-2} or 14 μm thick. During preoxidation of a coated, but unfired substrate, the organic binder is burnt off. This may result in a more reducing atmosphere than for the uncoated substrate.

A coating was briefly fired for 30 seconds then quenched (M3). The glass powder had partially fused allowing it to be sectioned then polished. Figure 5.2.10 shows the interfacial microstructure. A large quantity of iron oxide is present. As discussed earlier it is assumed to be essentially ferrous oxide (FeO). The iron oxide layer

Figure 5.2.10 Backscattered electron micrograph of iron oxide present at interface, M3.

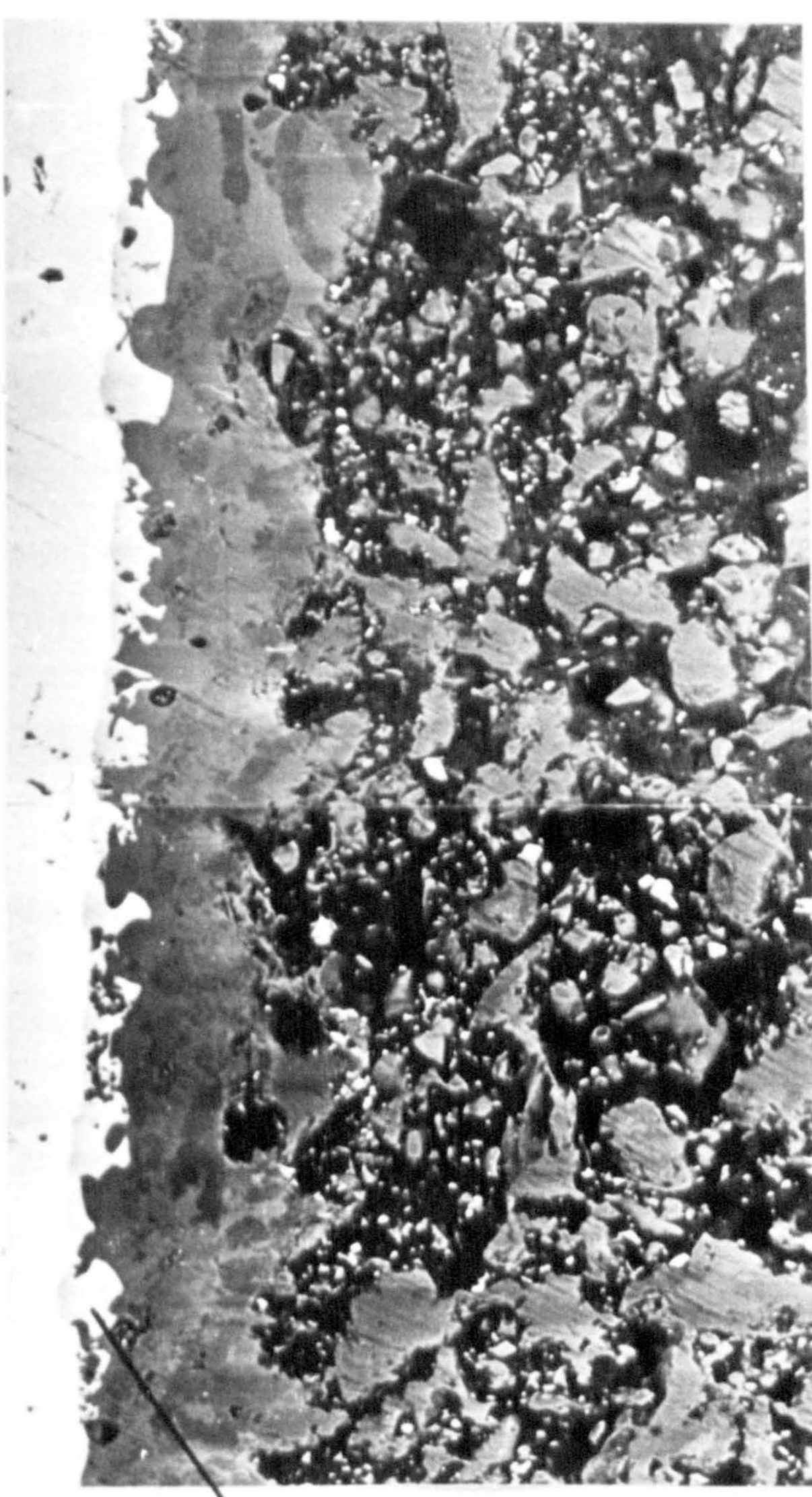
fired for 30 seconds
at 920°C M3
ferrous oxide
20 µm

extends to 15 μm from the substrate surface. It is very rough, probably due to glass particles being in contact with the mild steel during preoxidation. The mean amount of iron oxide present was evaluated at 4.04 mg cm^{-2} corresponding to an average thickness of 7 μm. This value is a low estimation because some iron oxide has already been taken into solution during the short 30 second firing. These results show that the glass powder coating greatly influences the amount of iron oxide formed. It is reduced from 8 mg cm^{-2} to 4 mg cm^{-2}.

5.2.5 Variation in firing parameters

The coatings were fired for times ranging from 30 seconds to 20 minutes and for temperatures between 930 to 990°C. Table 5.2.10 lists the conditions. The interfacial microstructure for the various coatings are shown in Figures 5.2.11(a) to (g) in the quenched state. Heat-treated coatings are shown in Figures 5.2.12(a) to (g). Quantitative element distributions in the coating adjacent to the interface are displayed in Figures 5.2.13(a) to (g). The concentrations for iron, silicon and potassium are displayed. Lithium was assumed present with a constant ratio to silicon as expected from the bulk glass composition.

5.2.6 Iron oxide dissolution

During firing the iron oxide layer is taken into solution by the coating. The amount of residual iron oxide decreases with firing time. By 5 minutes at 970°C (M9) only isolated pockets remain, Figure 5.2.2. Substantial contact is made between the coating and substrate.

Figure 5.2.11 Backscattered electron micrographs of coatings subjected to various firing conditions.

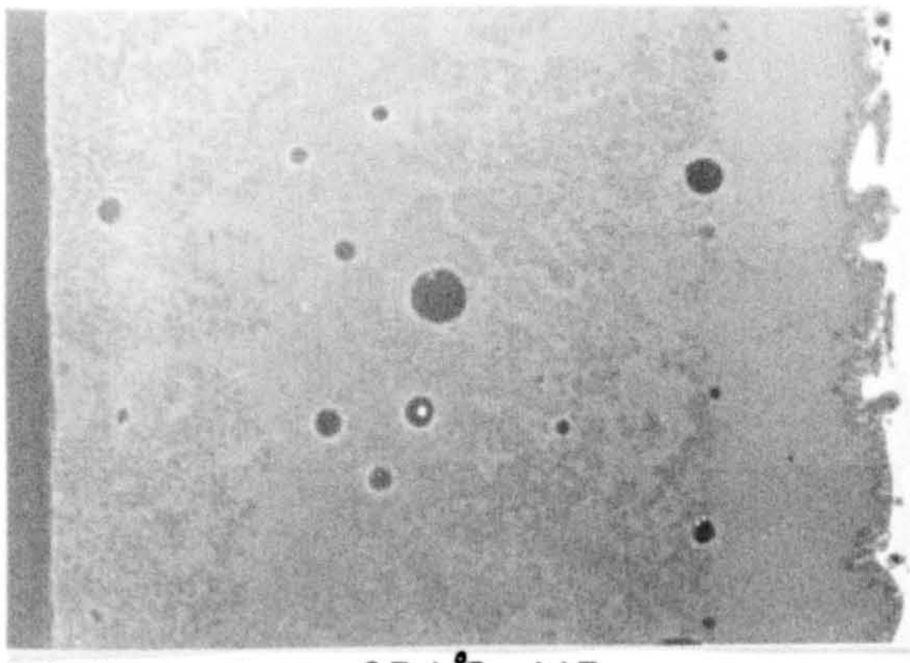

(a) 2minutes 956°C M5

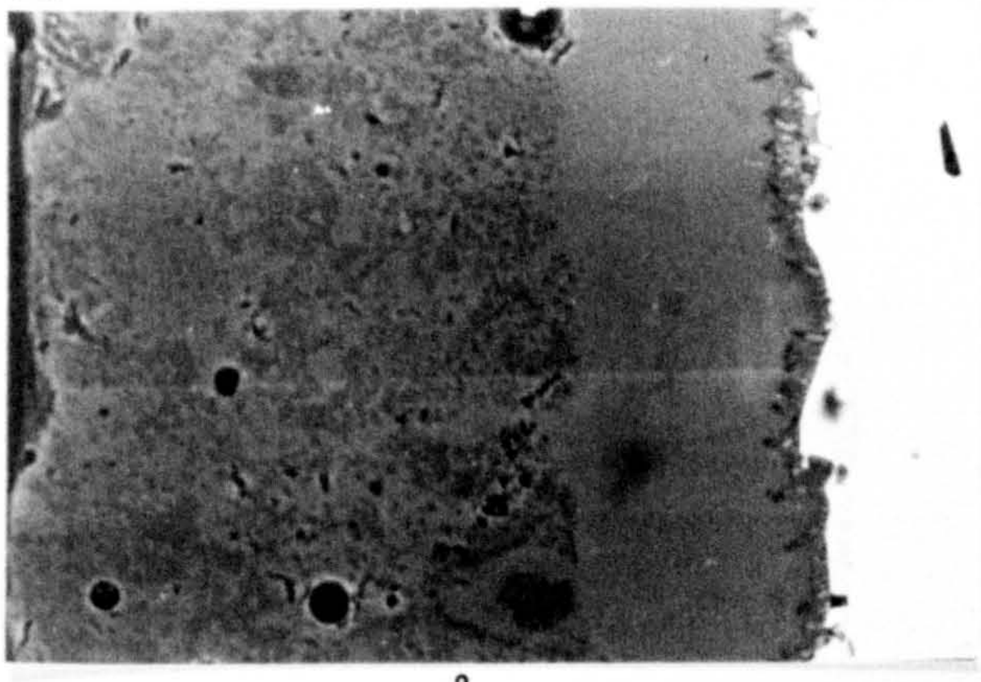

(b) 4minutes 963°C M7

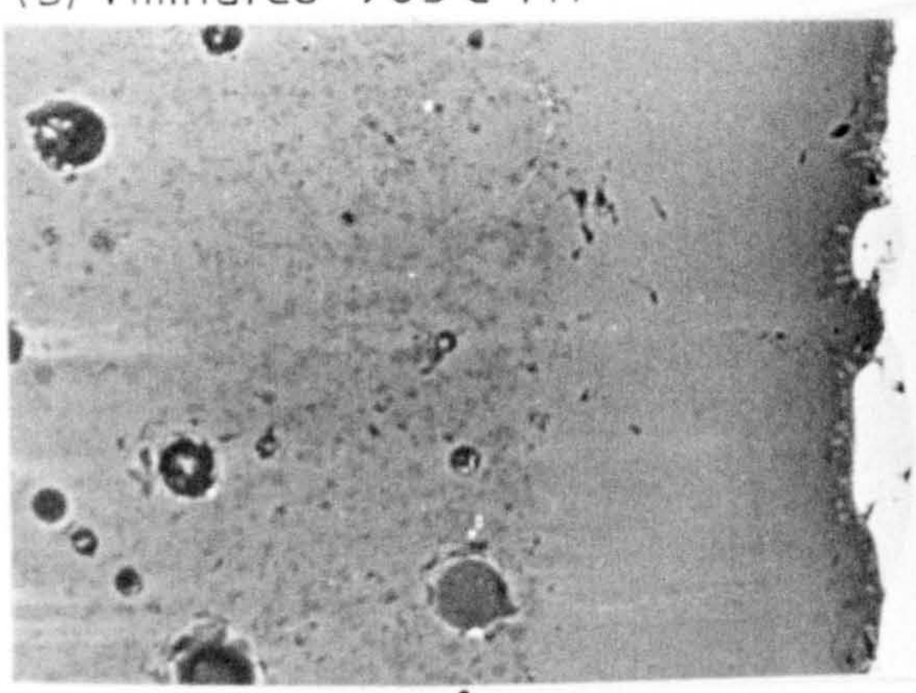

(c) 6minutes 976°C M10

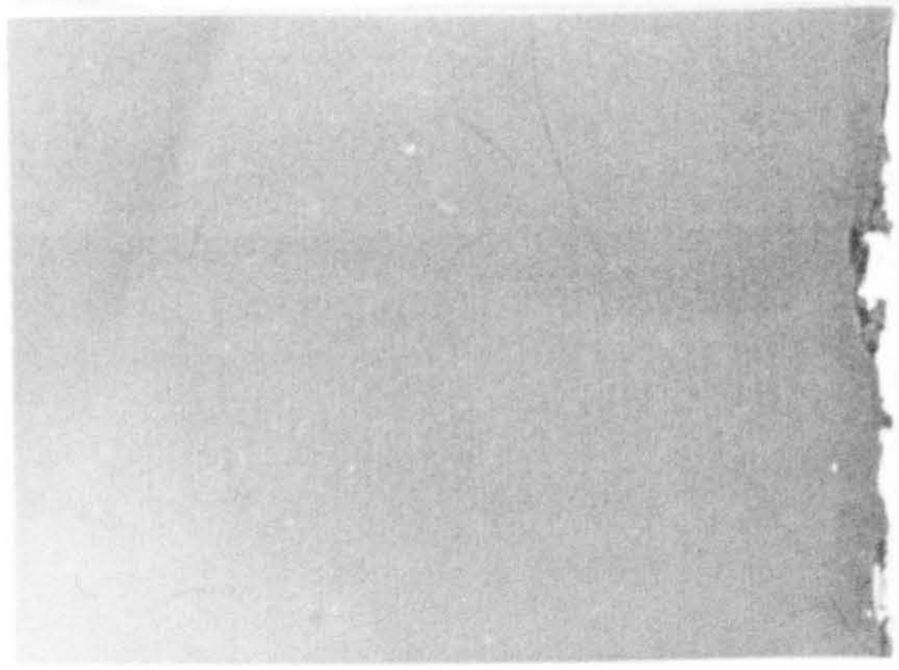

(d) 8minutes 970°C M12

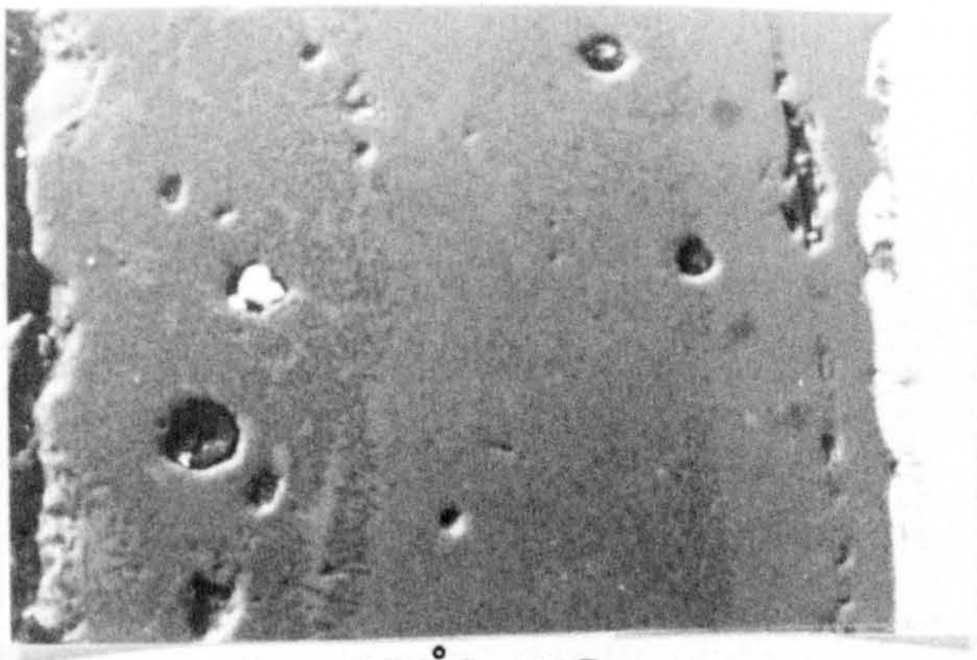

(e) 5mjnutes 930°C M15

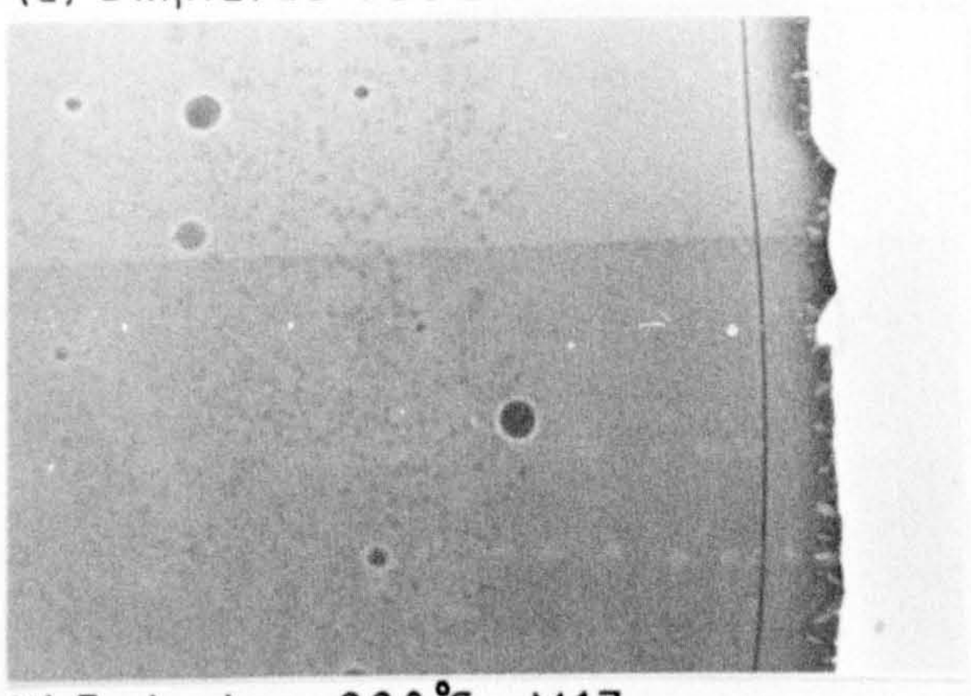

(f) 5minutes 980°C M17

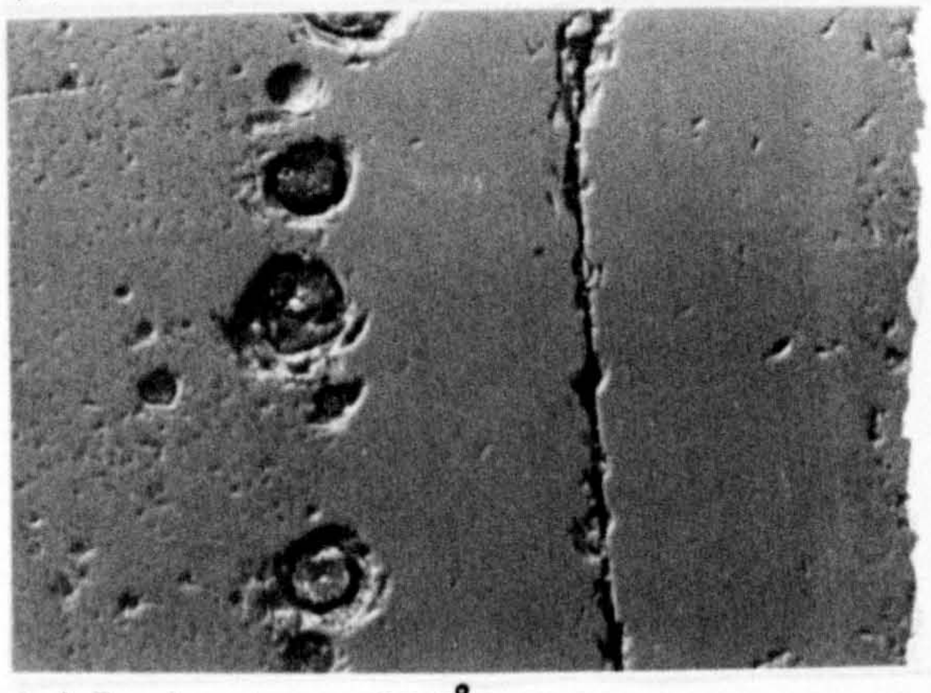

(g) 5minutes 990°C M18

20 μm

Figure 5.2.12 Backscattered electron micrographs of coatings subjected to various firing conditions then given a "standard" heat-treatment.

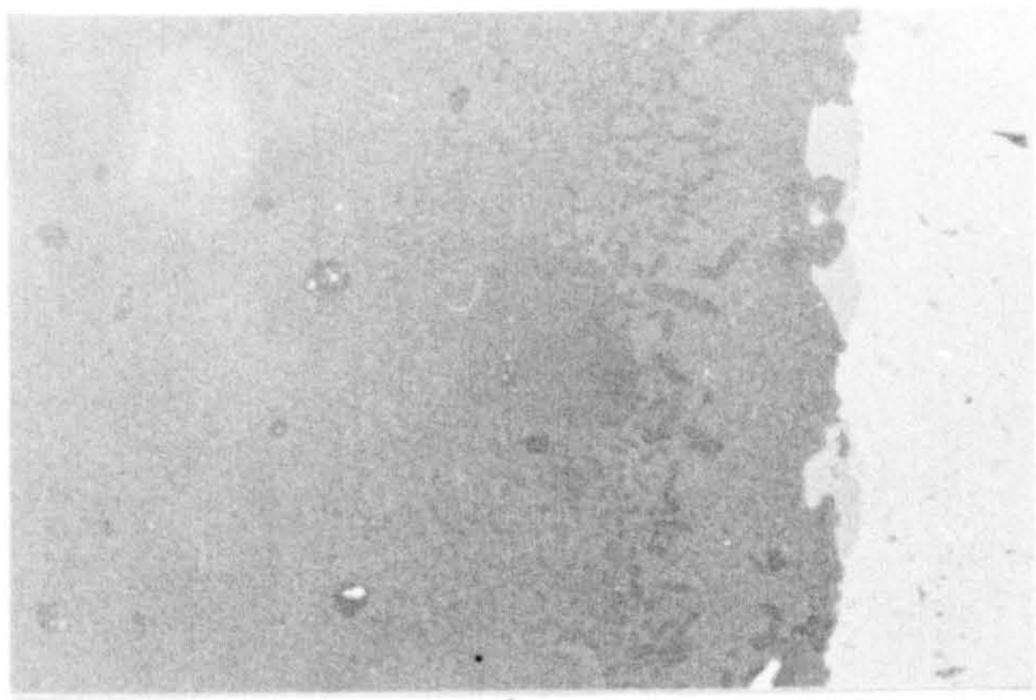

(a) 2 minutes 956°C M5H

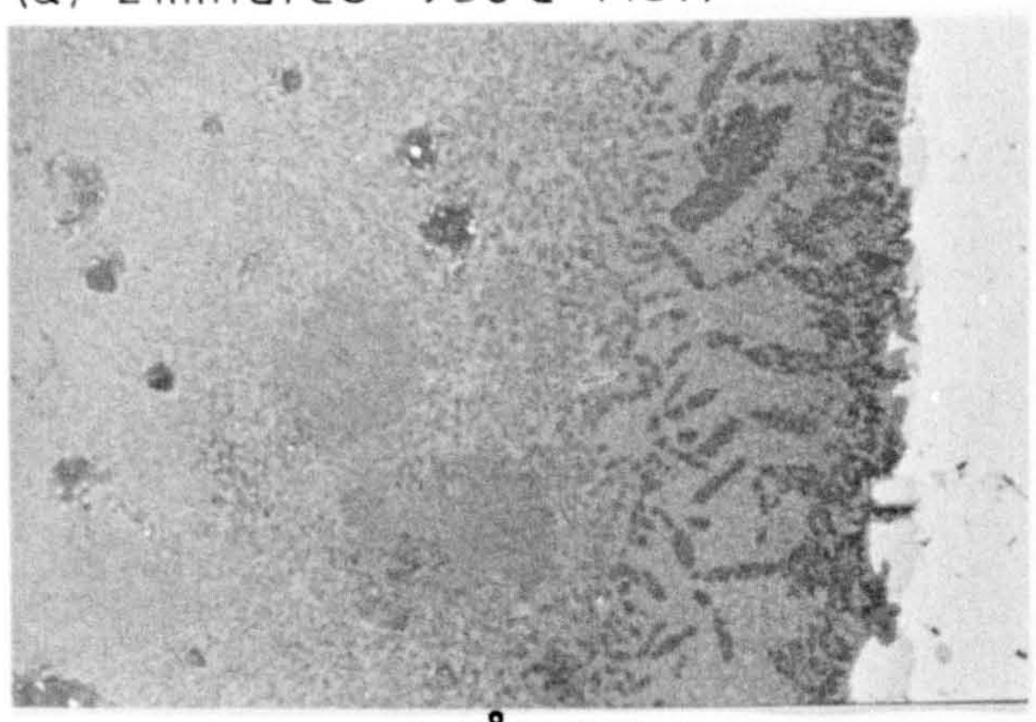

(b) 4 minutes 963°C M7H

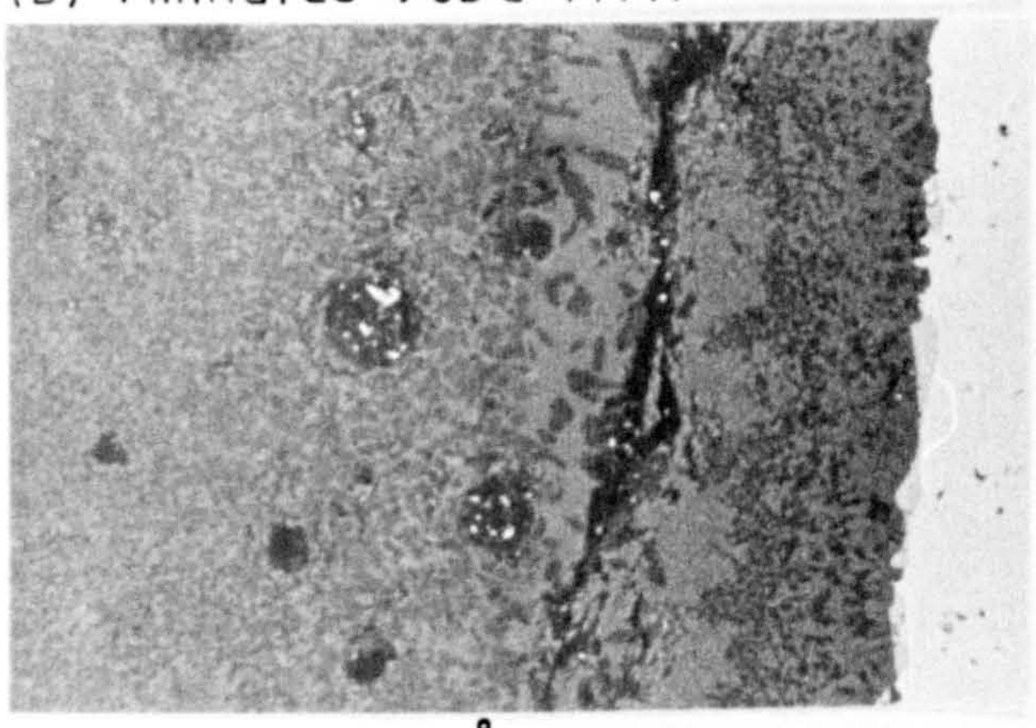

(c) 6 minutes 976°C M10H

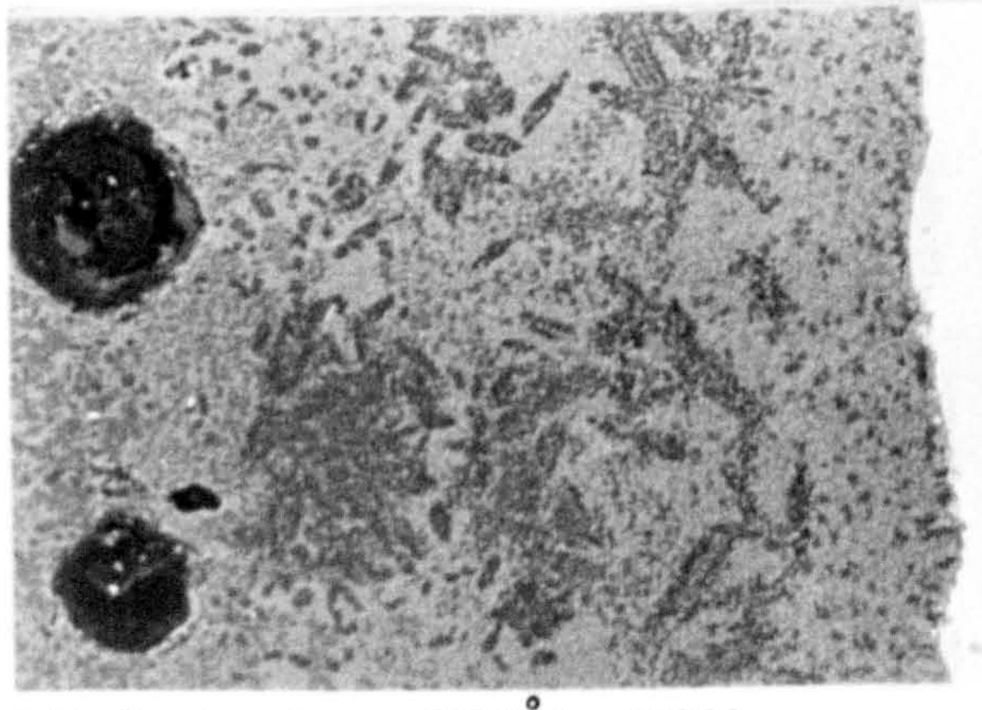

(d) 8 minutes 970°C M12H

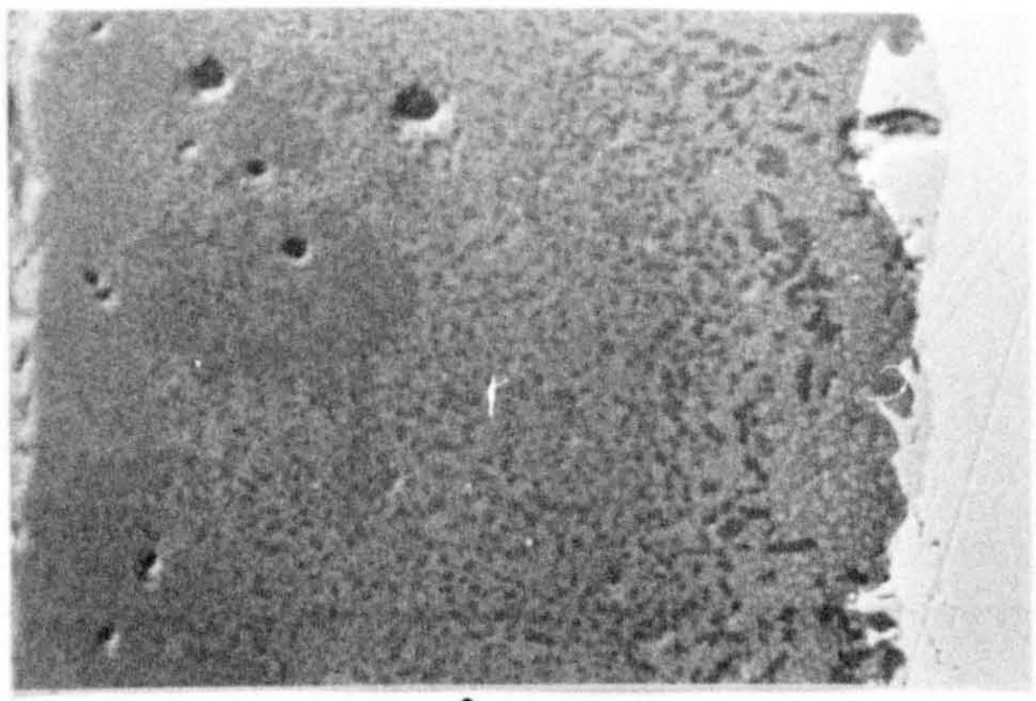

(e) 5 minutes 930°C M15H

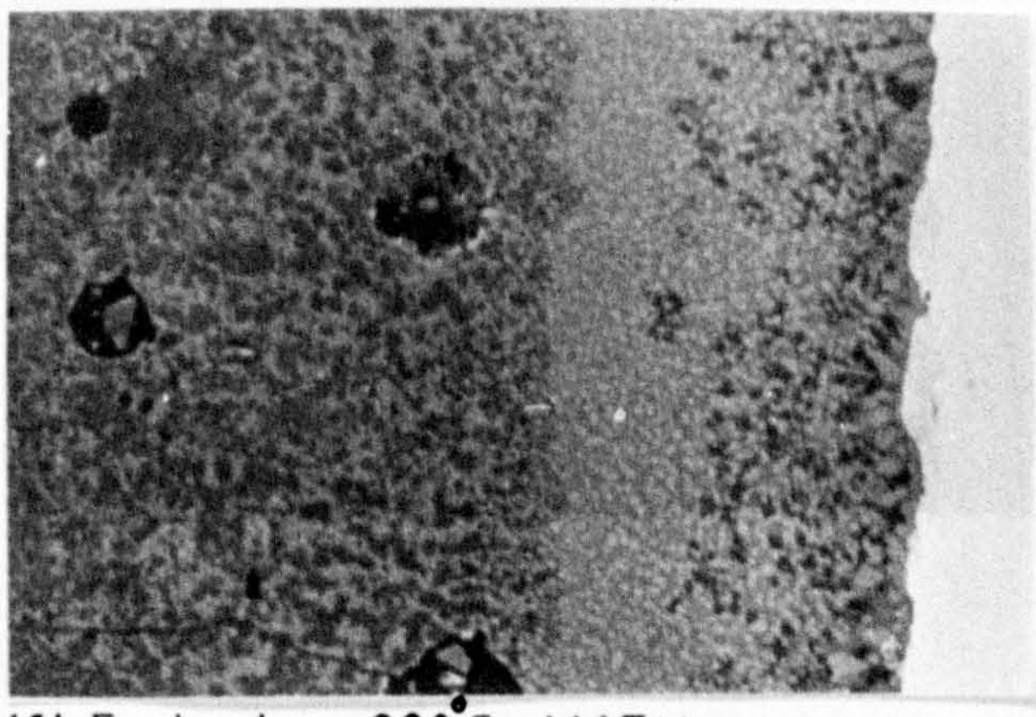

(f) 5 minutes 980°C M17H

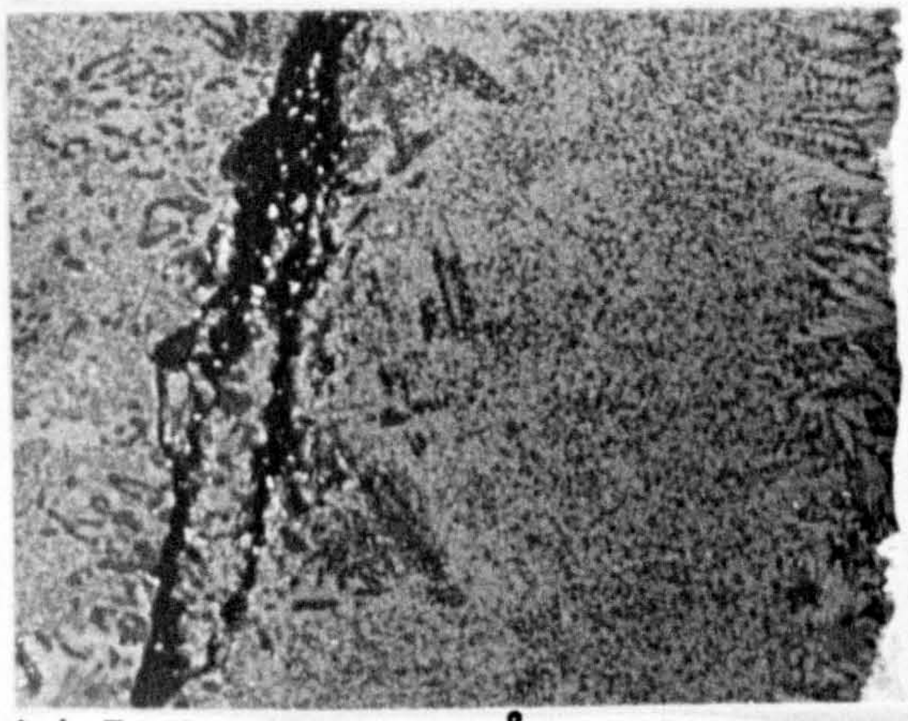

(g) 5 minutes 990°C M18H

20 μm

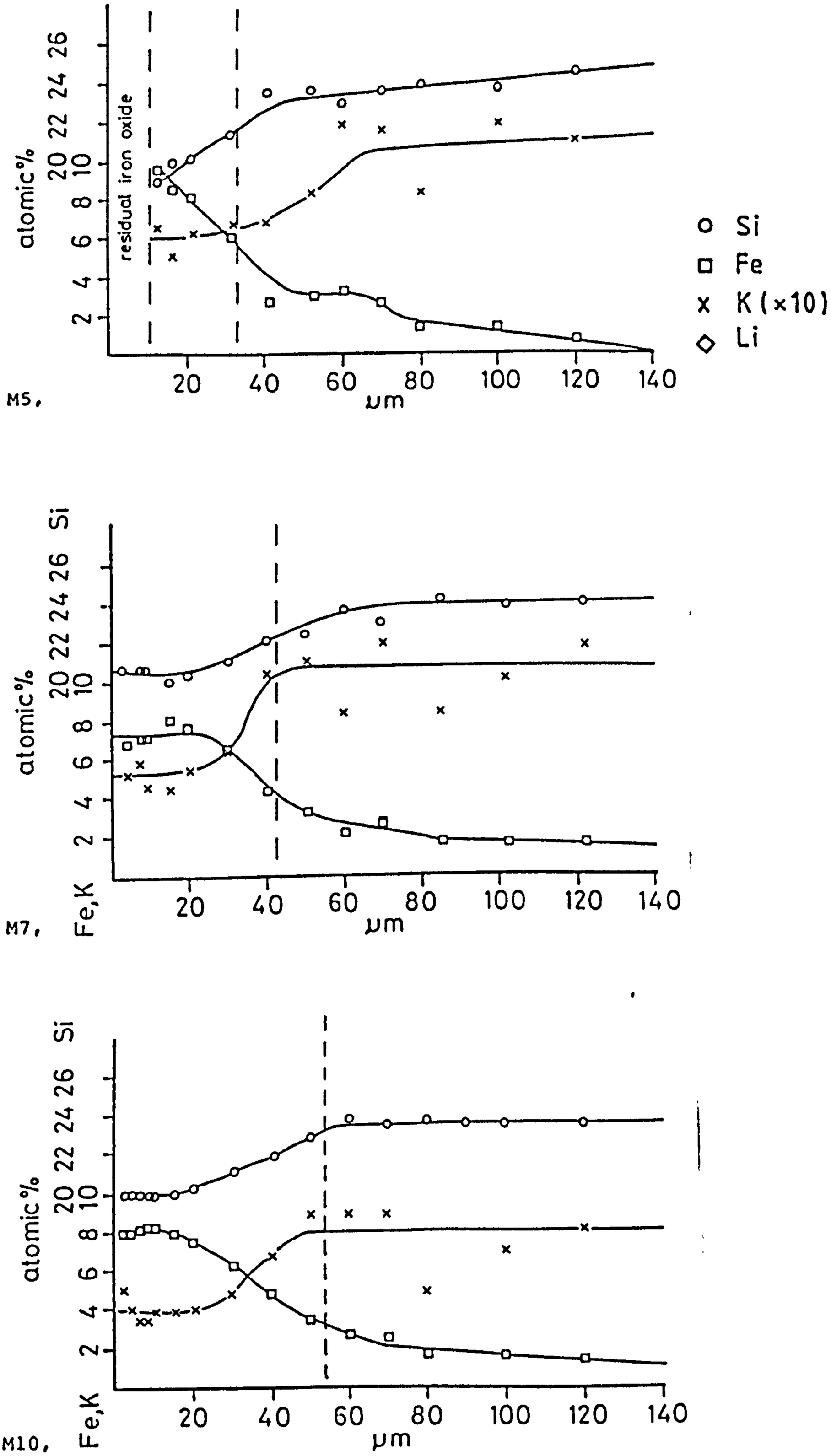

Figure 5.2.13 Quantitative element distribution across the interface of coatings subjected to various firing

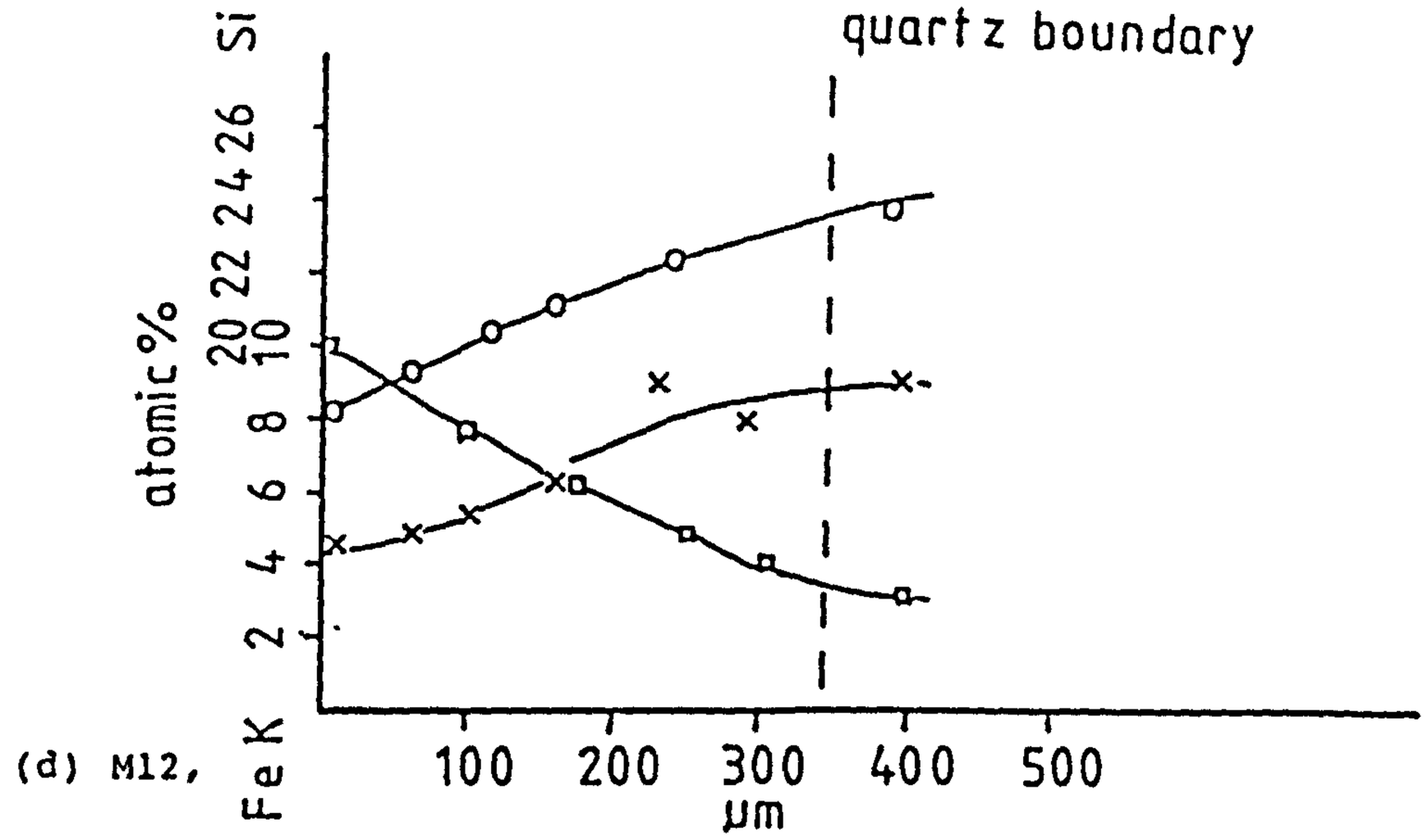
quartz boundary
Si
20 22 24 26
10
8
6
4
2
Fe K
atomic%
100 200 300 400 500
μm

(d) M12,

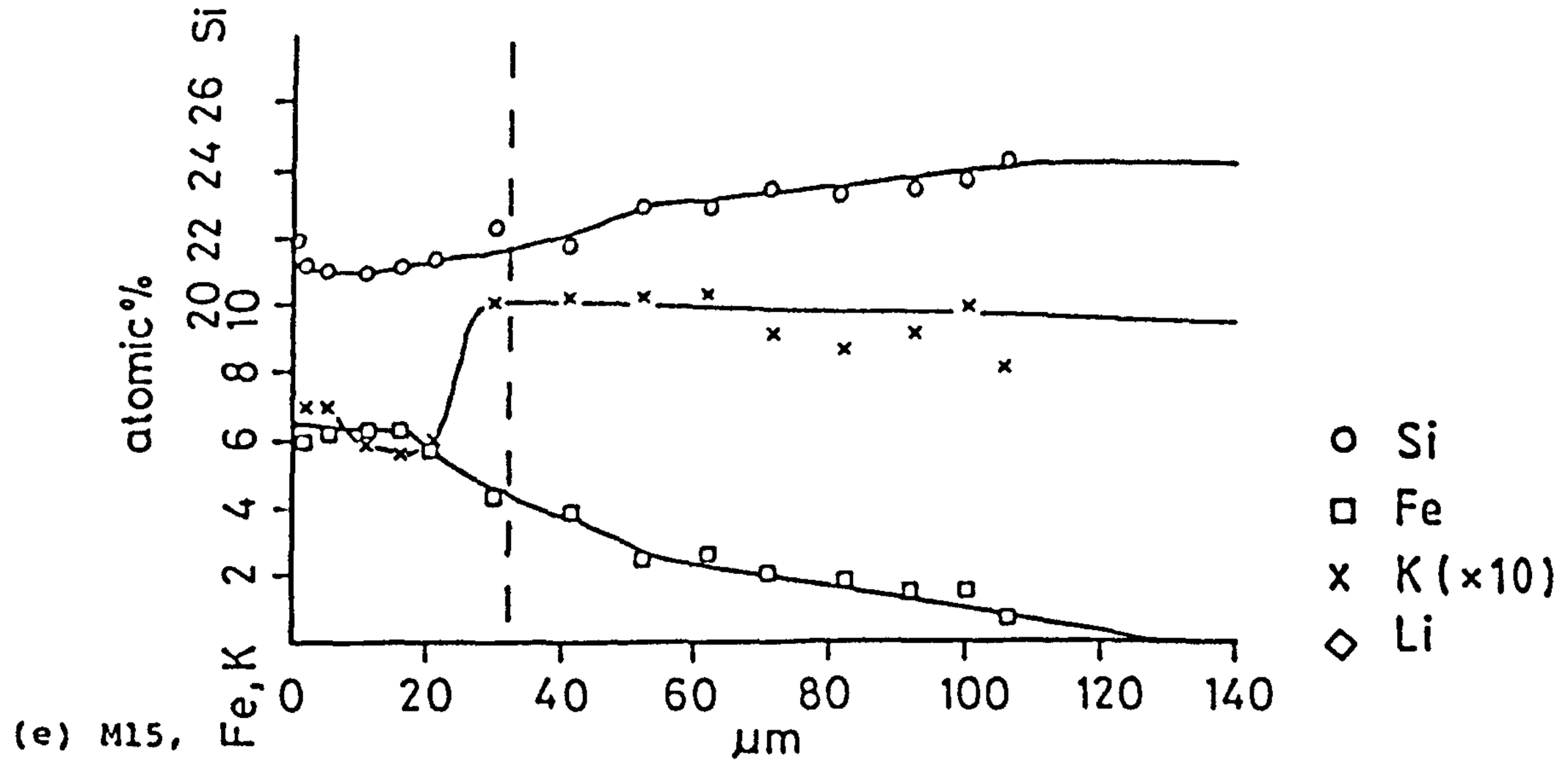

(e) M15,

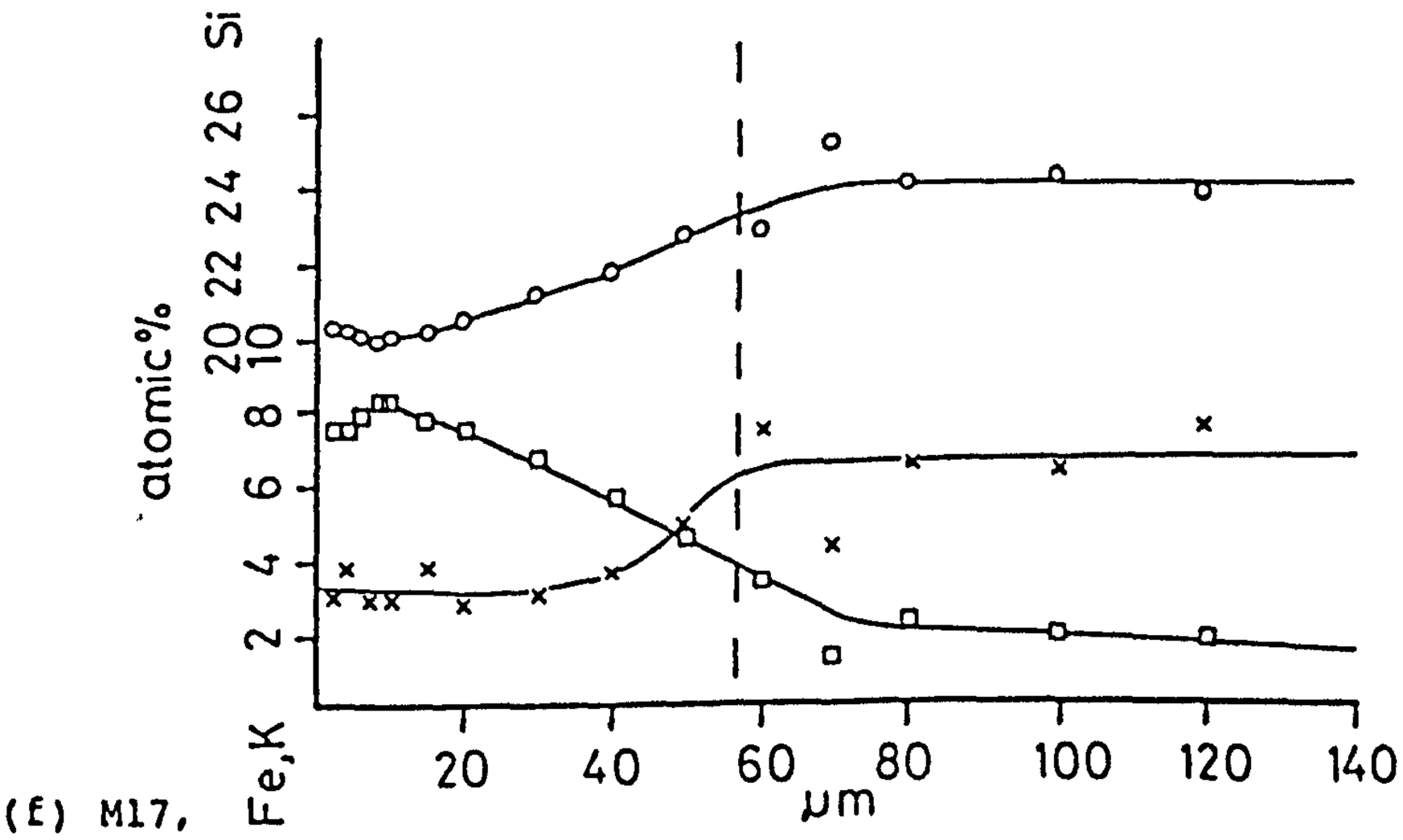

(f) M17,

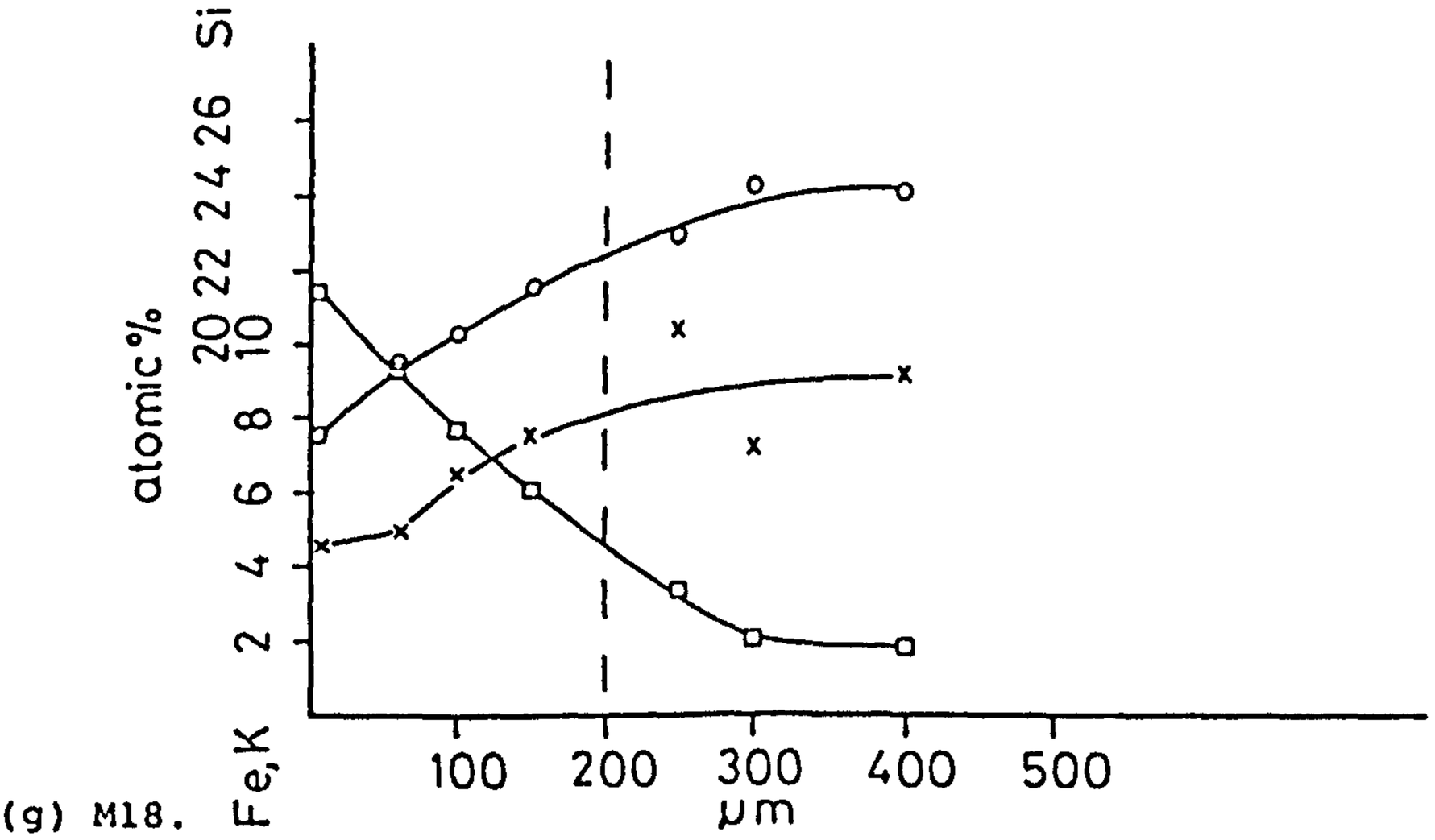

(g) M18.

For a firing time equal to or greater than 8 minutes at 970°C (M12), little residual iron oxide exists, Figure 5.2.11(d), spreading no longer occurs.

Increased firing temperature causes the dissolution rate to increase. Firing at 990°C or above for 5 minutes, (M18), Figure 5.2.11(g), results in the coating becoming non-spreading. Again very little residual iron oxide is present at the interface.

The iron profiles, Figure 5.2.13, have a constant concentration in the adjacent 15 μm of the coating. For all firing times the interface concentration of iron is approximately steady at 7.5 to 8 at% Fe (25-30 wt% FeO). Clearly the rate of solution of iron oxide must exceed the rate at which it diffused away from the interface. This value represents the saturation concentration of ferrous oxide in the coating. The iron level remains constant to 15 μm which corresponds to the extent of the initial preoxidised layer.

At distances greater than 15 μm the iron concentration gradually drops. In all the coatings examined iron was still detected at 140 μm.

It is possible to determine the mass of ferrous oxide taken into solution, by the coating, for each firing condition. To do this the iron profiles were expressed in wt% FeO. These concentrations need to be converted to gcm^{-3}. The density of the coating containing ferrous oxide must be known.

Table 5.2.10: Coating properties

Label	Firing Conditions		Appearance	Position of crystal boundary	
				β-quartz	Lithium disilicate
	Minutes	°C		μm (±2)	μm (±2)
M4	1	950	good wetting	19	45
M5	2	956	"	33	111
M6	3	956	"	38	120
M7	4	953	"	42	-
M8	5	960	"	41	-
M9	5	970	"	52	-
M10	6	976	"	58	-
M11	7	966	"	50	-
M12	8	970	Poor wetting	356	-
M13	15	967	"	-	-
M14	20	970	"	-	-
M15	5	930	Good wetting	32	90
M16	5	950	"	38	149
M17	5	980	"	56	-
M18	5	996	Poor wetting	-	-

Bulk glass B having increasing amounts of ferrous oxide added was prepared (Section 4.5). An inverse relationship is found between the glass density and ferrous oxide concentration, C_{FeO}, over the compositional range examined;

$$1/\rho = -2.245 \times 10^{-3} C_{FeO} + 0.42331 \qquad 5.1$$

The calculated mass of ferrous oxide taken in the solution by each coating is listed in Table 5.2.11. The amount of ferrous oxide which has entered the coating increases with firing time. For a firing time of 5 minutes the amount of ferrous oxide also increases with firing

temperature. For the longer firing times or higher firing temperatures little iron oxide remains at the interface. The total amount of iron oxide which has entered the coating is of the order of 5 mg cm^{-2}.

Table 5.2.11: Mass of iron oxide M_{FeO} taken into solution by coating

Label	Firing Condition		M_{FeO}
	Minutes	°C	$mg\,cm^{-2}$ (±0.1)
M5	2	956	3.8
M6	3	956	3.8
M7	4	953	4.2
M8	5	960	4.1
M9	5	970	5.1
M11	7	966	4.6
M15	5	930	3.3
M16	5	950	3.7
M8	5	960	4.1
M9	5	970	5.1
M17	5	980	4.9

5.2.7 Microstructural development

A boundary exists parallel to the interface where β-quartz first appears for the quenched coatings. The boundary moves away from the interface with increasing firing time and temperature. Table 5.2.10 and Figure 5.2.11. At this boundary the iron concentration is about 4 at% in all the coatings.

For a short firing time or a low firing temperature with a time

of 5 minutes, a second boundary is visible. See Figures 5.2.11(a) and (e). X-ray diffraction of the outer surface of the coating detected lithium disilicate as well as β-quartz for these two. The second boundary is where lithium disilicate first appears. Here the iron concentration has dropped to below 1 at% Fe. For the other firing conditions the second boundary is absent. The iron concentration does not drop below 1 at% Fe before the outer coating surface. These results are illustrated schematically in Figure 5.2.14(a).

The amount of iron oxide in solution strongly influences the coating crystallisation. For comparison bulk glasses B containing various amounts of ferrous oxide were prepared, (Section 4.5). These were ground to a fine powder, passed through a 200 mesh size sieve and then given a thermal treatment identical to the standard firing. The crystal phases present were determined by x-ray diffraction. The results are listed in Table 5.2.12. With no ferrous oxide present in the glass both lithium disilicate and β-quartz are present. The addition of 6wt% Feo suppressed the formation of lithium disilicate. With 12, 19 and 25 wt% FeO no crystallisation occurs.

The results so far have concentrated on the fired only coating. Firing conditions also influence the microstructure developed on heat-treatment. From Figure 5.2.12 it can be seen the start of the bulk coating microstructure corresponds closely to the original β-quartz boundary of the fired only coating. The lithium-iron-zinc-silicate crystals are developed in the zone extending from the interface to the start of the bulk microstructure. Before heat-treatment the iron concentration in this zone is above 4 at% Fe. Both increased firing time and temperature increase the width of the zone. The dark contrast matrix is absent for short firing times (M5) and low firing temperatures (M15). See Figures 5.2.12(a) and (e)

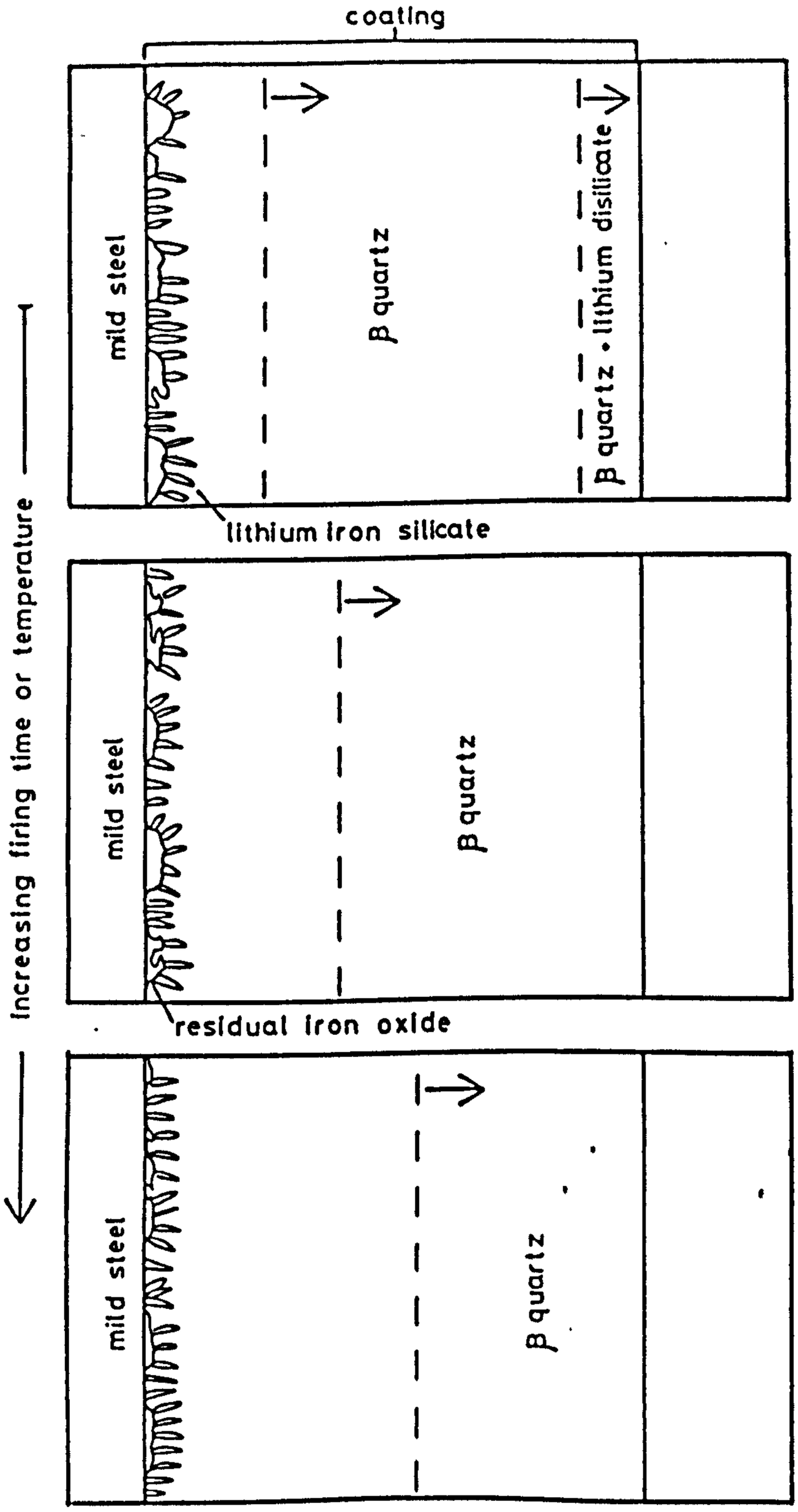

(a) fired only coatings

Figure 5.2.14 Schematic representation of microstructural development.

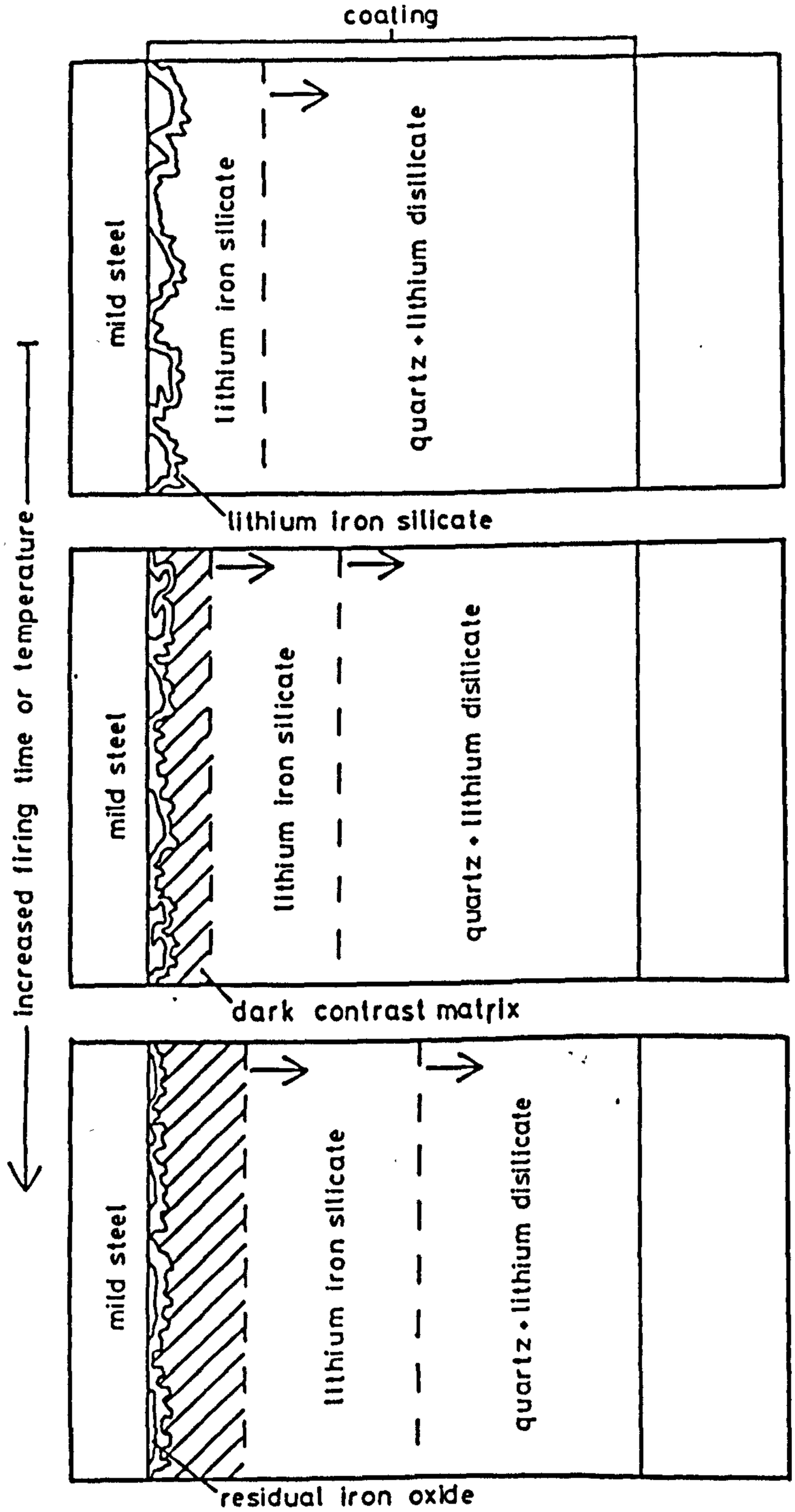

(b) heat-treated coatings.

respectively. For the other firing conditions the dark contrast matrix is present. It extends further into the coating for longer firing times and increased firing temperatures. See Figure 5.2.14(b), which shows schematically how the microstructure is developed.

Table 5.2.12: Influence of ferrous oxide on crystallisation

Weight of FeO added to bulk glass B Wt%	Crystal phases present
0	Lithium disilicate, β-quartz
6.06	β-quartz
12.04	no crystal phases
19.24	no crystal phases
25.17	no crystal phases

5.2.8 Diffusion of ferrous oxide in the coating

It is possible to estimate the diffusion coefficient of ferrous oxide in the enamel coating for the firing temperature range. The coated substrate was approximated to a pseudobinary system. All the glass components were considered as a single component into which the ferrous oxide diffused. For firing times up to 7 minutes iron oxide remains at the interface. The adjacent glass attains a constant concentration, C_o, of ferrous oxide. If the coating-oxide boundary is regarded as stationary, the system may be approximate to diffusion in a semi-infinite medium with a constant source concentration. For such a system the total mass of iron oxide, M_{FeO}, taken into solution after a time t is given by (see Appendix 2):

$$M_{FeO} = 2\ C_o\ (\tilde{D}_{FeO}t/\pi)^{\frac{1}{2}} \qquad C_o = 0.681\ g\ cm^{-3}\ (25\ wt\%)$$

A plot of M_{FeO} with $t^{\frac{1}{2}}$ is shown in Figure 5.2.15(a) using the values in Table 5.2.11. This yields a value for the effective binary diffusion coefficient:

$$\tilde{D}_{FeO} = 8.6\ (\pm 3)\ x\ 10^{-8}\ cm^2 s^{-1}$$

Temperature dependence of a diffusion coefficient is described by an Arrhenius equation:

$$\tilde{D}_{FeO} = \tilde{D}_o\ exp(-Q/RT)$$

Using the iron profiles collected from coatings fired at 930, 950, 960, 970 and 980°C for 5 minutes a value of $\tilde{D}_{FeO}$ can be calculated. A plot of $\log_e \tilde{D}_{FeO}$ with 1/T is shown in Figure 5.12.15(b). The activation energy Q is

$$Q = 266\ (\pm\ 37) \qquad kJ\,mol^{-1}$$

The movement of the β-quartz boundary is directly related to iron concentration. The phase first appears once the iron oxide concentration had dropped below 15 wt% FeO. This provides an accurate indicator to the extent of ferrous oxide diffusion. Assuming the boundary conditions stated above, it is possible to relate the β-quartz boundary position X_b with firing time using equation A.2.7.

$$\text{Let} \quad C_o = 0.681\ g\ cm^{-3}\ (25\ wt\%)$$

$$M_{FeO} = 0.385\ g\ cm^{-3}\ (15\ wt\%)$$

$$X_b = 0.9\ \tilde{D}_{FeO}\ t^{\frac{1}{2}}$$

Using the data in Table 5.2.10, a plot of X_b against $t^{\frac{1}{2}}$ is shown in Figure 5.12.16(a). The effective binary diffusion coefficient is

$$D_{FeO} = 8.67\ (\pm 1) \times 10^{-8}\ cm^2\ s^{-1}$$

D_{FeO} can be calculated for various firing temperatures (5 minutes). A plot of $\log_e D_{FeO}$ with 1/T, Figure 5.2.16(b) yields an activation energy

$$Q = 280\ (\pm 30) \qquad KJ\,mol^{-1}$$

Two problems are associated with both methods. Lithium oxide is not detected. As shown earlier the dissolution of iron oxide is not a simple solution. It involves the interdiffusion between FeO and Li_2O. The measured concentrations in the profiles, Figure 5.2.13, may not represent the true iron level in the coating adjacent the interface. For a coating fired under standard conditions (M9) the concentration is 25 wt% FeO when a constant Li/Si ratio is assumed. The windowless approach allows for the lithium movement towards the interface. The evaluated iron concentration is more likely to be closer to the actual value. It is found to be 23 wt% FeO. The difference is small. The second problem is that the iron oxide coating boundary is not stationary. It moves from about 15μm to the interface. A possible better approach may be a moving boundary system. But the iron oxide boundary is very irregular making it difficult to establish the boundary position.

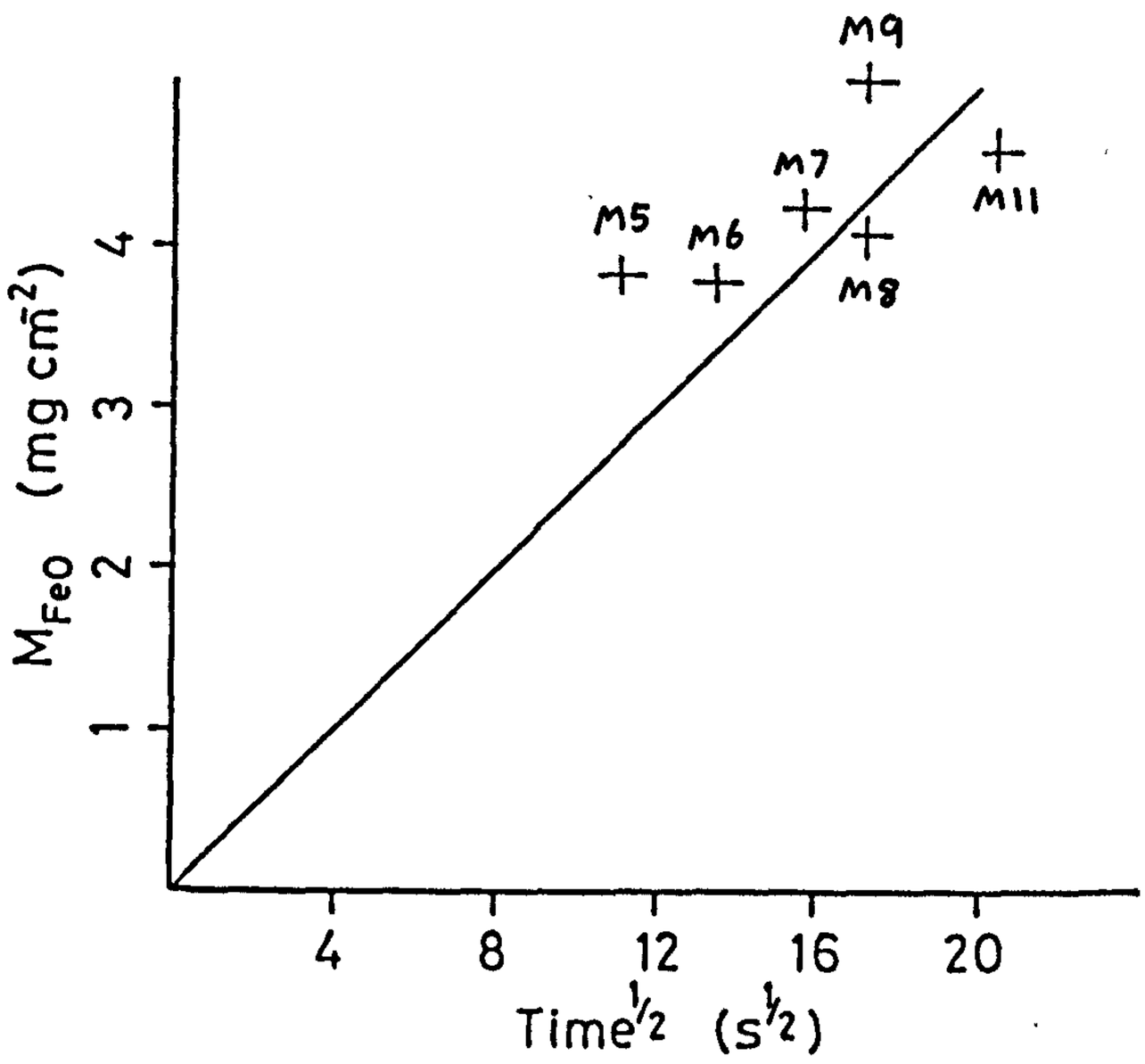

Temperature range 953-970°C
See table 5.2.11

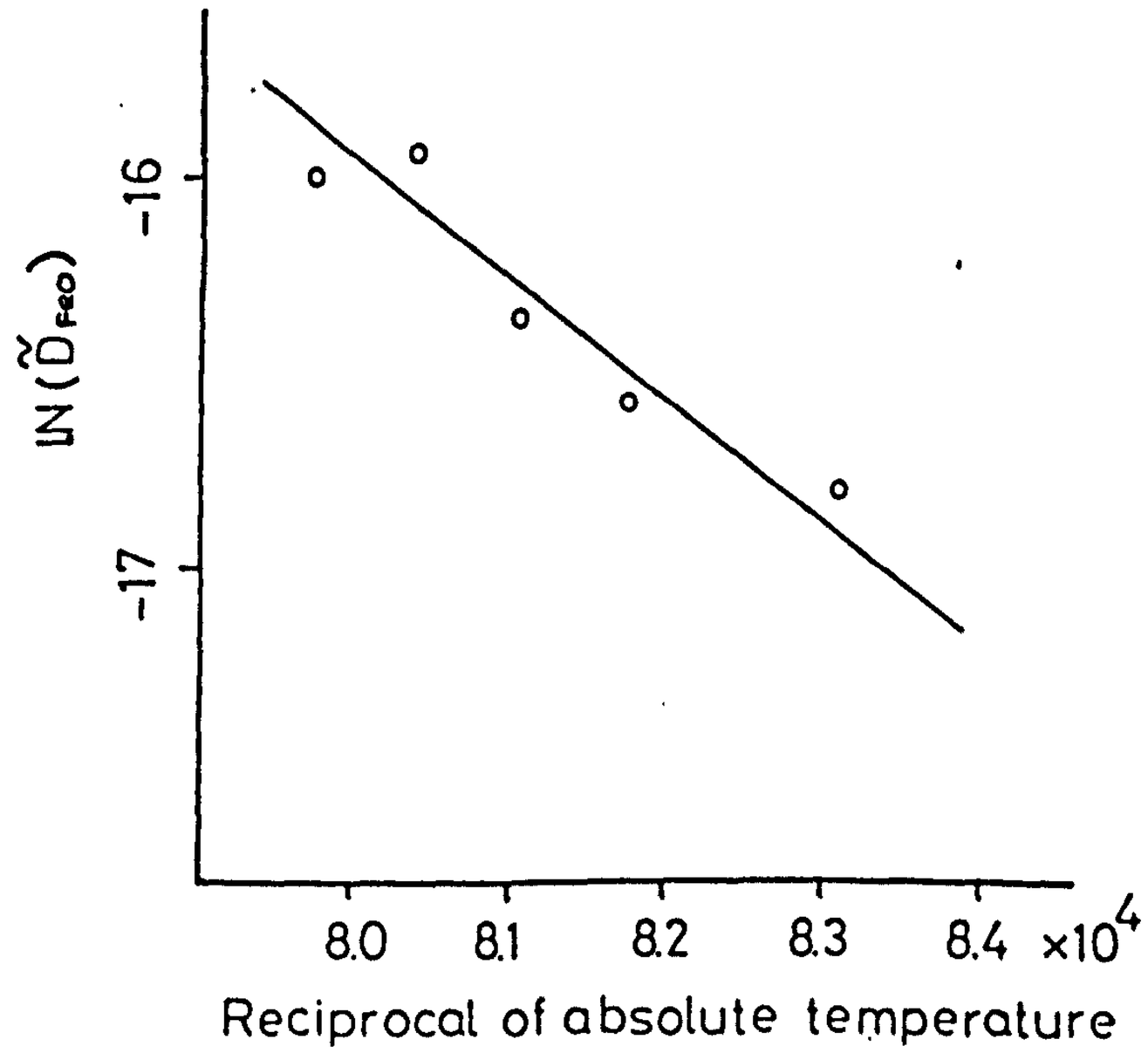

Figure 5.2.15 (a) Plot of M_{FeO} with increasing firing time ($t^{\frac{1}{2}}$).

(b) Plot of D_{FeO} with reciprocal of temperature.

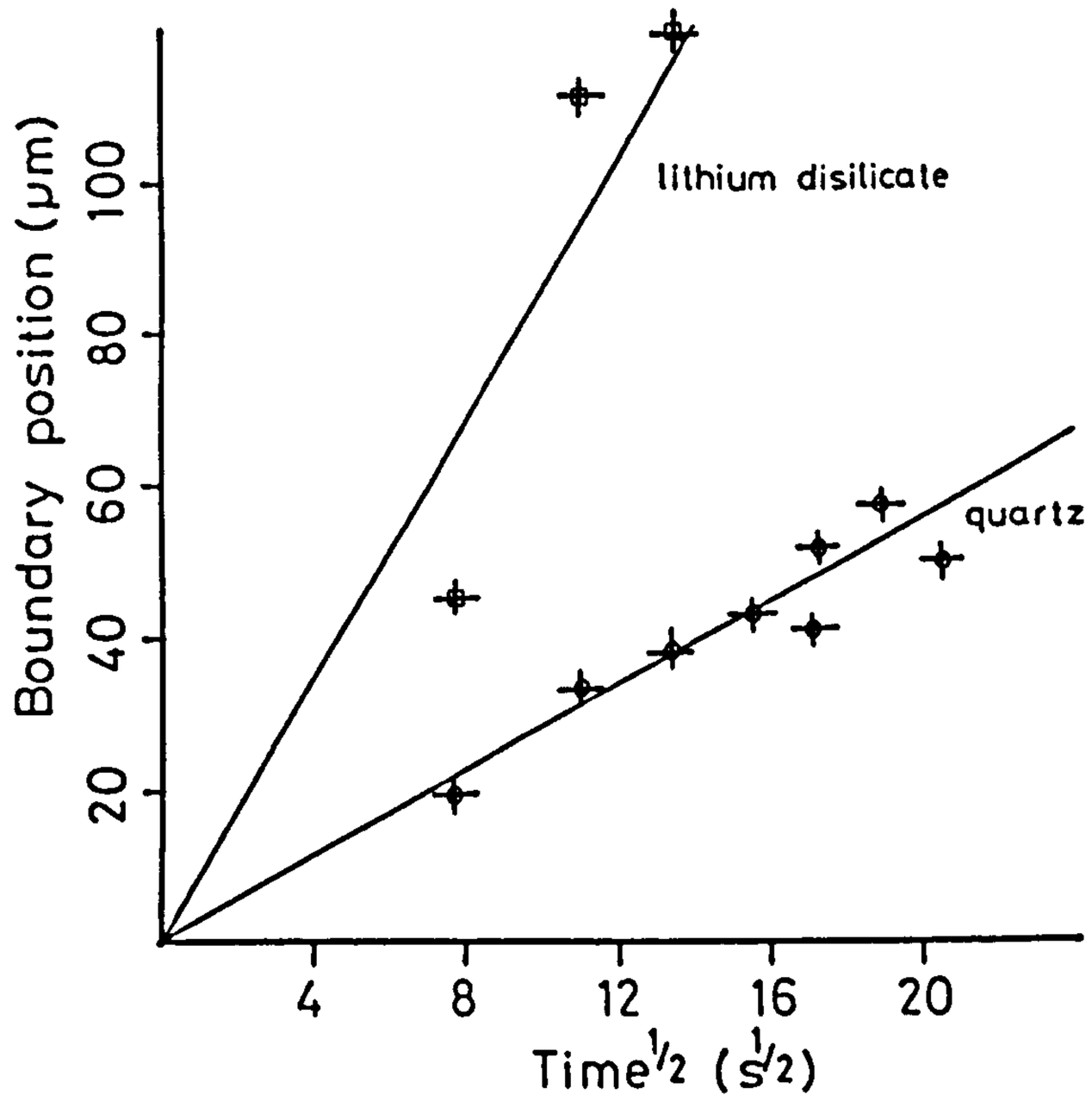

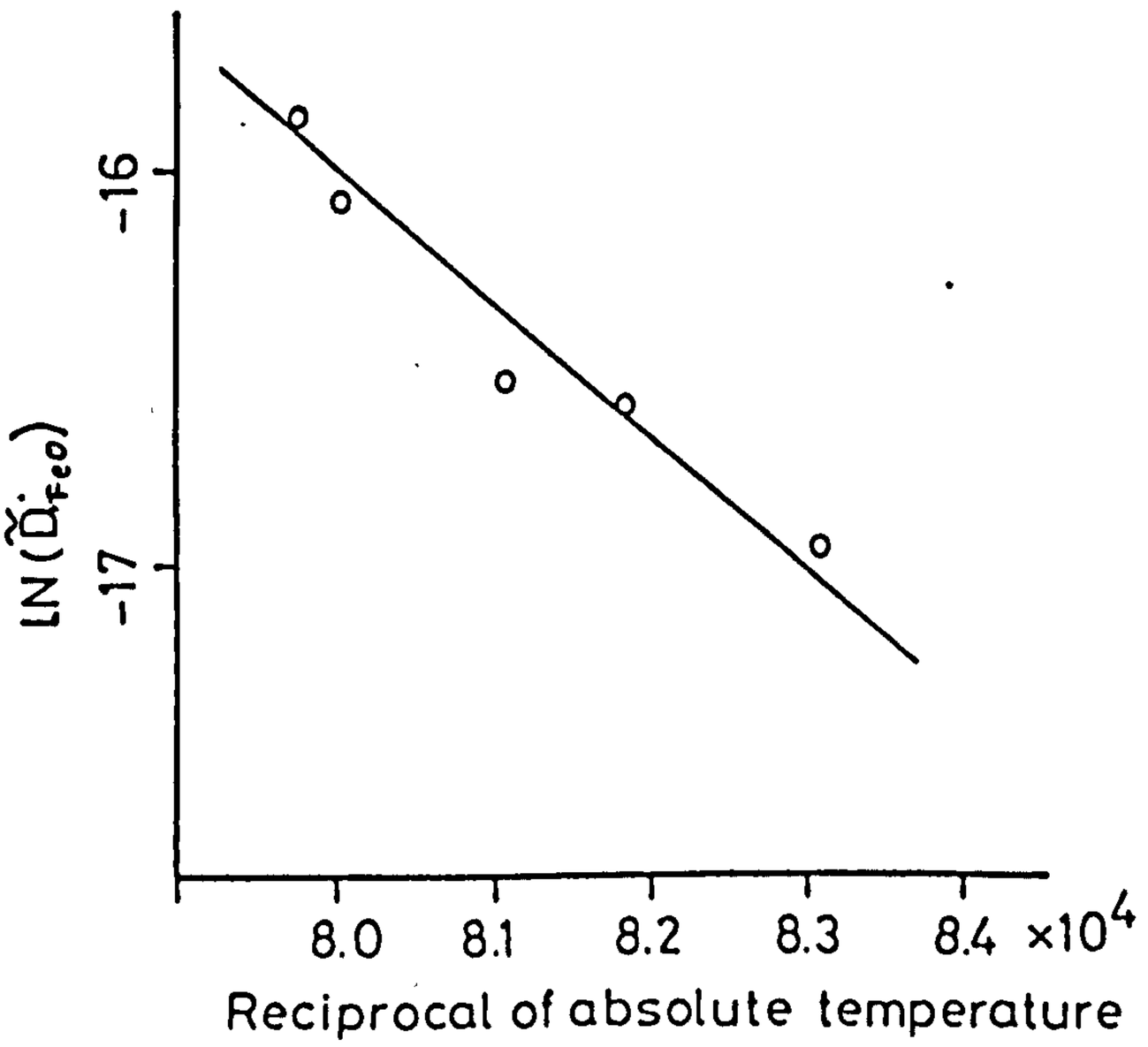

Figure 5.2.16 (a) Plot of X_b with increasing firing time ($t^{\frac{1}{2}}$).

(b) Plot of D_{FeO} with reciprocal of temperature.

5.2.9 Coating adhesion

Tensile adhesive strengths of the coatings were measured using the tensile pull method. Table 5.2.13 lists the adhesion of the various coatings both in the quenched and heat-treated condition. The tensile strength of an iron oxide layer formed on an uncoated mild steel surface preoxidised at 650°C for 15 minutes was also measured. This was done by adhering an aluminium stud directly to the iron oxide and applying a tensile load. Failure occurs with a mean value of 27 MN m^{-2}. The iron oxide is completely removed leaving a clean, metallic surface.

The tensile adhesive strength of all coatings greatly exceeds that of the iron oxide layer. They are regarded as excellent with a value typically 50-60 MN m^{-2}. There is no significant difference between the quenched and heat-treated coatings. The extensive crystallisation produced on heat-treatment appears not to be detrimental to coating adhesion.

Failure often occurs in the epoxy, much more than was the case for chrome-iron coatings. The coating adhesion values reported must be regarded as lower limits. This has made it difficult to discern any possible trends in adhesion with variations in the firing conditions. Adhesive strength is good for short firing times even though substantial amount of residual iron oxide is present at the interface. At long firing times, 7 min at 970°C (M11) or high firing temperature, 5 min 970°C (M9) a slight drop in strength is observed. Once all the oxide has been taken into solution adhesion can not be measured. A thin continuous coating is no longer formed.

The coating is partially removed on failure (providing the expoxy has not failed first). The exposed ceramic surface appears

Table 5.2.13: Coating adhesion

Label	Firing conditions		Tensile adhesion MN m^{-2}	
	Minutes	°C	Quenched	Heat-treated
-	oxide layer		27.2 ± 5 (0)	
M15	5	930	47.4 ± 10 (2)	43.9 ± 8 (5)
M16	5	950	55.5 ± 18 (1)	69.6 ± 13 (1)
M8	5	960	49.3 ± 29 (1)	64.1 ± 9 (5)
M9	5	970	36.8 ± 16 (0)	45.0 ± 11 (1)
M5	2	956		54 ± 18 (0)
M6	3	956		76.8 ± 9 (3)
M7	4	963		53.2 ± 11 (2)
M8	5	960		54.2 ± 14 (1)
M10	6	976		64.1 ± 9 (5)
M11	7	970		48.8 ± 10 (0)

( ) number of failures in epoxy out of a total of 5 measurements

Table 5.2.14: Composition of exposed coating surface

Region	Element at% (±0.1%)					
	Al	Si	P	K	Zn	Fe
Whole surface	0.5	17.2	0.4	0.7	2.5	78.9
Dark contrast features	1.3	45.7	1.0	1.1	5.6	45.7
Light contrast features	0	1.5 (excluding Li and O)	0.0	0.2	0.5	97.25

dull and black. Electron microscopy reveals two regions of different backscatter contrast. See Figure 5.2.17. Quantitative EDX analysis over a large area of the exposed surface detects a high concentration of iron, Table 5.2.14. A large amount of iron oxide is attached to the exposed coating surface. It corresponds to the bright contrast areas in the electron micrograph. The exposed metal surface is metallic and rough. It has a uniform backscatter contrast. Little or no residual iron oxide remains. On failure parts of the coating are removed. Fracture occurs along the coating mild steel boundary or the iron oxide mild steel boundary when pockets of iron oxide are encountered.

Abrasion of the substrate before preoxidation does not produce any measurable change in adhesion. It remains good.

Figure 5.2.17 Backscattered electron micrograph of exposed surface of coating removed during tensile adhesion testing (M9H).

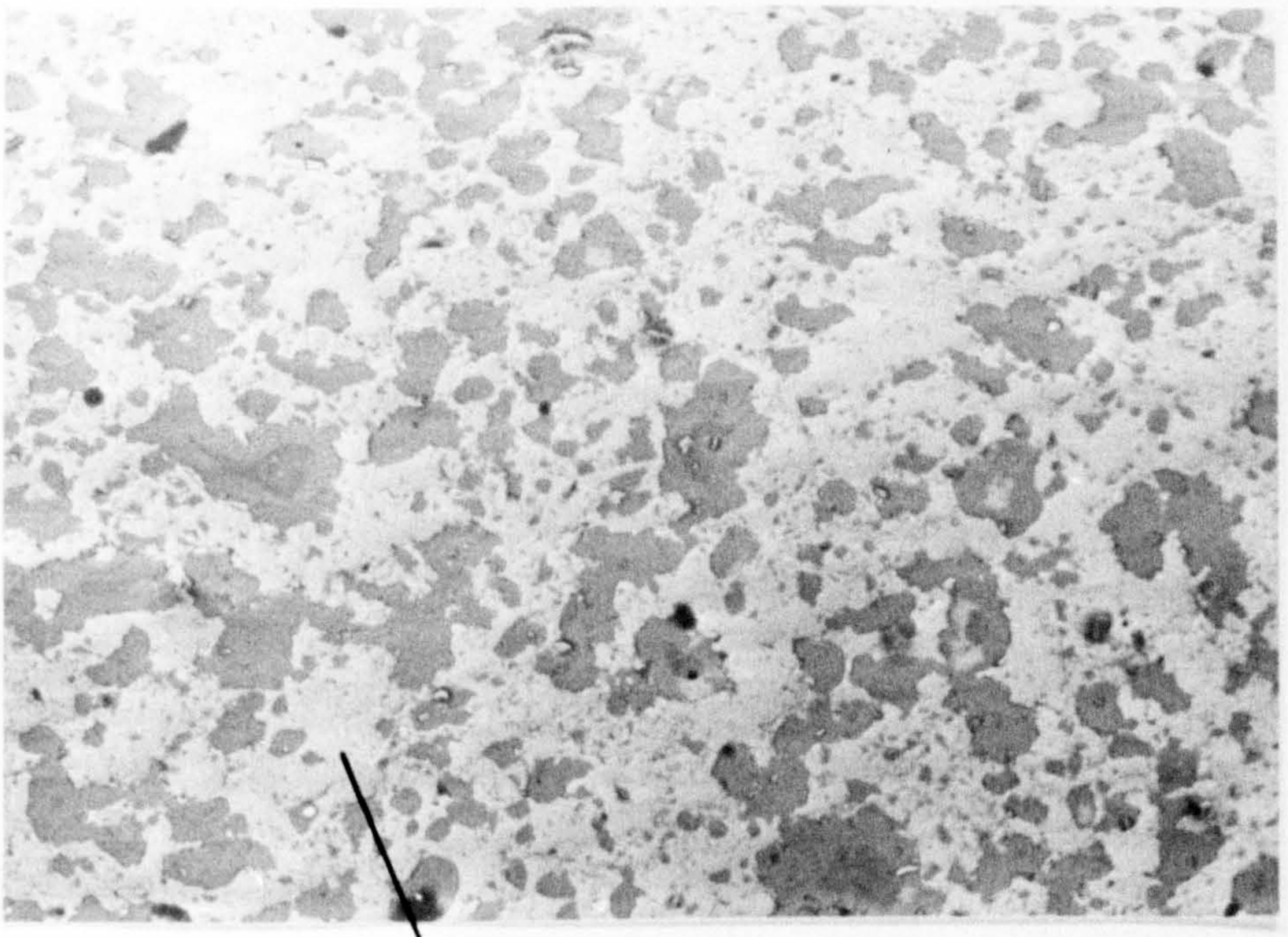

100 µm

ferrous oxide

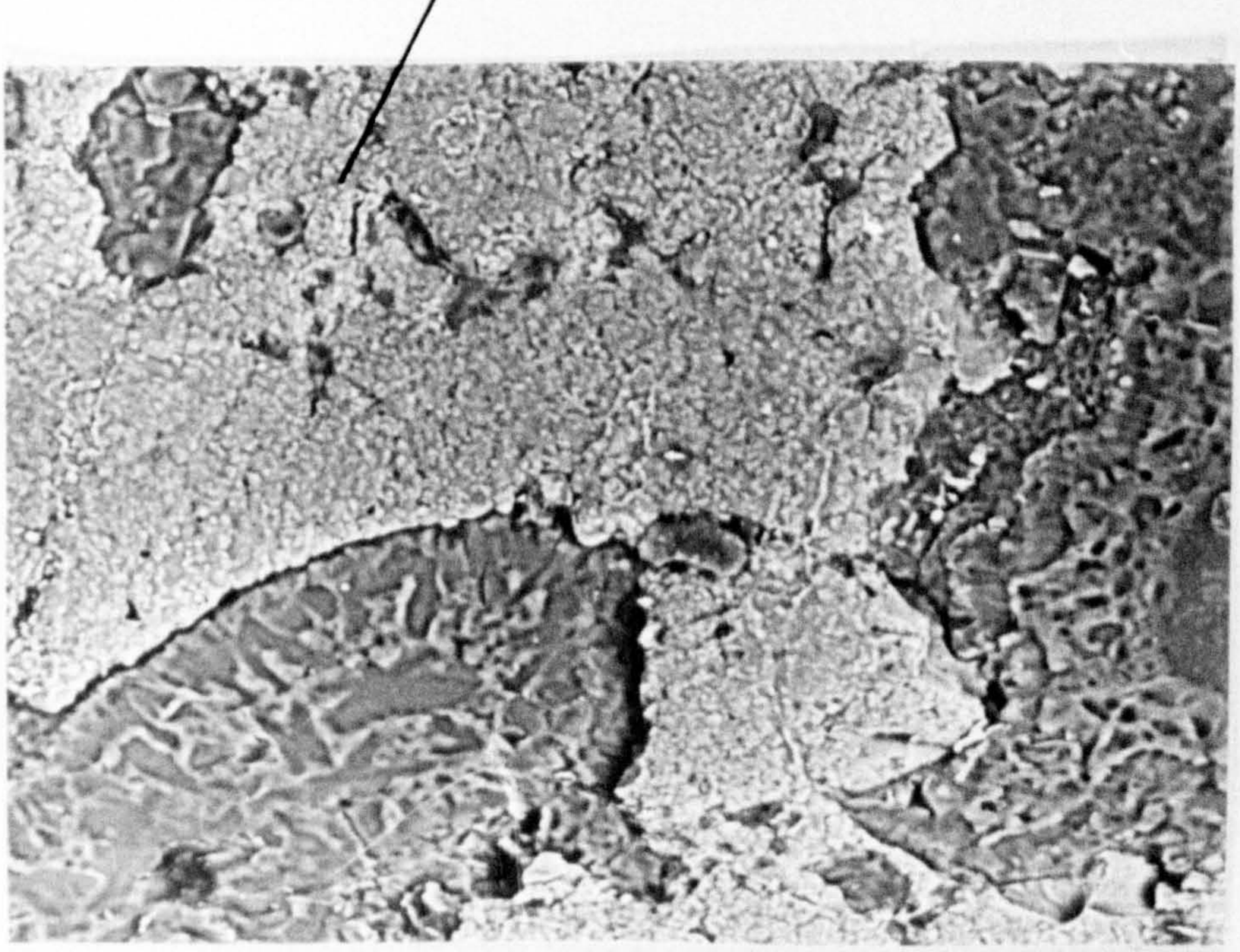

10 µm

5.2.10 Influence of adherence oxides

Wetting:

To the parent glass B, 0.25 wt% cobalt oxide (CoO) or nickel oxide (NiO) was added. Glass powder with and without adherence oxides was screen printed on to the mild steel surface. These were preoxidised in air by holding at 650°C for 15 minutes - the standard preoxidation. A firing was given using a temperature of 970°C and times of 5, 8, 15 minutes. The resulting coatings are described in Table 5.2.15. With no adherence oxides present, the coating begins to draw up after 8 minutes and by 15 minutes it ceases to wet the mild steel. The addition of minor amounts of adherence oxides cause wetting to continue for all firing times used. With nickel oxide the surface acquires a dull black appearance. Identified by x-ray diffraction as magnetite (Fe_3O_4). It first appears around the coating edge then increases towards the centre with firing time.

If the mild steel is not preoxidised before firing wetting will not occur. This remains so even if adherence oxides have been added.

Cobalt oxide (5 min 970°C): M19

Microstructure:

The interfacial microstructure of a quenched coating containing 0.25 wt% CoO is shown in Figure 5.2.18. All the features observed in a coating without adherence oxides are present. Residual iron oxide and dendritic growth of lithium-iron-zinc-silicate are observed. An additional feature is a small spherical, bright contrast phase

Table 5.2.15: Influence of adherence oxides on wetting ability of coatings on mild steel

Firing Time	Coating		
(970°C)	No adherence oxides	0.25 wt% NiO	0.25 wt% CoO
5	W	W	W
8	N	W	W
15	N	W	W

W - good wetting, thin Continuous Coating

N - non-spreading, drawn up Coating

immediately adjacent to the interface.

It is typically 1 μm in dimension. A thin layer having a similar bright contrast is attached to parts of the residual iron oxide. The contrast suggests both phases are metallic. Quantitative EDX analysis reveals the spherical phase to be a metallic alloy. It has a composition of 95 at% Fe and 5 at% Co. Table 5.2.16.

After heat-treatment a microstructure is developed similar to that when adherence oxides are absent. The extra metallic feature has increased in size to about 4 μm, See Figure 5.2.18. Its composition has an increased iron content to give a composition of 98 at% Fe and 2 at% Co. The quenched and heat-treated coatings were removed. X-ray patterns collected from the exposed coating surface (see Figure 5.2.19(a) and (b)). Both exhibit a single peak at 42.2 2θ (d = 2.14 Å), which relates to the presence of residual iron oxide, as discussed in Section 5.2.2.

Element distribution:

The element distributions across the interface of a quenched coating are displayed in Figure 5.2.20(a). In general it is similar to that without adherence oxides. However some additional features are noticeable:

- Iron shows a peak in its profile associated with the metallic alloy phase.

- Cobalt also shows a slight peak at this point.

Full quantitative profiles for silicon, potassium and iron are

Figure 5.2.18 Backscattered electron micrographs of coatings containing 0.25 wt% CoO on mild steel.

20um (a) 5 minutes 970°C M19

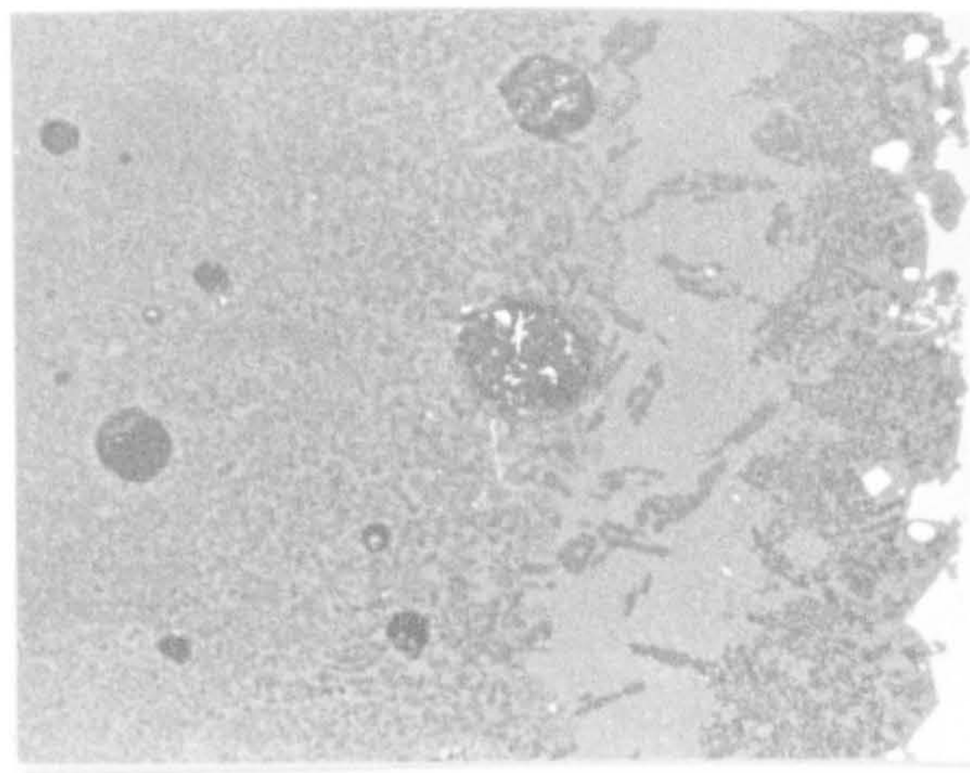

(b) M19H

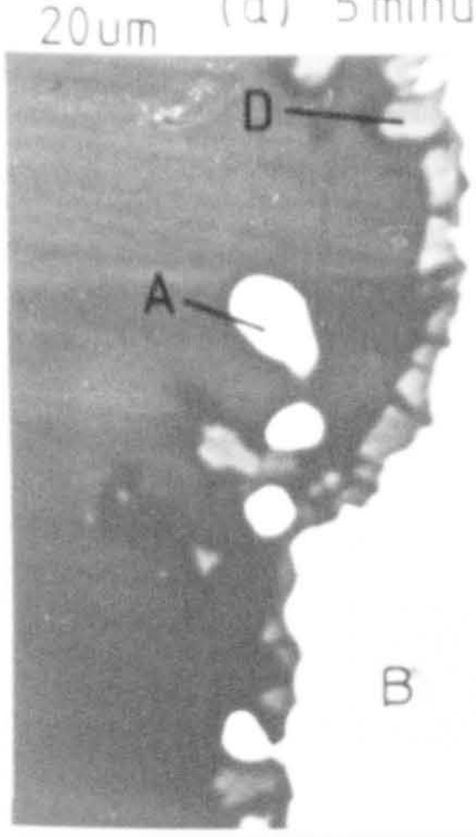

4 um B ferrous oxide
C dendrite

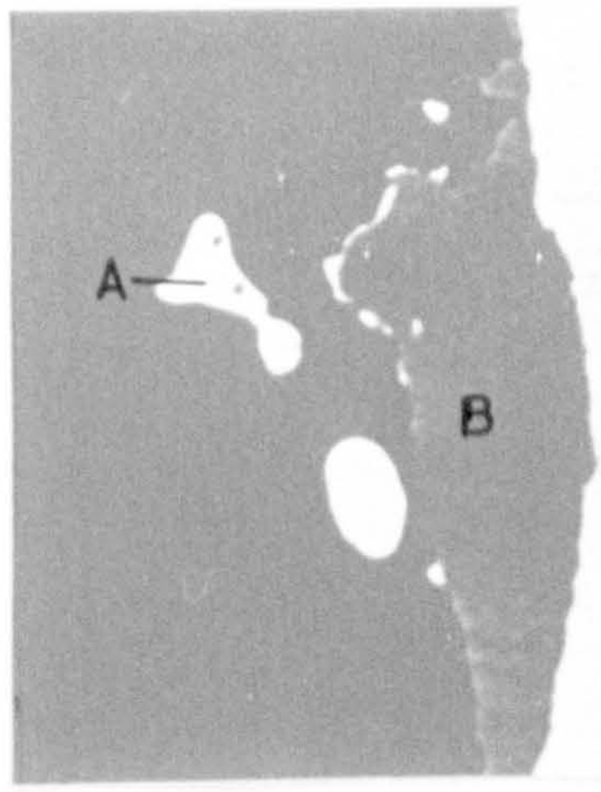

C mild steel

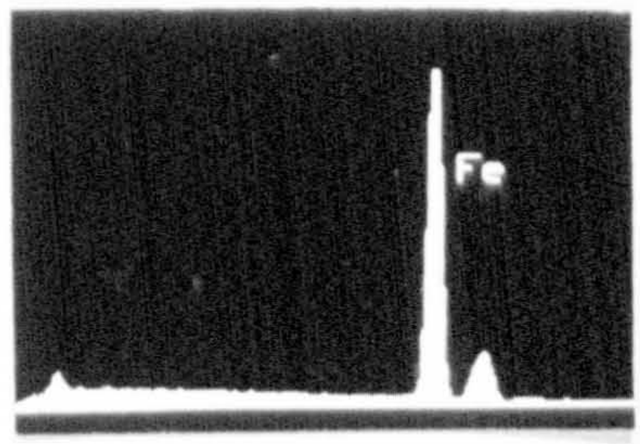

A metallic alloy

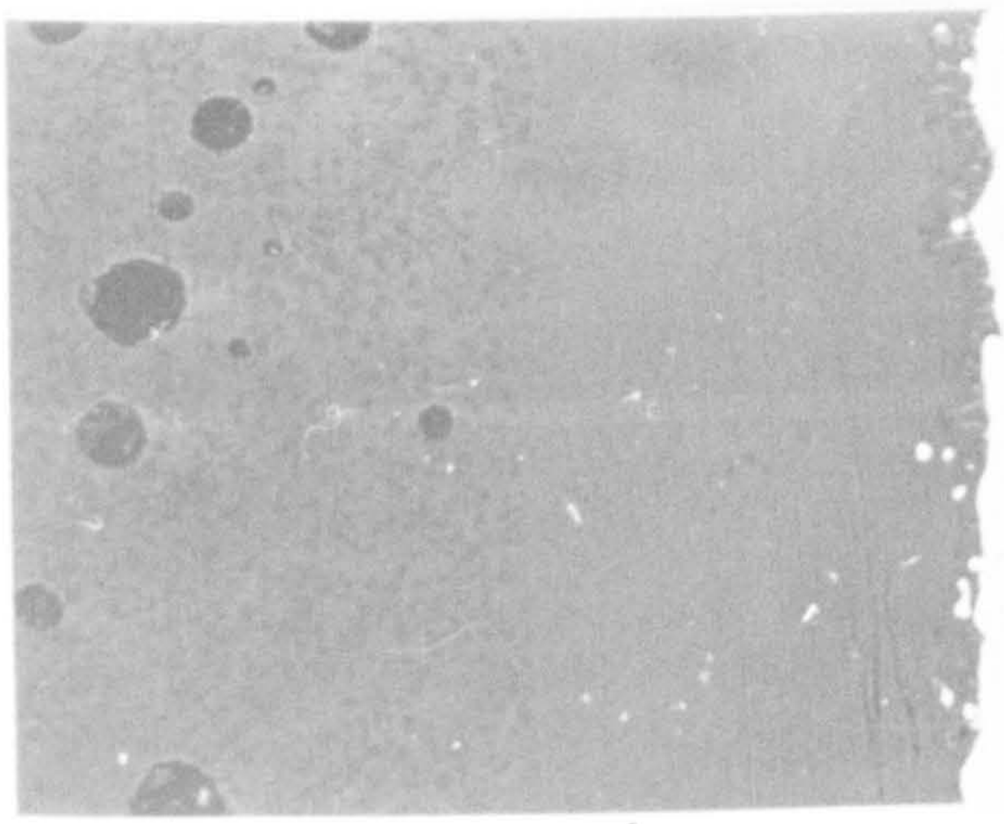

20 um (c) 15 minutes 970°C M21

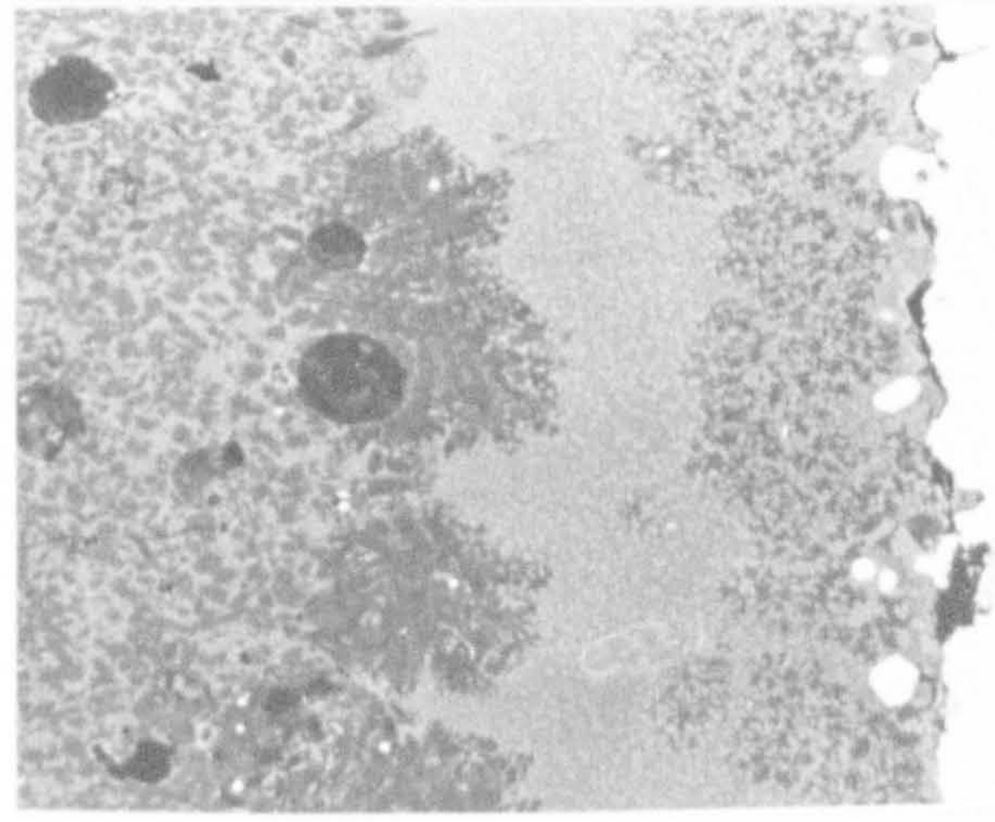

(d) M21H

Table 5.2.16: Composition of metallic alloy phase

Adherence oxide	Firing Conditions		Element at% (±0·1%)			
	Minutes	°C	Quenched		Heat-treated	
			Fe	Co	Fe	Co
CoO (M19)	5	970	94.7	5.3	98.0	2.0
(M21)	15	970	91.9	8.1	97.0	3.0
			Fe	Ni	Fe	Ni
NiO (M22)	5	970	95.9	4.1	95.4	4.6
(M24)	15	970	97.1	2.9	98.9	1.1

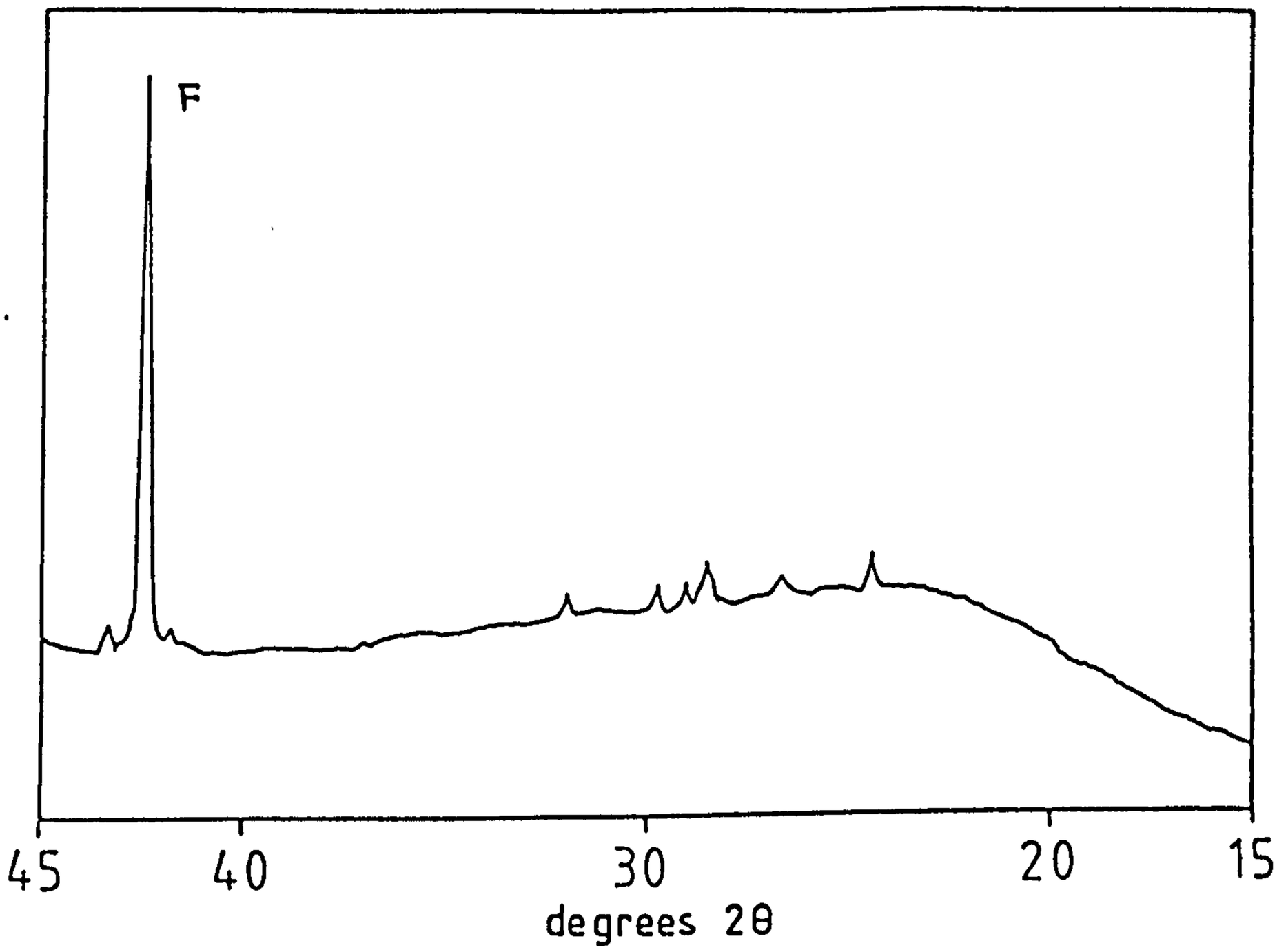

(a) fired only coating, M19.

F- ferrous oxide

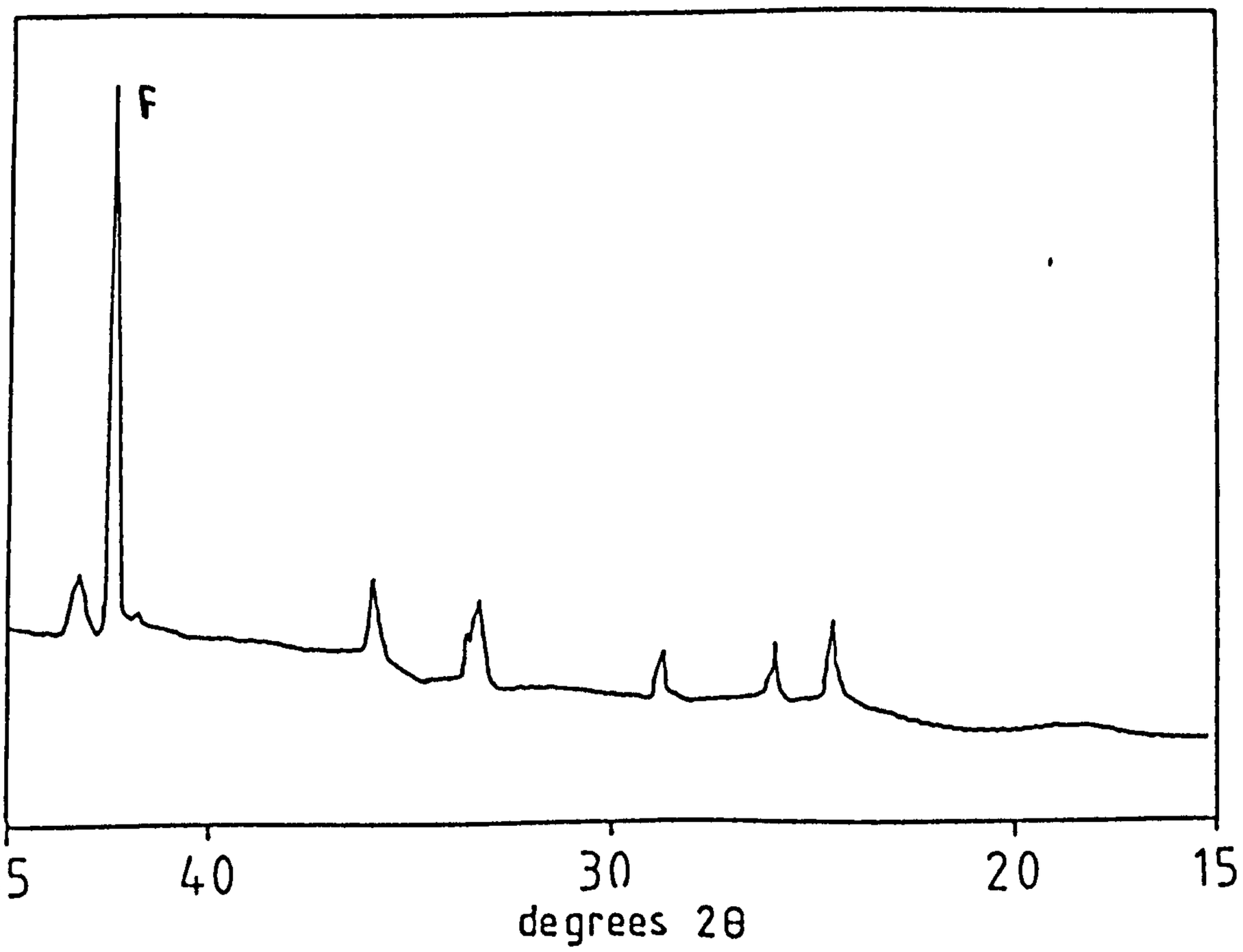

(b) heat-treated coating, M19H.

Figure 5.2.19 XRD patterns collected from the exposed coating surface.

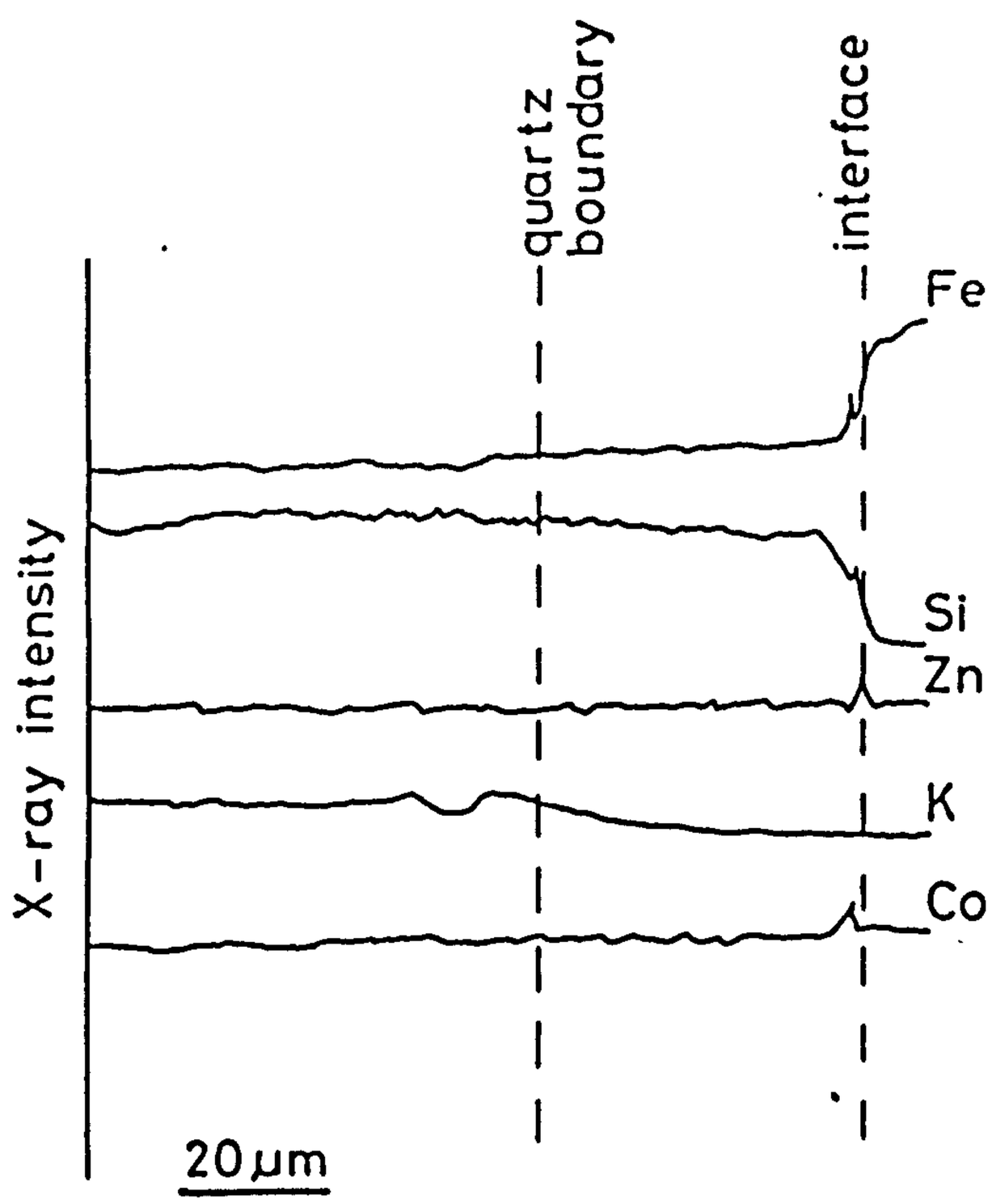

(a) fired only coating, M19.

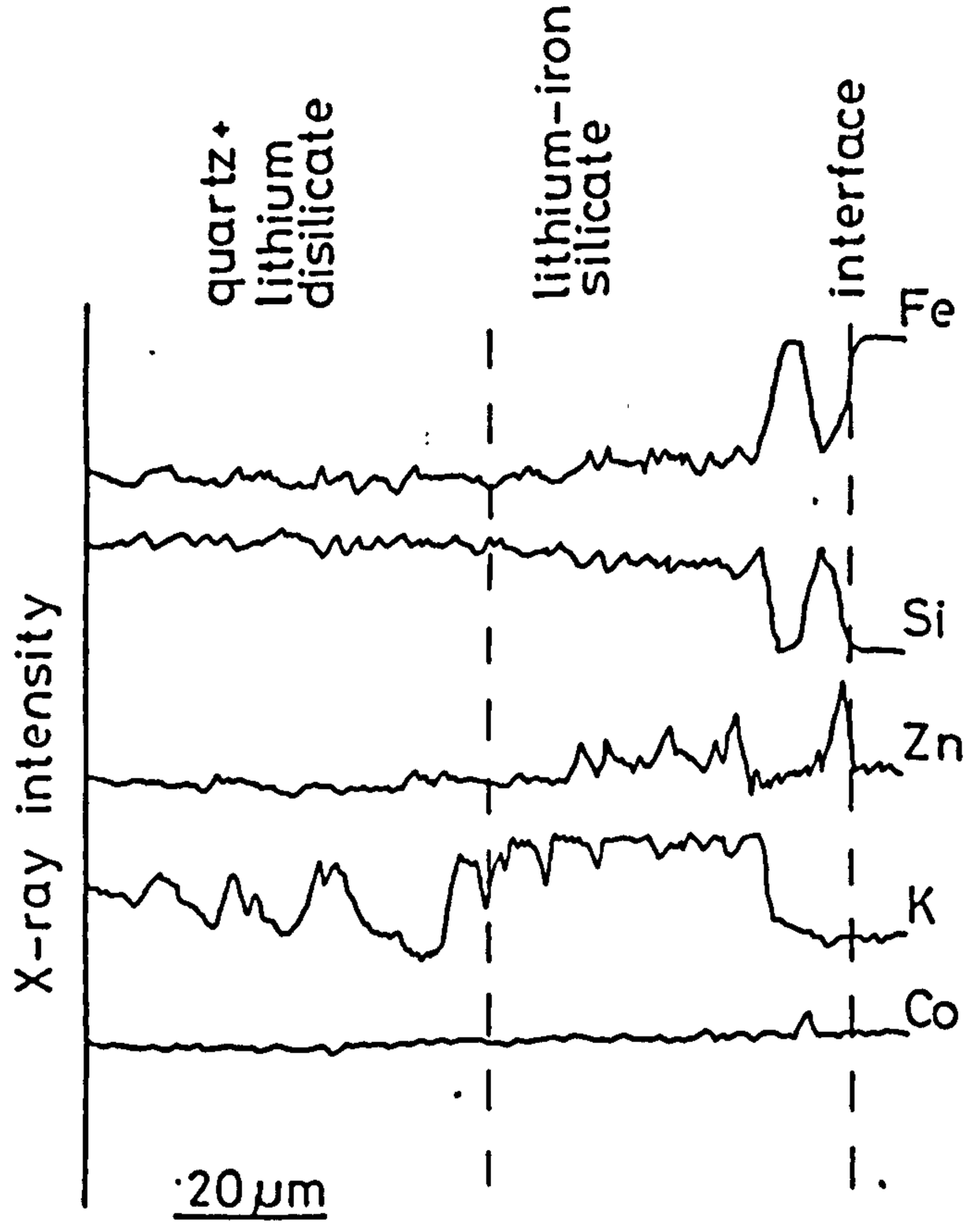

(b) heat-treated coating, M19H.

Figure 5.2.20 Element distribution collected from linescans conducted across the interface.

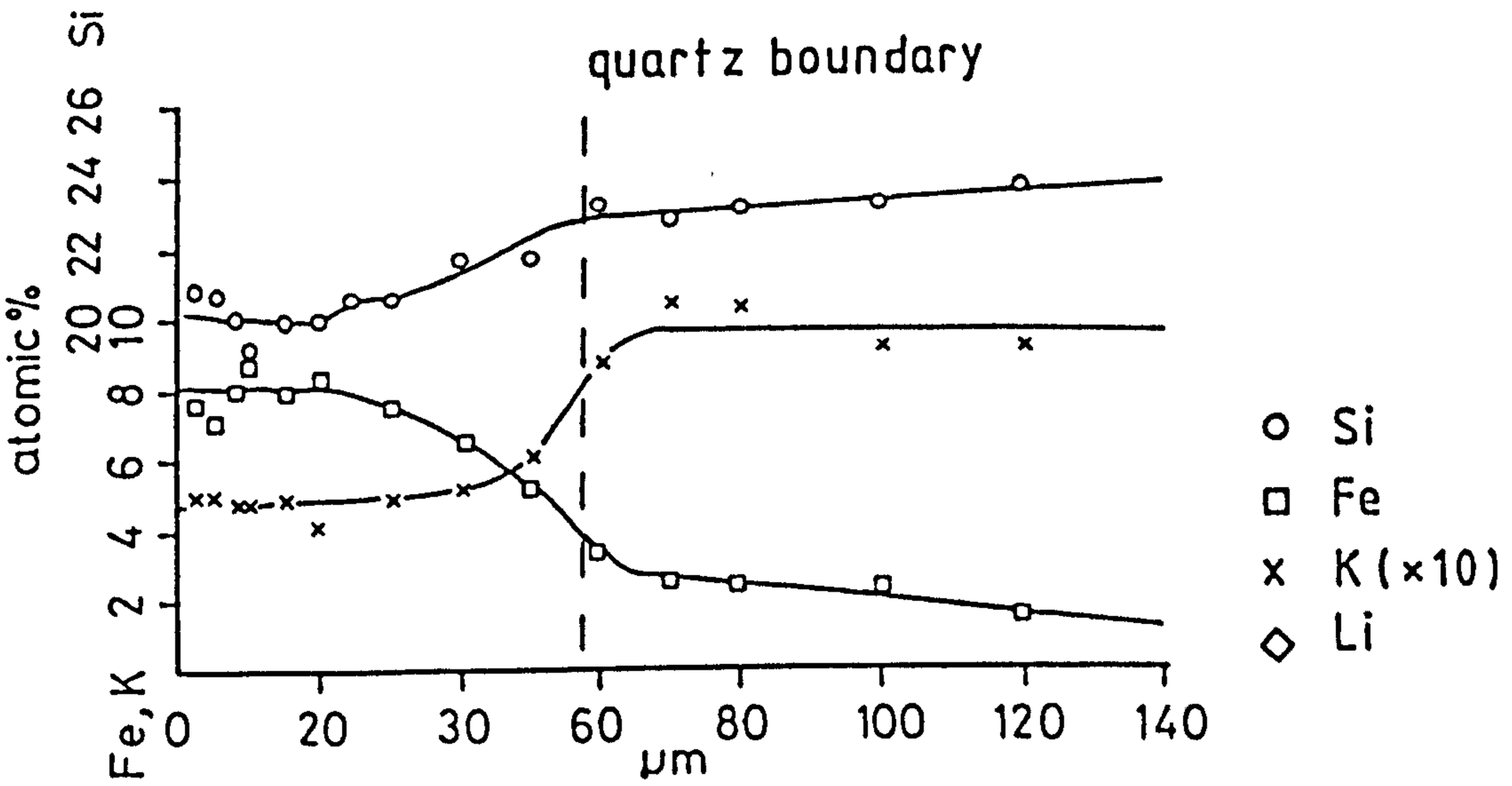

Figure 5.2.21 Quantitative element distribution across the interface of a fired only coating, M19.

given in Figure 5.2.21. Iron is present in the adjacent coating with a concentration of 8 at% (30 wt%).

For the heat-treatment coating the element distributions are displayed, Figure 5.2.20(b). It is similar to that without adherence oxides. The additional features noticeable are again a peak in the iron and cobalt profiles and a dip in the silicon profile. These occur where the probe crosses the metallic alloy.

Cobalt oxide (15 min 970°C): M21

The interfacial microstructure of a quenched coating is shown in Figure 5.2.18. Very little residual iron oxide now remains. Dendrites of lithium-iron-zinc-silicate are still present. The metallic alloy has a composition of 91.9 at% Fe and 8.1 at% Co.

After heat-treatment the metallic alloy phase has increased in size, Figure 5.2.18. The metallic alloy has an increased iron concentration to 97 at% Fe and 3 at% Co. Also noticeable is the occasional metallic phase in the bulk coating.

Nickel oxide (5 min 970°C): M22

Microstructure:

The addition of 0.25 wt% NiO has a more pronounced effect on the interfacial microstructure. Figure 5.2.22 shows the interface region of a quenched coating. There is no residual iron oxide remaining at the interface. Dendritic growth does not occur. A metallic phase appears adjacent to the mild steel. It has a spherical form and is typically 1 μm in diameter. Quantitative EDX analysis gives a

composition of 96 at% Fe and 4 at% Ni for this phase. Within the bulk coating a dispersion of fine metallic particles is noticeable. They exist in a region extending from the interface to the boundary when β-quartz first appears.

On heat-treatment the bulk microstructure developed is similar to that when no adherence oxides are present, Figure 5.2.22. The coating is easily detached during the preparation stage. This makes it impossible to examine the coating-mild steel boundary intact. It is assumed the coating pulls away from the substrate with no loss of material. Very few metallic alloy particles appear immediately adjacent to the interface. Those observed have not increased in size or changed significantly in composition. Quantitative EDX analysis gave a composition of 95% Fe and 5% Ni. The x-ray pattern collected from the exposed surface of a quenched coating is shown in Figure 5.2.23(a). No peaks are observed. For a heat-treated coating only minor peaks are present. A peak at 42.2° 2θ was not observed for either coating. No iron oxide is present at the interface to give the characteristic x-ray peak. This is in agreement with the observation of no residual iron oxide in the electron micrographs.

Element distribution:

The element distribution across the interface of a quenched coating are displayed in Figure 5.2.24(a). The most notiecable features are:

- Iron shows a peak adjacent to the interface corresponding to the metallic alloy phase.

- Nickel also has a small peak at this position.

Figure 5.2.22 Backscattered electron micrographs of coatings containing 0.25 wt% NiO on mild steel.

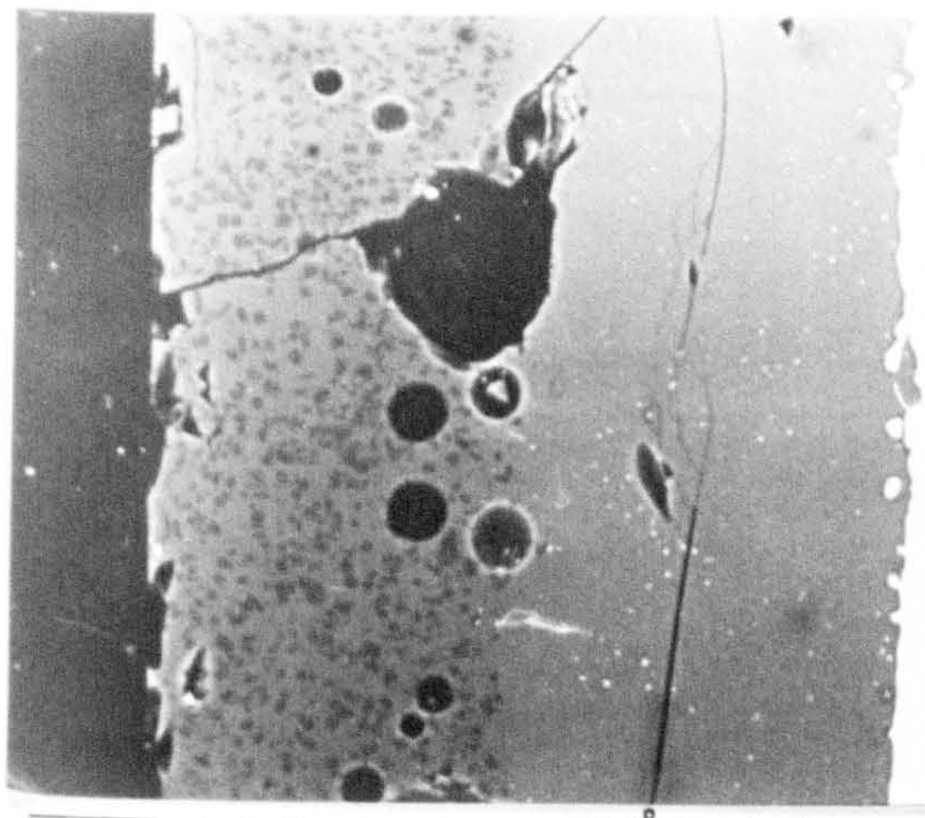

20 um (a) 5 minutes 970°C M22

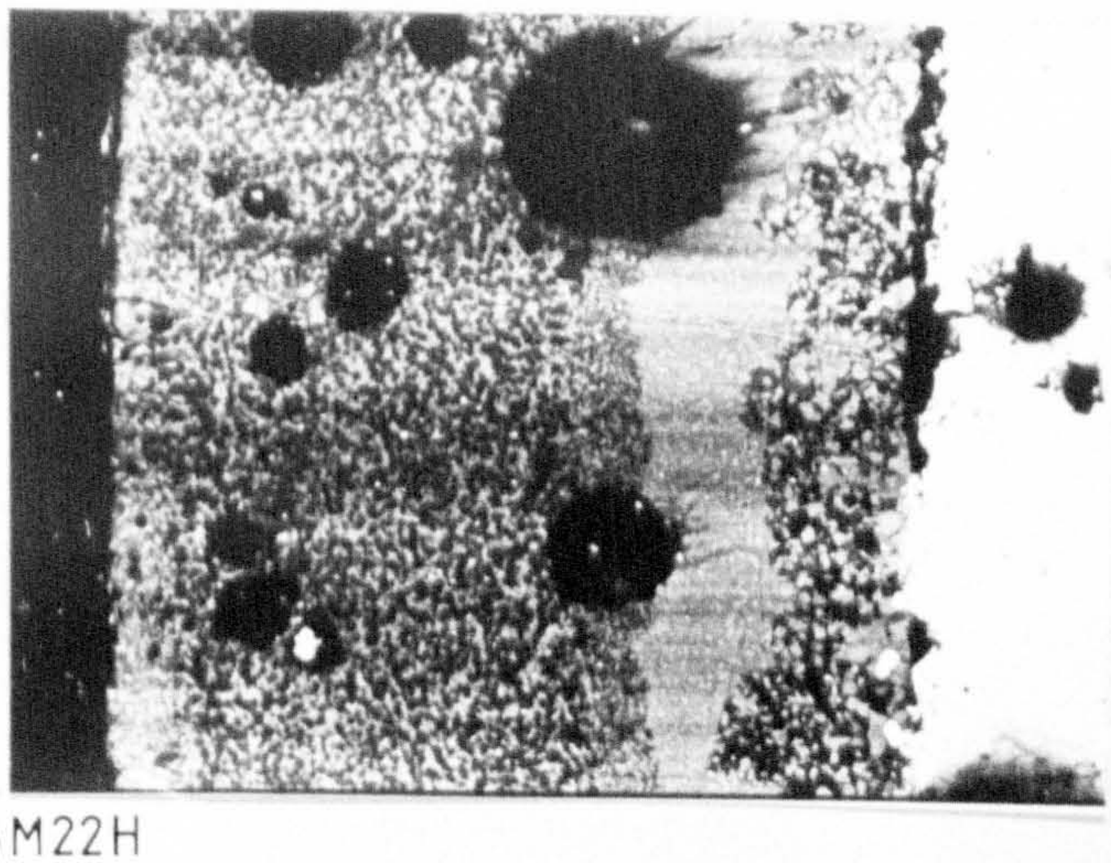

(b) M22H

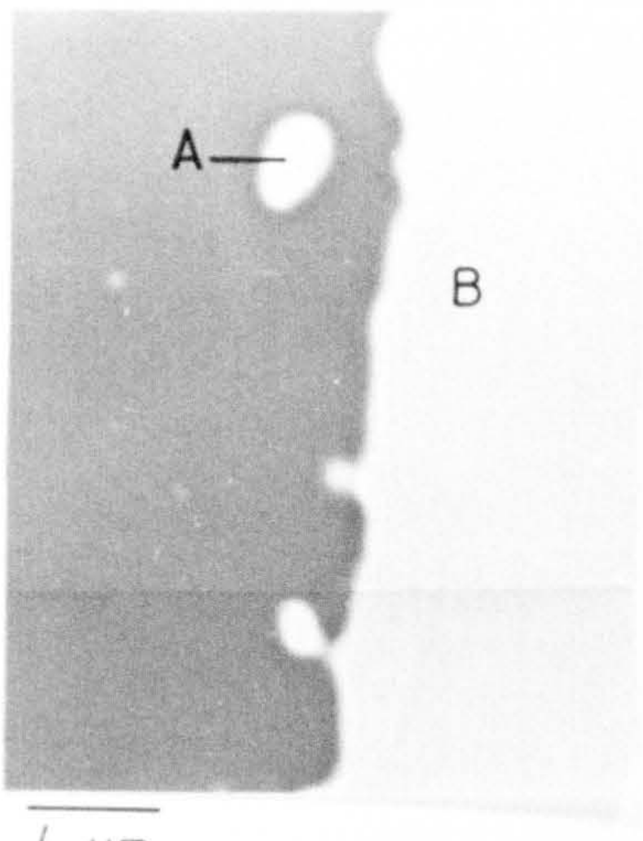

4 um

A metallic alloy
B mild steel

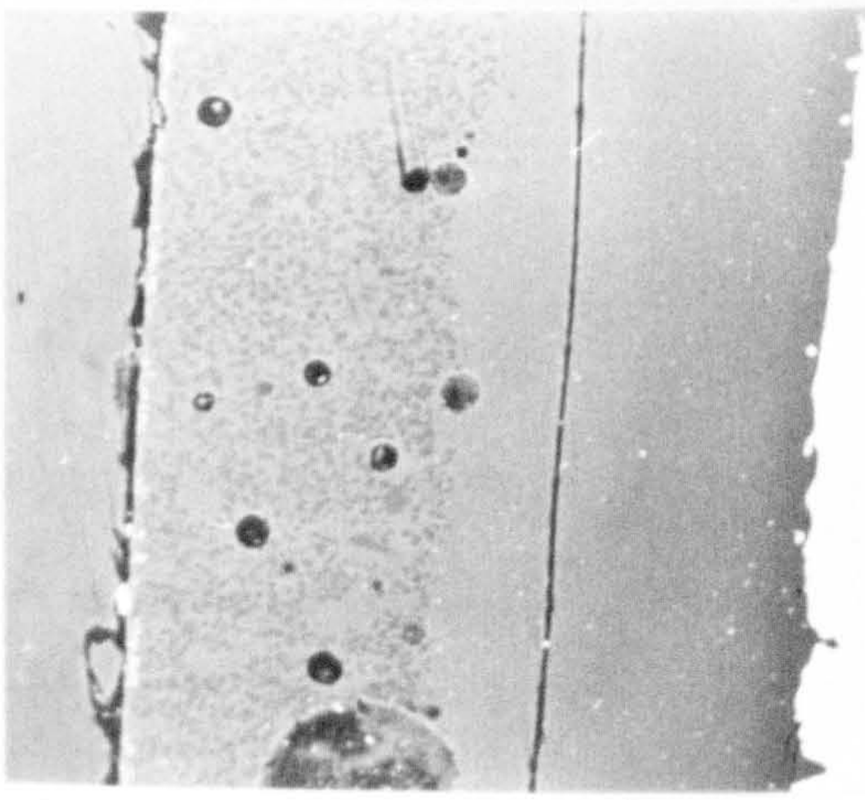

20 um (c) 15 minutes 970°C M24

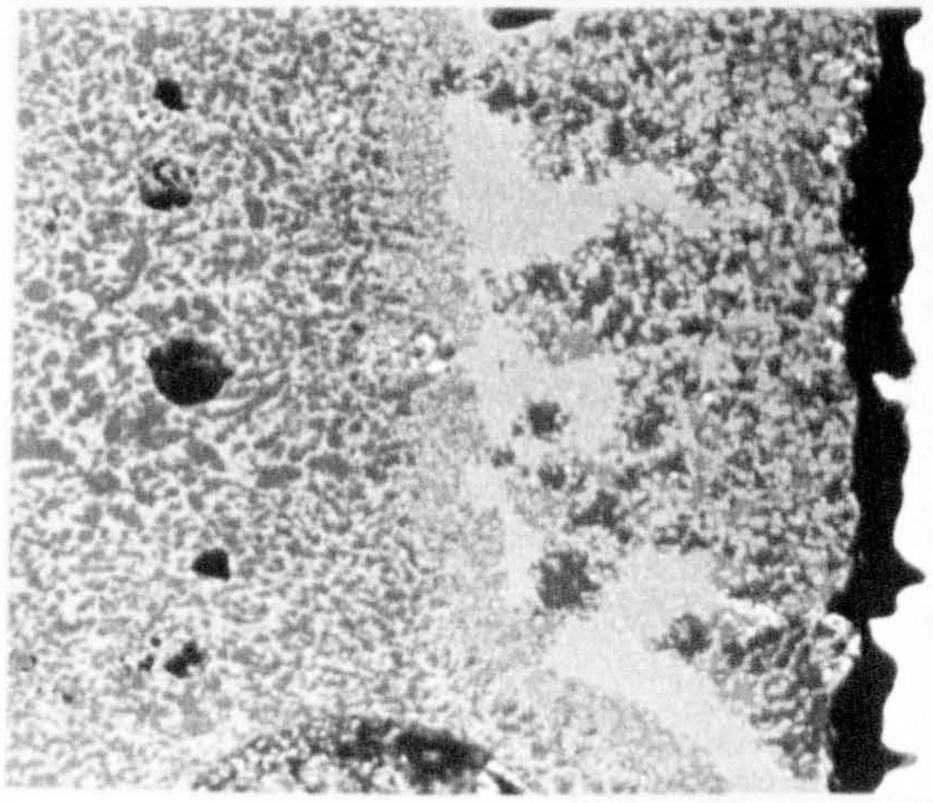

(d) M24H

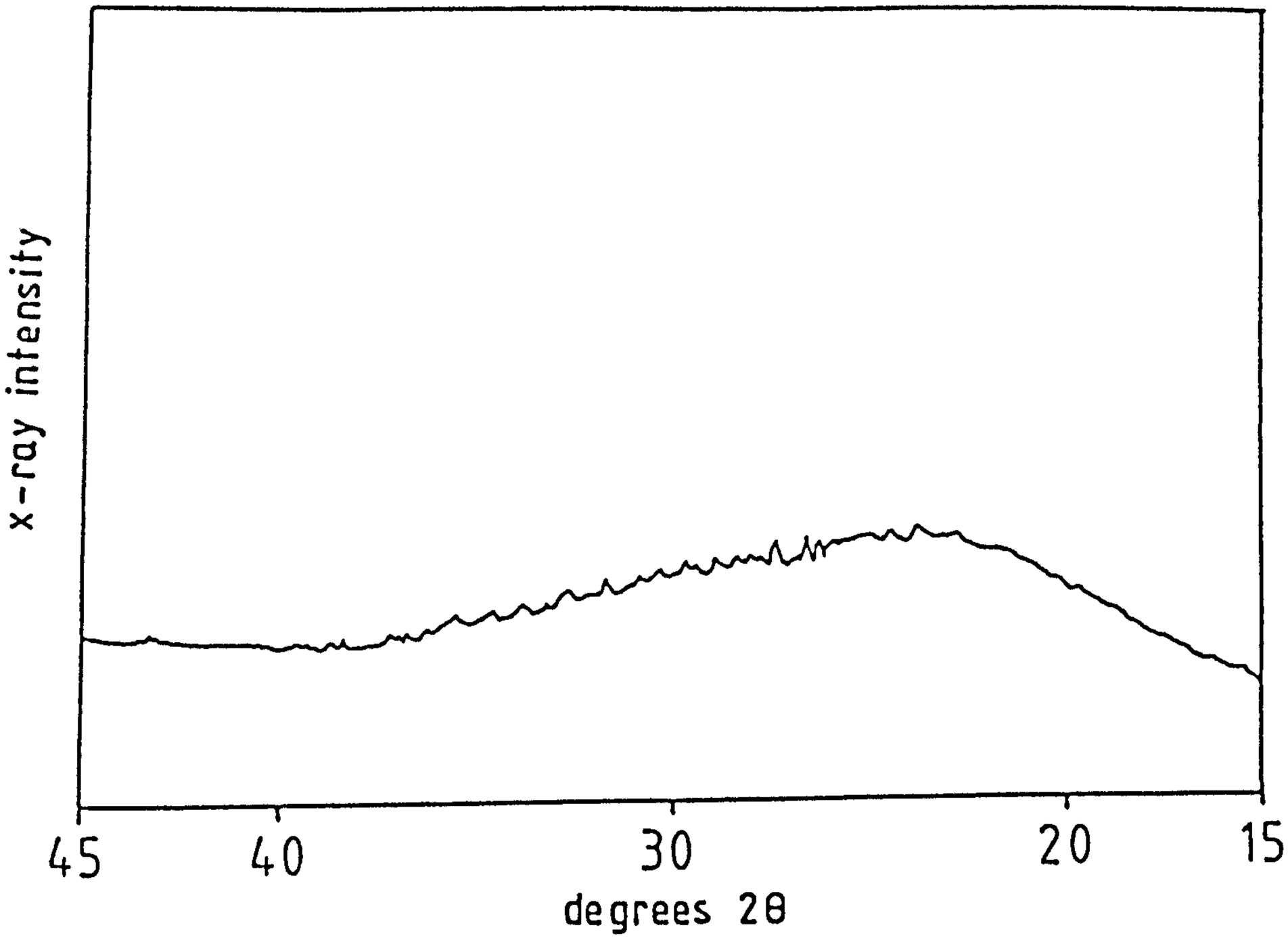

(a) fired only coating, M22.

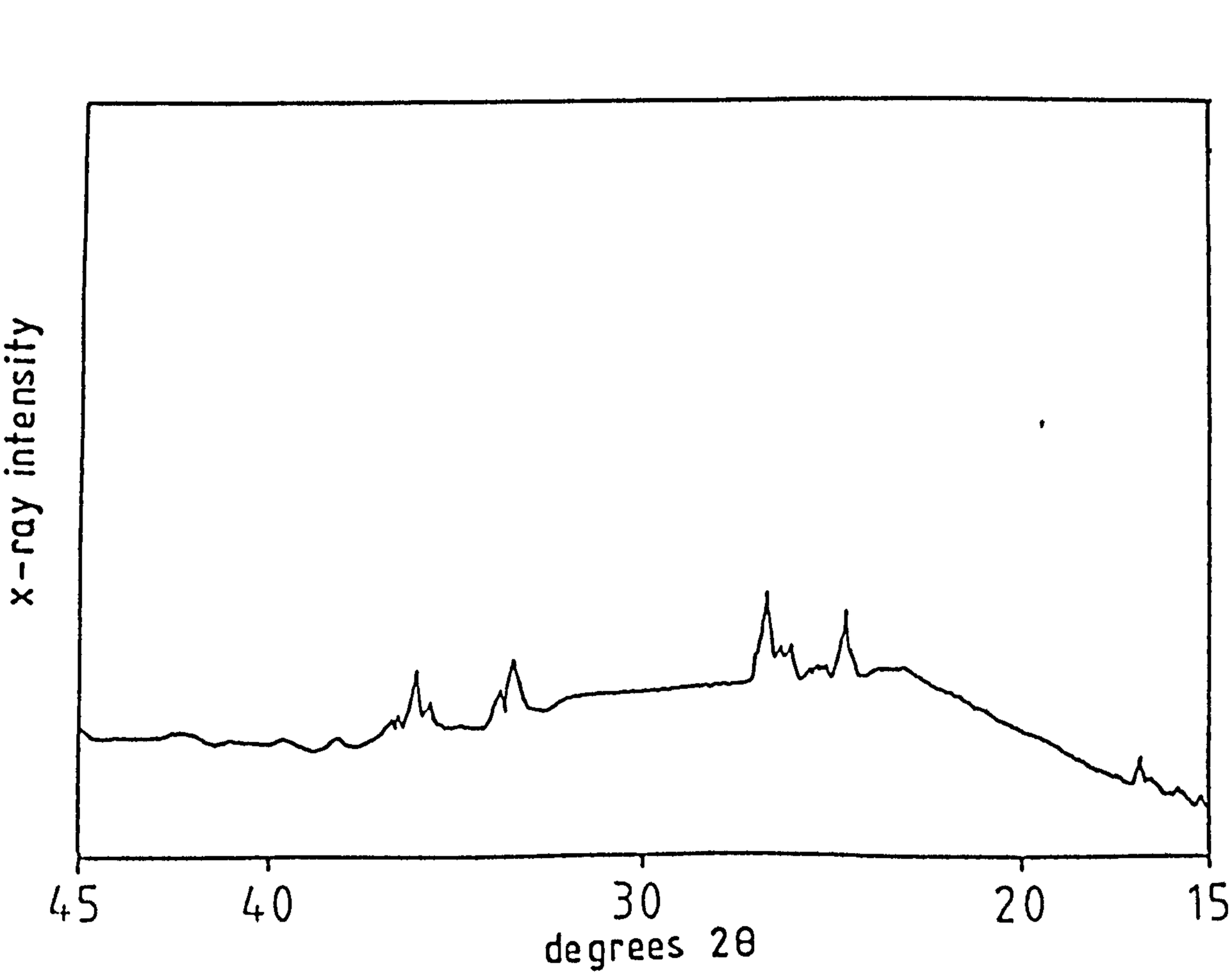

(b) heat-treated coating, M22H.

Figure 5.2.23 XRD patterns collected from the exposed coating surface.

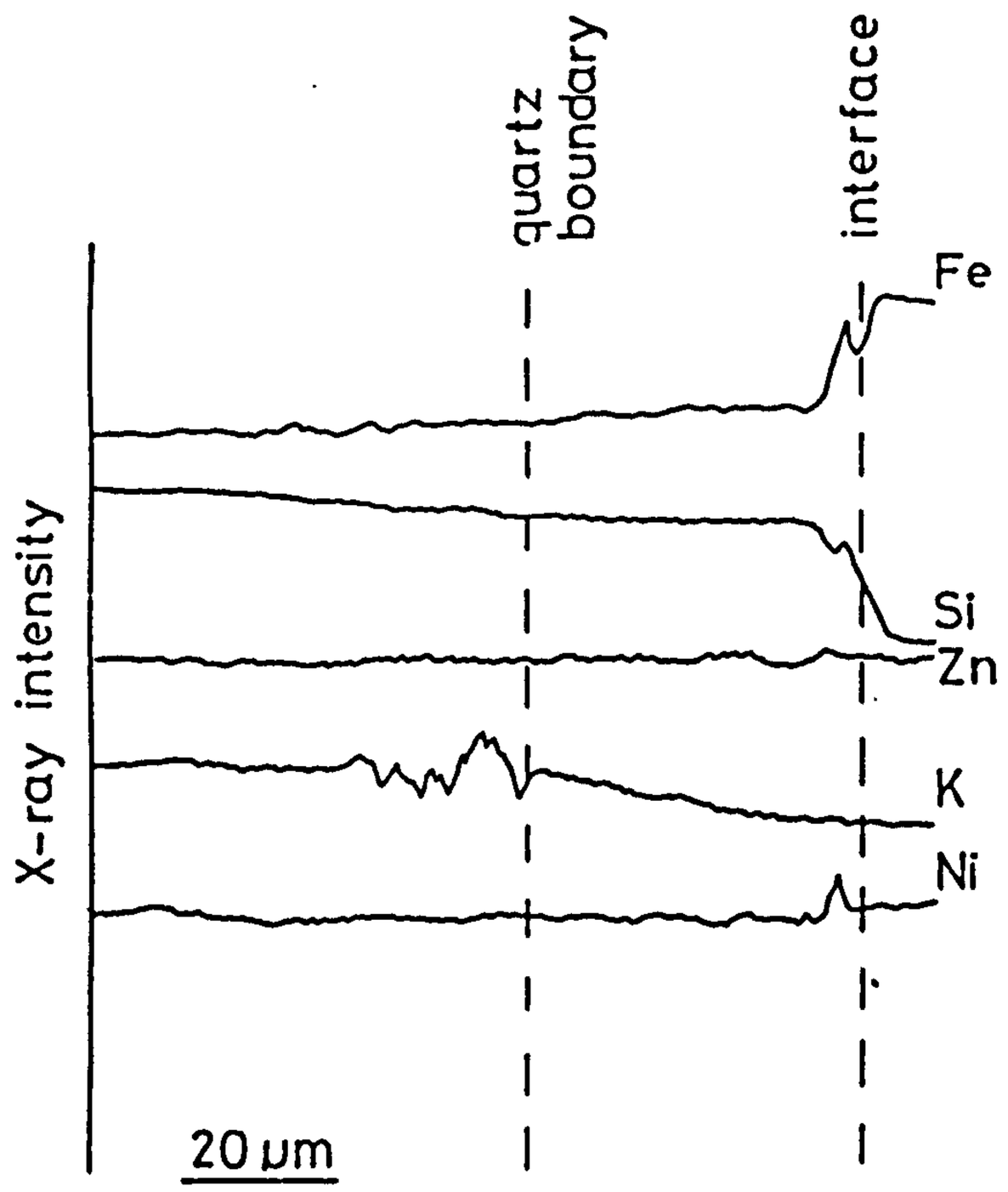

(a) fired only coating, M22.

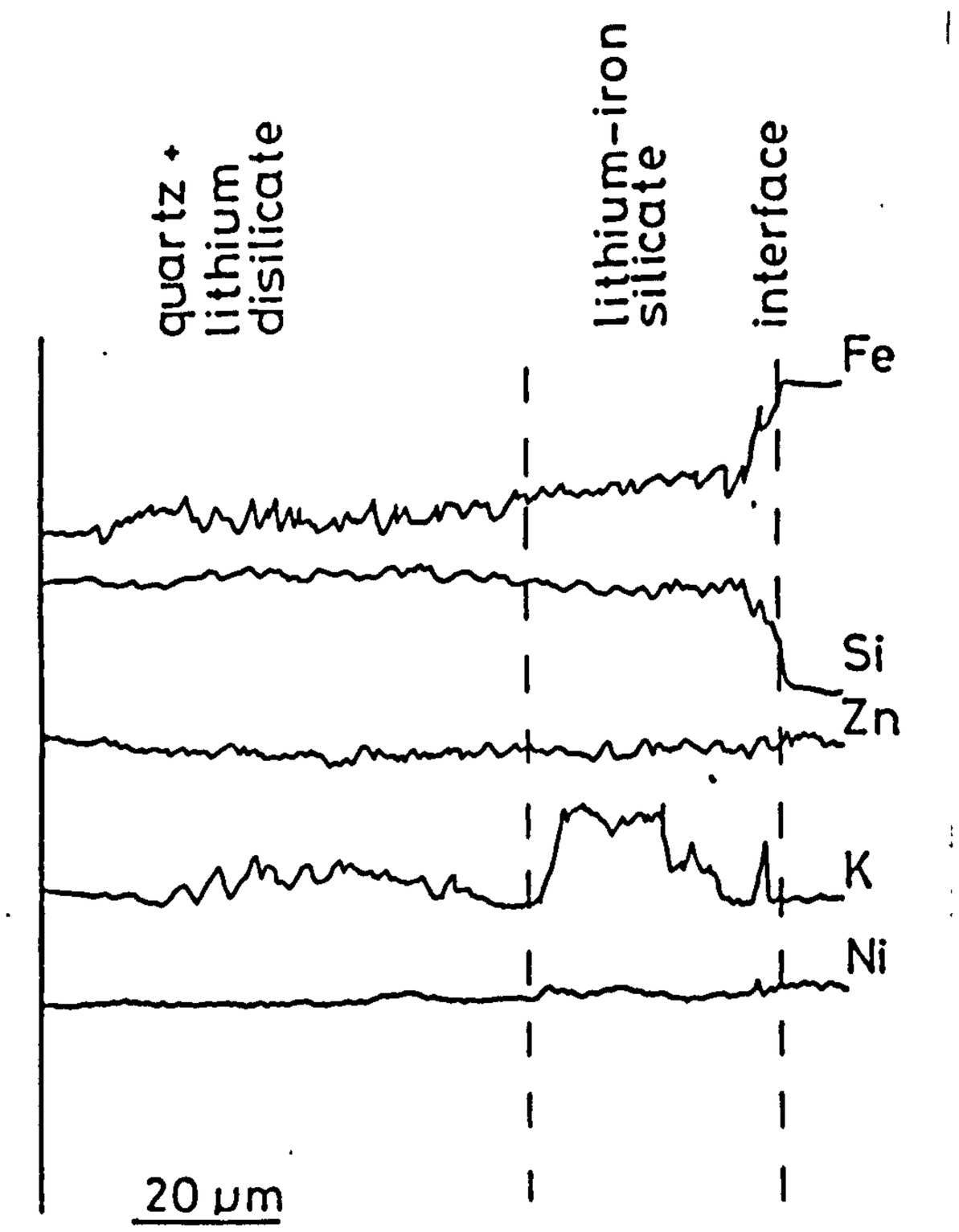

(b) heat-treated coating, M22H.

Figure 5.2.24 Element distribution collected from linescans conducted across the interface.

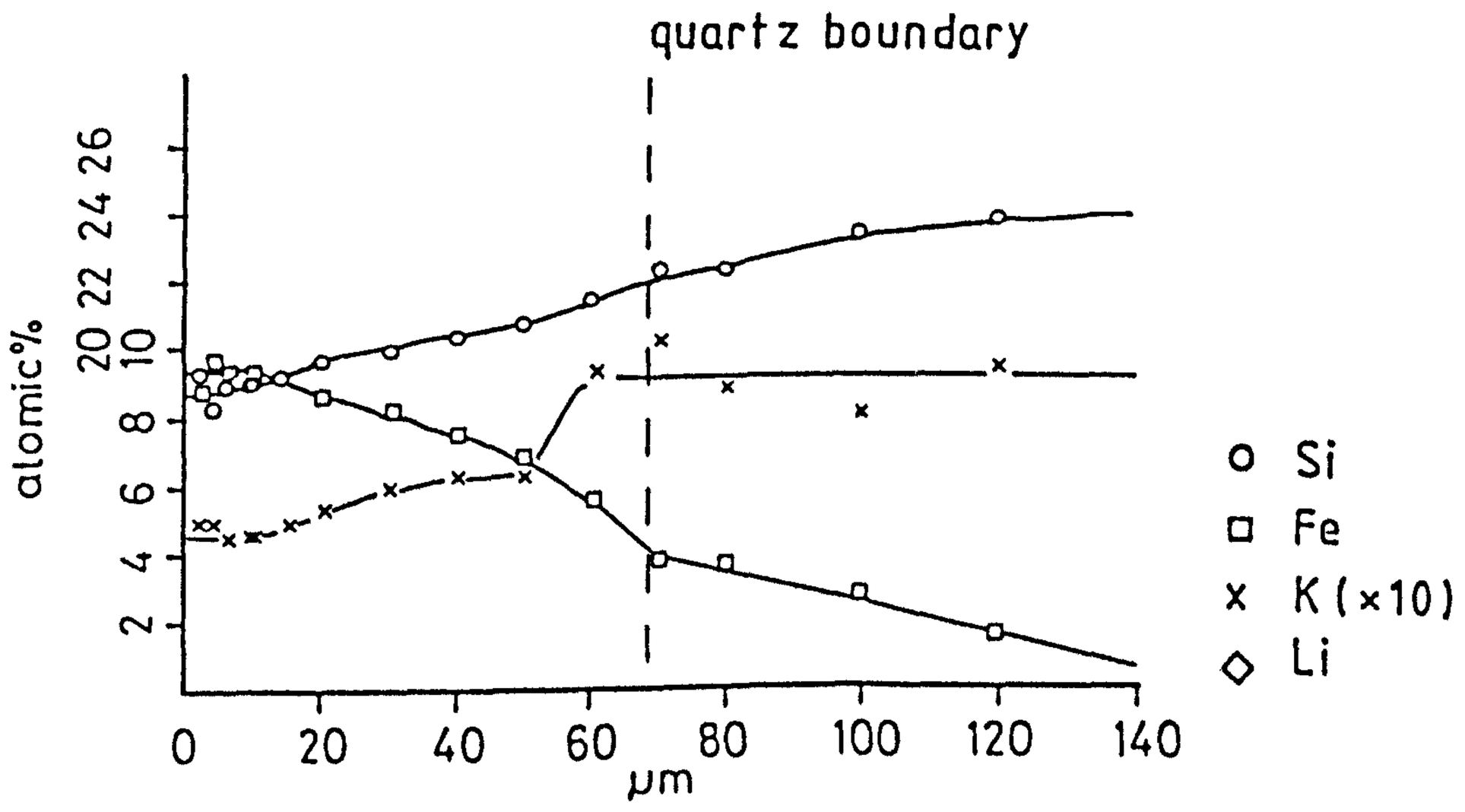

Figure 5.2.25 Quantitative element distribution across the interface of a fired only coating, M22.

- Silicon dips at this position.

- Zinc no longer exhibits a peak at the interface, related to the absence of the dendritic phase.

A quantitative profile is given in Figure 5.2.25. Iron reaches a concentration of 31 wt% FeO adjacent to the coating. It drops to 15 wt% at 70 μm. The element distribution across a heat-treated coating are shown in Figure 5.2.24(b).

Nickel oxide (15 min 970°C): M23

The microstructure for a quenched coating, Figure 5.2.22, is very similar to that described for a firing time of 5 minutes. The composition of the metallic alloy is 97 at% Fe and 3 at% Ni. Iron has increased slightly. After heat-treatment the microstructure is also very similar to that fired for 5 minutes, see Figure 5.2.22. The iron concentration in the alloy has increased to give a composition of 99 at% Fe and 1 at% Ni.

The addition of nickel oxide markedly influences the interfacial microstructure.

Coating adhesion was measured using the tensile pull method. The results are given in Table 5.2.17.

Cobalt oxide:

The addition of cobalt oxide to a coating given the standard firing did not influence coating adhesion. It remains excellent in both the quenched and heat-treated conditions. The coating adhesion is 65.8 and 60 MNm^{-2} respectively.

Table 5.2.17: Coating adhesion MN m^{-2}

Adherence oxide	Quenched	Heat-treated
CoO (M19)	65.8 ± 6 (2)	60.0 ± 9 (2)
NiO (M22)	30.0 ± 7 (0)	0

Table 5.2.18: Interfacial compositions of glass B fired on various substrate materials

Substrate Material		Adjacent glass composition at% (±0.1%)							
		Al	Si	P	K	Zn	Fe	Li	O
Mild steel not preoxidised	D2	1.7	23.0	0.3	1.1	0.4	0.5	14.4	58.2
Ferric oxide disc Fe_2O_3	D4	1.6	22.5	0.4	1.1	0.6	2.5	14.0	57.0
Ferrous oxide disc FeO	D3	1.5	18.4	0.6	0.8	0.4	9.5	11.5	57.0

Interface	Label	K/Si
Mild steel not preoxidised	D2	0.051
Ferric oxide disc Fe_2O_3	D4	0.049
Ferrous oxide disc FeO	D3	0.043
Expect bulk		0.041
Coating on mild steel	M9	0.019

Nickel oxide:

The addition of nickel oxide produces a marked change in coating adhesion. For the quenched coating the adhesion drops to 30 MN m^{-2}. Failure occurs in the coating bulk and not at the interface. The reduced adhesion is due to a weakening of the enamel coating bulk. The actual coating adhesion will exceed this and may still be excellent.

After heat-treatment the enamel coating does not bond to the mild steel. It cannot support any tensile load. Failure occurs along the coating-mild steel boundary. No residual iron oxide is detected on the exposed coating surface.

The presence of minor amounts of nickel oxide in the enamel coating is detrimental to coating adhesion. This is particularly so if the coating has been heat-treated.

5.2.11: Bulk glass B fired on iron oxide discs

Complex interaction must occur to give the observed interfacial features for adherence oxide containing coatings. The glass must interact with both the iron oxide and mild steel substrate. To gain more information a series of experiments were conducted. Bulk glass B, with and without adherence oxides, was heated on mild steel, ferrous oxide (FeO) and ferric oxide (Fe_2O_3). This is described more fully in Section 4.4. They were held for one 1 hour at 970°C then quenched. The interface composition was determined by quantitative EDX analysis. Lithium was assumed present with a constant ratio to silicon of Li/Si = 0.625 (that of bulk glass B). These are listed in Table 5.2.18. The potassium ratio to silicon is also shown. For

comparison the expected ratio from glass B and that measured for the adjacent coating M9 are given.

Unoxidised mild steel

There are no observable interactions. The glass separates easily from the mild steel. The amount of iron oxide taken in to solution is very low, typically 0.5 at% Fe just adjacent to the interface.

Ferric oxide

A narrow reaction layer exists between the iron oxide disc and glass. It also extends into the iron oxide disc, See Figure 5.2.26. X-ray diffraction and quantitative EDX techniques identified this phase as a lithium iron silicate. Iron is present in the trivalent state to give a formula 2 Li_2O. Fe_2O_3.2SiO_2. The glass just adjacent to the interface has an iron concentration of 2.5 at% Fe. The presence of adherence oxides in the glass had no noticeable effect and a metallic phase did not appear.

Ferrous oxide

Extensive interaction occurred between the glass and iron oxide. This is shown in Figure 5.2.26. Dendritic growth extends into the glass and is initiated at the ferrous oxide surface. Quantitative EDX analysis identified this dendritic phase as a lithium-iron-zinc-silicate. It is the same phase as the dendritic growth observed for the coated mild steel. Within the iron oxide a second silicate phase

is noticeable. Analysis indicates it is fayalite $Fe_2Si_2O_4$.

For glass B and glass B with cobalt oxide added no metallic alloy phases are present. When glass B has nickel oxide added a metallic phase appears. Immediately adjacent to the interface it has a relatively large size, typically 10 μm. The composition of this alloy was measured at 75 at% Fe and 25 at% Ni. A fine dispersion of metallic particles is noticeable in the glass bulk. They extend to where crystals first appear. Their size is too small for analysis by quantitative EDX. X-ray mapping using $Fe_{K\alpha}$ and $Ni_{K\alpha}$, suggests the phase is an metallic alloy of nickel and iron.

The iron concentration in the adjacent glass is typically 9.5 at% Fe in all three cases, Table 5.2.18.

Crystallisation of the interfacial glass region for glass B on ferrous oxide is very extensive. Much more so than between the glass B and ferric oxide or mild steel. Only with nickel oxide added to glass B is any reaction between the glass and ferrous oxide noticeable.

It should be noted that there is no loss of potassium in the adjacent glass when fired on the above three substrates. A potassium loss only occurs from a coating on a preoxidised mild steel substrate.

Figure 5.2.26 Backscattered electron micrographs of the interface between,

(a) ferrous oxide and glass B,

(b) ferrous oxide and glass B plus 0.25 wt% CoO,

(c) ferrous oxide and glass B plus 0.25 wt% NiO,

(d) ferric oxide and glass B,

(e) ferric oxide and glass B plus 0.25 wt% CoO,

(f) ferric oxide and glass B plus 0.25 wt% NiO.

ferrous oxide disc

ferric oxide disc

a

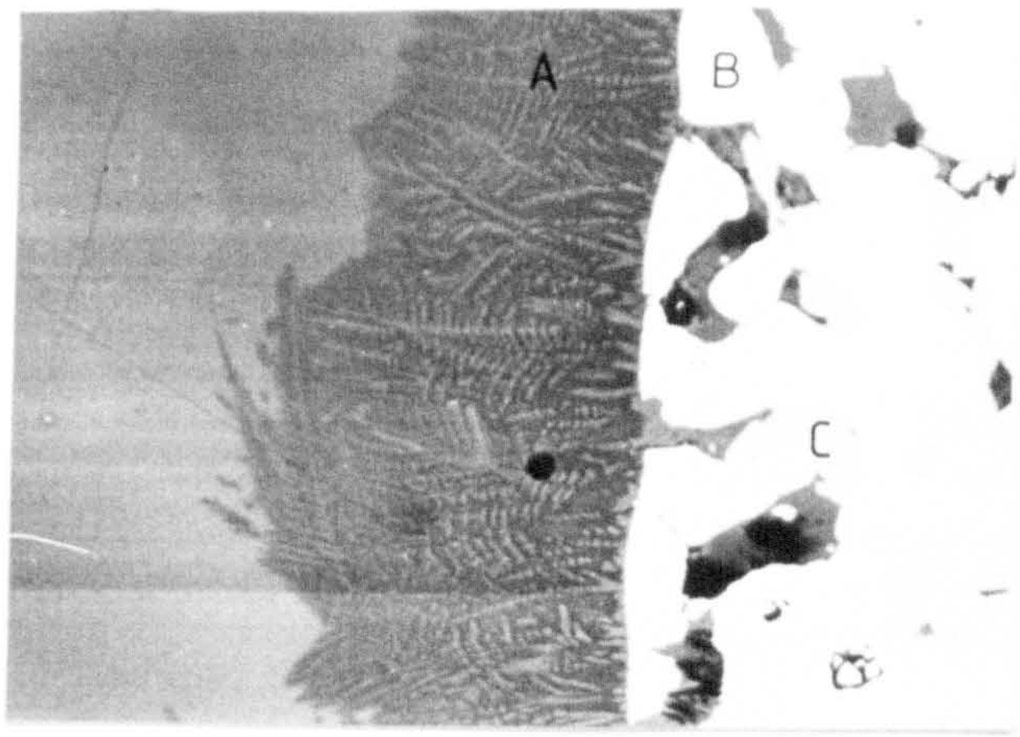

d

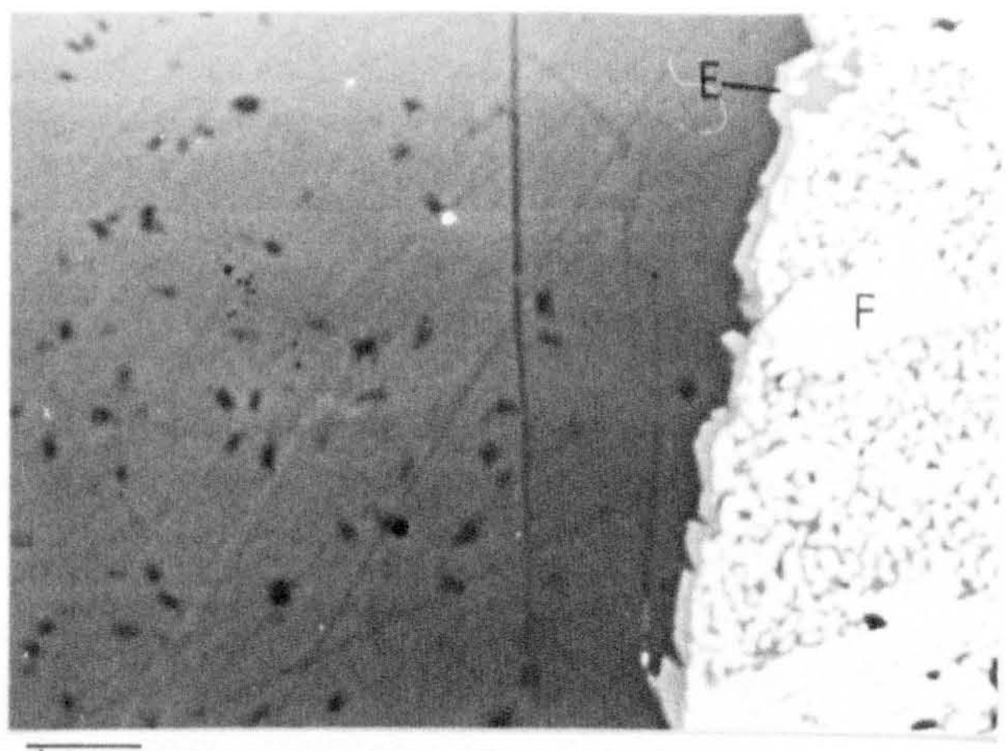

glass B

10 µm

4 µm

b

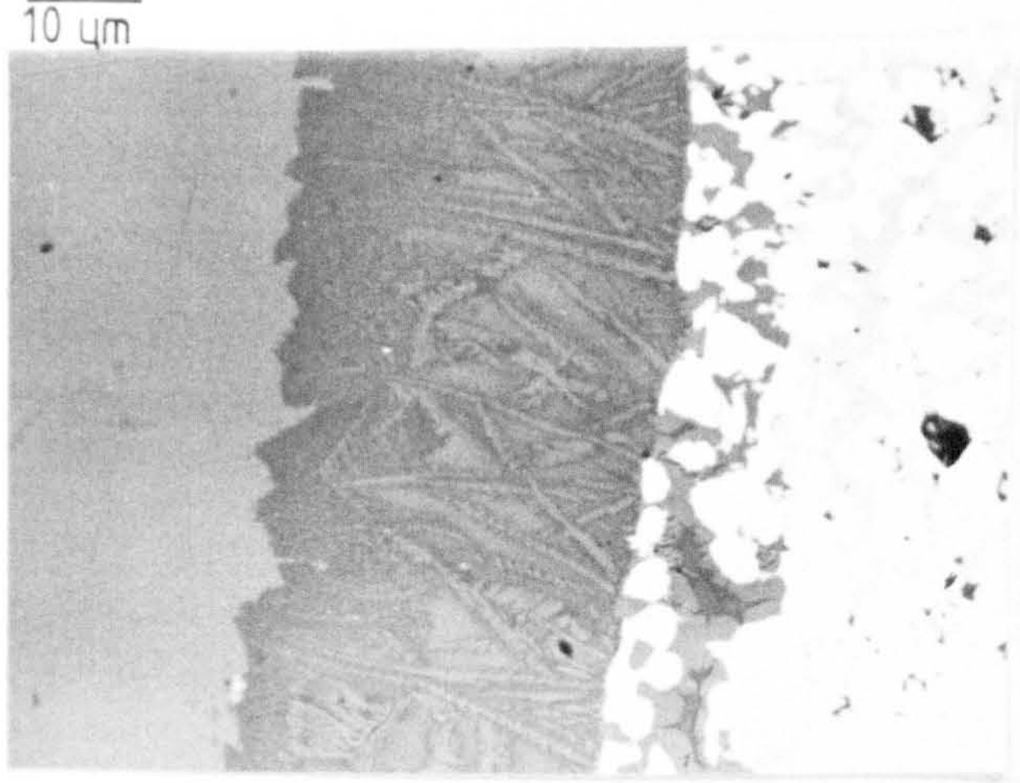

e

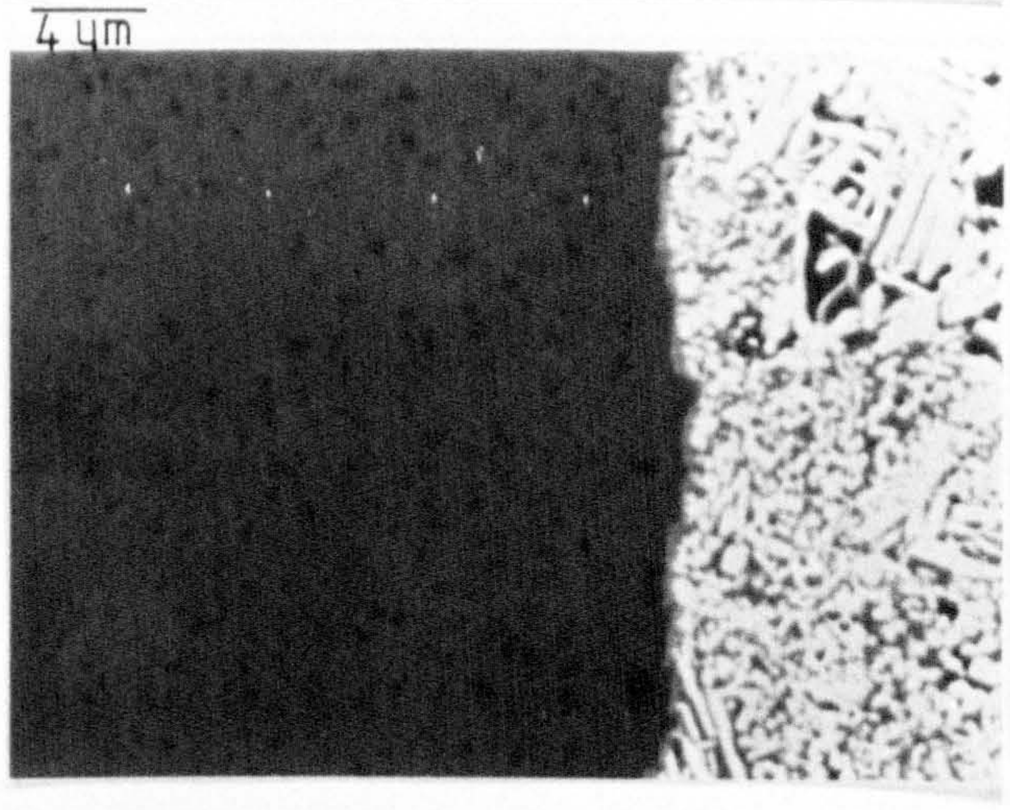

glass B +
0.25 Wt%
CoO

C

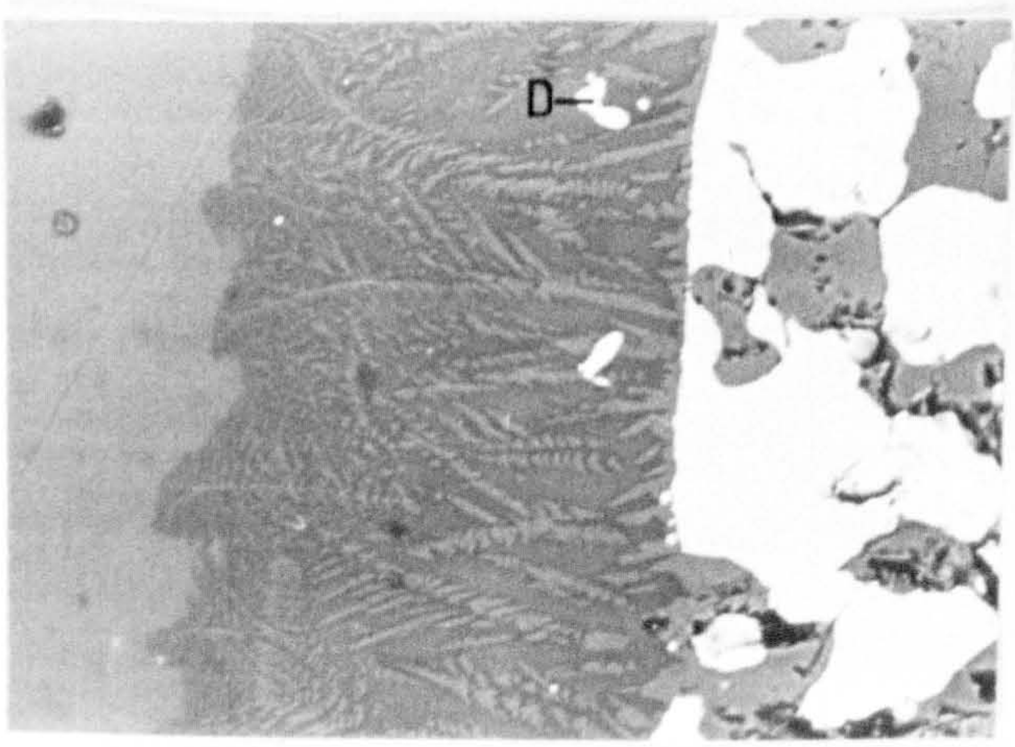

f

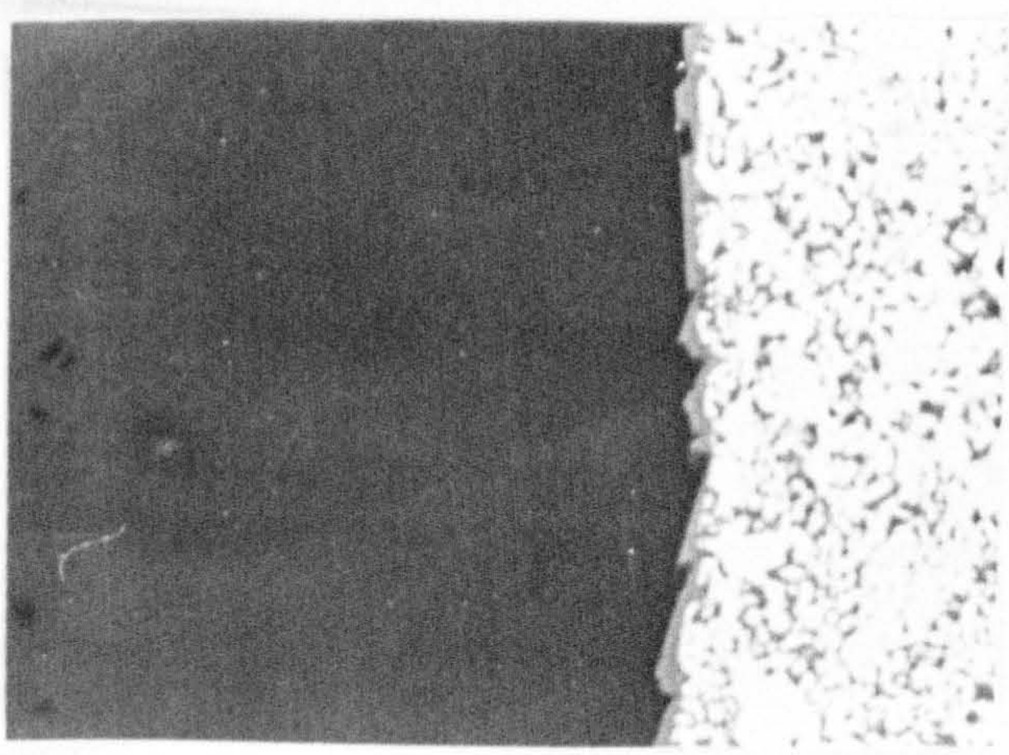

glass B +
0.25Wt%
NiO

A lithium zinc iron silicate $Li_2O.Fe_{0.8}Zn_{0.2}O.SiO_2$

B ferrous oxide

C fayalite

D metallic alloy

E lithium iron silicate $Li_2O.Fe_2O_3SiO_2$

F ferric oxide

Chapter 6

DISCUSSION

6.1 Devitrification of the bulk enamel coating

Since the microstructure developed will determine the enamel properties it is necessary that the crystallisation behaviour of the bulk coating be understood. A limited study of coating devitrification is presented in Section 5.1.4. These investigations concentrated on glass A, but results apply equally to glass B.

Crystallisation may be divided into two steps:

- Spontaneous crystallisation of the glass during firing.
- Intentional crystallisation resulting from a controlled heat-treatment.

Mixed modes of crystallisation have been observed in a complex glass-ceramic enamel by Douglas [80].

Crystallisation during firing:

With a "standard' firing treatment extensive spontaneous crystallisation is produced. Both glass A and B exhibit crystal growth below the firing temperatures. The D.T.A. curves, displayed in Figure 4.1, show two exothermic peaks for each glass. A peak at 665°C relates to the appearance of lithium disilicate ($Li_2O.2SiO_2$). The peak at 825°C is due to the formation of quartz (SiO_2). When the glass powder is heated rapidly to a typical firing temperature of 960°C the separation of both crystal phases from the glass is possible.

On completion of the "standard" firing (5 minutes at 960°C) lithium disilicate and β-quartz are the major, and only, crystal phases present. Bulk glass A when subjected to an identical thermal treatment developes α-cristobalite and lithium disilicate as the major crystal phases. The large surface area of the initial glass powder significantly influences the polymorph of silica formed. At the firing temperature α-cristobalite is the stable polymorph in the bulk glass. By starting with a glass powder the surface preferentially nucleates β-quartz.

In the very early stages of firing β-quartz is the first major crystal phase to appear. It resides in the surface area of the partially fused glass particles. Lithium metasilicate ($Li_2O.SiO_2$) is also developed, but on continued firing disappears. It may exist as a transient phase converting to the disilicate. This process has been suggested by McMillan et al (81) to explain the behaviour of a bulk glass-ceramic of similar composition.

Subsequent crystallisation involves bulk nucleation and growth. After a firing time of 2 minutes the glass powder is highly crystalline. Lithium disilicate and β-quartz are present as very fine grains of submicron dimensions. These are dispersed throughout the original glass particles. The crystallisation mechanisms cannot be deduced from the limited information in Section 5.1.4. Crystallisation in lithium silicate glasses has been extensively studied by McMillan (71) and Headley (72). The glass examined by Headley is of a similar composition to glass A, with P_2O_5 as the nucleating agent. He found Li_3PO_4 crystallites formed on heating to 1000°C. On reaching 1000°C they had a maximum size of 0.15 μm, increasing to 1 μm after 20 minutes. A subsequent thermal treatment of 15 minutes at 650°C and 20 minutes at 820°C caused cristobalite,

lithium metasilicate and lithium disilicate to crystallise by epitaxial growth on the exposed facets of Li_3PO_4 crystallites. It is possible that Li_3PO_4 acts as a nucleation site for the crystalline phases in the partially fused enamel. However β-quartz is formed within the central region of the partially fused particles whereas α-cristobalite is the stable form of silica in the bulk glass. The large surface to volume ratio of the particles must preferentially cause β-quartz to appear within the central regions possibly as a consequence of prior surface crystallisation. This is fortunate as the presence of α-cristobalite in the enamel is undesirable. At this stage the enamel is partially fused and highly crystalline.

On continued firing and with an increased removal temperature the microstructure is markedly changed. A coarsening process operates for both crystal phases. The mean crystal size increases to 1 μm or above. It is at this stage that the inhomogeneous microstructure is developed. The increased removal temperature rather than the longer firing time is the dominant factor. For firing times of 4 minutes or longer a temperature of 960-970°C is reached. The lithium disilicate liquidus lies in this temperature range. It is easy for small crystals of phase to dissolve while the large crystals grow. The resulting decrease in interfacial energy is the driving force behind the coarsening process. The β-quartz phase may also undergo coarsening but its higher liquidus temperature will result in the process proceeding at a slower rate. The β-quartz grains are in general of a smaller size.

The various steps by which the coating crystallises during firing is summarised in table 6.1.

Associated with the coarsening process is a redistribution of potassium within the coating to preferentially reside in the

Firing		Coating Crystallisation
Removal temperature °C	Time minutes	Start of firing
	-	Surface nucleation and growth of β-quartz. Minor amounts of lithium disilicate and lithium metasilicate.
906	0.5	Transformation of lithium metasilicate to disilicate.
920	1	Bulk nucleation and growth of β-quartz and lithium
940	2	disilicate.
968	4	Coarsening process. Inhomogenous microstructure
969	6	produced with large glassy regions.
Heat-treatment		
600°C	30 minutes	crystallisation of glassy
800°C	3 hours	areas. Mostly lithium disilicate formed.

Table 6.1. Coating Crystallisation.

uncrystallised regions. Potassium is not a major component of the crystal phases appearing. It will be displaced from regions where crystal growth is occurring, Figure 6.1. Alkali ions would be expected to have a high mobility in the glass at firing temperatures. Potassium may consequently be forced into the glassy regions where it rapidly diffuses to attain a constant concentration.

Other minor elements are much less mobile and will tend to reside in the crystal phases or in the immediately adjacent glass. This would explain why only potassium is found to exhibit a marked variation in concentration.

Crystallisation during heat-treatment

Heat-treatment of the coating results in further crystallisation of the glassy regions. The microstructure developed in these regions is different from the regions which undergo crystallisation during firing. The different composition (Potassium concentration) and different thermal treatment are the reasons for this. Lithium disilicate is produced preferentially during the controlled heat-treatment. The quantity of lithium disilicate to β-quartz is close to that for the heat-treated only bulk glass A. Most of the β-quartz is formed during firing, whilst lithium dislicate is developed during firing and also on heat-treatment.

The heat-treated coating has a much coarser microstructure than the bulk glass subjected only to a heat-treatment. Different microstructure types make comparison between bulk glass/glass-ceramic and coating properties unreliable. Crystallisation of the coating during firing may influence interactions between the coating and

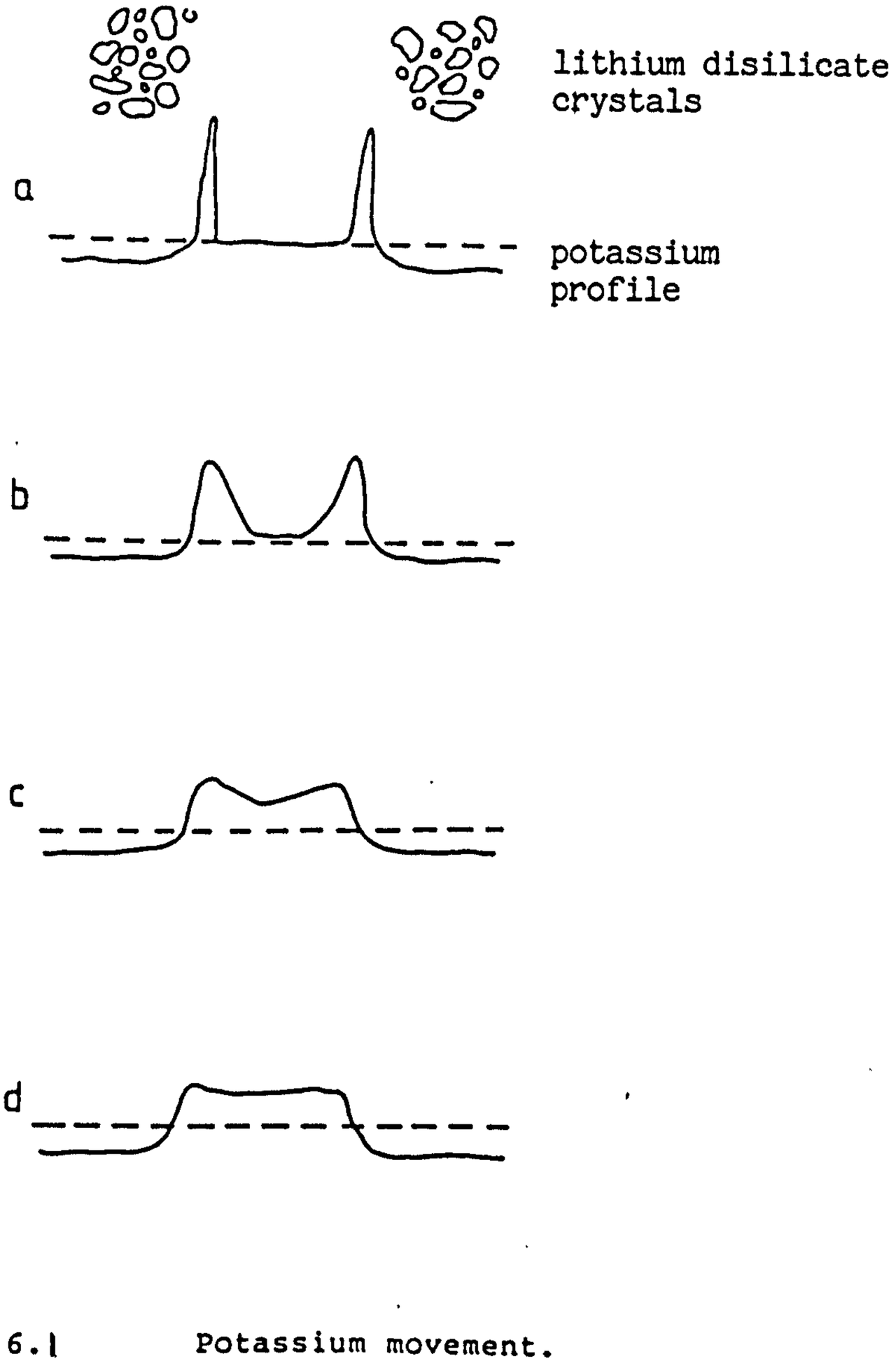

Figure 6.1 Potassium movement.

substrate. Elements which could react with the substrate may be prevented from doing so if they become incorporated in the crystal phases. The presence of crystals in the coating and the consequent change in residual glass composition will alter wetting and viscosity characteristics. Diffusion in the coating will also be restricted assuming it occurs predominantly within the glassy phase.

6.2 Enamel coatings on chrome-iron

6.2.1 Interfacial Structure

Before discussing the coating on chrome iron it will be useful to summarise the interfacial structure between the coating and chrome-iron alloy. The interfacial structure is very stable to considerable variation in the firing time. However the preoxidation treatment of the chrome-iron substrate has a marked influence on interfacial structure.

- **Preoxidised in wet hydrogen (C5, C5H, C16H, C17H).**

This was the "standard" pretreatment given. For the coating produced under "standard" firing conditions discrete boundaries are observed. These divide the interfacial area into the following regions:

- surface of chrome-iron alloy depleted in chromium
- a silica layer, 0.1 μm thick (SiO_2)
- a chromium oxide layer, with some iron oxide present in solid solution, 1 μm thick (90% Cr_2O_3, 10% Fe_2O_3).
- enamel coating.

This structure is illustrated schematically in Figure 6.2(a). The layer of silica is formed during the preoxidation in wet hydrogen. Silicon is present in the chrome-iron alloy as an impurity, with a concentration of 0.32 at%, see Table 4.3. Silicon has a high affinity for oxygen, that is a large negative free energy of oxide formation and so would be expected to compete with chromium to form a surface layer of SiO_2. With the conditions used to preoxidise the alloy a silica layer is able to form between the alloy and chromium oxide layer. Once formed the silica layer is continuous and subsequent formation of chromium oxide will be dependent on chromium diffusion through this layer.

The chromium oxide layer formed during the preoxidation of the alloy is essentially a chromium oxide (Cr_2O_3) with 10% iron oxide (Fe_2O_3) present in solid solution. On completion of the coating process the chromium oxide is retained as a discrete layer at the interface.

The boundary between the chromium oxide layer and coating is extremely sharp. Immediately adjacent to this boundary the coating microstructure is not noticeably different from that of the coating bulk.

For long firing times, well in excess of the "standard" firing time, an additional phase appears at the chromium oxide-coating boundary. With firing times in excess of 6 hours it forms a continuous layer. The phase is identified as a lithium chromium silicate, $LiCr(SiO_3)_2$ which exists in solid solution with chromium oxide (Cr_2O_3). Figure 6.2(b) illustrates this schematically.

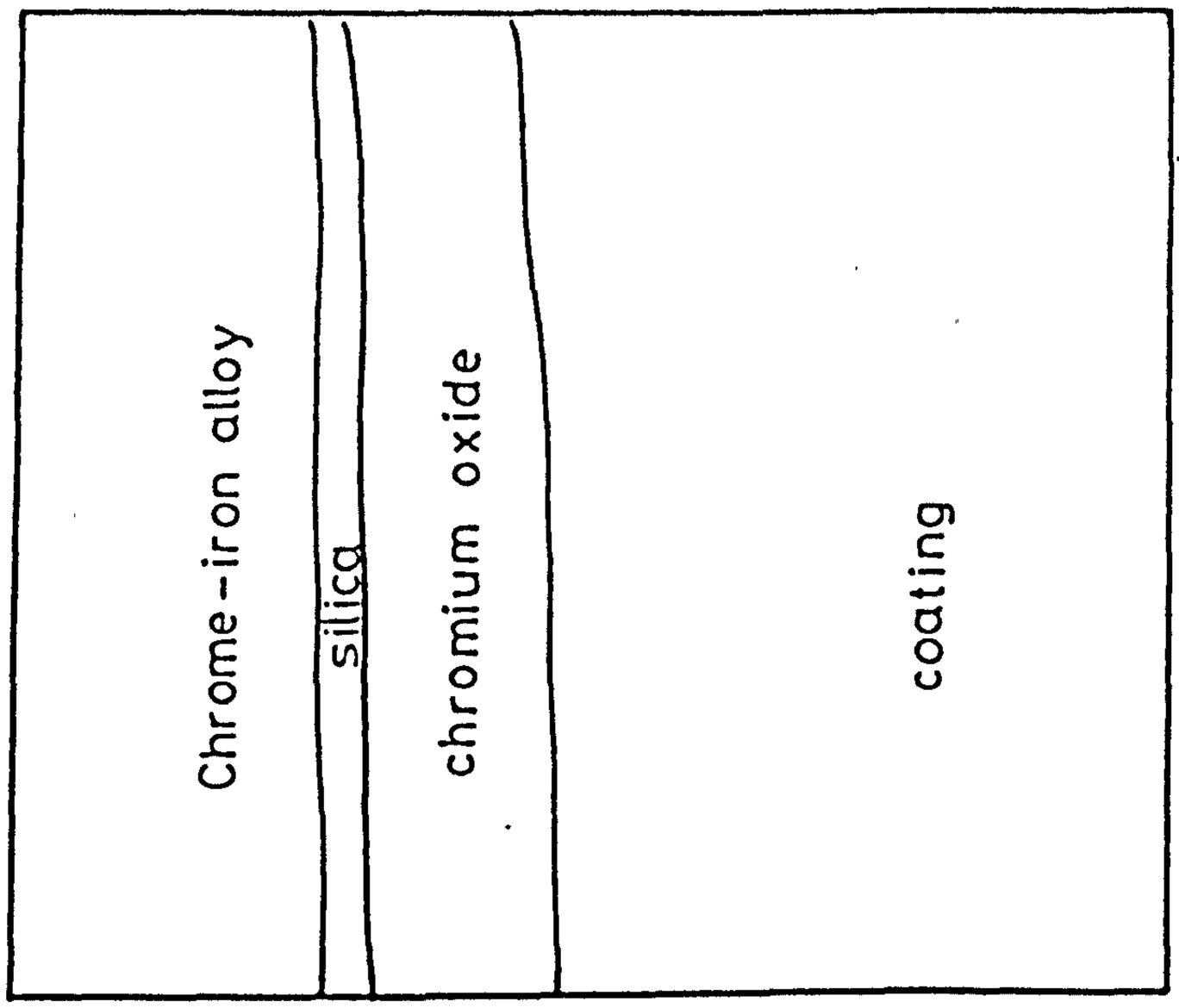

(a) short firing time.

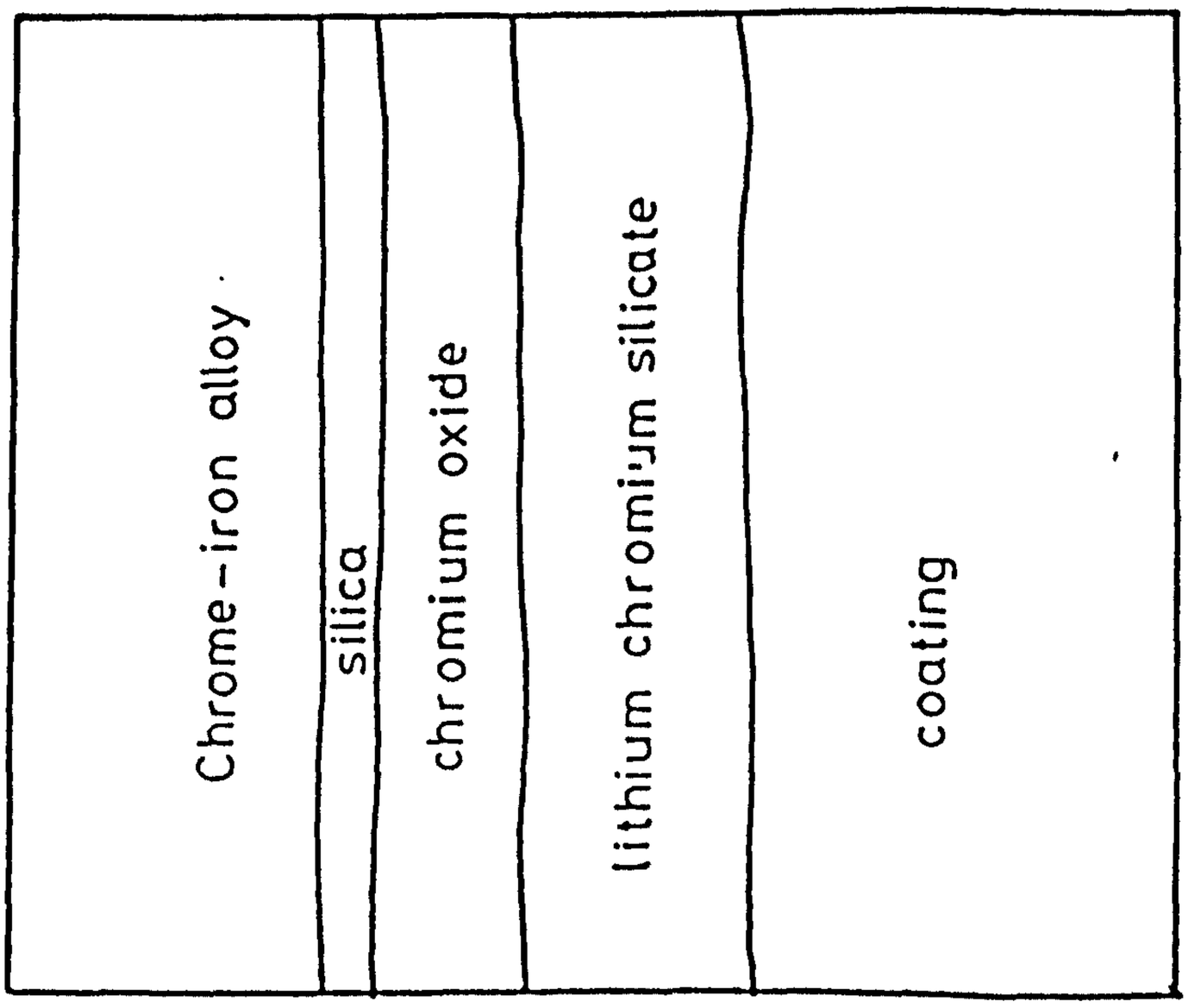

(b) long firing time.

Figure 6.2 Schematic representation of interface boundary layers for a coating on chrome-iron preoxidised in "wet" hydrogen.

- **Preoxidised in air (C18H, C19H).**

The coating was prepared using "standard" firing conditions in a neutral atmosphere of oxygen free nitrogen. A single boundary exists between the alloy and coating. Chromium oxide exists as a very narrow, discontinuous layer which extends at most 0.3 μm from the alloy surface. A fine, spherical metallic phase appears in the coating adjacent to the interface. Again the interface does not noticeably effect the adjacent coating microstructure. The interface structure is shown schematically in Figure 6.3(a).

- **No preoxidation (C20H, C21H).**

The coating was prepared using "standard" firing conditions in air. A single boundary exists between the alloy and coating. Chromium oxide is present at the interface appearing as a dispersed nodular phase in the adjacent 2 μm of the coating. At greater distances the coating is not noticeably influenced by the interface. Figure 6.3(b) illustrates this schematically.

Three main observations must be drawn from the above descriptions:

- Chromium oxide is present at the interface for each coating.
- There is evidence of interfacial reactions.
- The presence of the oxide interface does not noticeably influence the adjacent microstructure of the coating.

6.2.2 Interfacial Interaction

The following discussion is concerned with the interface between

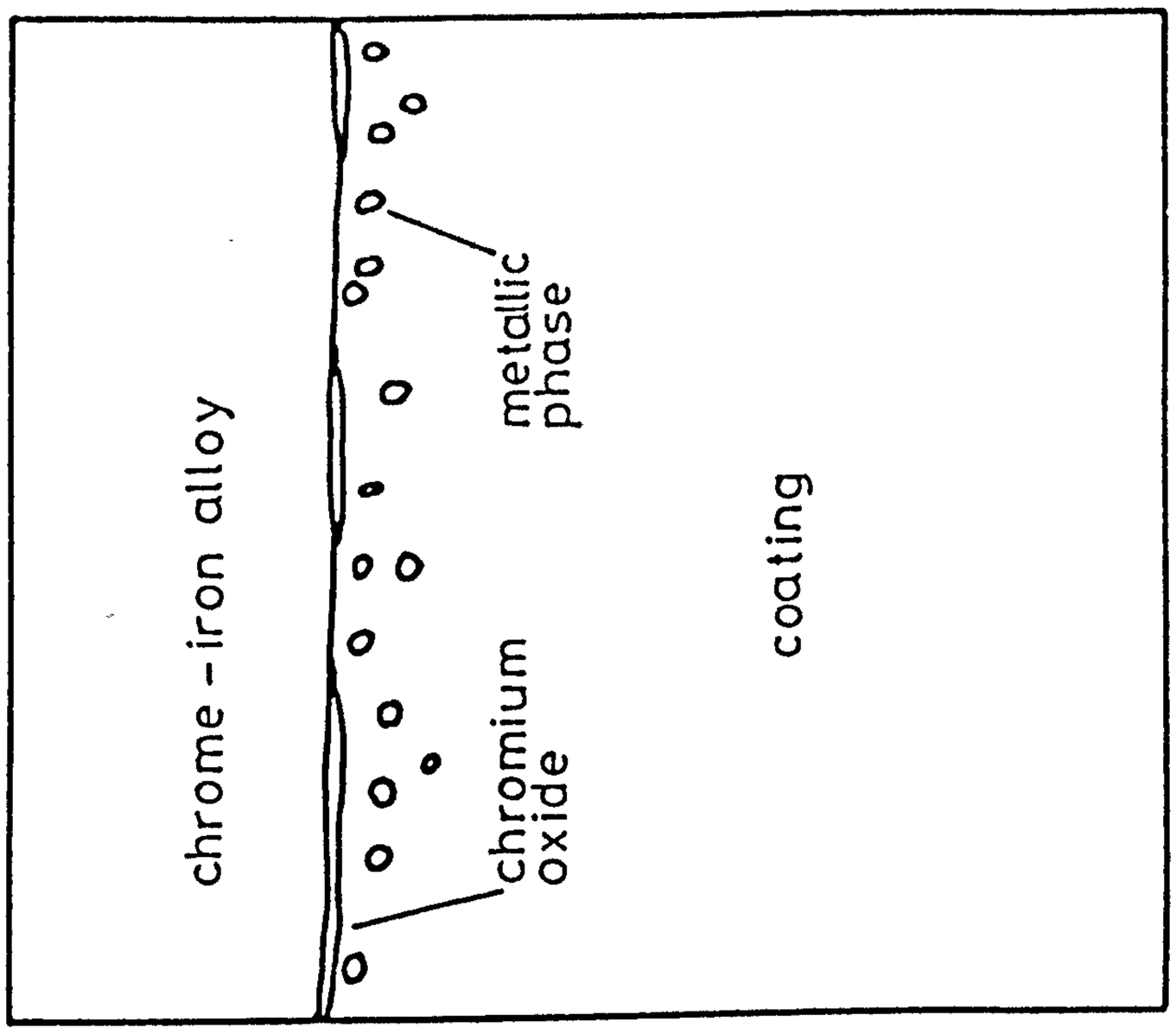

(a)preoxidised in air

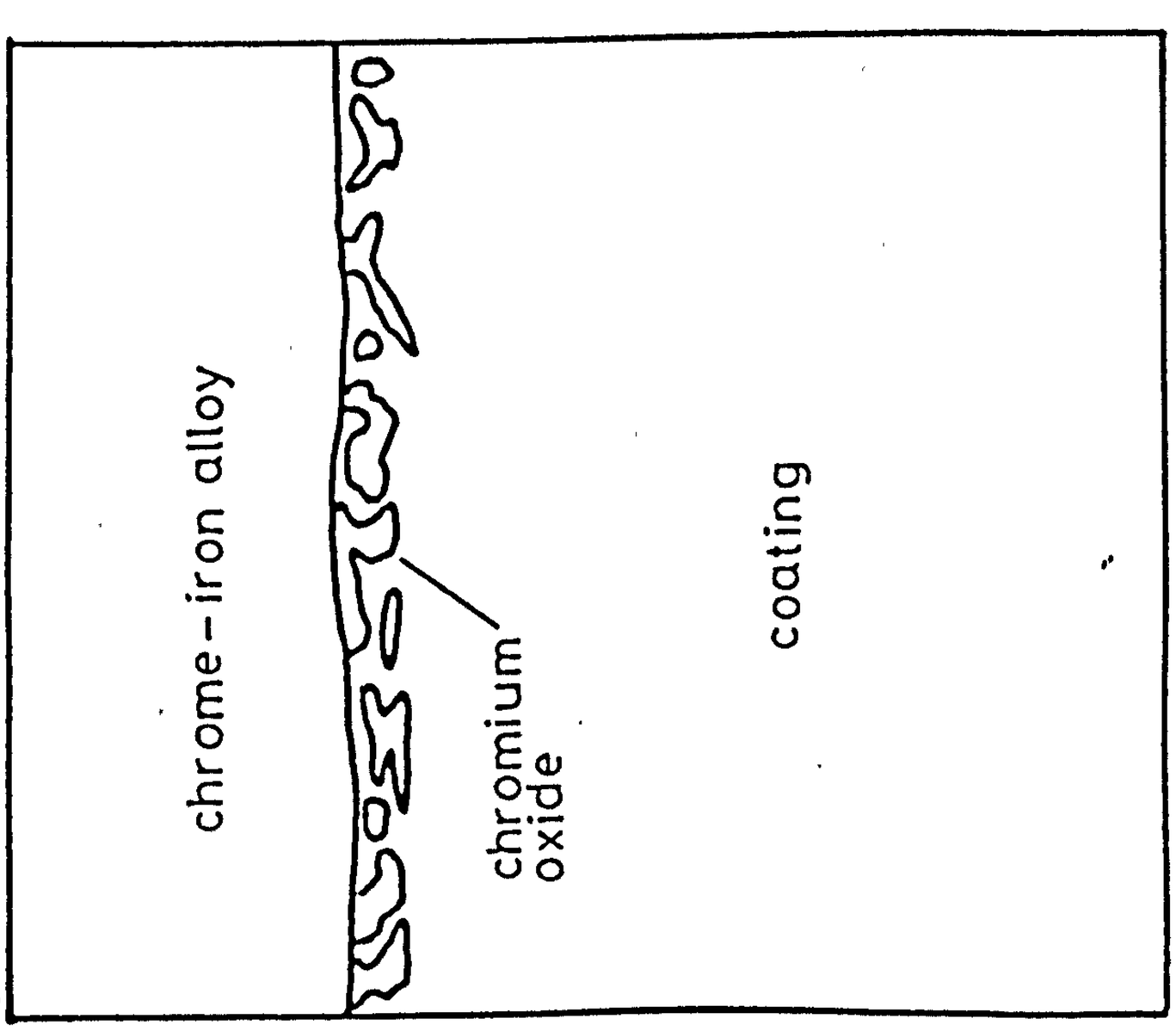

(b) not preoxidised.

Figure 6.3 Schematic representation of interface features for a coating on chrome-iron.

chrome-iron preoxidised in wet hydrogen and the coating. This preoxidation treatment has been developed to provide a good surface for enamel wetting and adhesion, Partridge (82), and it was selected for the standard alloy pretreatment in this project.

It is apparent that remarkably little interaction is observed between the substrate and coating. The interface remains extremely well defined. During firing the semi-molten enamel will wet and interact with the chromium oxide layer, and does not come in contact with the underlying alloy.

A reaction does proceed at the chromium oxide-semi-molten glass interface to produce lithium chromium silicate $LiCr(SiO_3)_2$. The melting temperature of this phase is 1260°C which precludes the possibility of the lithium chromium silicate being precipitated from the chromium containing coating during firing. It must be formed by a solid state phase boundary reaction. The reaction proceeds at a very slow rate and has a linear growth rate (Fig. 5.1.14). For a "standard" firing time of 5 minutes the reaction product will have attained a thickness of 140 Å. It is likely that the reaction proceeds throughout firing, but remains undetectable for normal firing times. This means that wetting and bonding of the coating to the chromium oxide involves the formation of a reaction product. It will also act as an additional barrier layer at the interface to any possible interactions between the coating and alloy. The reaction may be considered as an alloying between two oxides, and will proceed only if a decrease in free energy is achievable. Overall the reaction may be represented as

$$Cr_2O_3 + 2[Li_2O.\Delta.Si_{3.25}O_{6.5}]_{glass} \equiv 2LiCr(SiO_3)_2 + Li_2O.2\Delta.Si_{2.5}O_5{}_{glass}$$

$$\Delta G = neg$$

where $Li_2O.\Delta.Si_{3.25}O_{6.5}$ is the semimolten glass.

$\Delta \cong 0.12\ Al_2O_3\ 0.045\ P_2O_5\ 0.014\ ZnO\ 0.0625\ K_2O$.

$\Delta G_r \cong$ change in Gibbs free energy.

glass = glass adjacent to the interface

6.2.3 Dissolution of substrate oxides into the coating

Chromium is present in the adjacent coating at extremely low levels. This is observed in both the fired only and heat-treated coatings. For the standard coating in the fired only condition (C5) or after a heat-treatment (C5H) chromium has a concentration of 0.3 at% in the immediately adjacent coatings. it is not clear how the chromium is distributed among the various crystal phases and residual glass. Although present at extremely low concentrations, the chromium has diffused well into the coating. With a firing time of 5 minutes it penetrates to greater than 30 μm.

It has been assumed that chromium is present in the glass as trivalent ions, Cr^{3+}. In the chromium oxide layer or lithium chromium silicate layer the chromium ion will be trivalent and therefore likely to enter the glass as a trivalent ion. For multivalent ions an equilibrium ratio between the various valency will be established, in this case between Cr^{3+} and Cr^{6+}. The exact ratio will depend upon temperature, duration of firing/melting, glass composition, oxidising or reducing atmosphere. Work by Nath and Douglas (83) has shown that for a 21.6 Li_2O 78.4 SiO_2 melt at 1100°C $Cr^{6+}/Cr \times 100 = 11.9\%$. However if chromium was introduced as Cr_2O_3 it took 60 hours to reach this equilibrium composition. For the much shorter firing periods used to produce the coatings the equilibrium composition will not be established. Most, if not all the chromium, will be in the trivalent Cr^{3+} state.

The low chromium concentration at the interface represents the saturation level of chromium oxide in this coating composition. A low saturation concentration is typical of chromium oxide (Cr_2O_3) in silicate glass. Investigations by Manfredo (84) have found the saturation concentration to be 0.35 at% at 1500°C in a complex sodium silicate glass. For a sodium calcium silicate glass, Williams (85), the saturation concentration is 0.1 at% at 1500°C. The reason for the very low solubility of chromium oxide in glasses is its ability to form cationic complexes in the glass, see Farakawa and White (86). Chromium ions have a high ionic field strength (Z/a^2) equal to 0.78, Appendix 5. It tends to form its own strongly bonded polyhedra, differing from SiO_4 by having a higher coordination number. These are more difficult to link into the polyionic network of silicon tetrahedra. This is discussed by Volf (87).

It is the very low saturation level of chromium oxide in the coating that enables the retention of the preoxidised chromium oxide layer during the coating process. The dissolution rate of the oxide layer, will depend on the diffusion of chromium oxide away from the interface. As discussed in Appendix 2 this can be represented by:

$$J_{Cr_2O_3} = - D_B \frac{[Ci - Cx]}{\Delta X} \qquad A.2.9.$$

The value of [Ci - Cx] will be extremely small and consequently the dissolution rate of the chromium oxide layer very slow. Using the data from coating C5 the value of Ci-Cx between 2-20 μm is 7×10^{-3} g cm^{-3}. The low dissolution rate together with the slow interfacial reaction rate is the reason why the interface structure is insensitive to extreme variations in firing time.

Iron is present in the adjacent coating at very low concentrations but exceeding that of chromium. It attains a typical concentration of 0.75 at% after a "standard" firing time of 6 minutes (C5). From the results in section 5.2.10 the saturation concentration of Fe_2O_3 in glass B is 12 wt% or 2.5 at% Fe. The low level of iron in the coating does not represent a saturation concentration. Iron has diffused to at least 30 μm into the coating. The iron has two possible sources

- from the iron oxide present in solid solution with the chromium oxide layer.
- from oxidation of the iron in the alloy substrate and diffusion of the iron ions through the various boundary layers at the interface.

Consider the first source. The amount of iron oxide (Fe_2O_3) in solid solution with the chromium oxide about 10 at%, see Table 4.8. This is equivalent to about 10 wt% Fe_2O_3. The total oxide layer has a mass of 5.26×10^{-4} g cm^{-2} of which 5.26×10^{-5} g cm^{-2} is Fe_2O_3. By expressing the diffusion profiles in Figure 5.1.16 as wt% oxide it is possible to approximate the total amount of iron oxide in solution in the coating. The values given are the mass calculated between 2-30 μm. The iron oxide has diffused further than 30 μm so these values must be regarded as a minimum. The results are presented in Table 6.2. It is found the mass of iron is in excess of 10×10^{-5} g cm^{-2}. The amount of iron oxide in solution exceeds that present in the chromium oxide layer. This means the iron oxide must partly originate from the underlying metal substrate. Evidence in support of this comes from the observation that the iron oxide concentration in the

immediately adjacent coating is constant with firing time. If the chromium oxide layer were the only source of iron oxide then the level would fall with firing time.

Table 6.2: Mass of iron oxide (assumed as ferric oxide) taken into solution

Firing time minutes	Label	Mass of Fe_2O_3 (0-30 μm) g cm^{-2} x 10^{-5}
6	C5	9.87
20	C6	11.75
40	C7	12.22
60	C8	9.05
120	C9	11.75
180	C10	13.39

Typical mass ≡ 10 x 10^{-5} g cm^{-2}

The lack of information and small scale of the interface layers prevent a complete understanding of the process by which iron enters the coating. The iron must be oxidised at the alloy surface to give Fe^{2+} ions and the associated electrons. The iron ions and electrons must then diffuse through the silica, chromium oxide and lithium chromium silicate layers before reaching the coating . The multivalant nature of the iron and chromium ions should allow an electron hopping conduction mechanism. It is the diffusion of the iron ions which is the critical factor. The associated reduction reaction required to complete the cycle may be the reduction of oxygen at the coating-air surface or reduction of an oxide component in the

coating. There is insufficient information to take these ideas further.

6.2.4 The influence of substrate oxides on coating crystallisation

The presence of small quantities of transition metal oxides in glasses are known to influence the crystallisation process, McMillan (9). However the small concentrations of chromium and iron oxide in the adjacent coating do not noticeably influence the microstructure.

Chromium present as Cr^{3+} in a lithium disilicate glass was found by Thakus (88) not to be an effective bulk nucleating agent. In an aluminosilicate glass Cr^{3+} decreased the crystal growth rate, Mackenzie and Brown (89). A similar effect was also observed in a calcium-aluminosilicate glass by Williamson (85). Both attribute this to an increase in glass viscosity brought about by the additon of chromium oxide.

Iron present as Fe^{3+} was also found not to be an effective bulk nucleating agent by Thakus (88). Additions of minor amounts of Fe^{3+} (5 wt% Fe_2O_3) to a calcium magnesium aluminosilicate did not greatly effect the crystal growth rate, Williamson (85). From these results small amounts of Cr^{3+} or Fe^{3+} incorporated in a glass would not be expected to greatly influence the crystallisation behaviour. This agrees with what is observed.

6.2.5 Variation in preoxidation of the substrate

The preoxidation of the alloy substrate was altered to examine the effect on coating adhesion. It is also useful to discuss how these variations affect the possible interfacial reactions. The

interfacial structure has been described in Section 6.3.1. If preoxidation is not carried out in wet hydrogen the discrete chromium oxide layer is absent. There is strong evidence for the presence of chromium oxide at the interface for both coatings C18H, C19H and C20H, C21H. Preoxidised in air and not preoxidised respectively. The level of chromium and iron oxide in the adjacent coating is very similar for those in the "standard" coating (C5H, C5). Chromium has a typical concentration of 0.25% at%. The adjacent coating is again saturated with chromium oxide. The possible sources of chromium oxide are:-

1. - a preoxidised layer
2. - oxidation of alloy surface before the coating has fully fused during firing.
3. - oxidation of alloy surface once the coating has fully fused by diffusion of either molecular oxygen or oxygen ions.
4. - Redox reactions between the alloy and oxide components in the coating.

When the alloy substrate was not preoxidised (C20H, C21H) but fired in air the possible sources of chromium oxide are 2, 3 and 4. One or more of these mechanisms is able to keep the coating at the interface saturated with chromium oxide.

If the alloy substrate is preoxidised in air (C18H, C19H) then fired in oxygen free nitrogen the chromium oxide sources may be 1 and 4. The discontinuous narrow layer of chromium oxide is probably the remnant of the preoxidised oxide layer. The appearance of the spherical metallic precipitates close to the interface indicates a redox reaction. The inability to identify this phase makes it impossible to identify the redox reaction. It could be an oxide

component of the glass being reduced to a metallic state.

A glass-ceramic of similar composition has been used to coat a inconel 718 alloy by Watkins and Loehman (90). They found that chromium diffusing into the coating reacted with the lithium orthophosphate (Li_3PO_4) nuclei to form a metallic chromium phosphorus alloy, Cr_2P. This produced a marked reaction zone in the adjacent coating where the crystallisation mechanism was significantly altered. It was postulated the reaction occurring is

$$9Cr\ (alloy) + 2Li_3PO_{4glass} \equiv 2Cr_2P_{alloy} + 3Li_2O_{glass} + 5CrO_{glass}$$

In effect the phosphorus oxide component of the coating is being reduced while the chromium in the alloy is being oxidised and entering the coating. Investigations by Tomsia et al (91) examined the reactions between lithium disilicate and chromium metal in an evacuated atmosphere with a low partial oxygen pressure. These result in the saturation of the adjacent glass with chromium oxide. A metallic precipitate was observed and identified as a metallic alloy of composition $CrSi_x$. The reaction which produced this was

$$(1+2x)\ Cr + x\ SiO_{2glass} \equiv CrSi_x + 2xCrO_{glass}$$

$$2CrO_{glass} + SiO_{2glass} \equiv Cr_2O_{3glass} + SiO_{glass}.$$

Here the silicon oxide component in the coating is being reduced. It is possible that one or both of these reactions may be producing the observed metallic phase in coatings C18H and C19H.

The metallic phase is absent from coatings C20H and 21H which are fired in an air atmosphere. This suggests that a low partial

1 Using equation 2.9. and assuming standard conditions for the metal and metal oxide:

$$\Delta G_o = -RT \ln 1/p(O_2)$$

$p(O_2)$ was calculated using values of ΔG_o from table 2.1.

oxygen pressure, $P(O_2)$, is a requirement of the redox reaction that produces the metallic phase. The activity of an oxide, e.g. $\alpha(Cr_2O_3)$ at the interface is dependent on $P(O_2)$ in the ambient atmosphere and the amount of Cr_2O_3 already dissolved. At a pressure below the dissociation pressure,[1]

$$P(O_2) = 1.26 \times 10^{-22} \text{ atm for } Cr_2O_3 \text{ (1000°C)}$$

$$P(O_2) = 4.76 \times 10^{-14} \text{ atm for } Fe_2O_3 \text{ (1000°C)}$$

$$P(O_2) = 3.59 \times 10^{-16} \text{ atm for } FeO \text{ (1000°C)}$$

the chromium or iron oxide does not form and any oxide present dissociates. The oxide activity then decreases below unity at the interface. The result is an enhancement of any redox reaction which produces this oxide.

6.2.6 Wetting and adhesion for coatings on chromium iron

The wetting of the alloy substrate by the semi-molten coating during firing was always observed to be good. This was irrespective of the metal pretreatment. The coating remained as a thin continuous layer and did not form globules exposing the underlying substrate. The contact angles must be very low or the condition for spreading exist.

For the "standard" preoxidation in wet hydrogen a layer of chromium oxide is formed over the alloy surface as discussed earlier. This layer is retained during the coating process. For coatings on this substrate the semi-molton coating will be wetting a chromium oxide surface as opposed to a metal surface. The surface energy of a chromium oxide surface is likely to be similar to that for glasses, both being oxide materials. This is unlike the wetting of a metal

surface which has a significantly larger surface energy than glasses. In this situation wetting will normally occur because of the lowering of the surface energy of the metal on forming an interface. For the coating on chromium oxide good wetting or spreading necessitates a low interfacial surface energy. A high degree of chemical bonding is being achieved between the coating and chromium oxide to reduce the structural discontinuity across the interface. Wetting or spreading will also be facilitated by the solid state reaction at the interface. There is a contribution to the reduction of interfacial energy by the free energy of reaction per unit area, ΔG_R. The driving force for wetting can be represented by

$$\gamma Cr_2O_3 air - (\gamma Cr_2O_3 glass + \Delta G_R)$$

The value must be close to or exceed $\gamma_{glass-air}$ to give the observed wetting characteristics. Provided the discrete chromium oxide layer persists at the interface good bonding between it and the coating is possible and good wetting should occur. This explains why the coating continues to wet the substrate even for greatly extended firing times.

Adhesion of the coating to the substrate requires adhesion between each of the individual layers at the interface. That is between:

- coating and chromium oxide layer
- chromium oxide layer and silica layer
- silica layer and alloy

When the substrate was abraded with alumina grit before preoxidation in wet hydrogen adhesion was found to be excellent. See Table 5.1.5. This was the case for the quenched partially

crystallised coating and the heat-treated highly crystalline coating. Clearly good adhesion is developed across the chromium oxide-coating interface. For the heat-treated coating crystallisation extends right up to the chromium oxide surface. But it is not possible to say if a bond is developed between the chromium oxide and the crystal phases present or if an unresolved glassy layer exsists between the two. The former case would require an epitaxial match between the crystal phases and chromium oxide layer.

Adhesion of the chromium oxide layer to the alloy is via a silica layer. The silica layer is the weak point in the coating bond. When failure occurs it is mixed-partly along the interface and partly with in the coating. The failure at the interface tends to be along the alloy-chromium oxide interface. It is not possible to say if the failure is along the alloy-silica or silica-chromium oxide boundary.

If the initial abrasion stage is omitted during the substrate pretreatment, adhesion (although still reasonable) is significantly reduced. Failure now occurs completely along the alloy-chromium oxide boundary. The weak point is once again the silica layer. Abrasion is a critical factor in achieving coating adherence. The result of abrasion is to increase the adhesion of the chromium oxide layer to the alloy via the silica layer.

The effect of abrading the alloy surface prior to preoxidation will:-

- roughen the surface
- leave alumina grit embedded in the surface
- produce cold working of the surface.

As seen in Figure 4.8 the degree of roughening is high with many angular features of micron dimensions present. The chromium oxide

will have an increased keying to the alloy surface brought about by re-entrant angles of the angular surface. It is possible the increased mechanical bonding results in improved coating adhesion by keying the chromium oxide layer to the alloy.

Cold working of metal surfaces will influence the oxidation characteristics, see Wood (92), Giggins and Pelfit (93), Caplan et al (94). It may alter the rate of oxidation and oxide adhesion. Cold working will increase alloy interdiffusion at the metal surface. This may lead to a more rapid formation ofa protective oxide layer and hence a reduced overall oxidation rate. Alternatively, if no protective layer is formed cold working may increase the oxidation rate. Cold working will also effect the oxide adhesion. It may leave residual stresses in the alloy which cause the oxide to spall. Cold working provides sites for vacancies in the alloy surface. This prevents void formation coalescing at the alloy-oxide interface. The result is a greater contact between the oxide and alloy with greater adhesion.

There is however, no evidence that abrasion of the chrome-iron with alumina grit causes a change in oxidation. The chromium oxide formed on the abraded and unabraded alloy have identical x-ray patterns. There observed thickness once coated is similar suggesting a similar initial thickness preoxidised before coating. In both cases a layer of silica exists between the chromium oxide and alloy.

If the alloy substrate is not preoxidised or given a preoxidation in air (C2OH, C21H and C18H, C19H respectively) excellent coating adhesion is obtained. This is provided the substrate is first, abraded with alumina grit, see Table 5.1.5. A discrete layer of chromium oxide is not essential for good coating adhesion. However crystalline chromium oxide is still detected at the interface. This

also implies saturation of the adjacent coating with chromium oxide in solution. Under these conditions good adhesion is developed between the coating and substrate.

Once again abrasion is essential for good coating adhesion. The ideas discussed above will still apply but any increased keying will also now be between the coating and alloy.

The condition essential for good coating adhesion may be expressed as:

- Saturation of the coating at the interface with chromium oxide. Crystalline chromium oxide should be present at the interface either as a discrete layer or in a dispersed nodular form.
- The alloy surface must be abraded prior to any preoxidation or coating process.

6.3 The coating of mild steel

6.3.1 Introduction

The aim of this discussion is to provide an understanding of the requirements needed to produce a successful glass-ceramic coating on mild steel. From the results presented in Section 5.2 it is seen that many processes are occuring during the firing and heat-treatment stages. These processes influence the interfacial microstructure, element distribution, coating wetting power and coating adhesion. An attempt is made to understand the interfacial interactions and features observed.

The influence of adherence oxides, added to the coating, is also discussed.

It should be noted that a comprehensive analysis is hampered due to two factors.

- the inability to make direct and accurate measurements of lithium concentrations.
- the lack of detailed data on the Li_2O-FeO-SiO_2 system. No phase diagrams have been found in the literature; the standard equilibrium phases are not known; the liquidus temperatures of this system are not available; and there is no X-ray diffraction data for lithium iron silicate compounds in the literature.

6.3.2 Iron oxide dissolution

The coatings on mild steel exhibit extensive interaction at the interface. A mixed layer of ferrous oxide (FeO)and magnetite (Fe_3O_4) is formed on the mild steel with a "standard" preoxidation (15 minutes at 650°C in air). Under these conditions, it has a mean thickness of

7 μm (4.04 mg/cm^2). When fired the coating fuses and wets the iron oxide to form a continuous semi-molton layer. The iron oxide is believed to convert mostly to ferrous oxide once the firing temperature is reached. The ferrous oxide is then gradually taken into solution by the coating. It is found that a continuous coating is maintained during firing only when some crystalline ferrous oxide is detected at the interface. An understanding of the dissolution process is needed when considering the crystallisation and wetting characteristics of the coating.

The dissolution of the ferrous oxide may be expressed approximately by (Appendix 2)

$$J = -D_{FeO}\frac{(C_i - C_x)}{\Delta X} \qquad A2.9$$

C_i - the ferrous oxide concentration in the coating immediately adjacent to the interface (g cm^{-3})

C_x - the ferrous oxide concentration at a distance ΔX from the interface (g cm^{-3}).

The drop in concentration over the distance ΔX is assumed linear.

It is difficult to ascertain accurately the interfacial concentration. This is because of the inability to evaluate accurately the lithium concentration. Table 6.3. lists the interface compositions as determined by three separate techniques. The concentration of the major elements silicon, lithium and iron are shown only in at% values.

When assuming a constant lithium to silicon ratio (Li/Si = 0.625), [normal EDX technique], the adjacent coating attains an iron concentration of 7.8 at% Fe (25 wt% FeO). This concentration is

maintained to typically 15 μm into the coating (e.g. M9). The concentration remains constant with firing time and, as discussed in Section 5.2.6, this value may be regarded as a saturation concentration. A large amount of ferrous oxide can be incorporated into the coating (glass B), as has been reported elsewhere. For a commercial enamel, King et al [37] measured the solubility limit as 43 wt% FeO. In a sodium disilicate glass the solubility limit is 42 wt% FeO determined by Borom and Pask [43]. It should be noted that the solubility concentration of ferric oxide (Fe_2O_3) is much lower. For glass B fired on a ferric oxide disk (D4) the adjacent glass has an iron concentration of 2.5 at% Fe (12 wt% Fe_2O_3). This is in agreement with the above references. And is consistent with the iron oxide being present as essentially ferrous oxide (FeO) at the coating-metal interface.

The high saturation concentration produces a large concentration gradient of ferrous oxide within the coating. The value of $(C_i - C_x)$ is relatively large. Consider coating M9 subjected to the standard firing conditions. The value of C_i, the interface concentration, is 0.681 g cm^{-3}. At a 100 μm into the coating the ferrous oxide concentration has dropped to 0.12 g cm^{-3}. Over this distance $(C_i - C_x)$ is equal to 0.56 g cm^{-3}. Compare this with the drop observed for chromium oxide in the coatings on chrome-iron. The value of $(C_i - C_x)$ is 7×10^{-3} g/cm^3 over a smaller distance of 20 μm.

It is the large concentration gradient which provides the driving force for diffusion and consequently the dissolution of the ferrous oxide. The dissolution rate is relatively rapid so that by a firing time of 8 minutes at 970°C (M12) all the preoxidised ferrous oxide has been taken into solution. Saturation of the adjacent coating will not be maintained if no other source of ferrous oxide

exists. The coatings were fired in a neutral atmosphere so atmospheric oxidation is not possible. The only other source for oxidation of the mild steel is through redox reactions with the coating. As discussed later such a reaction does occur, but it is unlikely to provide sufficient ferrous oxide to maintain saturation.

Once all the crystalline ferrous oxide has been taken into solution the coating no longer forms a continuous layer but draws up into hemispherical beads. This is considered more full in Section 6.3.9.

Table 6.3 .: The interfacial composition of the coating determined by various methods

Element	Normal EDX	Windowless EDX	LIMA
	at%		
Si	20	18	19
Li	11.	17	17.5
Fe	7.8	6.0	6.0

6.3.3. Diffusion of ferrous oxide into the coating during firing

If the dissolution of ferrous oxide into the coating is considered as a pseudobinary system a binary interdiffusion coefficient (EBDC) $\tilde{D}_{FeO}$ can be evaluated. Depending on the method used the value for $\tilde{D}_{FeO}$ is

ferrous oxide mass method - $8.60\ (\pm 3) \times 10^{-8}\ cm^2\ s^{-1}$

boundary movement method - $8.67\ (\pm 1) \times 10^{-8}\ cm^2\ s^{-1}$

These values compare well with EBDC values calculated for ferrous oxide diffusing into glasses. An extensive investigation was undertaken by Borom and Pask [95]. They examined the interdiffusion between various iron oxide disks and sodium disilicate glass. Using their data a EBDC value is evaluated as 6.85×10^{-8} cm^2 s^{-1} at 960°C. Further work by Borom and Pask [96] looked at the diffusion of ferrous oxide into a sodium disilicate glass coating on iron. A value of $\tilde{D}_{FeO}$ is found to be 4.38×10^{-8} cm^2 s^{-1} at 960°C. For a commercial enamel on mild steel, Ritche et al [97] calculated $\tilde{D}_{FeO}$ as 1.3×10^{-8} cm^2 s^{-1} at 800°C.

The diffusion of ferrous oxide into a crystallisable lithium silicate glass (glass B) occurs with a similar diffusion coefficient to that for sodium disilicate glasses at 960°C. It implies that ferrous oxide is relatively highly mobile in the semi-molten coating during firing. Using the approximate relation

$$X^2 \simeq \tilde{D}t$$

an estimate of the diffusion distance X can be obtained. For a firing period of 5 minutes the ferrous oxide will penetrate to at least 50 μm.

6.3.4 Interfacial enrichment of lithium in the coating

The approach of considering ferrous oxide diffusing into a single component coating does not describe the dissolution process correctly. The various oxide components in a multicomponent glass (or coating) will have different mobilities. The concentration

distribution will depend on these individual mobilities. See Appendix A2.

There is an apparent enrichment in the interface region of lithium oxide. The windowless EDX and LIMA compositional profiles, Figure 5.2.7, give an interfacial composition showing an increased lithium concentration. See also Table 6.3. The actual lithium concentration appears to be 17 at% Li as opposed to 11 at% Li obtained assuming a constant Li/Si ratio. Pask and Boroom [95] found an enrichment of sodium oxide at the interface between wustite and sodium disilicate glass.

From Table 5.2.5 the ratio of the minor element components aluminium, phosphorus and zinc may be regarded as having a constant ratio to silicon. This ratio is maintained on the solution of ferrous oxide. Potassium exhibits a decrease in its ratio to silicon. As discussed in section 6.3.8 a redox type reaction results in a loss of potassium. It is possible to consider the coating as a two component solvent. The components being

- Lithium oxide (Li_2O)
- Silica (SiO_2) plus the minor metal oxides (Al_2O_3, P_2O_5, K_2O and ZnO).

Ferrous oxide, the solute, undergoes dissolution into the two component solvent. The system may be represented by a ternary molar composition diagram shown in Figure 6.4.

The initial coating or glass B composition is represented by point A. In the ideal binary approach, in which the coating is considered as a single component, the concentration path lies along line AC. The saturation interface concentration is point C. Here the

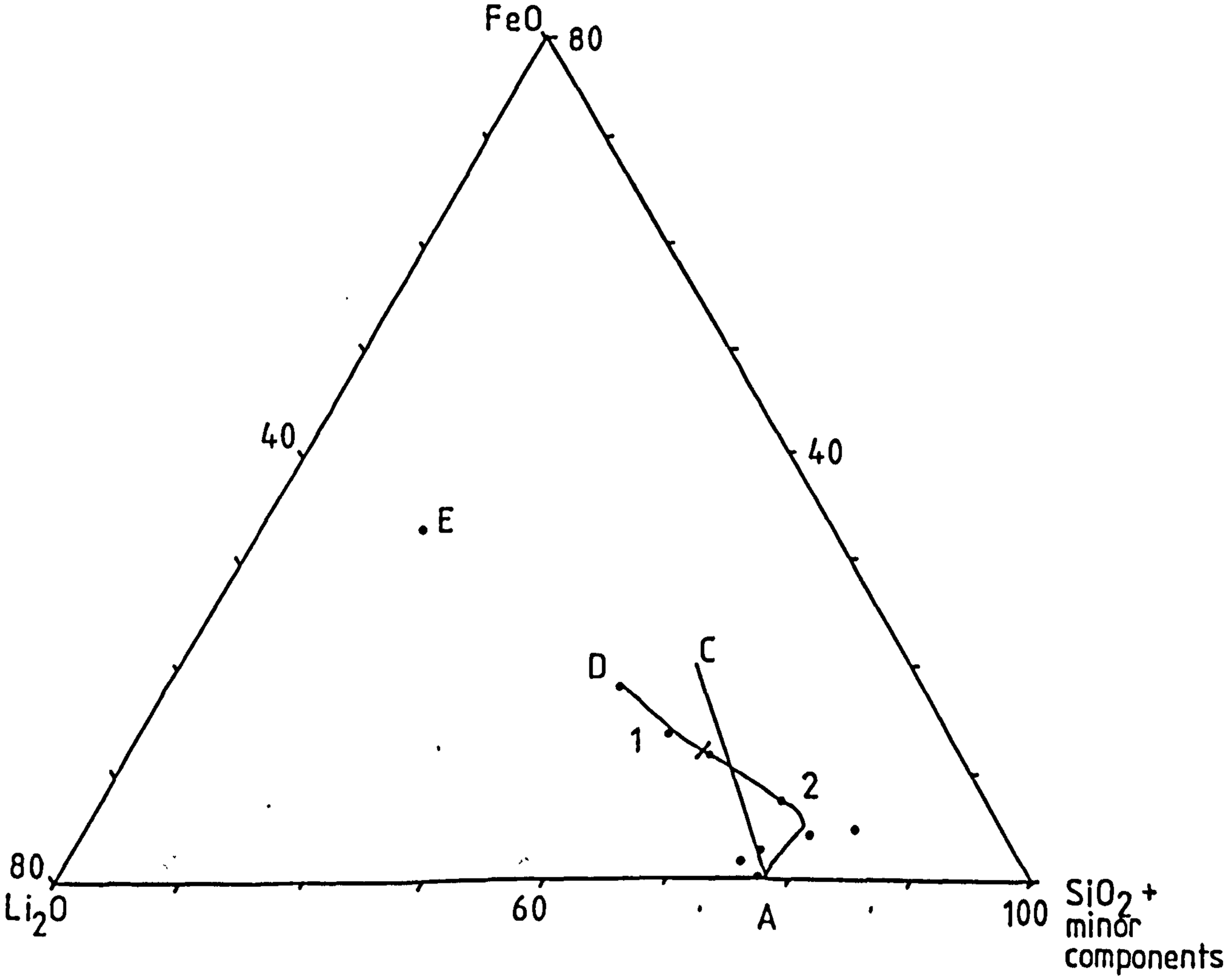

Figure 6.4 Ternary molar composition diagram FeO-Li_2O-SiO_2+ minor oxides.

concentrations for iron and lithium are 7.8 at% Fe and 11 at% Li. These are the compositions given by the normal EDX method.

The concentration profile given by the windowless EDX method is believed to provide a more accurate representation of the lithium levels. If it is plotted on the ternary composition diagram, Figure 6.4, the concentration path is not linear but "S" shaped, curve AD. The interface concentration has shifted to point D which is enriched with lithium.

For a two component solvent into which dissolution of a solute occurs it is possible to show

$$\frac{D_{Li_2O}}{D_{SiO_2}} \equiv \frac{W_{Li_2O}\ dW_{SiO_2}/dx}{W_{SiO_2}\ dW_{Li_2O}/dx}$$

This expression is explained in Appendix 2. It relates the interface concentrations of the solvent components, W_{SiO_2} and W_{Li_2O}, to their intrinsic diffusion coefficients, D_{Li_2O} and D_{SiO_2}. It predicts an enrichment of the more mobile component of the solvent (or semi-molten coating in this case) at the interface during the dissolution of the solute (ferrous oxide).

The self diffusion coefficients for O^{2-}, Si^{4+}, Li^{+}, Fe^{2+} and Na^{+} in various glasses at 1000°C are listed in Table 6.4. The values are largely obtained by extrapolating data collected from different temperature ranges. The self diffusion coefficients for lithium ions have been evaluated at low temperatures (200-500°C) only. In this temperature range the values are similar to those for sodium ions. Extrapolation to 1000°C gives values again similar to those for sodium ions evaluated at 1000°C.

Examination of Table 6.4. shows lithium ions to be much more mobile than silicon ions in glasses at 1000°C. Assuming the ions diffuse with their associated oxygens it is reasonable to say D_{Li_2O} will greatly exceed D_{SiO_2}:

$$D_{Li_2O} >> D_{SiO_2}$$

From equation A2.10 an enrichment of lithium oxide in the interface region would be expected. The oxygen ions maintain electrical neutrality. The assumptions above require oxygen to be the fastest diffusing species. Table 6.4. shows this is not the case. Oxygen ions are the slowest diffusing species. Electrical potential gradients will be set up and strongly influence the dissolution process. It is not possible to consider fully the electrical potential gradients and their influence. The coating is too complex having many components of differeing mobilities. Also it is not possible by the methods used to evaluate accurately the lithium concentration.

Table 6.4. Self diffusion coefficients.

ion	ΔT	D(1000°C)	Material	ref.
O^{2-}	350-450	3.85×10^{-14}	$18Li_2O.82\ SiO_2$	98
O^{2-}	550-700	3.77×10^{-14}	$13Na_2O.87SiO_2$	99
O^{2-}	800-1470	1.0×10^{-8}	$15.5Na_2O.12.8CaO.71.7\ SiO_2$	100
O^{2-}	625-830	3.4×10^{-10}	$45\ CaO.13.Al_2O_242SiO_2$	101
O^{2-}	765-845	3.9×10^{-12}	"	102
Si^{4+}	600-1300	3.9×10^{-9}	$26.Na_2O.73.6SiO_2$	103
Si^{4+}	660-760	3.56×10^{-10} -3.56×10^{-13}	$45CaO.13Al_2O_342SiO_2$	104
Fe^{2+}		1×10^{-7}	$FeO-SiO_2$	105
Fe^{2+}	1250-1350	6×10^{-6}	$11FeO-39SiO_2$	106
Li^{+}	270-440	6.5×10^{-6}	$25Li_2O-75SiO_2$	107
Li^{+}	290-450	2.8×10^{-5}	$33Li_2O-67SiO_2$	107
Li^{+}	285-420	5.4×10^{-6}	$18Li_2O-82SiO_2$	107
Na^{+}	850-1210	1.6×10^{-5}	$33Na_2O.17SiO_2$	108 a
Na^{+}	850-1050	1.47×10^{-5}	"	108 b

6.3.5 Coating crystallisation -Dendritic growth

The presence of ferrous oxide in the coating is seen to influence strongly both the spontaneous crystallisation during firing and the controlled crystallisation on heat-treatment.

For all the quenched coatings (M4 to M11 and M15 to M17) there is a region adjacent to the interface where crystallisation is absent. Immediately adjacent to the interface crystal growth is noticable but extends at most 4μm into the coating. It has proved difficult to identify this phase accurately due to the inability to directly measure the lithium concentration and because of its close proximity to the mild steel substrate. The indications are that it is a lithium iron zinc silicate having the formula

$$Li_2O\ Fe_{0.8}\ Zn_{0.2}\ O.\ SiO_2$$

The coating adjacent the interface attains a composition given in table 6.3. The "windowless EDX method" composition, when expressed as oxide molar percentage values, may be represented by a point D in figure 6.4.

For all firing times up to 7 minutes (M11) and firing temperatures up to 980°C (M17) the dendritic crystal phase does not extend beyond 4μm. No trend in its growth can be related to firing time. The dendritic crystal phase is beleived to appear as the semi-molten coating is rapidly cooled on quenching.

Apart from the dendritic growth, the adjacent coating remains glassy during firing. Only when the iron concentration has dropped below 4at%Fe does crystallisation appear. This is best represented in figure 6.5, a possible representation of the psuedo-binary system FeO-glass B. No literature exists on the Li_2O-FeO-SiO_2 system so the actual liquidus compositions and temperatures are not known. The

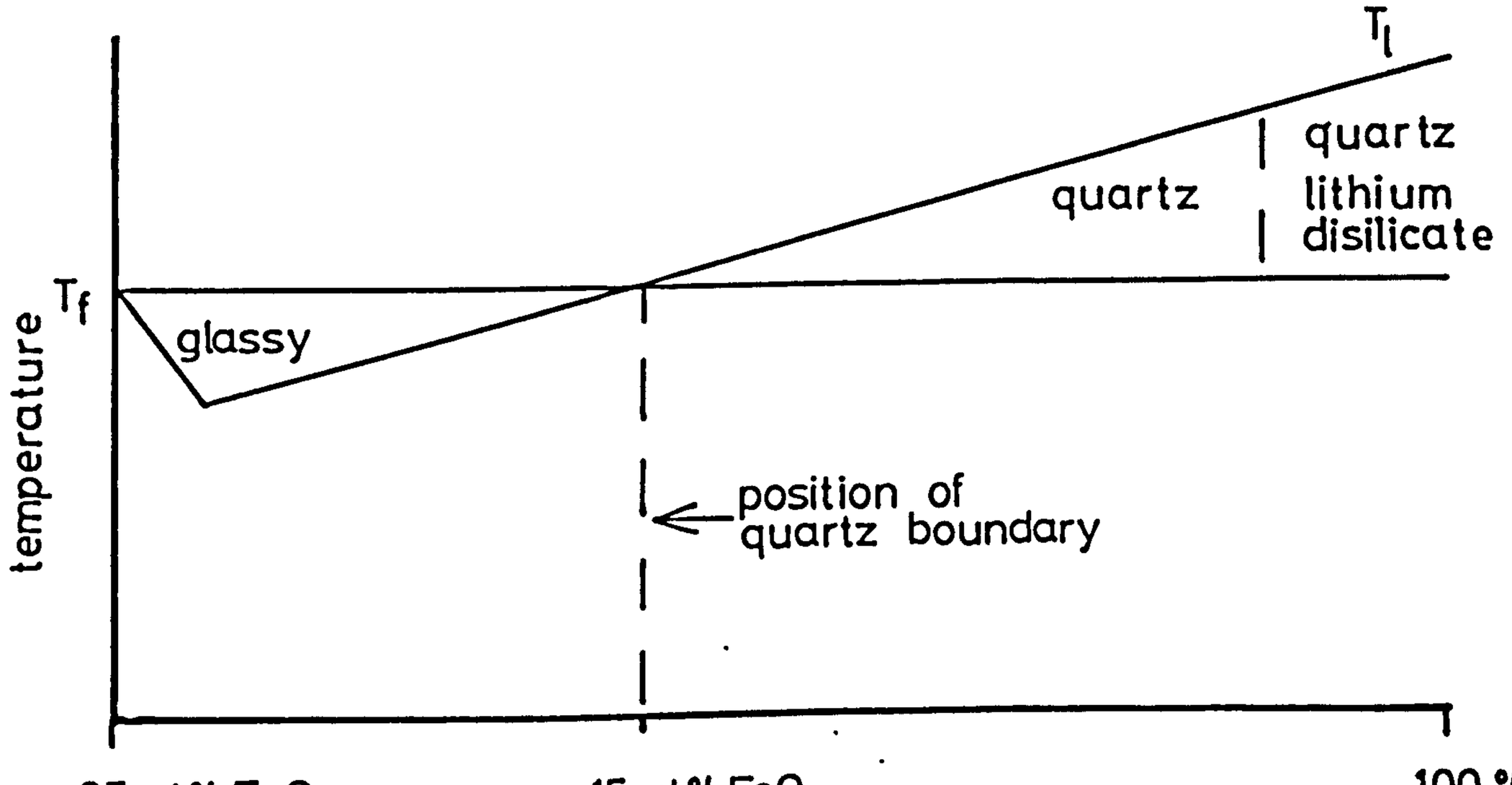

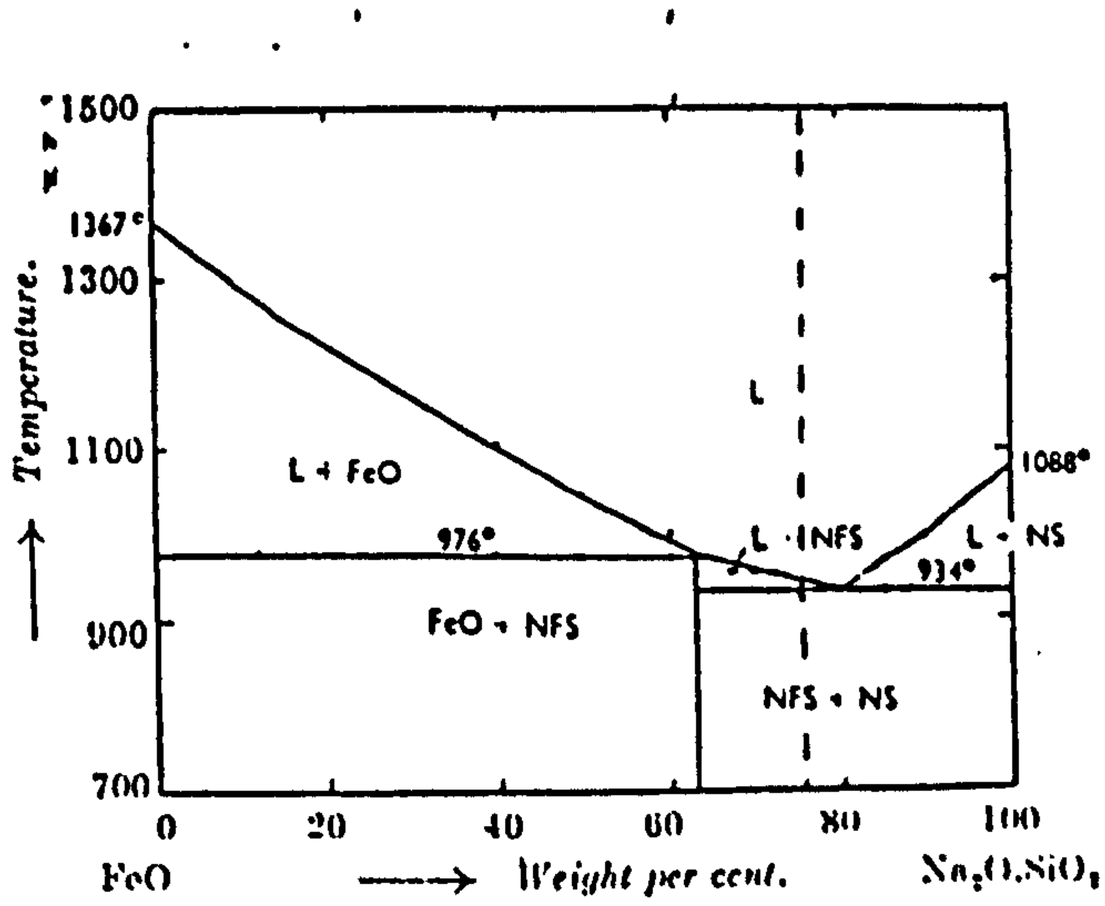

Figure 6.5. Possible representation of the psuedo-binary system FeO - glass B.

Na_2O-FeO-SiO_2 system has been studied by Carter et al (109). The FeO-$Na_2O.SiO_2$ binary phase diagram is reproduced in figure 6.5. It has a similar shape to that proposed for the FeO-glass B system between ferrous oxide concentration 0 to 25wt%.

On quenching, the interface region of the coating becomes supercooled and the conditons for dendritic growth must persist. The crystalline ferrous oxide and mild steel surfaces appear to act as a nucleating surface for the lithium iron zinc silicate phase. This phase then grows dendritically into the super cooled coating. The composition of the adjacent 15μm of the coating is essentially constant. Dendritic growth may be expected to extend well into this region. However, the quenching will produce a rapid increase in glass viscosity quickly stopping dendritic growth. See equation A1.5. Consequently the growth period will be extremely short, controlled by the rate of cooling. This accounts for the small extent of dendritic growth and the similar size observed for different firing times.

The large composition difference between the lithium iron zinc silicate dendrites and the saturated coating means ion diffusion is an important factor in the dendritic growth. Lithium, iron, zinc (and their associated oxygens)' must be removed from the glass adjacent to the growth front. Silica ions (and their associated oxygens)' must be expelled into the adjacent glass. The dark contrast tip observed ahead of each dendrite is evidence for this.

The absence of any isolated crystals of lithium iron zinc silicate in the adjacent coating indicates the absence of suitable bulk nuclei. It is only the interface which acts as a suitable nucleating surface for this phase.

'not necessary.

Examination of the glass disc heated on ferrous oxide (D3) supports the idea that crystalline ferrous oxide acts as a nucleating surface. The dendritic growth is much more extensive for this couple. The high ferrous oxide concentration, close to saturation, will extend further into the glass. Also the greater thermal mass will produce a slower cooling rate and hence a greater growth period on cooling.

Dendritic growth appears to originate at the metal-coating interface in places where no pockets of ferrous oxide are observed. This is particularly so for longer firing times and higher firing temperatures. However, x-ray diffraction of the exposed coating surface detects only a single peak at 42.2° 2θ associated with ferrous oxide, even when very few pockets of ferrous oxide are observed and the coating mild steel interface predominates. See figure 5.2.11(f) showing coating M17. It would seem that crystalline ferrous oxide is present along the entire coating-mild steel interface, but often too narrow to detect.

This ferrous oxide layer is very effective in nucleating the dendritic phase. An effective heterogeneous nucleating surface operates by reducing the barrier to nucleation represented by the surface energy. See appendix 1. This may imply epitaxy between the crystalline ferrous oxide and lithium-iron-zinc-silicate. It is generally regarded that a disregistry of less than 5% is needed. See McMillan [9]. The lack of any crystallographic data on lithium-iron zinc silicate phases prevents verification of a possible lattice match.

6.3.6 Coating crystallisation - Microstructural development of the fired only coating.

The microstructure of a fired only coating varies considerably throughout its thickness, the extent of which is critically dependent on the firing conditions. During firing ferrous oxide is continually diffusing into the semi-molten coating. It is present at such high concentrations that a compositional gradient is set up through the coating. Consider figure 6.4. The interface composition is represented by D. With increasing distance into the coating the composition will move along path DA. Close to the outer coating surface the composition is given by point A.

Over such a wide compositional range, different regions would be epxected to show differing crystallisation with identical thermal treatments. The compositonal profile will extend further into the coating with increasing firing time and temperature. For example the position at which the ferrous oxide concentration drops to 4at%Fe (the point where β-quartz appears) will gradually extend into the coating (Table 5.2.10).

In the compositional range extending from the interfacial concentration of 7.8at%Fe to 4at% Fe devitrification is inhibited (apart from limited dendritic growth). This is represented by region 1 in figure 6.4. The liquidus curve is believed to be below the firing temperature (≃970^{o}C) in region 1 as shown in figure 6.5.

In the compostiional range between 4at%Fe to 0.5atFe β-quartz is formed. At 4at%Fe the liquidus temperature reaches the firing temperature as illustrated in figure 6.5. This is represented by region 2 in figure 6.4. Within region 2 the lower levels of ferrous oxide inhibit the crystallisation of lithium disilcate only.

Beyond 0.5at%Fe to the outer coating surface, point A, both β-quartz and lithium disilicate appear.

6.3.7 Coating crystallisation - Microstructural development of the heat-treated coating

The different compositional regions have different crystallisation characteristic when subjected to a heat-treatment.

In region 1 (7.8-4at%Fe) granular crystals of lithium iron zinc silicate are formed. They have the same composition as the dendritic growth in the fired only coatings:

$$Li_2O.Fe_{0.8}Zn_{0.2}O.SiO_2.$$

The original dendritic growth extends to form a continuous layer between the substrate and crystallised coating. Carter et al [109] found that a sodium iron silicate phase was produced in the ternary Na2O-FeO-SiO2 system with a formula

$$Na_2O.\ FeO.\ SiO_2$$

By comparison a similar phase would be expected to form in the ternary Li_2O-FeO-SiO_2 system. When Na replaced by Li. The formation of a lithium iron zinc silicate with the formula above seems reasonable. This gives support to the experimentally determined composition of this phase which was achieved by an indirect approach.

There is considerable redistribution of the minor elements during heat-treatment in region 1. Zinc and phosphorus ions are incorporated into the crystal phase. This is most noticable for zinc. By examining the table in appendix 5 the Zn^{2+} ions are seen to have a similar ionic radius and field strength as Fe^{2+} ions when in octrahedral coordination. The Zn^{2+} ions would therefore be expected to substitute for the Fe^{2+} ions.

The preferential location of the minor element phosphorus in the lithium iron zinc silicate phase is of interest. It may be related to the initial formation of a phosphate crystallite which acts as a

nucleating agent, similar to that observed for the glass composition when ferrous oxide is absent.

Aluminium and potassium preferentially remain in the matrix phase (table 5.2.7). It is not clear if the matrix is crystalline or amorphous. The matrix phase also exhibits a banded structure, dependent on the firing conditions and also determines the potassium distributions. Although having a reduced concentration in region 1 for the fired only coating, the potassium is seen to be preferentially located in the light contrast matrix. It is possible to explain these observations if the dark matrix phase is crystalline. The sharp boundary between the dark and light matrix would not be expected if both were glassy. It is believed that the dark matrix phase is a crystalline form of silica, possibly quartz. Table 5.2.8 lists the peaks in the x-ray pattern obtained from the exposed interface between ferrous oxide and glass B. A substantial peak exists at $26.4^{o}2\theta$ (3.37Å). This is very close to the position of the main quartz peak:

3.34 Å α-quartz

3.40 Å β-quartz

However, no standard x-ray data exists for $Li_2O.FeO.SiO_2$ and thus it is not possible to say if the peak at 3.37 Å is due to the lithium iron zinc silicate phase or quartz.

Examination of table 5.2.7 gives an O/Si ratio of 2.4 for the dark matrix phase. For quartz a value of 2 would be expected. Some of the silicon may be substituted by aluminium and phosphorus with minor amounts of potassium and lithium present to keep electrical neutrality. If we consider the total amount of network formers i.e. Si+P+Al given by analysis, the "silicon" concentration becomes 29.6at% Si and the O/Si ratio is reduced to 2.1 closer to that of quartz.

There is a good possibility that the dark matrix phase is quartz with some substitution. As discussed in Section 6.1.1. potassium may preferentially reside in the glassy areas. It is not a major component of any crystal phase appearing. Consequently it will be expelled from crystallising regions and reside in the residual glassy areas. The light matrix is the main glassy region in the coating.

In region 2 (4-0.5at%) both lithium disilcate and β-quartz are produced giving a highly crystalline microstructure with little matrix phase. It is characteristic of the microstructure formed in the coating on chrome-iron. The presence of less than 4at%Fe does not influence noticably the crystallisation of the coating during heat treatment.

6.3.8 Potassium distribution

Potassium appears to have a concentration much lower than expected in the interface region of the fired only coatings. This is most marked in the region where the iron concentration exceeds 4 at% Fe (15 wt% FeO). In figure 6.4 this corresponds to region 1. Possible explanations for this are:

- a loss of potassium occurs under the electron beam during the measurement of potassium concentrations in iron rich glasses.
- possible interdiffusion effects leading to potassium diffusing away from the interface.
- a loss due to an interfacial reaction.

The first explanation may be excluded. Analysis of iron containing glass B, See table 3.7, gives potassium concentrations

close to that expected. The second explanation may also be excluded. A potassium loss is not observed in the interface region when a disc of glass B is heated on a ferrous oxide disc (table 5.2.18).

We have therefore to conclude that a redox reaction of the type 2.4. , Section 2.4.4 is occurring. The iron in the substrate is being oxidised while the potassium oxide component in the coating is reduced.

The reaction can be represented by

$$Fe_{(substrate)} + K_2O_{(glass)} \equiv FeO_{(glass)} + 2K \text{ vapour}$$

Potassium has a boiling point of 760°C and will be a vapour at the firing temperature.

A similar reaction is reported in the literature to occur between mild steel and sodium oxide containing glasses. In this case sodium vapour is formed. For example see Pask and Tomsia [32], Pask [39], Hoge et al [44].

At 1000°C the redox reaction above between iron and potassium oxide has a negative Gibbs free enrgy. From Table 2.1 it is found to be -13.4 kJ $mole^{-1}$. The reaction will proceed readily if the oxides are in their standard states. It should be noted that potassium oxide decomposes above 827°C and that the oxides are not in standard states but are component oxides of the coating. For the reaction to continue the potassium vapour must be removed from the interface region. It may do so by

- diffusing through the semi-molten coating as bubbles of potassium vapour.
- react with any oxygen present

- react with the oxide components in the glass.

It is not clear which of these (if any) predominates. Potassium vapour will be extremely reactive at the firing temperature.

A loss of potassium is not noticeable when glass B is fired on an unpreoxidised mild steel substrate (D2), see Table 5.2.18. The loss of sodium oxide from a sodium disilicate glass heated on mild steel is found to be dependent on the amount of ferrous oxide already in solution. See Hodge et al [44]. The activity of sodium oxide (α (Na_2O)) increased rapidly as ferrous oxide is added to the glass. It is possible that a certain ferrous oxide concentration is required in the coating before potassium oxide has an activity sufficient for the reaction above to proceed.

The effect of the redox reaction is to provide an additional source of ferrous oxide. Using the potassium concentrations observed in coating M9 the potassium loss and ferrous oxide produced can be evaluated. At 60 μm the potassium concentration is assumed to drop from 2.5 at% to 0.8 at% and remain at this level up to the interface. If the loss is due entirely to the redox reaction a ferrous oxide gain of 0.16 mg cm^{-2} results. It is significantly smaller than the ferrous oxide produced by preoxidation (4 mg cm^{-2}). This reaction is not a major source of ferrous oxide.

There is no loss of other oxide components from the coating. By examining Table 2.1 the only other reaction thermodynamically feasible with the oxides in their standard states is between phosphorus oxide and iron. As this does not occur the activity of phosphorus oxide in the coating must be such that the reaction is unfavourable. Also there may be no means of removing phosphorus vapour produced by such a reaction.

A redox reaction between other oxides in the coating is unfavourable in their standard states. Since they do not form vapours at the firing temperature there is no mechanism by which the reaction would proceed under a low partial vapour pressure (C.F. sodium oxide).

6.3.9 Wetting

To obtain a thin continuous coating on the mild steel substrate pockets of residual crystalline ferrous oxide must be observed at the interface. See the results in Section 5.2.6. Once the majority of the ferrous oxide has been taken into solution during firing the coating draws up into beads. This limits the firing time and temperature for which a coating can be produced. At 970°C the firing time must not exceed 7 minutes (M11) or for 5 minutes the firing temperature must not exceed 980°C (M17).

On firing, the glass powder fuses and gradually forms a semi-molten layer. This will meet an essentially ferrous oxide surface. On continued firing the oxide dissolution proceeds and coating appears eventually come into some contact with the metal surface. Ferrous oxide being observed in pockets but may also extend along the entire interface to some unobservable thickness.

To have a continuous layer the condition for spreading or a low contact angle must be met. The condition may be represented as

$$\gamma_{SV} - \gamma_{SL} > \gamma_{LV}$$

The situation is complicated due to the coating forming an interface with both ferrous oxide and mild steel. A low interfacial energy γ_{SL} favours the above condition. This requires a good chemical

bond across the interfaces. Both crystalline ferrous oxide and the coating saturated with ferrous oxide have oxide structures and thus it is not unreasonable to expect a chemical bond to be formed across the interface. The adjacent coating is saturated with ferrous oxide. This is the requirement for the development of a chemical bond between a glass and metal as discussed in Section 2.4.3. A low value for γ_{SL} is therefore expected.

The semi-molten coating will have a strong driving force for the solution of ferrous oxide. See Pask [29]. For the FeO - $Na_2O.2SiO_2$ system Lacy and Pask [110] have evaluated the free energy data for the solution of ferrous oxide in sodium disilicate glass. At the solubility limit (0.683 mole fraction FeO) a value of -10kJ $mole^{-1}$ was evaluated for a temperature of 1000°C. The reduction in free energy of the system brought about be the solution of ferrous oxide will contribute to the driving force for wetting. The condition for spreading may be expressed by

$$\gamma_{SV} - (\gamma_{SL} + \Delta G_{solution}) > \gamma_{LV}$$

Once the ferrous oxide has been completely taken into solution the semi-molton coating is in contact only with the mild steel. The free energy of solution of the ferrous oxide will no longer contribute to the driving force for wetting. A chemical bond and low interfacial energy γ_{SL} will exist only if the adjacent coating remains saturated with ferrous oxide. However unless there is a source of ferrous oxide this condition can not be maintained. The coatings were fired in a neutral atmosphere so atmospheric oxidation is not possible. A redox reaction has been identified between potassium oxide and mild steel. Using the concentration profiles in section 5.2.5 and equation A.2.9

is possible to estimate the flux of ferrous oxide into the coating. For coating M11 (7 minutes at 966°C) a value of 0.24 Mg cm^{-2} $minute^{-1}$ is calculated. This represents the flux of ferrous oxide into the coating just before it becomes depleted. The total amount of ferrous oxide formed by the redox reaction is 0.16 Mg cm^{-2}. The redox reaction is unable to maintain saturation. As a consequence the condition for spreading or low contact angle is not met and the coating draws up into beads.

A similar situation has been observed by Pask and Fulrath [31] for molton sodium disilicate glass on mild steel. If the glass was placed on an oxidised surface the contact angle approached zero. Once the glass reached the iron surface by dissolving all the iron oxide the contact angle approached 55°.

6.3.10. Coating adhesion

The coatings exhibit good adhesion to mild steel when they are in a fired-only or heat-treated condition. A typical tensile adhesion strength of > 50 MN m^{-2} is observed. The adhesion appears uneffected by the firing conditions. Provided a fully fused continuous coating is formed, adhesion is good.

Good wetting of coatings on mild steel substrates is often associated with good adhesion characteristics. See Pask and Fulrath (31). It implies a small interfacial energy γ_{SL} brough about by the development of a good chemical bond across the interface. The conditions for good bonding must be met for the coating and substrate. The adjacent coating is saturated with the oxide (FeO) of the substrate material (mild steel). However substantial amounts of ferrous oxide remains at the interface. The coating wets

and bonds mostly to a ferrous oxide surface. The presence of crystalline ferrous oxide at the interface between commercial enamels and mild steel is often regarded as detrimental to coating adhesion. Adhesion of ferrous oxide to iron and steels is not particularly good as discussed by Kantz (38). Good adherence between an enamel and mild steel is traditionally explained by the theory in section 2.4.3. It implies that only a monolayer of iron oxide is maintained at the interface and the adjacent enamel is saturated with iron oxide.

There is some evidence that this may not always be the case. Investigations by Ritche et al [97] looked at an enamel on mild steel. They concluded that a ferrous oxide layer exists at the interface and has a width of 1-3 μm. Others have also reported the presence of iron oxide at the interface, see Richard and Demard [111]. The adhesion strengths reported here also indicate that good bonding must be formed between the residual ferrous oxide and mild steel. The uncoated iron oxide layer produced during preoxidation has a relatively poor tensile adhesion strength. The coating process leads to an improvement in adhesion of the ferrous oxide layer to mild steel.

It is believed that a crystalline ferrous oxide layer is present along the whole of the interface of an adherent coating even when no residual ferrous oxide is observed in the electron micrographs. There is some evidence to support this:

- X-ray diffraction detects only a single peak at 42.2° 2θ associated with ferrous oxide even when only minor amounts of residual ferrous oxide are observed by electron microscopy.

- The adjacent coating is saturated with ferrous oxide so at least mono oxide layer would be expected at the interface according to the theory in Section 2.2.

- The entire interface is effective in nucleating the lithium iron zinc silicate phase. Ferrous oxide provides an effective nucleating surface for the phase.

If it is accepted that crystalline ferrous oxide is present along the interface many of the observed features can be explained. As mentioned earlier a good bond would be expected between ferrous oxide and the lithium iron zinc silicate phase due to a epitaxial match. The ferrous oxide layer can be visualised as producing a transition layer exhibiting good bonding to both the mild steel and coating. Provided crystalline ferrous oxide remains at the interface, good coating adhesion can be expected and will not be influenced by the length of the firing period . This agrees with the coating adhesion measurements on the fired only coatings.

When the coating is heat-treated coating adhesion should remain good. The original dendritic growth extends to form a continuous layer along the interface, bonding to the ferrous oxide layer. This again agrees with the observation that good coating adhesion is retained after heat-treatment.

6.3.11 · Influence of adherence oxides

The addition of minor concentrations (0.25 wt%) of nickel or cobalt oxide to the initial glass B composition has a considerable influence. The effects common to coatings containing either adherence oxide are:

- The appearance of small, spherical metallic alloy particles in the coating adjacent to the coating mild-steel interface.

- Continued wetting of preoxidised mild steel substrate for a firing time in excess of 15 minutes. Much longer than a coating not incorporating an adherence oxide.

The metallic alloy phase is formed during firing and is retained on heat-treatment. It appears not to influence the coating microstructure developed. Cobalt oxide has no effect on the residual ferrous oxide but this is not the case for nickel.

The appearance of metallic precipitates at the interface between enamels and mild steel is expected. Such features have been observed by other workers. Nedelikavic [112] examined a simple soda borosilicate enamel, containing either nickel or cobalt oxide, on a low carbon steel. He found that metallic precipitates formed immediately adjacent to the interface. They had a composition of $Fe\text{-}Ni_3$ or an unspecified $Fe\text{-}Co_x$ depending on the adherence oxide added. For a commercial enamel of Armco iron Borom and Pask [43] observed extensive formation of metallic dendrites within the enamel bulk. Their composition varied with distance from the interface reflecting the iron oxide concentration in the enamel.

The adherence oxides are considered as participating in the formation of metallic alloys with mild steel. These alloys can readily adjust themselves to maintain chemical equilibrium with the changing composition of the coating adjacent to the interface. Chemical bonding is maintained across the interface and consequently good wetting characteristics are continued.

For cobalt oxide containing coatings a redox reaction occurs

with the mild steel substrate to produce cobalt metal. The reaction may be expressed as:

$$xFe + xCo^{2+} \equiv xFe^{2+} + xCo \qquad 6.3.1$$

The cobalt metal then alloys with the mild steel:

$$(1-x)Fe + xCo \equiv Fe_{(1-x)}\ Co_x \text{ alloy} \qquad 6.3.2$$

A similar reaction may occur for nickel giving a nickel-iron alloy. From the data in Table 2.1 it is possible to evaluate the Gibbs free energy for the above reaction 6.3.1. For oxides in their standard states and at 1000°C:

$$CoO \quad \Delta G = -90.8 \text{ kJ mol}^{-1}$$

$$NiO \quad \Delta G = -128.5 \text{ kJ mol}^{-1}$$

The change in Gibbs free energy associated with the alloy formation may also contribute to the overall reduction in Gibbs free energy.

The composition of the alloy and coating of the interface may be adjusted in an effort to maintain equilibrium conditions. This can be represented by

$$Fe_{(1-x)}Co_x + mFe^{2+} + nCo^{2+} \equiv Fe_{(1-x-p)}\ Co_{(x+p)} + (m+p)Fe^{2+} + (n-p)Co^{2+} \qquad 6.3.3$$

It is likely that these or similar reactions are producing the metallic particles observed in Section 5.2.10. There are however some difficulties:

- The alloys are essentially iron with only minor amounts of cobalt or nickel.

- The alloy particles are isolated from the base metal and not plated along the mild steel surface.

- The alloy particles often appear adjacent to the residual ferrous oxide pockets. Occasionally the alloy is plated out on the ferrous oxide surface.

The addition of nickel oxide to the coating produces some additional features not observed with cobalt oxide. These are:

- the absence of residual ferrous oxide at the interface even for a "standard" firing time (5 minutes at 970°C M21).
- the absence of dendritic growth
- a fine dispersion of metallic particles of submicron dimensions throughout the coating bulk
- a loss of coating adhesion on heat-treatment

It is possible to explain these features if nickel oxide reacts with ferrous oxide according to:

$$3FeO + NiO \equiv Fe_3O_4 + Ni \qquad 6.3.4$$

Electrochemical studies on the redox behaviour of various metal ions in molten glasses have been carried out by Takanaski and Miura [113]. The results allow the reducing power of the ions to be evaluated. These are listed in Table 6.5. for a sodium disilicate

glass. It is energetically favourable for Ni^{2+} to be reduced to Ni with Fe^{2+} being oxidised to Fe^{3+}. Such a reaction is not favourable with cobalt ions. It is assumed that reaction 6.3.4 proceeds only with nickel oxide. This is supported by the observation that only nickel oxide containing glass B when fired on a ferrous oxide disk shows the presence of metallic particles.

The presence of nickel oxide in the coating promotes a more rapid dissolution of the ferrous oxide layer. Adherence oxides, particularly nickel oxide, are known to promote the formation of Fe_3O_4 at the expense of ferrous oxide (FeO). This is observed by Nedelikovic [112]. Investigations by King et al [37] have shown iron oxide scale is dissolved more rapidly if it contains the reducible oxides of cobalt and nickel. They also found a pellet of Fe_3O_4 was attacked and dissolved much more rapidly than a Fe_2O_3 or FeO pellet. It was concluded that one of the main functions of adherence oxides is to oxidise crystalline ferrous oxide (FeO) to Fe_3O_4 thus aiding its dissolution. It is believed a similar reaction is occurring for the coatings in this project.

The consequence is that for a "standard" firing the nickel oxide containing coatings dissolve all the ferrous oxide. No residual ferrous oxide remains at the interface. This is confirmed by an absence of a single peak at 42.4° 2θ for the x-ray diffraction pattern collected from the exposed ceramic surface.

The absence of crystalline ferrous oxide at the interface means there is no nucleating surface for the dentritic phase. Hence dendritic growth of lithium iron zinc silicate does not occur as the coating is cooled. The lithium iron zinc silicate phase appears in the interfacial region after heat-treatment. Bulk nucleation and growth operate in this region, identical to when nickel oxide is

absent. But there is no crystalline ferrous oxide to act as a transition layer and to which the lithium iron zinc silicate phase can bond. As a result, coating adhesion is lost on heat-treatment.

The fired only coating retains some adhesion although reduced. The more variable structure of the glassy coating may be able bond to the metal surface. The bonding mechanism will be similar to that for traditional ground coat enamels and discussed in Section 2.3.

Reaction 6.3.4 also occurs between nickel oxide and ferrous oxide in solution. The metallic particles throughout the coating bulk are evidence for this.

Clearly nickel oxide has a considerable effect on the interfacial structure. It causes the loss of adhesion and does not act as an "adhesion promoter".

Table 6.5. Reducing power of various ions in a molten sodium disilicate glass.

$Zn^{2+} + 2e^- = Zn$

$Co^{2+} + 2e^- = Co$

$Fe^{3+} + e^- = Fe^{2+}$

$Ni^{2+} + 2e^- = Ni$

increasing reducing power.

Chapter 7:

Conclusions and Future Work

Crystallisation of coatings is complex. Ignoring the influence of solution of the substrate metal oxide, the crystallisation of the coating is markedly effected by the coating process itself. It can be divided into two stages:

- spontaneous crystallisation during firing, producing an inhomogenous, partially crystallised coating.

- controlled crystallisation during heat treatment in which residual glassy areas crystallise to give a highly crystalline coating.

The large surface area of the initial glass powder influences the crystal phase produced in spontaneous crystallisation in that it favours the rapid formation of β-quartz in glasses of the composition used in this work. Subsequent crystallisation is governed by bulk nucleation, coarsening and a polymeric transformation of β-quartz to α-cristobalite. The crystal phases produced during firing are:

- β-quartz
- lithium disilicate
- Cristobalite (for extended firing times only).

The heat-treatment stage results in crystallisation of residual glassy

areas with the formation of crystal phases:

- β-quartz (minor amounts)
- lithium disilicate

The consequences of starting with a fine powder as opposed to a bulk glass are:

- the formation of β-quartz in favour of α-cristobalite
- a coarser, more granular microstructure,

The nature of the metal oxide formed on the substrate is of critical importance. Such an oxide can be formed either by a preoxidation stage or during the firing stage. The metal oxide present at the interface between the substrate and coating influences:

- coating wetability
- coating adhesion
- devitrification characteristics of the adjacent coating
- interfacial reactions.

Glass A and glass B are of very similar compositions. The slight difference allows thermal expansion co-efficients to be matched to the substrate metals. The only major difference between the two

coated metal substrate systems is that one substrate contains 17wt% chromium.

The two metal substrates form different oxide scales. On oxidation the chrome-iron substrate forms essentially a chromium oxide (Cr_2O_3) layer. The mild steel substrate can form a mixed iron oxide scale. At the firing temperature the iron oxide exists as ferrous oxide and it remains as ferrous oxide at the coating-mild steel interface.

It is the properties of the two substrate oxides that produce the different coating characteristics in each system. The most influential properties are:

1. Solubility in the adjacent coating at the firing temperature.
2. Nucleating ability of the substrate oxide surface.
3. Influence of substrate oxide dissolved in the coating on cyrstallisation processes.
4. Redox and other chemical reactions with the adjacent coating.
5. Adhesion to the fired only or heat-treated coating.
6. Adhesion to the metal substrate.

Each of these will now be considered in turn and a comparison made, between the two substrate oxide types.

1. The saturation concentration of chromium oxide (Cr_2O_3) is very low in these glasses. At the firing temperature it is only 0.3at%Cr. The dissolution rate of chromium oxide is

correspondingly very low and the oxide layer remains at the interface for greatly extended firing times. Also it is not necessary to preoxidise in wet hydrogen. Oxidation during the firing stage (if fired in air) produces sufficient substrate oxide.

Ferrous oxide (FeO) has a much greater saturation concentration. At the firing temperature (~970^{o}C) it is equivalent to 7.8at% Fe. The ferrous oxide, as a consequence undergoes rapid dissolution. This places a limit on firing times and temperatures which can give a satisfactory coating (when an inert firing atmosphere is used).

2. Crystalline chromium oxide does not appear to act as a nucleating surface. There is no preferential appearance at any phase in the coating immediately adjacent to the interface.

Crystalline ferrous oxide acts as a nucleating surface for a lithium iron zinc silicate phase. On cooling from the firing stage, the phase is initiated at the ferrous oxide present at the interface. Conditions exist for subsequent dendrite growth of the lithium iron zinc silicate into the coating.

3. The very low levels of chromium oxide in the adjacent coating do not noticably influence the crystallisation process.

Ferrous oxide is present at high concentration in the adjacent coating, producing a compositional gradient. Two

composition regions can be identified, both having different crystallisation characteristics. In the region between 7.8-4at%Fe, crystallisation is inhibited by the high iron content. On heat-treatment a lithium iron zinc silicate is formed here having the formula

$$Li_2O.Fe_{0.8}Zn_{0.2}O.SiO_2$$

In the region between 4 to 0.5at% Fe β-quartz is produced during firing. With heat-treatment both β-quartz and lithium dislicate are formed.

4. For extended firing periods a reaction is observed between chromium oxide and the coating. It proceeds at a very slow rate and is undetectable for "standard" firing conditions. The reaction product is lithium chromium silicate:

$$LiCr(SiO_3)_2$$

It forms a solid solution with chromium oxide.

No reaction is observed between ferrous oxide and the coating. A redox type reaction has been identified between the mild steel and potassium oxide in the glass. The reaction provides an additional source of ferrous oxide. It is however, a minor source compared to the amount preoxidised.

5. The coating adheres strongly to both chromium oxide and ferrous oxide. For the chromium oxide layer bonding may be via the lithium chromium silicate layer. Such a layer will only be 140Å

thick for a standard firing (if formed at standard firing periods).

The coating bonds to the ferrous oxide via the lithium iron zinc silicate phase. An epitaxial match exists between these two crystal phases.

6. Both substrate oxides must bond well to their respective substrates to give the observed good coating adhesion.

For a discrete chromium oxide layer (formed by preoxidation in wet hydrogen) bonding is via a silica layer. Good bonding, irrepsective of how the oxide is produced, requires abrasion of the substrate prior to oxidation.

Ferrous oxide must also adheres well once the firing process is complete.

Coating adhesion for both systems is believed to be via the substrate oxide. This oxide bonds well to both fired only or heat-treated coating and respective substrate.

The influence of adhesive oxides is to promote wetting of the coating on mild steel. This is achieved via complex redox reactions at the interface. Nickel oxide has additional effects not exhibited by cobalt oxide. This results in a more rapid dissolution of residual ferrous oxide. For "standard" firing conditions, no crystalline ferrous oxide remains at the interface. Coating adhesion is affected and completely lost on heat-treatment.

Many of the observations made in this project remain unexplained. Much more work needs to be done, both on the glass-ceramic-metal interface and on the lithium silicate-substrate oxide systems. Some areas are identified below:

Very little work is published on the Li_2O-FeO-SiO_2 system. If a detailed study is to be undertaken on the coating of mild steel with a lithium silicate type glass-ceramic, the characteristics of this system need to be known. Useful information would include: glass forming regions; thermodynamic phase composition and phase development from glasses; liquidus temperatures and compositions. The work in this project has provided limited information on this system but under non-equilibrium conditions.

The crystallisation mechanisms of the bulk coating need to be examined further. Starting with a powder strongly affects the microstructure developed. In particular it is not well known why the large surface area favours the formation of β-quartz as opposed to α-cristobalite. And why is it that this phase is produced in the centre of the glass particles and in the glassy regions during heat-treatment?

In examining the coating on chrome-iron, a much higher resolution technique is needed. This could be achieved using a

SIMS or Auger technique. The role of the silica layer needs further investigation. It is involved in bonding of the chromium oxide layer to the chromium-iron substrate. The reason for improved adhesion on abrasion is not fully understood. It increases the adhesion of the chromium oxide to the substrate and apears to be the critical pre-treatment for coating chrome-iron.

For coatings on mild steel, several unanswered questions exist. The mechanism by which the ferrous oxide bonds to the mild steel needs investigation. The influence of ferrous oxide on crystallization mechanisms must be examined. For example, why do minor amounts (4at%) inhibit the formation of lithium disilicate. The properties of a high ferrous oxide containing glass in which the lithium iron zinc silicate crystallises requires evaluating. The adjacent 50μm of the coating has this composition. Its properties such as thermal expansion coefficient or viscosity will determine coating characteristics.

The role of adherence oxides needs more analysis. The mechanism by which they influence wetting is not fully understood. If the adherence oxide's main purpose is to provide a source of ferrous oxide, the metallic phase formed should have a high cobalt or nickel concentration. For the sytems studied here, this is not the case. Nickel oxide has long been regarded as an adherence

promoter in traditional enamels. The evidence from this project is that nickel oxide is detrimented to adhesion in a glass-ceramic enamel. More work would be justified to examine this in greater detail - in particular why nickel oxide promotes the rapid dissolution of ferrous oxide.

In a broader context, much work needs to be done in examining other glass-ceramic-metal systems. The potential for glass-ceramic enamels is good considering the considerable improvements in enamel characteristics. An area to examine first is other chromium containing alloys. If these form a well adhering chromium oxide scale (which is often the case) it should be possible to produce a strong adhering coating. Due to the extremely low solubility of chromium oxide, coating microstructure will be unaffected adjacent to the interface. This means that well characterised coatings of small thickness (typically <10μm) can be achieved. A possible example could be a chemical protection or abrasion resistant layer on a nimonic alloy or stainless steel. It would also be useful to examine alloys which produce different well adhering oxides. For example glass-ceramic coatings on Fecralloy which forms an adherent alumina oxide layer.

Other metal-ceramic coating systems of interest would include:

Coating		Substrate
Electrical insulating glass Ceramic coating	-	Copper
Electrical insulating glass Ceramic coating	-	Tungsten
Chemical and oxidation resistant glass-ceramic coating	-	Titanium

Each of these systems have practical applications. It would be useful to examine each of the above systems in detail. In particular how the oxide characteristics influence coating adhesion and coating microstructure.

APPENDIX

A.1 Glass-ceramics

Glass-ceramics are polycrystalline solids produced by the controlled crystallisation of a glass. They have a fine grained, submicron, randomly oriented microstructure with some residual glass but no porosity.

To achieve controlled crystallisation, efficient nucleation producing 10^{12}-10^{15} nuclei per cm^2 is necessary. This requires the addition of nucleating agents to the parent glass composition and the carrying out of a controlled heat-treatment.

The initial process discovery was made by Stookey [11], using photosensitive glasses with minor additions of gold, silver and copper. Nucleating agents may be divided into noble metals e.g. compounds of Pt, Au, Ag, Cu which tend to reduce to the neutral state forming metallic precipitates, Stookey [114], or they are refractory oxides effective in promoting phase separation which in turn induces formation of nucleating phases. Such oxides include: P_2O_5 [115] and TiO_2 [116].

Crystallisation can be divided into a nucleation process and a subsequent growth of the nuclei. Homogeneous nucleation requires the formation of crystal nuclei in the glass melt. A decrease in free energy is obtained by conversion from the liquid to the crystal phase but this is countered by an increase of free energy due to the formation of a crystal liquid boundary and its associated interfacial energy. Only after the nuclei have reached a critical radius, r*, are they stable. The free energy barrier G* associated with the formation of a critical site nuclei is:

$$G^* = \frac{16\pi\sigma^3}{3(\Delta G_f)} \qquad \text{A1.1}$$

σ - interfacial energy [or surface tension]

ΔG_f - free energy of formation of the crystal phase per unit volume.

According to the classical nucleation theory, see Turnbell [117], the rate of formation of nuclei will be a product of the number of critical sized nuclei present per unit volume and the rate at which atoms are attached to the nuclei.

$$I = A \exp \frac{-\Delta Ga}{kT} \exp \frac{-\Delta G^*}{kT} \qquad \text{A1.2}$$

I - rate of nucleation

A - constant term

ΔG_a - kinetic barrier to nucleation

ΔG^* - thermodynamic barrier to nucleation.

The value of G* may be related to the heat of fusion per unit volume, H_f:-

$$I = A \exp \frac{-\Delta Ga}{kT} \exp \frac{-16\pi o^3 Tm^2}{3\Delta T^2 \Delta H_f{}^2 kT} \qquad \text{A1.3}$$

T_m - liquidus temperature

ΔH_f - Heat of fusion per unit volume.

A plot of nucleation rate I against temperature is shown in figure A.1. At small under-coolings the second exponential term dominates and I increases with increasing under-cooling. At greater undercoolings the first term dominates. A maximum nucleation rate will occur at a particular under-cooling.

To obtain the copious nucleation required for glass-ceramics heterogeneous nucleation is essential. Heterogeneous nucleation involves the development of nuclei on impurity particles. The effect of these particles is to reduce the value of G* in a super saturated melt by decreasing the interfacial free energy. The nucleation rate I is still given by equation A1.3 with an addition factor $f(\theta)$, which lies between zero and unity.

The rate at which the crystal nuclei grow depends on the rate at which atoms arrive and remain at the surface of the nucleus. The atoms must be able to cross the interface i.e. they require sufficient energy to surmount an energy barrier G_a. The rate of crystal growth U is given by Jackson [118]:-

$$U = f\lambda V_o \exp\left(\frac{-\Delta Ga}{kT}\right)\left[1-\exp\left(\frac{\Delta G}{kT}\right)\right] \qquad A1.4$$

λ - interatomic spacing

V_o - vibrational frequency of atoms

ΔG_a - activation energy required to cross interface

ΔG - free energy of formation

f - fraction of preferred growth sites.

This may be expressed in terms of melt viscosity (η).

$$U = \frac{f[1-\exp(\Delta G/kT)]kT}{3P\lambda^2\eta} \qquad A1.5$$

At low under-coolings U is proportional to ΔG but at large under-coolings, to $1/\eta$. Hence the growth rate will exhibit a maximum. The maximum growth rate occurs at much smaller under-cooling

than is the case for the maximum nucleation rate figure A1.

The controlled heat-treatment will involve heating to a temperature T_n, where the nucleation rate is a maximum and, after the required time, heating to a temperature, T_g, where growth readily occurs. In an ideal material little overlap between the nucleation and growth curves occurs.

Glass-ceramics can be obtained from a range of glasses, Table A1, producing materials having a wide range of different properties. The essential requirement of a suitable glass-ceramic material are that it is easy to melt and fabricate, sufficiently stable not to undergo uncontrolled devitrification and able to nucleate and crystallise to form the desired crystal phases.

Table A.1: Typical glass-ceramic systems [McMillan [9]]

System	Nucleating Agent	Crystal Phases
Li_2O-Al_2O_3-SiO_2		
Al_2O_3 > 10%	TiO_2, P_2O_5	β-spodumene/β-eucrptite solid solutions.
Al_2O, < 10%	P_2O_5	Lithium disilicate, Quartz
Li_2O-ZnO-PbO-SiO_2	P_2O_5	Lithium dislicate, Lithium zinc silicate, Quartz
MgO-Al_2O_3-SiO_2	TiO_2	Cordierite, Cristobalite
ZnO-Al_2O_3-SiO_2	P_2O_5, TiO_2	Willemite

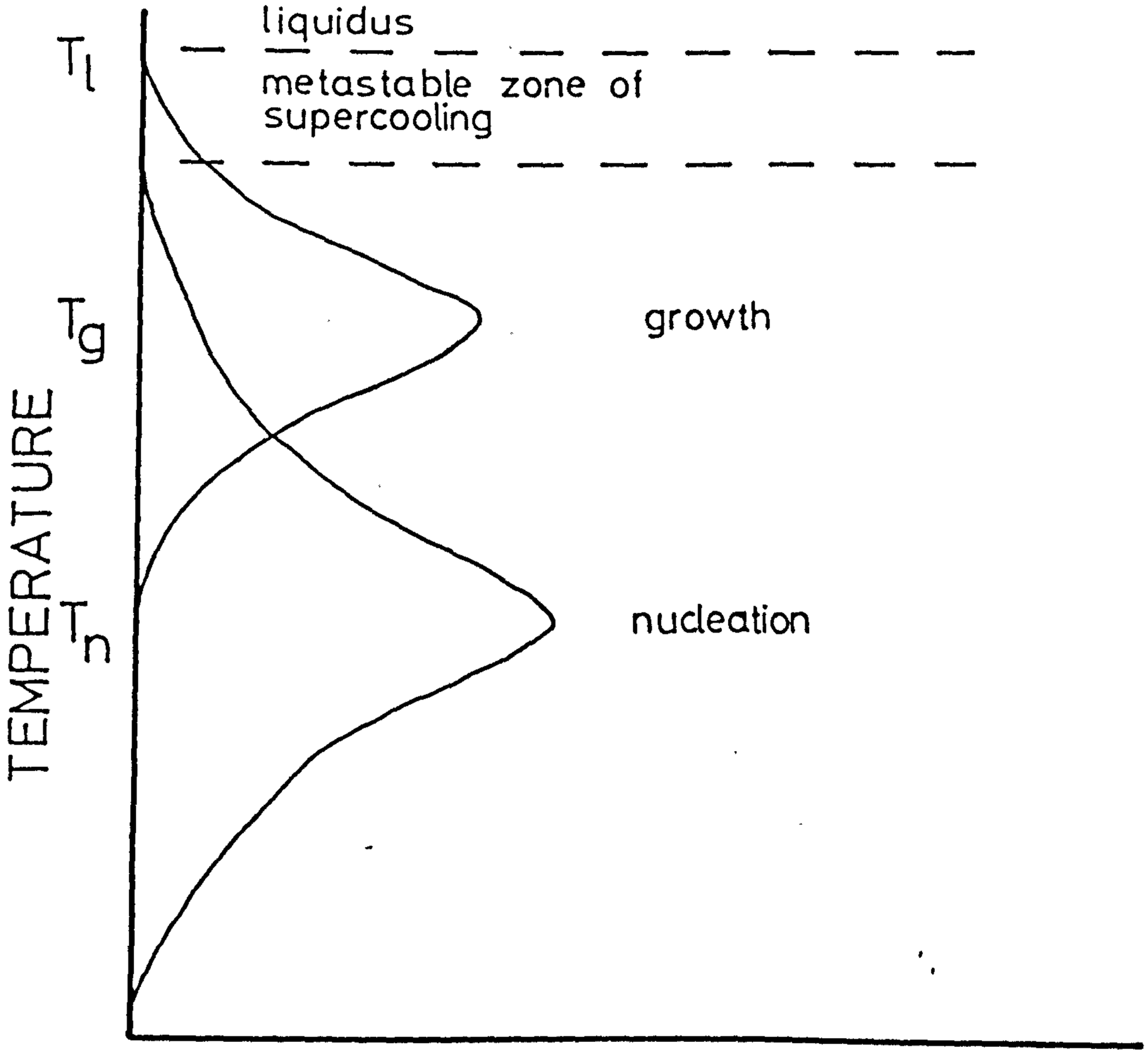
liquidus
T_l
metastable zone of supercooling
T_g
growth
TEMPERATURE
T_n
nucleation
RATE

Figure A.1

A.2 Diffusion

A.2.1 Introduction

Interdiffusion in a binary system resulting from a chemical gradient is described by Fick's first law

$$J = -\tilde{D}\frac{\partial c}{\partial x} \qquad \text{A2.1}$$

J Flux at material per unit time per unit area

$\tilde{D}$ Interdiffusion coefficient

C Concentration per unit volume

In general $\tilde{D}$ is found to be dependent on concentration.

The variation with time is given by Fick's second law

$$\frac{\partial c}{\partial t} = \frac{\partial}{\partial x}\left(\tilde{D}\frac{\partial c}{\partial x}\right) \qquad \text{A2.2}$$

and if $\tilde{D}$ is independent of concentration

$$\frac{\partial c}{\partial t} = \tilde{D}\frac{\partial^2 c}{\partial x^2} \qquad \text{A2.3}$$

When considering diffusion of a particular species, such as a metal oxide, in to a multicomponent glass the flux is correctly described by Onsagers extension of Fick's laws [119]

$$J_i = -\sum_{g=1}^{n} \tilde{D}_{ij}\frac{\partial Ci}{\partial x} \qquad \text{A2.4}$$

In practice this involves many difficulties and a simpler approach considers the metal oxide diffusing into a multicomponent

glass as a pseudobinary system. A proportional constant relates the flux of a component, the metal oxide, to the concentration gradient when all the other components in the glass are combined as a single species.

The binary diffusion coefficients in Fick's equations are replaced by an effective binary diffusion coefficient (EBDC)$\tilde{D}_B$.

A.2.2 Diffusion into a semi-infinite medium

If the boundary conditions are

when $t = 0$ $\quad C = C_i$ at $x = 0$

$\quad C = C_o$ at $x > 0$

when $t > 0$ $\quad C = C_i$ at $x = 0$

i.e. a glass containing initially a concentration C_o of the metal oxide is brought into contact with the oxide and the interface concentration of the oxide in the glass remains at C_i for $t > 0$, are substituted into Fick's second law;

$$C(x,t) - C_o = C_i - C_o \, [1 - \mathrm{erf}(x/2\sqrt{\tilde{D}_B t}) \qquad \text{A2.5}$$

where x distance from interface

t time from start of interdiffusion

and $\mathrm{erf}\ \lambda = \frac{2}{\sqrt{\pi}} \int_0^{\lambda} e^{-\lambda^2} \, d\lambda$

See Crank [120]

If the glass is initially free of the metal oxide $C_o = 0$.

$$C(x,t) = C_s[1 - \mathrm{erf}(x/2\sqrt{D_B t})] \qquad \text{A2.6}$$

and the total mass of metal oxide passed across the interface at x = 0 after a time t_i is

$$M = 2C_i\sqrt{\frac{\tilde{D}_B t}{\pi}} \qquad \text{A2.7}$$

The temperature dependence of a diffusion coefficient is usually found to follow on Arrhenius relation

$$\tilde{D}_B = \tilde{D}_o \exp(-Q/RT) \qquad \text{A2.8}$$

$\tilde{D}_o$ a constant

Q activation energy

R Universal gas constant

However, activation energies derived from an Arrhenius plot of interdiffusivities must be treated with caution. The activation energy Q will be a combined value for the various species interdiffusing.

A.2.3 Dissolution processes

The rate of dissolution of an oxide layer, on a metal substrate, into a molten glass, will have an important influence on wetting, adhesion development and composition of the adjacent glass at the interface. From equation A2.1 and approximating a linear drop in concentration of metal oxide over a distance x into the glass,

$$J = - \tilde{D}_B \frac{C_i - C_x}{\Delta x} \qquad A2.9$$

A low dissolution rate will be favoured by a small EBDC and a low interface or saturation concentration of the metal oxide.

The various species present in a multicomponent glass will have different mobilities and the concentration distribution should depend upon their individual intrinsic diffusion coefficients. The principles for a 3 component system have been discussed by Oishi [A9]. Consider a two component glass consisting of components 1 and 2. During the dissolution of component 3, the metal oxide, into the glass, the relative interdiffusivities between components 3 and 1 may not be equal to that between components 3 and 2. Oishi (121) has shown that

$$\frac{D_1}{D_2} = \frac{W_1}{W_2} \frac{dW_2/dx}{dW_1/dx} \qquad A2.10$$

If the intrinsic diffusion coefficient of component 1, in the glass, is greater than component 2, the W_1/W_2 ratio at the interface tends to increase and the ratio of the concentration gradients decreases. This is shown schematically in figure A2.

Such a simplified approach has ignored effects of change im balance and dependence on concentration of the intrinsic diffusion coefficients.

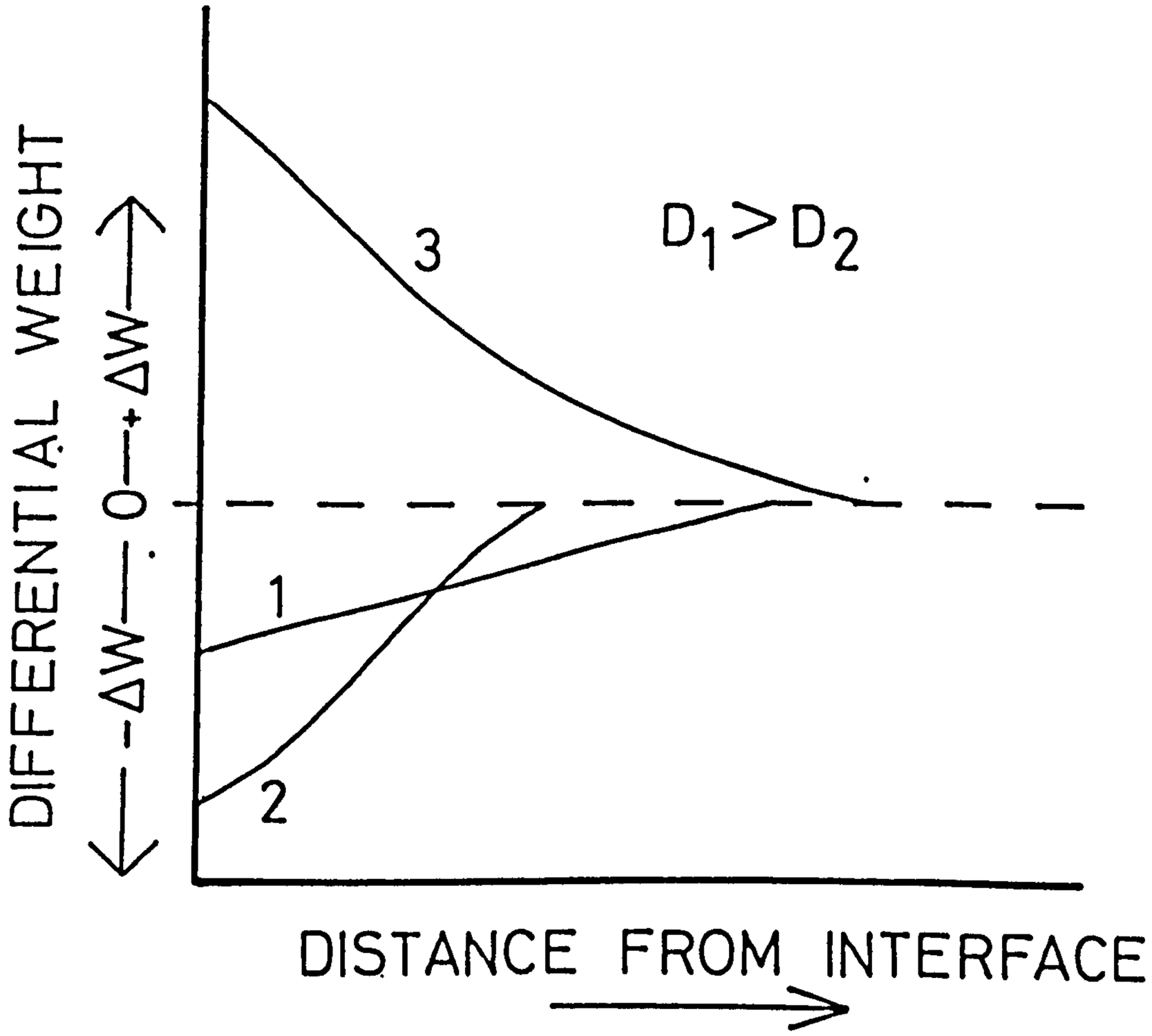
DIFFERENTIAL WEIGHT
-ΔW — 0 — +ΔW
3
1
2
$D_1 > D_2$
DISTANCE FROM INTERFACE

Figure A.2.

Appendix 3. Spectrophotometer method for the determination of the ferrous-ferric ratio in glass.

The method is briefly outlined below. For a more detailed description see Maxwell and Brangs [122].

The coating was removed from the substrate by impact. Care was taken not to incorporate any oxide from the adjacent uncoated metal. It was then ground to a fine powder and passed through a 200 mesh size sieve.

Up to 50mg was placed on a 175ml platinum crucible followed by 4ml of 1:1 suphuric acid and 2ml of 40% W/W hydroflouric acid. This was left for 5 minutes. The contents were then washed into a 100ml polypropylene flask using 45ml of W/W boric acid. To this 10ml of 1:1 sulphuric acid was added followed by 0.5g of sodium hydrogen carbonate.

Once effervescence ceased 5ml of 30%W/V ammonium thiocyanate were added. The absorbance was then measured at 470nm within 5 minutes. The absorbtion is due to Fe^{3+} ions. A Varian digital superscan 3nv - visible spectrophotometer was used with silica cells.

After measuring absorbance, 50mg of solid ammonium persulphate was added followed by moving to dissolve. The absorbance was remeasured not before 4 mins but not later than 9 minutes. In this stage any Fe^{2+} is oxidised to Fe^{3+}. The absorbance relates to the total iron content. The percentage of Fe^{2+} ions was evaluated using:

$$Fe^{3+}\% = \frac{\text{absorbance before addition of ammonium persulphate.}}{\text{absorbance after addition of ammonium persulphate}}$$

Determined Fe^{2+}:Fe^{3+} ratios:

	Fe^{3+}	Fe^{2+}
Fired only enamel (M9)	16.5 13.7	83.5 86.3
Heat-treated enamel (M9H)	9.9	90.1
FeO	13.4	86.6
Fe_2O_3	80	20
Fe_2O_3 containing glass	100	0

Appendix 4: LIMA analysis

Analysis was carried out by Loughborough Consultants Limited [All]. To obtain a concentration probe, regions were analysed at increasing distances into the coating.

LIMA utilises a pulsed laser which operates at the 0.53μm wavelength. It is focused onto the area of interest on the sectional and polished sample in an ultra-high vacuum chamber. The intense pulse volatilises a small volume of the sample. This is ejected into the vacuum as molecular ions. The ejected material is analysed by a time of flight mass spectrometer.

LIMA has a spacial resolution of 1-5μm with a depth of about 0.5μm. Alignment is achieved via an optical microscope and vidicon camera.

It is possible using LIMA to analyse for all elements in the periodic table. The technique allows a direct determination of litrium concentrations.

The results are obtained in relative ion intensity measures for each detectable element. To convert these to actual concentrations the following method was used. The peaks collect at the 4 furthest points from the interface 150μm were averaged. The peak ratios then related to the concentration in this region evaluated by conventional EDX analysis. Litrium was assumed present, a constant ratio to silicon. A scaling factor was obtained and used to convert the peak ratio of each element to a concentration.

To obtain a scaling factor for iron the concentration adjacent to the interface obtained using "windowless" EMX analysis was used. The element concentrations were then normalised and expressed as at% values.

This technique was used only to collect a compositional profile for coating M9. It could not be used to analyse individual litrium iron zinc silicate crystals. The resolution is vapour and it was not possible to identify this phase from the matrix by optical microscopy.

Appendix 5. Some properties of various cations.

Element	C.N.	Z/a^2	ionic radius r Å
Al^{3+}	4	0.99	0.39
Si^{4+}			
k^{+}	6	0.13	1.38
Zn^{2+}	4	0.53	0.60
	6	0.45	0.75
Fe^{2+}	6	0.45	0.77
Fe^{3+}	4	0.88	0.49
Fe^{3+}	6	0.75	0.65
Cr^{3+}	6	0.78	0.615
Cr^{6+}	4	2.13	0.33
	6	1.71	0.52
Li^{+}	4	0.27	0.59
	6	0.23	0.74
p^{5+}	4	1.02	0.17
	6	2.16	0.35

Reactions at the interface between a glass ceramic and a metal and their effect on devitrification

A. J. Sturgeon, D. Holland

Department of Physics, University of Warwick, Coventry CV4 7AL, England

G. Partridge, C. A. Elyard

GEC Engineering Research Centre Stafford Laboratory, P.O. Box 30, Lichfield Road, Stafford ST17 4LN, England

Manuscript received 23 October 1985

Scanning electron microscopy and energy dispersive x-ray analysis of the interface between a glass ceramic and a metal have been used to determine the interactions occurring at the interface during the coating of a chrome–iron alloy and mild steel by a lithium aluminosilicate glass ceramic. The relative solution of iron or chromium from the substrate into the glasses is shown to have a major influence on the microstructure and phase composition of the resulting glass ceramic. The diffusion profiles of minor constituents are also affected.

The use of ceramic or vitreous coatings to give oxidation and corrosion resistance to metal substances is of major technological importance. Traditionally the enamelling of metals such as steels, cast iron, and aluminium with vitreous coatings has been used to provide such protection.[1,2] Possible future applications may also include the protection of refractory alloys in turbine blades and the provision of electrically insulating coatings on metal plates for substrate use in microelectronics.[3] Such uses may require close control of certain enamel properties.

It has been shown that glass ceramics can be made to bond to various metals either in the ceramic state, by the use of intermediate bonds,[4] or starting from the glassy state, as in vitreous enamelling, followed by a suitable heat treatment to achieve conversion to a glass ceramic.[5,6] Such a schedule is represented in Figure 1. Glass ceramic coatings can provide distinct advantages such as increased hardness, improved mechanical strength, and also better control of the thermal expansion coefficient of the coating so that it closely matches that of the substrate. This results in a lower residual stress at the interface, giving improved thermal shock resistance. Careful choice of chemical composition and crystal phases generated can give good chemical resistance and suitably tailored electrical properties. Table 1 shows the typical range of properties of glasses and glass ceramics.

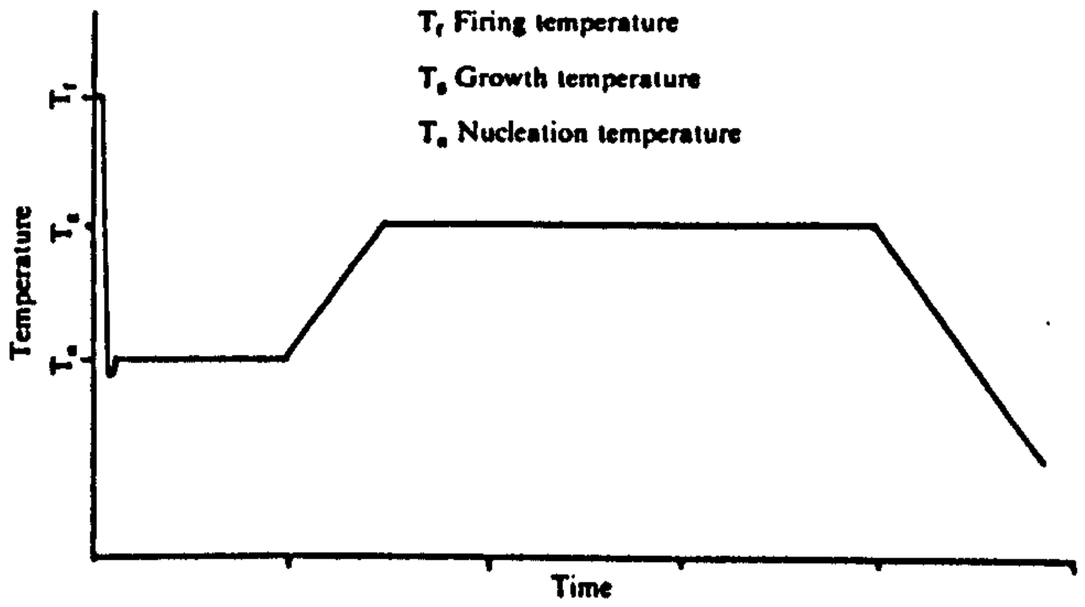

Figure 1. *Typical thermal heat treatment schedule for enamelling with a glass ceramic*

The essential requirements for glass ceramic coatings on metals are that the parent glass has a sufficiently low viscosity to flow at a reasonable temperature, that it is able to wet the metal surface, and that it forms a strong adhesive bond to the metal.

Several mechanisms have been suggested to explain adhesion of enamels[7–9] and these fall into two main catagories, chemical bonding and mechanical keying: it is generally believed that chemical bonding is the major factor in forming good adhesion. Chemical bonding requires a transition from the metallic

Table 1. *Typical ranges of properties for glass ceramics and glasses*[4]

Property	*Unit*	*Glass ceramic*	*Glass*
Linear thermal expansion coefficient 20–500°C	(deg $C^{-1} \times 10^7$)	−40 to +200	+5 to +120
Cross breaking strength	(kg/cm^{-2})	1000 4000	500 900
Impact strength (Charpy)	(kg cm)	3·5 7·5	0·5 1·0
Dielectric breakdown strength	(kV/mm)	28 50	25 45

structure of the metal to the essentially covalent structure of the glass, with the necessary conditions of chemical equilibrium and electronic continuity being met. Excellent coating adhesion is observed with metals which form strongly adhering oxides (e.g. Fe–Cr–Al alloys and chrome irons) and with the formation of a strong bond between the oxide and glass, the oxide acting as a transition layer.

For metals with weakly adhering oxides (e.g. ferrous oxide on mild steel) the adhesion is thought to occur by saturation of the adjacent glass with the metal oxide with little or no oxide remaining at the interface. Adhesion is then principally between the base metal ions dissolved in the glass at the interface and the base metal.

Typical coating procedure is to oxidise the metal to form an adherent oxide layer if possible, apply the coating, and subject the assembly to firing and heat treatment. In some cases, the metal oxide is formed during the firing stage rather then by previous oxidation. If the oxide is not protective, the subsequent thermal heat treatments must be carried out under inert atmospheres. If the oxide adheres well to the metal, a thin discrete layer should be present after firing; for a weakly adhering oxide it is essential that sufficient metal oxide be produced to saturate the adjacent glass by diffusion during firing, but not leave a discrete and weak oxide layer in the final product. In practice, 'adherence oxides' are added to commercial coating compositions to help achieve this condition.

Although the use of glass ceramic coatings is well established, there is little information on the interactions which occur at the interface, their effect on devitrification of the coating, and how this influences coating adhesion. In this paper we report some of the results of investigations of interfacial reactions of chrome–iron and mild steel with lithium aluminosilicate glasses.

Further results concerning the considerable influence of adhesion oxides on the interfacial reactions and the effect of Cr^{3+}, Fe^{2+}, and Fe^{3+} on the bulk glasses will be reported in subsequent publications.

Experimental

Pretreatment of the metal

The two alloys examined were a 17% chrome–iron alloy (Krupp Stahlwerke) and a low carbon (<0·01% C) mild steel (Vitrostall).

Before coating, the chrome–iron was degreased, abraded, and oxidised in an atmosphere of wet hydrogen between 900 and 1000°C for 6 h. This produces a well adhering layer of chromium oxide (Cr_2O_3) ~ 1μm thick, which protects the metal substrate against further oxidation during subsequent thermal treatments in air.

The mild steel was degreased but not abraded. After coating with the glass powder, the metal was oxidised for 15 min at 650°C in air, producing a ferrous oxide layer ~ 15 μm thick between the glass powder and the metal. When cooled to room temperature this oxide transformed to a mixture of ferrous and ferric oxide, which is not protective and further heat treatments under an atmosphere of nitrogen were necessary.

Glass coating

The compositions used were based on the lithium aluminosilicate system with various additions, typically of less than 5 wt%, of K_2O, ZnO, or P_2O_5. The precise composition and heat treatment schedule were selected to produce a final coating with a thermal expansion coefficient which was slightly below that of the substrate metal so that a compressive stress was formed in the glass ceramic at the interface.

The glass was prepared from calculated proportions of Analar grade reagents, the mixture being homogenised by rolling and then melted at 1 350°C for 3 h in a Pt/10% Rh crucible in an electrically heated furnace. The melt was cast into deionised water and remelted. The final product was ball milled for 36 h to produce a fine powder (~ 10 μm) and mixed with an organic binder to form an ink. The ink was applied to the metal surface by standard screen printing techniques and dried to produce a uniform layer of glass 200 μm thick. Firing of the coatings at 965°C for 5 min produced fusion of the glass powder and wetting of the metal. A two stage heat treatment of the type illustrated in Figure 1. was then applied to the coating to form a glass ceramic.

Examinations of the coatings

The coatings were examined after quenching from the firing temperature and after the full heat treatment schedule. The samples were cut in cross section using a diamond saw, mounted in a conducting bakelite, and polished to a 1 μm finish. A carbon coating was deposited to prevent charging and the sections were examined using a Cambridge scanning electron microscope with an energy dispersive x-ray analyser. Back scatter imaging of the polished samples revealed the microstructure through atomic number contrast. The distribution of the constituent elements across the interface was determined by spot analysis with a beam current of 3×10^{-12} A, an accelerating voltage of 20 kV, and a sampling period of 100 s. Treatment of the collected x-ray spectrum allowed full quantitative analysis of all detectable elements except oxygen and lithium. Line scans observing the x-ray K line fluorescence of selected elements allowed a semi quantitative determination of concentration across the interface to be obtained: the electron beam traversed a distance of 50 μm over a period of 500 s. Due to difficulties in identifying the phases which occurred at the interface of the coating with mild steel, 'windowless' analysis was used to gain an approximate idea of the oxygen content. With the window between the detector and the sample chamber removed, x-ray spectra may be collected from elements with atomic numbers down to 6 (carbon). Using an accelerating voltage of 10 kV and a beam current of 3×10^{-12} A, the approximate concentrations were determined using a SiO_2 standard for Si and O and a Fe_2O_3 standard for Fe.

Table 2. *Windowless energy dispersive x-ray analysis of $LiFeSi_2O_6$ standard*

Element	*Standard*	*Detected*		*Nominal*
Approximate wt %				
Si	SiO_2	27·2		26·1
O	SiO_2	46·8		44·6
O	Fe_2O_3	43·8		44·6
Fe	Fe_2O_3	22·1		25·9
Li	(not detectable)			3·4
Normalised at %				
		(a)	(b)	
Si	SiO_2	22·6	23·6	22
O	SiO_2	68·2		67
O	Fe_2O_3		66·7	67
Fe	Fe_2O_3	9·2	9·6	11

Oxygen determined by using (a) SiO_2 and (b) Fe_2O_3 standards

Comparison with a standard composition, $LiFeSi_2O_6$, containing these elements indicates that reasonable results may be obtained, as is shown in Table 2. Any charge imbalance may be assumed to be due to the presence of lithium ions, which cannot be detected even with the window removed.

Results

Chrome–iron

The microstructure of a coating quenched after firing at 970°C for 6 min is shown in Figure 2; it consists of a well defined layer of metal oxide (~1 μm thick) separating the metal and the coating. Energy dispersive x-ray analysis shows this layer to be rich in chromium and x-ray diffraction analysis of the oxide surface, exposed after dissolving the metal in acid, identified the oxide as Cr_2O_3.

The coating shows residual porosity from the sintering process and has a nonuniform microstructure consisting of featureless regions surrounded by areas containing a dark phase, identified as lithium disilicate. X-ray diffraction analysis indicates the presence of both lithium disilicate and quartz, the latter being barely resolved from the residual glass background. By observing the devitrification at various stages during the firing process it becomes apparent that lithium disilicate crystals are clustered in the regions corresponding to the original glass particle surfaces. The firing temperature is close to the liquidus of this phase, resulting in a high growth rate and a coarse microstructure compared to the bulk material.

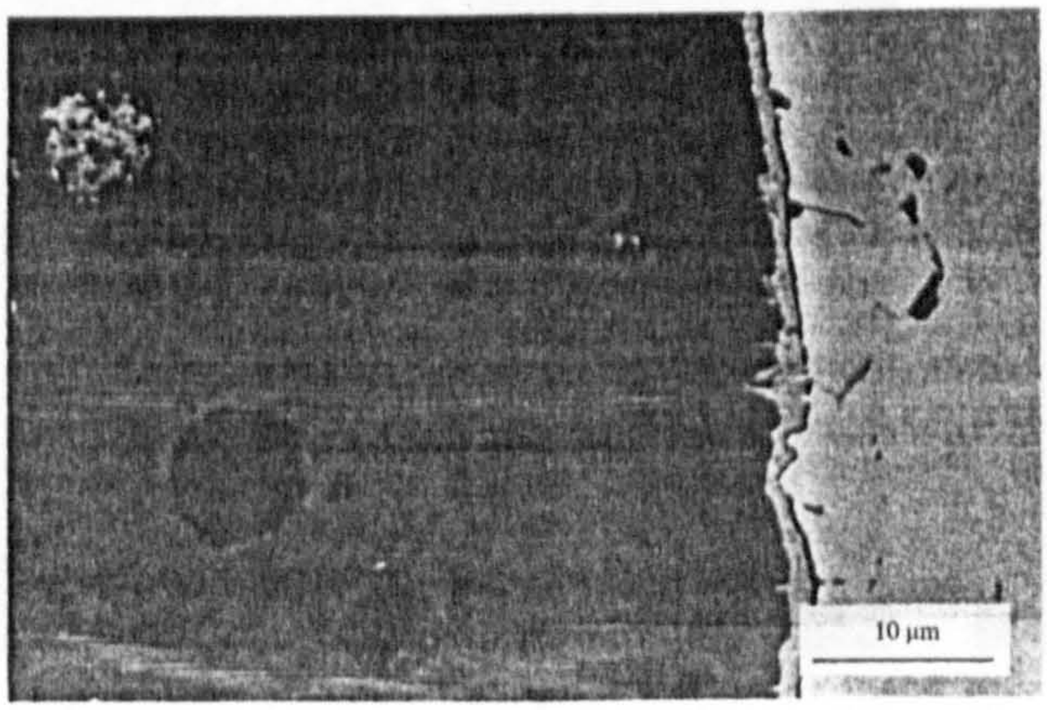

Figure 2. *Back scattering electron micrograph of a coating, rapidly cooled after firing on chrome–iron.*

Energy dispersive x-ray analysis shows that potassium is preferentially concentrated in the featureless regions, whereas no such variation was observed for other detectable elements. This is illustrated in Figure 3. which shows x-ray spectra collected from a region containing the dark phase and from an adjacent featureless region.

The distribution of elements across the interface is illustrated in Figure 4. The profiles of silicon, aluminium, phosphorus, and zinc are constant within the coating but drop rapidly to background at the inter-

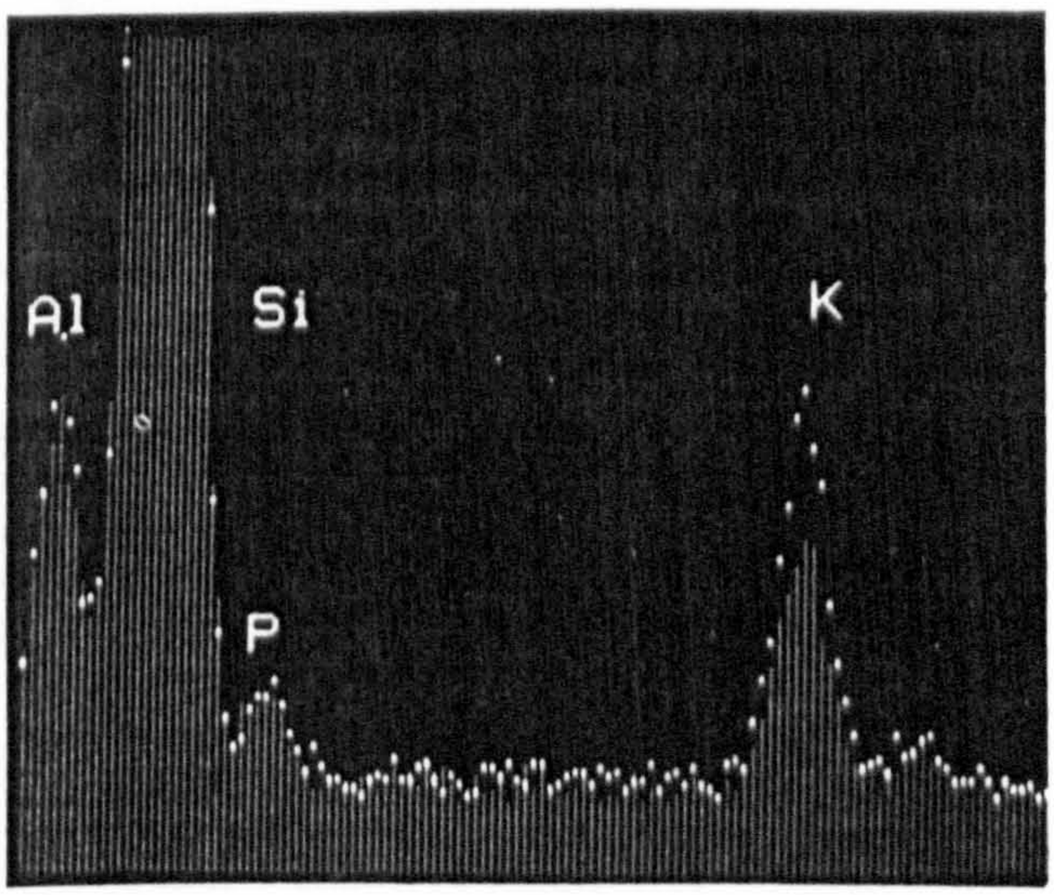

Figure 3. *X-ray spectra collected from featureless (outlined spectrum) and lithium disilicate (full spectrum) regions, showing the variation in potassium concentration*

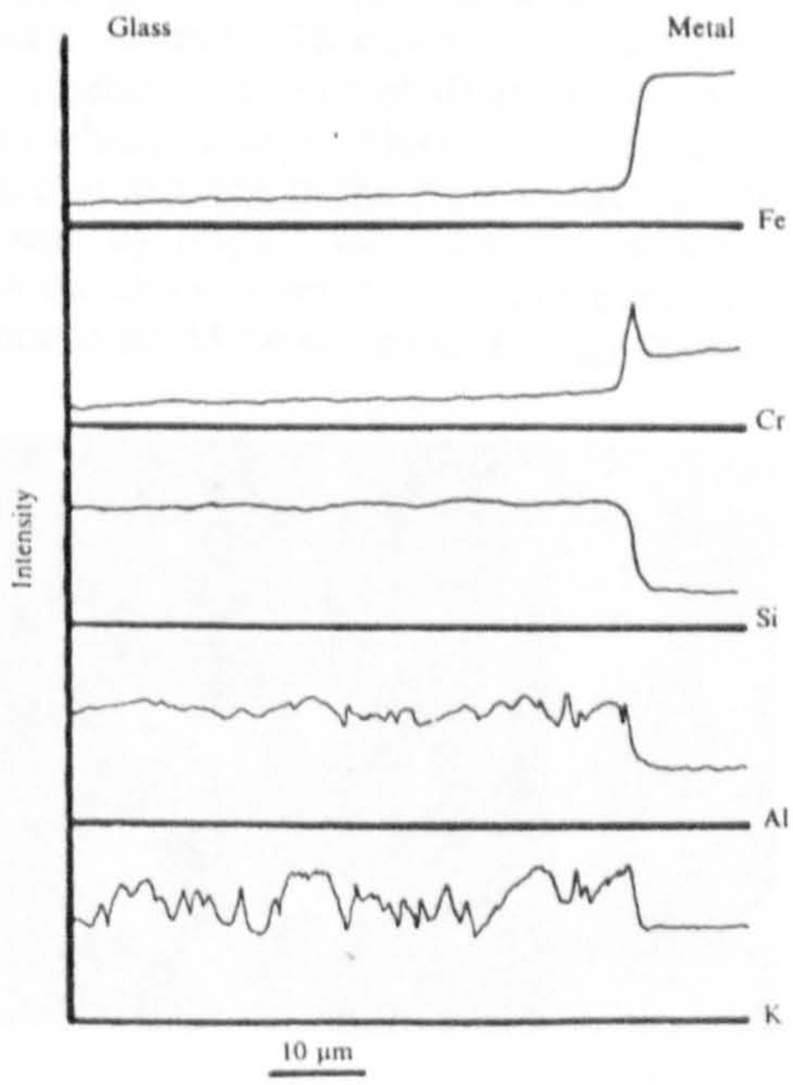

Figure 4. *Distribution of elements across the interface between a coating rapidly cooled after firing, on chrome–iron*

face. Iron is detected at an appreciable level only in the metal substrate. The chromium profile shows a peak at the oxide layer and a depletion zone of 8 μm in the metal. Diffusion of chromium into the coating is seen over a distance of 5 μm but drops to less than 0·5 wt% by 4 μm. The potassium profile is irregular, showing decreased concentration in the areas where lithium disilicate crystals occur and an increased concentration where this phase is absent; a high potassium concentration is also generally observed adjacent to the interface, often extending up to 10 μm and corresponding to a deficiency of the lithium disilicate phase in this region.

As may be seen in Figure 5, the heat treated coating shows almost complete crystallisation, with a small residual glass fraction, up to the boundary between the oxide and the glass ceramic, while the oxide layer remains unaltered. X-ray diffraction analysis of the coating indicates an increased amount of lithium disilicate, but little variation in the amount of quartz present, and this phase is now clearly visible due to crystallisation of the glassy regions and a coarsening process during the heat treatment stage. Differences in the microstructure can be distinguished, with the original featureless region now exhibiting a finer, more interconnected microstructure than the regions which had observable crystallisation before heat treatment.

The distribution of elements across the interface, as shown in Figure 6, has remained essentially unaltered. The chromium exhibits a peak corresponding to the oxide layer and no further diffusion into the coating is observed: this lack of appreciable diffusion of chromium during firing and heat treatment allows the retention of the oxide layer and, as a result, gives good adhesive properties.

The variation in the potassium concentration is associated with crystallisation during the firing, the potassium being retained in the residual glassy regions. The high concentration observed adjacent to the interface before heat treatment is associated with the absence of lithium disilicate. After heat treatment the peak immediately adjacent to the interface remains, although not extending as far into the coating.

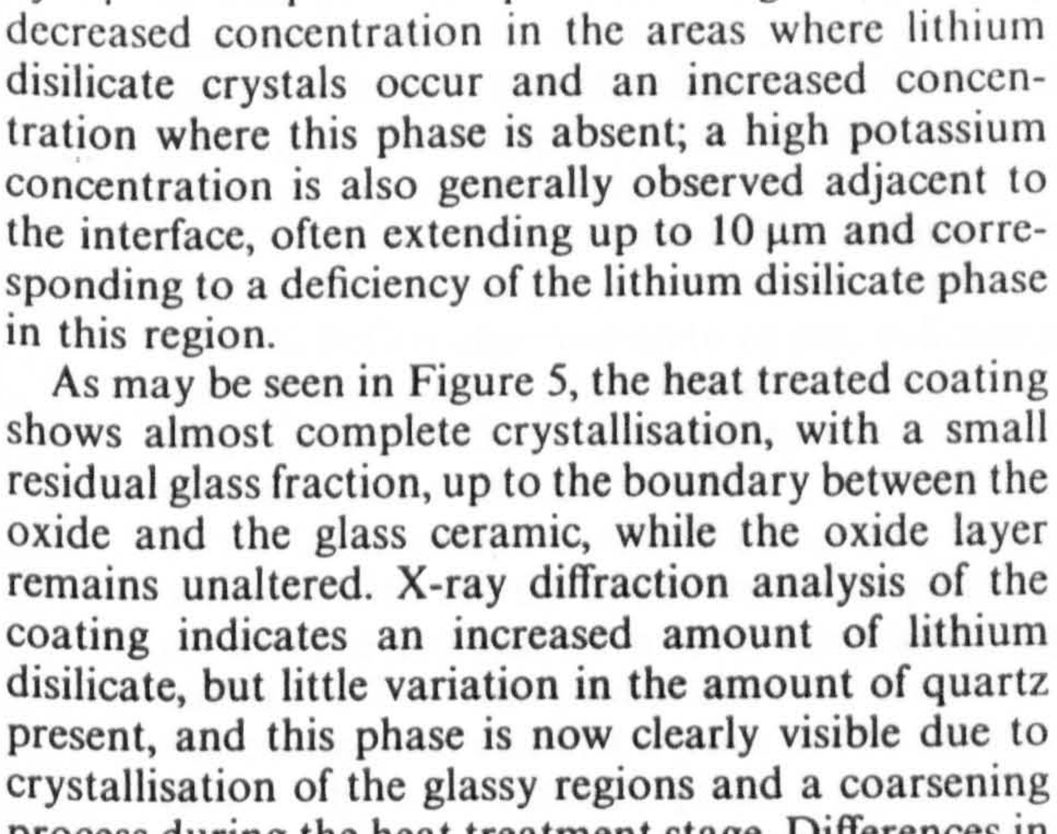

Figure 5. *Back scattering electron micrograph of a coating subjected to heat treatment, on chrome iron*

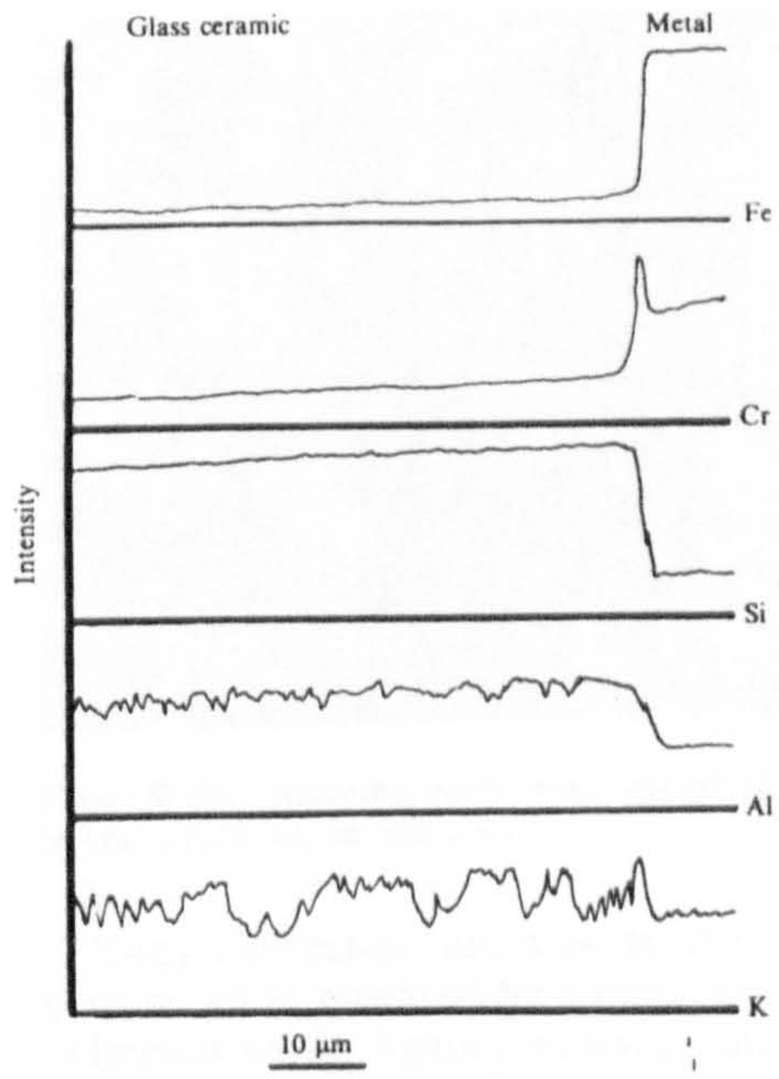

Figure 6. *Distribution of elements across the interface between a coating, subjected to heat treatment, on chrome–iron*

It may be associated with a glassy layer at the boundary, or alternatively the presence of alkali ions may be a network requirement necessitated by the presence of chromium ions in this region. Recent work suggests the former to be more appropriate.

Mild steel

The microstructure of a coating quenched after firing at 970°C for 5 min is shown in Figure 7. A relatively smooth interface is observed, with isolated pockets of residual ferrous oxide, and dendritic growth occurs at the interface, extending 5 μm into the coating. The bulk of the coating again consists of a network of lithium disilicate crystals. However, an additional feature is the presence of a zone of 40 μm adjacent to the interface in which no crystallisation is detected.

X-ray diffraction analysis of the glass surface at the interface exposed by impact indicates the presence only of ferrous oxide; no other peaks associated with the dendrite phase could be detected. Energy disper-

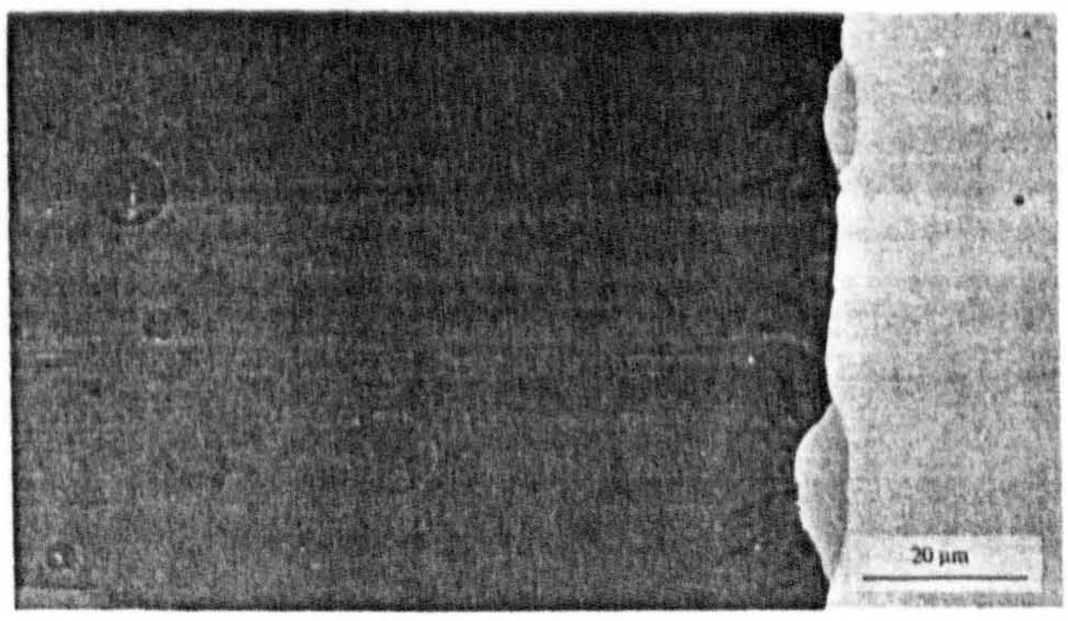

Figure 7. *Back scattering electron micrograph of a coating, rapidly cooled after firing, on mild steel*

sive x-ray analysis has indicated this phase to be a lithium iron silicate, with the normalised at% composition Li_2 Si $Fe_{0\cdot8}$ $Zn_{0\cdot2}$ O_4. The dark dendrite tip is deficient in both iron and zinc.

The distribution of elements is presented in Figure 8. The profiles of aluminium and phosphorus are constant within the coating, decreasing on approaching the interface. The silicon profile exhibits a decrease starting at about 80 μm, with a slight peak at 5 μm followed by a rapid drop to background. The iron profile shows that considerable diffusion into the coating has taken place: a constant concentration of 20 wt% FeO is observed up to 10 μm, indicating saturation of the adjacent glass, this is followed by a gradual decrease up to 40 μm, and iron can still be detected by spot analysis at distances greater than 100 μm. A dip in the iron profile is observed at the interface, associated with the tip of the dendritic phase, followed by a rapid increase to a level corresponding to the substrate. The zinc profile shows a constant level in the coating but exhibits a peak at the interface in the region where the dendritic phase is present. The profile for potassium shows a reduction in concentration extending to 40 μm and has dropped to the background level at the interface.

The microstructure of the heat treated coating is shown in Figure 9 and well defined zones are now visible. At the interface the original dendritic growth has extended from a continous layer of crystals attached to the metal substrate and residual oxide so that small crystals of the same composition form a band extending 35 μm from the interface. This merges with a second zone consisting of large crystals of lithium disilicate, which extend from 25 to 40 μm from the interface, crystal size decreasing with distance. Beyond 40 μm both lithium disilicate and quartz crystals appear.

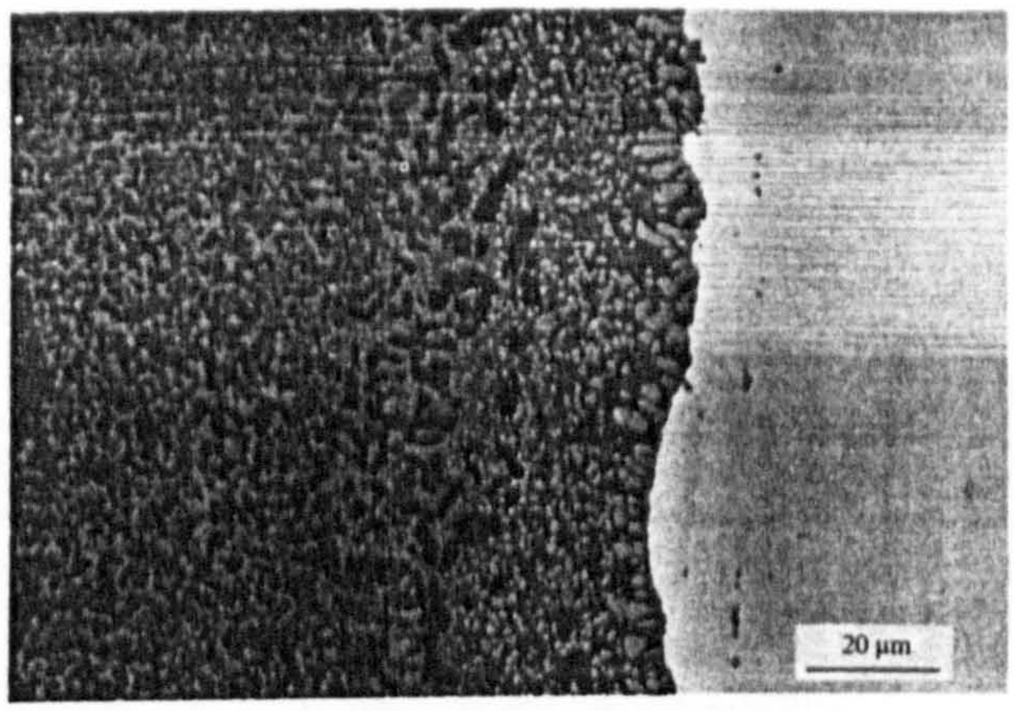

Figure 9. *Back scattering electron micrograph of a coating, subjected to heat treatment, on mild steel*

X-ray diffraction analysis of the interface of the glass ceramic, removed by impact, shows the presence of ferrous oxide. Again it is not possible to assign any peaks to the iron rich phase present, but energy dispersive x-ray analysis has indicated these crystals to be a lithium iron silicate, as described above, and identical to the dendritic phase present before heat treatment. The element ratios determined are $Fe_{0\cdot8}$ $Zn_{0\cdot2}$ Si_1 O_4 and assuming that iron is present as Fe^{2+} and that charge balance is maintained by lithium ions, we obtain the formula Li_2 $Fe_{0\cdot8}$ $Zn_{0\cdot2}$ SiO_4.

The distribution of elements across the interface is shown in Figure 10. This demonstrates a large redistribution during the heat treatment stage, which is more pronounced in a region extending up to 40 μm from the interface, where the lithium iron silicate phase is present. The silicon and iron distributions no longer exhibit smooth variations but fluctuate about a

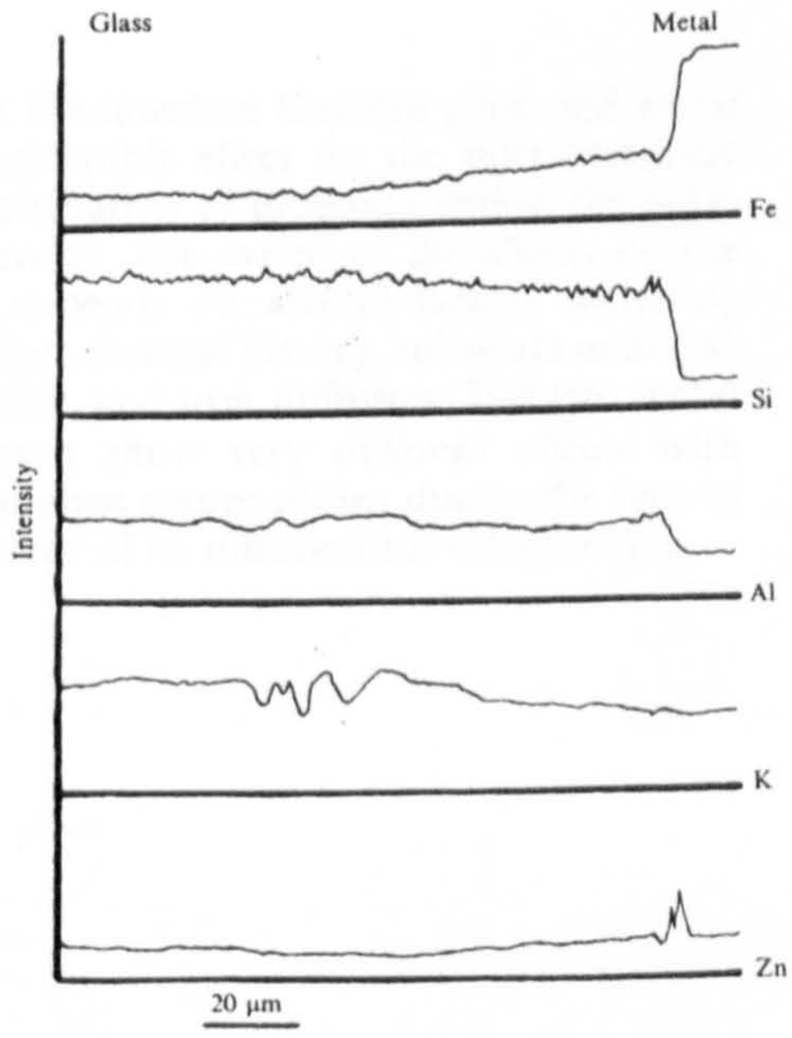

Figure 8. *Distribution of elements across the interface between a coating, rapidly cooled after firing, on mild steel*

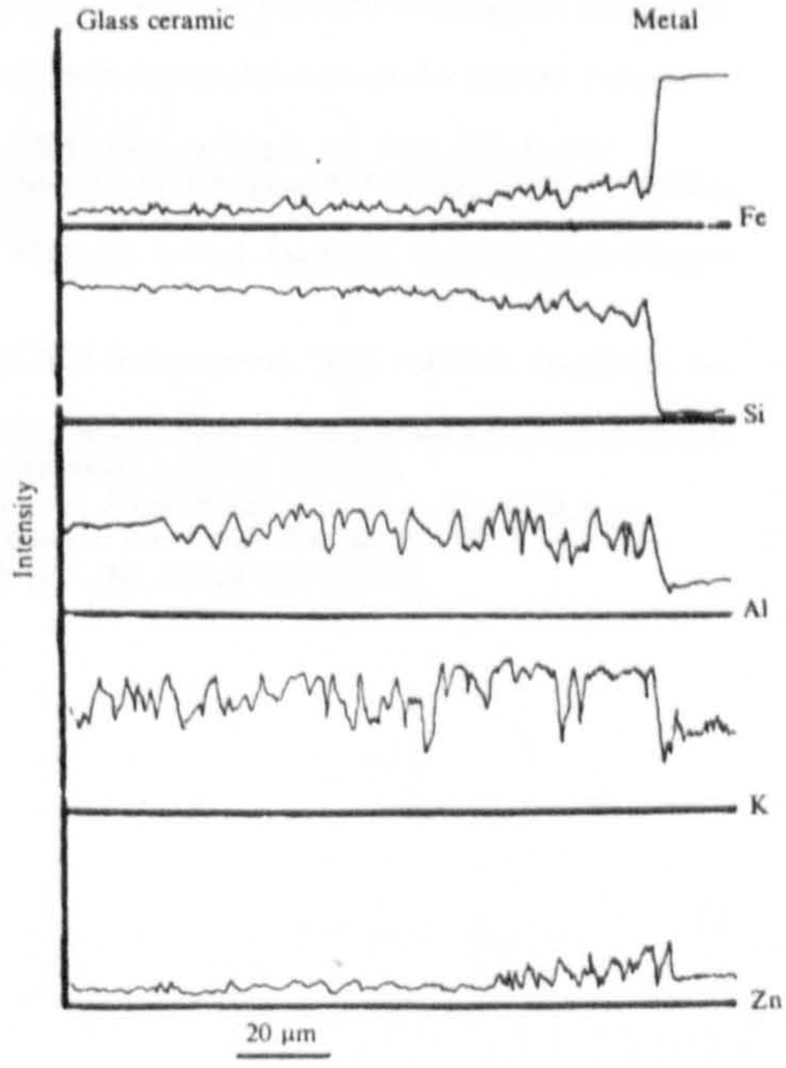

Figure 10. *Distribution of elements across the interface between a coating, subjected to heat treatment, on mild steel*

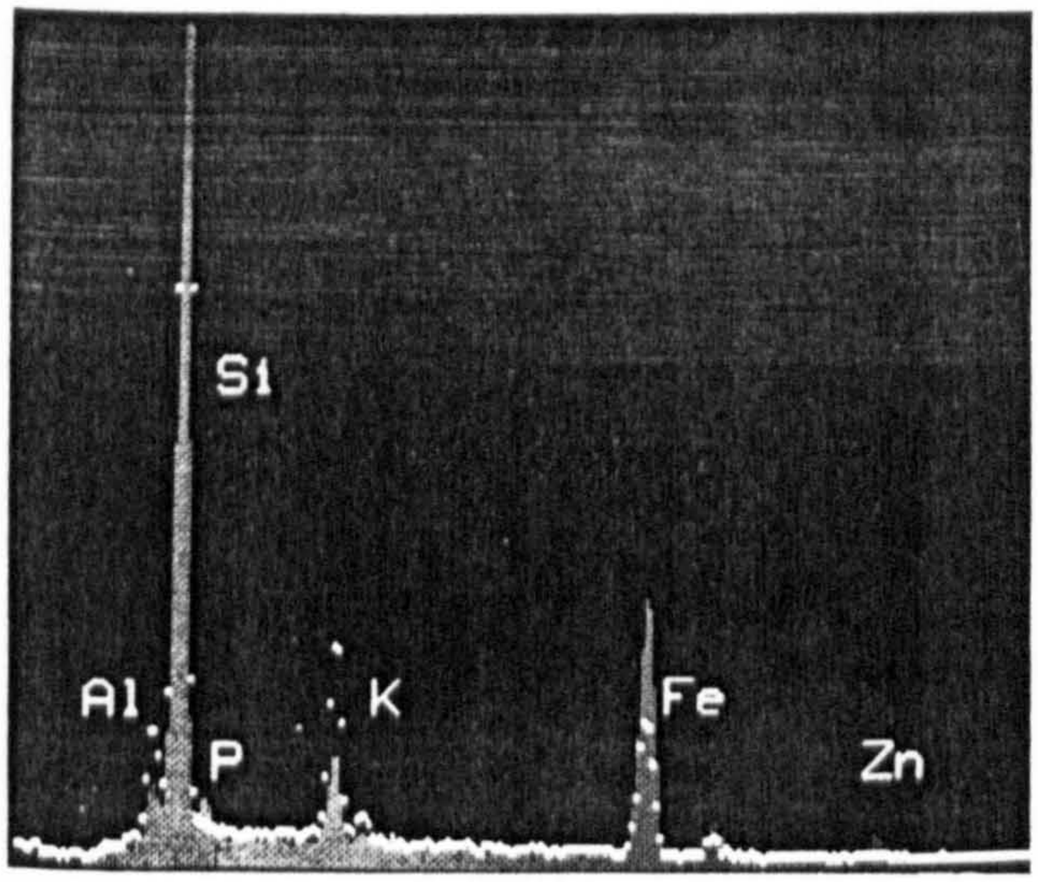

Figure 11. *X-ray spectra collected from the lithium iron silicate phase (full spectrum) and from the adjacent region (outlined spectrum)*

gradual slope. The peaks in the iron profile correspond to positions where lithium iron silicate crystals are present and the peaks in silicon to the uncrystallised regions. The potassium and zinc profiles show a build up in concentration at the interface, extending to 40 μm for potassium and 30 μm for zinc. The zinc profile closely follows the iron profile, due to the incorporation of zinc into the iron silicate structure. The potassium and aluminium profiles resemble the silicon profile, suggesting that these remain in the residual glass.

Figure 11 shows energy dispersive x-ray spectra collected from the iron rich crystal phase and from the adjacent glass areas. The zinc is seen to be incorporated in the crystal phase, while potassium and aluminium reside in the glass regions.

Conclusion

Interactions at the interface between glass and metal may have considerable effect on the microstructure and on the distribution of elements within the adjacent glass ceramics. The extent of the effects on the glass ceramic depends on several factors including glass composition, thermal history, substrate material, type of oxide film, and iron diffusion. The two metal substrates chosen show very different effects with nearly identical glass compositions due to the type of ion and the extent of its diffusion into the coating.

In the case of chrome–iron, the low rate of dissolution allows the retention of the oxide layer during firing and heat treatment. This is a consequence of the low solubility of Cr_2O_3 in the glass and the dissolution process being diffusion controlled. For a soda–lime glass, solubility is 0·006 mole fraction at 1300°C[10] and has been determined to be 0·007 mole fraction at 1000°C for this composition. The oxide provides a transition layer between the base metal and the coating, resulting in excellent adhesion. The adjacent microstructure is not noticeably affected by the very low chromium concentrations.

In mild steel the iron diffuses rapidly into the coating. The initial oxide layer is believed to be ferrous oxide. This and the deep blue colour of the coating after firing suggest that the iron is diffusing mainly as Fe^{2+}. The value for the diffusion coefficient of Fe^{2+} in a $Na_2O.2SiO_2$ glass at 1000°C is 5×10^{-8} $cm^2\ s^{-1}$.[11]

The high iron concentration present in the coating adjacent to the interface has a noticeable effect on the microstructure during heat treatment, with the precipitation of a lithium iron silicate phase in preference to both quartz and lithium disilicate. Bonding will now depend on the compatibility of this phase with the metal substrate.

Distribution of minor elements present in the coating is greatly altered. A loss of potassium occurs at the interface and a build up of zinc is observed immediately adjacent to the interface. During heat treatment the elements are redistributed with a build up of both potassium and zinc in the interface region. Zinc is incorporated in the lithium iron silicate phase and potassium remains in the residual glass.

References

1. Andrews, A. I. (1935). *Enamels*. The Twin City Printing Co., Champaign, Illinois.
2. Hlavac, J. (1983). *The technology of glass and ceramics*. Elsevier, Amsterdam. Pp. 399–411.
3. Onyshkevych, L. (1981). *Ceramic Engng Sci. Proc.* **2** (3–4), 166.
4. McMillan, P. W., Partridge, G., Hodgson, B. P. & Heap, H. R. (1966). *Glass Technol.* **7** (4), 128.
5. McMillan, P. W., Hodgson, B. P. & Partridge, G. (1966). *Glass Technol.* **7** (4), 121.
6. B. P. 1, 312, 700.
7. King, P. W., Tripp, H. P. & Duckworth, W. H. (1959). *J. Am. Ceram. Soc.* **42**, 504.
8. Pask, J. A. (1964). In *Modern aspects of the vitreous state*. Edited by J. D. Mackenzie. Butterworths, London. Pp. 1–28.
9. Pask, J. A. (1971). *Proc. Porcel. Enam. Inst. Tech. Forum* **33**, 1.
10. Manfredo, L. J. (1984). *J. Am. Ceram. Soc.* **67**, C-155.
11. Borom, M. P. (1968). *J. Am. Ceram. Soc.* **51**, 490.

References

1. Maswell, K.H., White, D., (1986), Vitreous Enamelling: A Guide to Modern Enamelling Practise, The Institute of Ceramics, Pergamon Press.

2. Andrews, A.I. (1961), Porcelain Enamels, The Twin City Printing Co., Champaign, Illinois.

3. Vargen, V.V. (1967), Technology of enamels.

4. Havac, J. (1983), The technology of glasses and ceramics, Elsevier, Amsterdam, pp 399-411.

5. Epper, R.A. (1971), Advances in Nucleation and Crystallisation of glasses, Am. Ceram. Soc., Colombus, Ohio.

6. Epper, R.A. and Mcleran, J.W. (1967), J. Am. Ceram. Soc. 50, (3), 152.

7. Patrick, R.F. (1951), J. Am. Ceram. Soc. 34, (3), 96.

8. The Metals Handbook (1964), 8th Ed. Vol. 2, Heat-treating, cleaning and finishing, A.S.M., Ohio, 573.

9. McMillan, P.W. (1979), Glass-Ceramics, Academic Press, London.

10. Watanabe, R.A., Caporali, R.W., Mould, R.G. (1967), Symposium on nucleation and crystallisation of glasses, Am. Ceram. Soc. pp23.

11. Stookey, S.D. (1956), B.P. 752, 243.

12. Atkinson, D. (1976), J. Mat. Sci., 11, (1) 994.

13. Kingery, W.D., Bowen, H.K., Uhlmann, D.R. (1976), Introduction to Ceramics, 2nd Edition, John Wiley and Sons, New York.

14. McMillan, P.W., Tesh, D. (1975), J. Mat. Sci., 10, (1) 621.

15. Partridge, G., (1981), GEC Journal of Science and Technology, 47, (2), 11.

16. Makarova, T.M., Moltchenov, V.S. (1970), Trans. Glass Inst., 39, 170.

17. Scott, K.T. (1984), British Ceramic Proceedings, 34, 8.

18. U.S. Patent (1965), 984, 446.

19. Davis, S.E., Partridge, G., Thomas, E.J.R., (1977), B.P. 1, 467, 459.

20. Andras, R.L., Chyungy, K., Readle, R.F., (1982), U.S. Patent 4, 358, 541.

21. R.C.A. Review, (1981), Special issue on porcelain enamelled steel boards for electrical applications, 44 (2).

22. McMillan, P.W. (1971), B.P. 1, 232, 621.

23. French patent (1967), 1, 543, 892.

24. McMillan, P.W., Partridge, G., (1969), B.P. 1, 171, 784.

25. McMillan, P.W., (1966), Glass Technol. 7, (4), 121.

26. Johnson, R.E. (1959), J. Phys. Chem. 63, (1), 655.

27. Aksay, I.A., Hoge, C.E., Pask, J.A., (1974), J. Phys. Chem. 78, (12), 1178.

28. Young, T., (1805), Phil. Trans. Roy. Soc., London, 95, 65.

29. Pask, J.A. (1964), Modern aspects of the viterous states, Vol. 3, Butterworth and Co., ppl-18.

30. Shartiss, L., Smock, A.L., (1951), J. Res. Nat. Bur. Stand. (U.S.), 46, 385.

31. Pask, J.A., Fulrath, R.M. (1962), J. Am. Ceram. Soc., 45, (12), 592.

32. Pask, J.A., Tomosia, A.P., (1985), Mat. Res. Soc. Proc., 40, 411.

33. Healy, J.H., Andrew, A.J., (1951), J. Am. Ceram. Soc., 34, (7), 207.

34. King, R.M., (1957), Metals Procds. Mfg., 14, 58.

35. Dietzel, A. (1934), Enailware-Ind., 11 (19), 161.

36. Stanely, H.F. (1934), J. Am. Ceram. Soc., 17, (6), 163.

37. King, B.W., Tripp, H.P., Duckworth, W.H., (1959), J. Am. Ceram. Soc., 42, (11), 504.

38. Kautz, K. (1936), J. Am. Ceram. Soc., 19, (4), 93.

39. Pask, J.A. (1971), Proc. Porcelain, Enamel Inst. Tech. Forum., 33, 1.

40. Ivanova, O.R., (1982), Protection of Metals, 18, (5), 609.

41. Pankratz, L.B., (1982), U.S. Bureau of Mines, Bulletin 672.

42. Brennan, J.J., Pask, J.A., (1973), J. Am. Ceram. Soc., 56, (2), 58.

43. Borom, M.P., Pask, J.A., (1966), J. Am. Ceram. Soc., 49, (1), 1.

44. Hoge, C.E., Brennan, J.J., Pask, J.A., (1973), J. Am. Ceram. Soc., 56, (2), 51.

45. ASTM C313, Adherence of Porcelain Enamel and ceramic coatings to sheet metal.

46. PEl T-29, Adherence of Porcelain Enamel Copper Coats Direct to Steel.

47. Tsien, W., Mecusker, J., Thaler, B., (1981), RCA Review, 4, (2), 210.

48. Civan, S., Huget, E.F., Risinger, R.J., (1974), J. Dent. Res., 53, 240.

49. Chang, M.P., Beech, D.R., (1980), Australian Dent. Journal, 25, 6.

50. Berndt, C.C., McPherson, R., (1981) Surfaces and Interfaces in Ceramic and Ceramic/Metal Systems (Ed J.A. Pask and A.G. Evans), Plenum N.Y., pp 619.

51. Suga, T., Elssner, G., (1985), Mat. Res. Soc. Symp. Proc., 40, 203.

52. ASTM C633.

53. Sced, I.R., Mclean, J.W., (1972), Brit. Dent. J., 132, (6), 232.

54. Fairhurst, C.W., (1985), Ceram. Eng. Sci. Proc., 6 (1-2), 66.

55. 2005 Araldite adhesive, Ciba-Geigy Plastics, Duxford, Cambridge.

56. Bowen, D.K., Hall, C.R. (1975), Microscopy of Materials, MacMillan Press, London.

57. Maurice, F., Meng, L., Tixies, R., (1978), Microanalysis and Scanning electron microscopy, Les Editions de Physique, Orsay, France, (English Ed).

58. Newbury, D.E. (1977), Scanning electron microscopy, 1, ITT Research Institute, Chicargo, pp553.

59. Fontaine, G., (1979), Chapter 2 in Microanalysis and Scanning Electron Microscopy, Les Editions de Physique, Orsay, France, (English Ed).

60. Reuter, W., (1972), X-ray optics and microanalysis, University Press, Tokyo, pp121-130.

61. Heinrich, K.F.J., (1966), X-ray optics and microanalysis, Hermann, Paris, pp159-165.

62. Cambridge Instruments, Rustat Road, Cambridge.

63. K.E. Developments, The Mount, Cambridge.

64. Link Systems, Halifax Road, High Wycombe, Bucks.

65. Henoc, J., (1979), Chapter 5 in Les Editions de Physique, Orsay, France.

66. Barbi, N.C., (1974), I.I.T., Research Institute, Chicago, pp151-157.

67. Reed, EDAX Edition, 3, (5), 10.

68. Philips Electronic Instruments, Philips Gloeilampentabriew, N.V., Eindhovern, Netherlands.

69. Klug, H.P. and Alexander, L.E., (1954), X-ray diffraction, Wiley.

70. Stanton and Redcroft, TG-750, Copper Mill Lane, London.

71. McMillan, P.W., (1974), Proc. 10th Int. Cong. on Glass, 1, Kyoto, Japan, pp14.1-14.2.

72. Headly, T.J., Loehman, R.E., (1984), J. Am. Ceram. Soc., 67, (9), 620.

73. Partridge, G., (1979), Glass Technol., 20, (6), 246.

74. Krupp Stahlwerke, Krupp Steel Co. Ltd., Speedwell Industrial Est., Staveley, Chesterford, Derbyshire.

75. Vitrostall

76. Thomas, D.R., Jones, D., (1983), The vitreous enameller, 11, 11.

77. Hauffe, K., (1965), Oxidation of metals, Plenum Press, New York.

78. Blythe Colours.

79. Dek Instruments Ltd., Model 240 printer, 22 Albany Road, Weymouth, Dorset.

80. Douglas, M.M., (1972), J. Mat. Sci., 7, (1), 184.

81. McMillan, P.W., Philips, S.V., Partridge, G., (1966), J. Mat. Sci., 1, (3),269.

82. Partridge, J.H., (1949), Glass-Metal Seals, The Society of Glass Technology, Sheffield.

83. Nath, P., Douglas, R.W., (1965), Phys. Chem. Glasses, 6, (6), 197.

84. Manfredo, L.J., McNally, R.N., (1984), Com. Am. Ceram. Soc. C155-C158.

85. Williamson, J., (1970), Mineralogical Magazine, 37, (291), 741.

86. Toshiharu, F., Whitel, W.B., (1983), Mat. Res. Bull., 18, (5),959.

87. Volf, M.B., (1984), Chemical approach to glass, Glass Science and Technology, 7, Elsevier, Amsterdam.

88. Thakur, R.L., (1971), Advances in nucleation and crystallisation in glasses, Am. Ceram. Soc., No. 5, 166.

89. Mackenzie, K.J.D., Brown, I.W.M., (1975), Phys. Chem. Glasses, 16, (1), 17.

90. Watkins, R.D., Lochman, R.E., (1986), Advanced Ceramic Materials, 1 (1), 77.

91. Tomsia, A.P., Pask, J.A., (1985), J. Am. Ceram. Soc., 68, (1), 20.

92. Wood, G.C., (1970), Oxidation of Metals, 2 (1), 11,

93. Giggin, G.S., Pettit, F.S., (1969), Trans of the Metallurgical Society of AIME, 245, 2509.

94. Chaplan, D. et al., (1970), Corrosion Science, 10, 9.

95. Borom, M.P., Pask, J.A., (1968), J. Am. Ceramic Soc., 51 (9), 488.

96. Borom, M.P., Pask, J.A., (1967), Phys. Chem of Glasses, 18 (5), 194.

97. Ritche, D., Schaeffer, H.A., White, D. (1983), J. mat. Sci. 18, (5),599.

98. Tamzawa, K . et al, (1981), Nippon Kaguka Kaishi, 13, 1523.

99. DiMarcello, F.V.., (1966), Am. Ceram. Soc. Bull. 45, 420.

100. Ivingery, C.D. and Lecron, J.A., (1966) Phys. Am. Chem. glasses, 1, 87.

101. Hagel, W.C. and Mackenzie, J.D., (1964), Phys. Chem. glasses, 5, 913.

102. Wollast, R. et al, (1973), Silic. Ind. 38, 169.

103. Schaeffer, H.A., (1971) In. Congr. Glass. Versailles, 1, 133.

104. Johnson, J.R., (1964), J. Am. Ceram. Soc. 47[4], 198.

105. Yung, A.A., (1959), J. Chem. Phys. 31[6], p. 1627.

106. Beier, W. and Frischat, G.H., (1980), J. Non. Cryst. Solid. 38/39, 569.

107. Mulkin, V.I. and Mogutnov, B.M., (1961) Dokl. Akad. Nauk. SSS12 141 1127.

108. (a) Negodaev, G.D. et al, (1971), Radionimiya 13 651.
(b) Negodaev, G.D. et al, (1972), cv. Electrochem, 8, 227.

109. Charter, P.T. et al, (1952), J. Soc. Glass. Technol., 36, (170), 142.

110. Lacy, A.M., Pask. J.A. (1970), J. Am. Ceram. Soc., 53, (10), 559.

111. Richard, G.M. Demard, S.L., (1974), Enamail Metal, 20, 1.

112. Nedelikovic, A.I., (1976), The Vitreous Enameller, 27(3), 45.

113. Tatrahashi, K., Miura, Y., (1974), 10th Int. Cong. Glass, Sec.8, 15.

114. Stookey, S.D., (1959). Glastech. Ber. V. Int. Glass. Cong., 32, 5.

115. McMillan, P.W., (1970), B.P. 943, 599.

116. Stookey, S.D., (1960), B.P. 829,447

117. Turnbull, D., (1956), Solid State Physics, Vol. 3, Academic Press.

118. Jackson, K.A., (1967), J. Chryst. Growth, 1, 1.

119. Onsager, L., (1945), N.Y. Acad. Sci., 46, 241.

120. Crank, J., (1975), Mathematics of diffusion, 2nd Ed., Clarendon Press, Oxford.

121. Oishi, Y. Cooper, A.R., Kingery. W.D., (1965), J.Am. Ceram. Soc., 48 (2), 88.

122. Maxwell C.J. and Brangs M.P. (1984). Glass Technol. 24 (5), P244.

123. Loughborough Consultants Limited.

124. Smith, E.B., (1983), Basic Chemical Thermodynamics, 3rd Ed., Oxford University Press, Oxford.

Figure B4. The Willingdon Levels cross-profile